Swirling flows in automotive aftertreatment systems

Padula, Gianluca

Award date:
2021

Awarding institution:
Coventry University

Swirling flows in automotive aftertreatment systems

by

Gianluca Padula

January 2021

Faculty of Engineering, Environment and Computing

A thesis submitted in partial fulfilment of the University's requirements for the Degree of Doctor of Philosophy

Certificate of Ethical Approval

Applicant:

Gianluca Padula

Project Title:

CFD modeling of swirling flows in automotive aftertreatment systems

This is to certify that the above named applicant has completed the Coventry University Ethical Approval process and their project has been confirmed and approved as Low Risk

Date of approval:

11 October 2019

Project Reference Number:

P95665

Acknowledgements

First of all, I would like to express my sincere gratitude to my director of studies, Dr. Svetlana Aleksandrova, for guiding me throughout this work and for her continuous support. My gratitude goes also to Dr. Humberto Medina and Prof. Stephen Benjamin for their precious advice and insightful discussions. A special thanks to Mr. Lawrence King and Mr. Robert Gartside for their endless support and the practical guidance during the time spent in the laboratory.

I would like to acknowledge my PhD colleagues and friends Dimitar, Marco, Samuel, Panos, Jono, Dhila, Abhi and Tasos. I really treasured the time spent together: you have all been part of this journey and you have managed to make it amazing.

All my gratitude goes to my mum and dad, for their endless and unconditional love, support and encouragement: you have always been by my side and always inspired me. To Rossella and Delio for always believing in me and for all the moments of joy and happiness that you give me. To my little wonderful precious niece Ludovica: you fill my heart with joy and give me a reason to smile every day.

I want to thank someone special, Azzurra, for her immense support and encouragement, for being there every time I needed and for making me laugh even in my darkest times. Thank you so much for all you have done during these past months and thank you, from the bottom of my heart, for being part of my life, making it better every day.

Finally, I would like to acknowledge my dear friends Nunziante, Marco, Federica, Fabio, Claudio, Anita, Lorena and Matteo for all the cheerful moments and the wonderful time spent together.

Abstract

Swirling flows are present in many engineering applications, such as emissions aftertreatment or turbomachinery. However, due to the complex physics of the flow involving high pressure gradients, a range of flow instabilities and highly anisotropic turbulence, experimental and numerical studies of such flows are challenging. This study is focused on improving our understanding of the swirling flows, along with the development of experimental and numerical methods suitable for practical applications.

One important topic overlooked in the existing literature is the effect of asymmetry (often encountered in applications) on the swirling flows. In this study, a swirling flow in a sudden expansion with a downstream resistance has been used to investigate the effect of offset inlet on the flow structure. It is shown that the flow undergoes significant changes, with the swirling "jet" in the diffuser following a complex path rather than proceeding in the axial direction, and both the wall separation zone and the central recirculation zone change their size and shape. This is a unique 3-dimensional effect that cannot be observed in 2-dimensional geometries often used. The impact of asymmetry on the global parameters such as flow uniformity and total pressure loss (often used for device performance assessment) has however been shown to be small.

The study provides a critical assessment of some measurements techniques adopted for the study of swirling flows, such as Hot Wire Anemometry (HWA), wall pressure measurements and Particle Image Velocimetry (PIV). The experimental data collected for a simplified geometry (annular pipe) provides detailed information about the swirling flow downstream a swirl generator, which can be used for the definition and development of inflow boundary conditions for complex flow modelling approaches (LES and DES) and for model validation. It has also been shown that the effect of swirl dominates the flow structure, and that the Reynolds number has no significant effect on the flow for the cases considered.

Finally, a new formulation for the model of high resistance devices has been proposed and developed. The novel porous modelling approach allows to retain the low computational requirements of standard porous medium models and their capability to provide reasonable predictions of first order properties, such as velocity, while improving the prediction of flow structure and turbulence downstream the device where

the classical porous medium approach fails. Another advantage of the new approach is its high flexibility for the inclusion of the complex flow passages to account for the geometry of the device.

Table of contents

List of figures

List of tables

Nomenclature

Abbreviations

ASM	Algebraic Stress Model
CAD	Computer Aided Design
CFD	Computational Fluid Dynamics
CV	Control volume in CFD
DCC	Direct Cross Correlation
DES	Detached Eddy Simulation
DNS	Direct Numerical Simulation
FFT	Fast Fourier Transform
GUI	Graphic User Interface
HWA	Hot Wire Anemometry
LDA	Laser Doppler Anemometry
LES	Large Eddy Simulation
OFA	Open Frontal Area
PIV	Particle Image Velocimetry
RANS	Reynolds Averaged Navier Stokes
ROI	Region Of Interest
RSM	Reynolds Stress Model
SF	Shape function for modified porous medium approach

VFM	Viscous Flow Meter

Greek letters

α	Porous medium viscous resistance coefficient ($kg/m^3\,s$)
α_p	HWA probe yaw angle (°)
α_{mod}	Modified formulation of the viscous resistance coefficient ($kg/m^3\,s$)
β	Porous medium inertial resistance coefficient (kg/m^4)
Δp	Pressure drop in the porous medium formulation (Pa)
Δp_{PM}	Pressure drop through the monolith section in CFD results (Pa)
ε_{piv_N}	Standard deviation from the running average in PIV
γ_s	Flow angle (°)
ρ	Air density (kg/m^3)
θ_p	HWA probe pitch angle (°)
θ_s	Angle between swirl generator blocks (°)
ζ_Y	Vorticity component normal to the XZ section (rad/s)

Symbols

$\bar{U}$	Mean velocity (m/s)
$\bar{U}_N$	Running average in PIV measurements (m/s)
$\dot{m}_{emp}$	Empirical mass flow rate through the VFM(g/s)
A	Area of the section (m^2)
C_p	Pressure coefficient
C_{hr}	High resistance coefficient used for the SF formulation
D	Displacement between inlet and sudden expansion axis (m)
d_h	Hole diameter for pressure measurements (m)
d_t	Pressure tap diameter (m)

$E(f)$	Energy density spectrum
f	Frequency (Hz)
f_s	Sampling frequency (Hz)
f_t	Frequency of interest (Hz)
$f_{app}Re_x$	Apparent Fanning friction factor in Shah's correlation
f_{app}	Apparent Fanning friction factor in Shah's correlation
fRe	Fanning friction factor in Shah's correlation
h	Pitch factor coefficient in HWA measurements
H_d	Hydraulic diameter of a monolith channel (m)
k	Yaw factor coefficient in HWA measurements
$K(\infty)$	Incremental pressure drop number in Shah's correlation
L	Reference length (m)
L_h	Hole depth for pressure measurements (m)
L_s	Signal length for frequency analysis
l_s	Turbulence length scale (m)
L_{exp}	Monolith length in experiments (m)
L_{sim}	Porous region length in simulations (m)
$P(f)$	Power spectral density
p_{back}	Differential back pressure at the VFM (Pa)
p_{VFM}	Differential pressure through the VFM (Pa)
r_i	Inner radius of the annular pipe (m)
r_o	Outer radius of the annular pipe (m)
Re_x	Reynolds number calculated using the hydraulic diameter of the monolith channel
Re_{in}	Reynolds number calculated at the swirl generator inlet section

Re_{noz}	Reynolds number calculated at the swirl nozzle section
S	Swirl number/level
T_i	Turbulence intensity
U	Axial velocity component (m/s)
u'	Root-mean-square of the velocity fluctuations (m/s)
u_s	Superficial velocity (m/s)
U_x	Local velocity component at the HWA (x direction) (m/s)
U_y	Local velocity component at the HWA (y direction) (m/s)
U_z	Local velocity component at the HWA (z direction) (m/s)
U_{eff_n}	Effective cooling velocity HWA with probe *normal* (m/s)
U_{eff_p}	Effective cooling velocity HWA with probe *parallel* (m/s)
U_{eff}	Effective cooling velocity HWA (m/s)
V	Tangential velocity component (m/s)
x^+	Non-dimensional axial coordinate in Shah's correlation

Chapter 1

Introduction

1.1 Background

Air pollution is globally recognised as a primary source of disease and premature mortality (Teitelbaum et al. (1993), Landrigan et al. (2018), Das and Horton (2018), Fowler et al. (2020)). During the last year, a strong correlation between air pollution and COVID-19 outbreak has been observed in many countries, suggesting a possible link between poor air quality and increased mortality risk due to COVID-19 exposure, as reported in the studies by Magazzino et al. (2020), Marquès et al. (2021) and Fattorini and Regoli (2020) among others.

Several countries have adopted regulations on the pollutant emissions, aiming to reduce their impact on mortality rates and diseases (Fowler et al., 2020; Thakrar et al., 2020). The *EU Clean Air policy* adopted by the EU countries (European Commission, 2013) and the *Clean Air Act* adopted by the USA have demonstrated a strong effect on the reduction of deaths and diseases related to air pollution. The U.S. EPA has estimated that the introduction of the Clean Air Act has prevented (by 2020) nearly 230,000 deaths and reduced the impact of related diseases (e.g. myocardial infarction and asthma) by the order of million of cases, not to mention the high benefits achieved in terms of economy (USEPA Office of Air and Radiation, 2010).

The *Air quality in Europe* report by EEA (2020) has identified several sources of air pollution in Europe:

- burning of fossil fuels (e.g. for electricity generation, transport and households);
- industrial processes;
- waste treatment;

- agriculture;
- natural sources (among which volcanic eruptions, windblown dust, sea-salt spray).

Transport has been identified as a substantial contributing factor to air pollution (Colvile et al., 2001) and the most recent data published for Europe (Figure 1.1 from EEA (2020)) confirm that the emissions of pollutants from on road and off-road transport still represents a significant share of the total emissions, in particular for nitrates (NO_x), particulate matter (PM), carbon oxide (CO) and black carbon (BC).

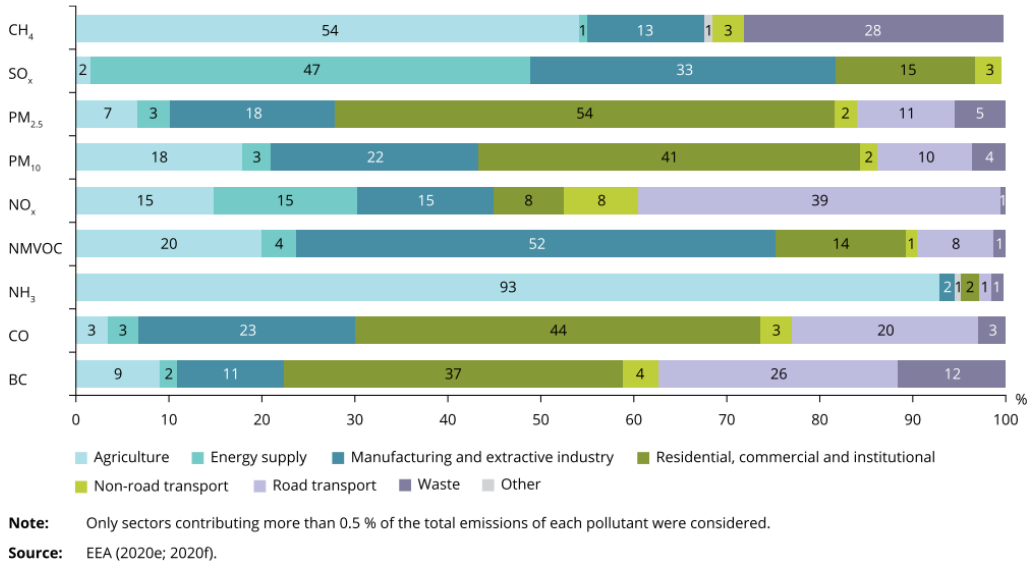

Figure 1.1 Contribution to EU-28 emissions from the main source sectors in 2018 of several air pollutants: methane (CH_4), sulphates (SO_X), nitrates (NO_X), particulate matter (PM_{10} and $PM_{2.5}$), ammonia (NH_3), non-methane volatile organic compounds ($NMVOCs$), carbon oxide (CO) and black carbon (BC). Source: EEA (2020).

1.1.1 Emission standards in automotive sector

Stringent regulations to tackle the pollutant emissions from the automotive sector have been implemented by several countries all over the world, since the first standards proposed in EU and USA in the 1970s (Winkler et al., 2018). A significant reduction of the emissions from the transport sector has been observed in the EU and in the USA (Figure 1.2) during the past 3 decades, as a consequence of the *EURO* emission standards (currently *EURO 6*) and the *Tier* emission standards (currently *Tier 3*) respectively.

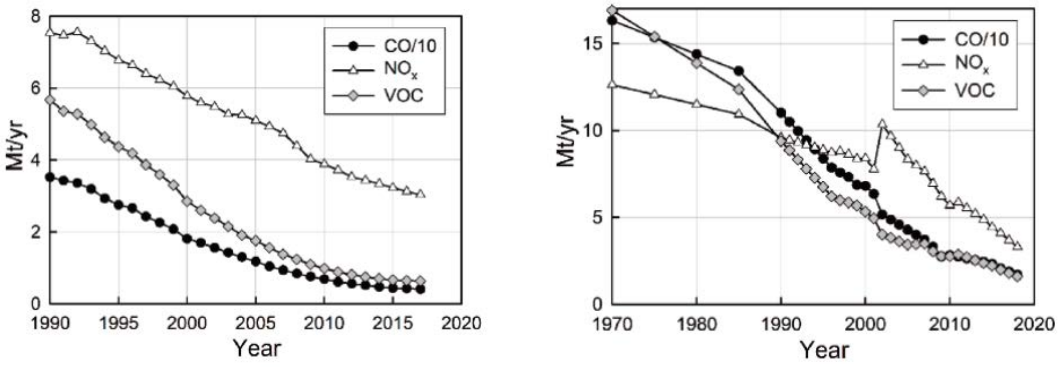

(a) EU **(b)** USA

Figure 1.2 Trends in emissions of air pollutants from highway vehicles: nitrates (NO_X), carbon oxide (CO) and volatile organic compound (VOC) emissions in EU (a) and USA (b). Figure elaborated by Wallington et al. (2020) from data published in 2018 by the European Environment Agency (EEA) and the U.S. Environmental Protection Agency (EPA).

More efforts are required to further reduce the pollutant emissions in the automotive sector, as shown by Edwards et al. (2017) for the CO_2 emissions. In addition, it has been shown by the studies of Hooftman et al. (2018) and Mera et al. (2019) that the real driving emissions of NO_x from passenger cars can be higher then the limits imposed by the regulations. Thus, more studies are required to improve the efficiency of engines and after-treatments systems to further reduce pollution from the automotive sector.

1.1.2 Catalytic converters and exhaust pipe

The use of catalytic converters in after-treatment systems to reduce the pollutant emissions from internal combustion engines has been proven to be effective (Koltsakis and Stamatelos (1997), Kašpar et al. (2003), Piumetti et al. (2015), Joshi (2020), Beall and Cutler (2020)). The reduction of the pollutants (such as CO or NO_x) occurs in the monolith substrate of the catalytic converter (Figure 1.3a). The monolith consists of a honeycomb structure with small channels (hydraulic diameter of ≈ 1 mm), with a typical cell density of 400 cpsi in automotive applications (Kašpar et al., 2003). The ceramic or metallic substrate of the monolith is coated with precious metals (e.g. platinum Pt) which represent the active catalytic materials (Govender and Friedrich, 2017). The recent application of 3D printing techniques for the production of monoliths widen the possibilities for the design of complex shapes, with a reduction of the material waste during the production phase (Thakkar et al. (2017), Ruiz-Morales et al. (2017), Parra-Cabrera et al. (2018)).

The monolith is enclosed in a container with a *matting* material to absorb the vibrations (Figure 1.3a). The cross sectional area of the catalyst is often larger then the

exhaust pipe cross section, thus increasing the contact surface between exhaust flow and catalyst (Figure 1.3a,b). The presence of the expansion upstream the catalyst is beneficial to reduce the exhaust flow velocity before impacting on its surface (Bella et al., 1991). Consequently, a redistribution of the flow at the catalyst front surface occurs, as will be shown in Chapter 5 and Chapter 6. The design of the exhaust system aims to reduce the pressure drop through the catalyst and increase the flow uniformity upstream to improve the reduction of the pollutants.

The exhaust pipe shape is often the result of a compromise between the constraints imposed by the car and the space available (Figure 1.3b). As a result, a displacement of the pipe upstream and/or downstream the catalytic converter section is often encountered in automotive applications. As it will be shown in Chapter 6, the misalignment between the pipe inlet and the diffuser axis has a significant effect on the flow entering the catalyst due to the asymmetry.

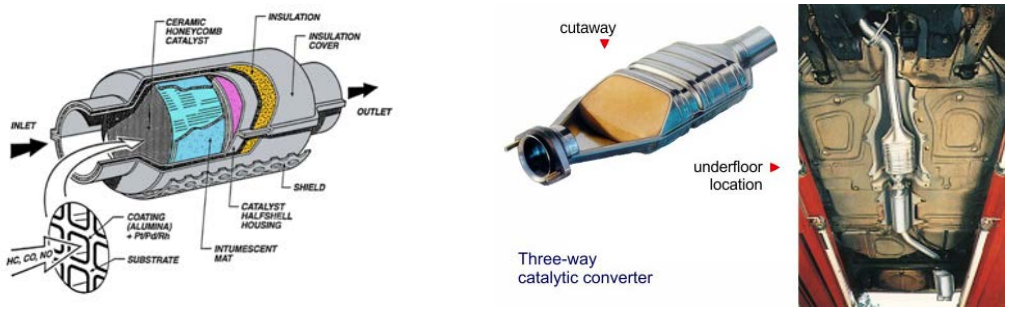

(a) Converter schematic **(b)** Exhaust pipe

Figure 1.3 Schematic of a three-way catalytic converter with a ceramic substrate for a passenger car (a). Source: MECA (2009). Three-way catalytic converter enclosure and exhaust pipe on a gasoline car. (b) Source: Majewski (2000).

In order to reduce the cost and time of the aftertreatment system design stage, computer aided engineering is widely used. Computational Fluid Dynamics (CFD) simulations are a powerful tool for predicting gas flow, heat transfer and species conversion in the catalysts systems, and are widely used in industry to design and optimise after-treatment systems, as reported in Su et al. (2019). However, the high computational costs of high fidelity CFD simulations mean that simplified models such as porous modelling approach are used for catalysts and filters. These models have several drawbacks, in particular low accuracy of the flow predictions downstream of the catalyst (Cornejo et al., 2018b).

The prediction of the flow upstream and downstream the multiple high resistance devices that constitute an after-treatment system is crucial since those devices are commonly used in series. A new formulation for the model of such devices is proposed in Chapter 7.

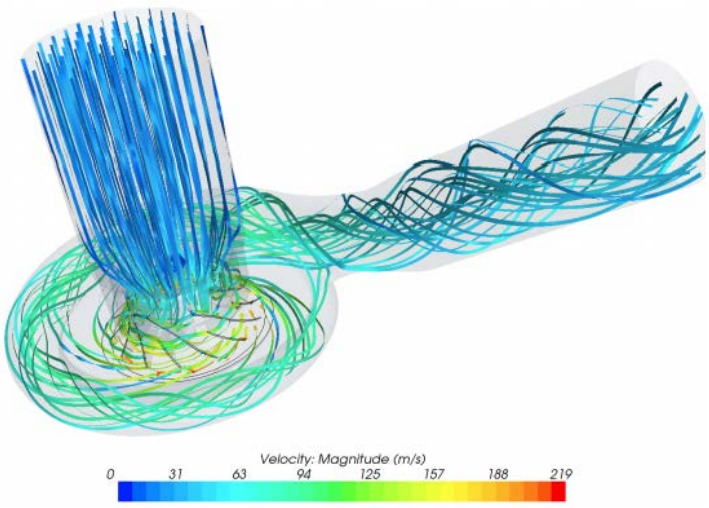

Figure 1.4 CFD simulation of a turbocharger. Source: Bergqvist (2014).

1.1.3 Turbochargers

While the role of the aftertreatment systems is to remove pollutants generated by the engine, pollution reduction "at source", i.e. during the combustion process, is the primary means of overall pollution reduction, improving fuel efficiency and reducing CO_2 emissions in particular. One of the ways to reduce the pollutant emissions and improve fuel consumption is engine downsizing coupled with turbocharging (Lecointe and Monnier (2003), Hiereth and Prenninger (2007), Fraser et al. (2009), Heywood (2018)). The presence of the turbocharger imposes rotation on the flow and, consequently, the exhaust gases exiting the engine presents a residual swirl component, due to the presence of the turbine blades inside the turbocharger (Figure 1.4).

The swirl component in the flow entering the diffuser causes a significant redistribution of the flow entering the catalytic converter, as shown in Chapter 5 and Chapter 6.

1.2 Thesis outline

Chapter 2 presents a literature review of experimental and numerical studies on swirling flows. Chapter 3 presents a description of experimental setup and the methodology used for the measurements, the numerical simulations and the uncertainty analysis of the results.

The results of the experimental and numerical activities carried out on the pipe with annular cross section, which has been used to study fundamental properties of swirling flows, and to refine experimental and numerical techniques are included in Chapter 4.

The analysis of swirling flows inside the axisymmetric sudden expansion with downstream resistance is presented in Chapter 5, where a laser measurement technique (Particle Image Velocimetry) is used to gain details of the flow inside the sudden expansion region, and for assessment and validation of the CFD simulations carried out for the same geometry. In Chapter 6, asymmetry is added to the sudden expansion configuration in order to establish how the flow in an automotive aftertreatment system is affected by a combination of asymmetry and swirl.

Chapter 7 presents a novel approach to modelling high resistance devices (based on a porous medium model) that improves the prediction of the flow properties downstream the monolith and allows flexibility in the definition of the geometry of the device modelled.

Finally, Chapter 8 presents the conclusions of the current study, highlights the novelty of the work and proposes some recommendations for future work.

Chapter 2

Literature review

The complexity of swirling flows has been has been widely studied, for a wide range of conditions and configurations. The presence of high radial pressure gradients, vortex breakdown, unsteady phenomena (such as precessing vortex core), in addition to turbulent shear layers make the study of swirling flows particularly complex. A good understanding of the mechanisms governing such flows is needed to make meaningful progress in applications.

The review presented in this chapter provides an overview of some relevant studies from literature, aiming to identify the potential and limitations of the experimental and numerical techniques used in the study of confined swirling flows.

2.1 Swirling flows in engineering applications

A *swirl motion* can be observed in numerous natural flows, such as cyclones, tornadoes, blood in veins and arteries or water at the intersection between rivers and waterfalls. The direct and/or indirect use of swirling flows is common to several engineering and industrial applications, ranging from aerospace and automotive to chemistry, meteorology and food preparation. The presence of a swirl component in the flow has been proven to be beneficial: it can improve and promote *mixing* (Alahmadi and Nowakowski, 2016; Hoekstra et al., 1999; Hreiz et al., 2011; Zhou, 2017) or *stabilise combustion* systems (Lilley, 1977; Syred, 2011) and improve *heat transfer* (Chang and Dhir, 1995; Martemianov and Okulov, 2004; Promvonge et al., 2012; Thulukkanam, 2013).

At the same time, uncontrolled swirling motion could be problematical or even detrimental. Problematic swirl motion has been identified in the formation of the roll-up vortices downstream wings, where the swirl motion is undesired, leading to increasing drag. Problems arise in particular configurations, such as at the leading edge of delta (or

Gothic) wings, as known since the pioneering study of Peckham and Atkinson (1957). The formation of the roll-up vortices at the leading edges of such wings can lead to a sudden change in the flow structures, with a sudden lift drop at high angles of attack, which could lead to uncontrolled stall (Gursul, 1994).

The presence of swirl is helpful to achieve the separation of the single components in multiphase flows, leading to the development of the *centrifugal cyclone separators*. The increased centrifugal force due to the presence of the swirl component pushes the denser phase towards the external part of the separator, while the less dense phase follows the path of axial internal flow (Dhakal et al., 2014; Vedantam and Joshi, 2006).

The use of swirl in *combustion* has been extensively investigated, because it increases mixing between air and fuel and improves the stability of the flame (Lilley, 1977). The interaction between the flow and the rotor and stator blades in the turbojet engines is an active field of research. The presence of a residual swirl component has been observed in the exhaust gases flowing out from the combustion chamber (Syred, 2006).

Swirl injectors are used to increase the atomization of the fuel, with a beneficial effect in terms of combustion efficiency and a consequent reduction of pollutant emissions (Ceglia et al. (2014), Moon et al. (2008)). The flow exiting gas turbines, with high degree of swirl, and its interaction with the control surfaces is one of the issues investigated with both experiments and numerical simulations (Roux et al., 2005). A similar effect has been observed in internal combustion engines. The use of turbo-charged engines causes the presence of a residual swirl component in the exhaust flow, with a direct impact on the efficiency of the after-treatment systems used to reduce pollutant emissions (Zhang and Romzek, 2008).

2.1.1 Properties of swirling flows

The analysis of the physics involved in the flow motion with increasing intensity of swirl has been made in several studies. Detailed reviews of both numerical and experimental studies on swirling flows have been presented by Lilley (1977),Gupta et al. (1984), Sloan et al. (1986) and, more recently, by Lucca-Negro and O'Doherty (2001) and Syred (2006). The above mentioned works are used in the current study as a primary source for the discussion.

2.1.2 Swirl level

Different non-dimensional parameters have been proposed in literature to quantify the swirl intensity in a flow (Steenbergen, 1995). These include a *swirl number*, for which several formulations exist. The most commonly used formulation of swirl number

S usually defines it as *the ratio of the axial flux of momentum to the axial flux of axial momentum times the equivalent exit radius* (Lucca-Negro and O'Doherty, 2001). This definition leads to the following expression for the swirl number for axial symmetric cases

$$S = \frac{1}{R} \frac{\int_0^R r^2 UW \, \mathrm{d}r}{\int_0^R rU^2 \, \mathrm{d}r} \tag{2.1}$$

In which R is the radius of the pipe, U is the axial component of the velocity and W is the tangential component of the velocity.

The use of Equation 2.1 allows the classification of swirling flows, distinguishing between *low* to *moderate* swirl from *high* swirl flows. The values used to identify the thresholds between the three categories vary upon the different studies and depend on the definition adopted. In the current thesis, the classification is based on the study by Gupta et al. (1984), for which high swirling flows are defined when $S > 0.5$.

The complexity of swirling flows has been assessed in several experimental studies. Early studies aimed to identify the flow structures, trying to understand how they generate and evolve in the flow field with increasing swirl levels (Benjamin, 1962; Chanaud, 1965; Harvey, 1962; Lewellen, 1971; So, 1967). The differences between the flow regimes identified with the swirl level have been observed in the large scale effects on the flow. The temporal evolution of a swirling jet for increasing swirl level is shown in Figure 2.1, reported in the review by Lucca-Negro and O'Doherty (2001).

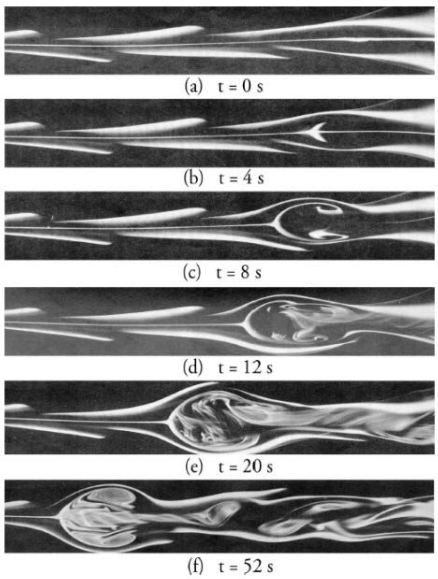

Fig. 6. Formation of an axisymmetric bubble by core swelling (from Ref. [16]).

Figure 2.1 Formation of the axisymmetric recirculation bubble. From Lucca-Negro and O'Doherty (2001)

When the *swirl* velocity component (also defined as *tangential* or *azimuthal* component) is added to a turbulent jet its large scale characteristics are modified, so that the jet is very different from the corresponding non-swirling case (Lucca-Negro and O'Doherty, 2001). By increasing the swirl level an axisymmetric recirculation zone appears in the flow field for the first time (the *vortex breakdown* in Figure 2.1b-d). With higher swirl, the recirculation zone moves upstream (Figure 2.1e-f).

Central recirculation zone

At low and moderate swirl levels, the axial and tangential components are not coupled and the adverse pressure gradient is not strong enough to cause axial recirculation (Lucca-Negro and O'Doherty, 2001). Therefore, if compared to the non-swirling turbulent free jet, the main change caused by the swirl component is an induced radial pressure gradient. This results in the growth of a spiral structure as shown in Figure 2.2a for S = 0.13. With increasing swirl levels, the adverse pressure gradient becomes strong enough to overcome the kinetic energy of the fluid particles in the axial direction. This causes the growth of a recirculation zone along the centreline of the flow when a critical swirl level is reached, Figure 2.2b for S = 0.48.

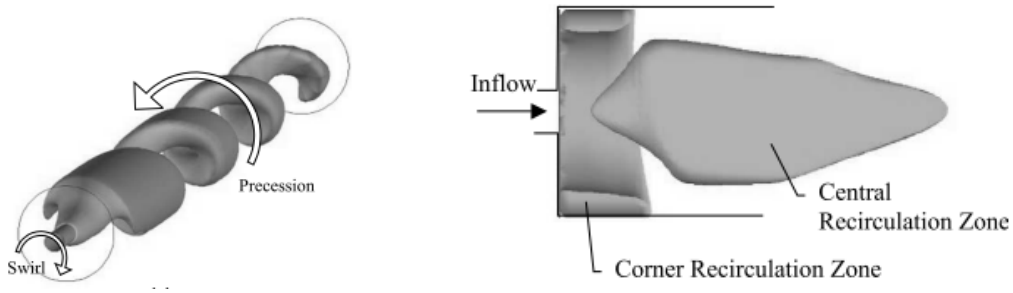

(a) S = 0.13 **(b)** S = 0.48

Figure 2.2 Swirling flow (S = 0.13) exhibiting its spiral nature (a). Swirling flow exhibiting the central recirculation bubble (b). Source: Guo et al. (2002).

The formation of the central recirculation zone has been investigated in several studies, e.g. Gupta et al. (1984) and Syred (2006). A schematic representation (Figure 2.3a) of the process leading to the formation of the central recirculation region is reported in the study by Syred (2006). The process leading to the formation has been summarised (Syred, 2006) in the following steps:

- the presence of swirl in the flow exiting the nozzle causes a radial pressure gradient ($\propto w^2/r$);

- the tangential component of the velocity, thus the radial pressure gradient, decreases because of the expansion;
- a negative axial pressure gradient near the axis consequently arises, inducing a reverse flow that leads to the formation of the central recirculation zone;

The formation of the central recirculation zone thus depends on the decay of the swirl component in the expansion direction. The typical structure of the central recirculation zone is *toroidal*, as shown in Figure 2.3b for a swirl number S = 1.57.

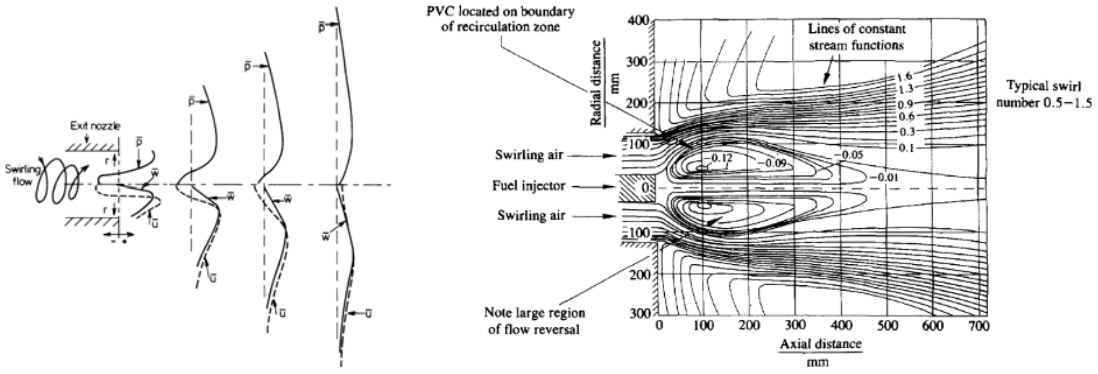

(a) CRZ formation **(b)** CRZ structure

Figure 2.3 Diagram of the process that leads to the formation of the central recirculation zone (a). Typical shape of a central recirculation zone for S = 1.57 (b). Source: (Syred, 2006)

The presence of a recirculation bubble could be interpreted as a bluff body around which the fluid is forced to flow, as suggested by Harvey (1962). Under such conditions, a form of the so called *vortex breakdown* phenomenon occurs. The central recirculation zone increases its dimensions with increased swirl levels, while the stagnation point moves upstream.

The formation of the central recirculation zone has been explained by Escudier and Keller (1985) as the result of a shear-layer instability. Their experiments proved that with increasing swirl a cold flow exhibits transition from super-critical to sub-critical conditions across the recirculation region. However, the authors suggested that the reduction of density associated with the increased temperature in combustion could cause a different behaviour of the flow.

Precessing vortex core

A periodic oscillatory motion around their core axis has been observed in some swirling flows. This particularly unsteady complex flow structure could lead to asymmetry in the flow and it is identified as *Precessing Vortex Core* (PVC). The PVC is

usually associated with the vortex breakdown and the recirculation on the centreline axis, but some experimental studies, such as the one of Dellenback et al. (1988) have shown that it could occur even at low swirl levels.

The vortex core becomes unstable and departs from the symmetry axis. The peculiar characteristics of the phenomenon is the precession around the axis (Chanaud, 1965) with a frequency that increases with increased swirl levels (Figure 2.4). As highlighted by Syred in its review (Syred, 2006), this phenomenon is particularly problematic in combustion systems, since it leads to instability and oscillations of the flame.

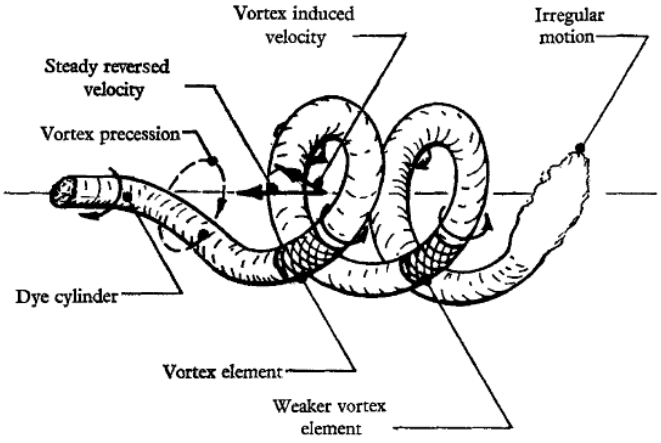

FIGURE 5. A sketch of the periodic motion in the vortex whistle at large amplitude as deduced from observation. The motion is that of a rotating spiral vortex.

Figure 2.4 Schematic of the periodic motion of a rotating spiral vortex typical of the PVC phenomenon. Source: Chanaud (1965).

2.1.3 Experimental studies of swirling flows

Swirling flows are highly sensitive to the disturbances caused by intrusive probes (Harvey, 1962) and more in general instrumentation (e.g. a probe holder), which can alter the flow distribution and cause an erroneous measurement, for example when Hot-Wire Anemometry (HWA) is used. This aspect is particularly relevant for confined swirling flows, since the competing forces acting on the fluid can be highly altered even by small probing elements (Lucca-Negro and O'Doherty, 2001; Syred, 2006). The development and application of non-intrusive techniques has made a great contribution to the understanding of the characteristics of a swirling flow. The use of non-intrusive methods, such as Laser Doppler Anemometry (LDA) and Particle Image Velocimetry (PIV), has given quantitative results about the velocity flow field and its fluctuations and a significant improvement in the understanding of swirling flows (Escudier et al., 1980).

Comprehensive reviews on the numerous studies on swirling flows have been included in several publications, e.g. Lucca-Negro and O'Doherty (2001); Syred

(2006); Vondál and Hájek (2011). Here, only some relevant examples are reported, to emphasise that the use of non-intrusive techniques has allowed a more detailed characterisation of swirling flows.

In the experiment of Dellenback et al. (1988) a swirling water flow was forced through an axisymmetric expansion with a 1:2 ratio. The axial and tangential velocity components were measured using the LDA technique. From the analysis of the results, the authors gained a better understanding of the Precessing Vortex Core (PVC), an unsteady phenomenon associated with the swirling flows. The study from Dellenback et al. (1988) has provided experimental data for the validation of several numerical studies.

More recently, together with LDA studies, such as the one of Shiri et al. (2008), the application of the Particle Image Velocimetry (PIV) has given better insight into the flow features typical of swirling flows, as shown by Graftieaux et al. (2001) and by Mak and Balabani (2007). Both studies present the implementation of the Proper Orthogonal Decomposition (POD) analysis, used to extract more details from the PIV data. This technique is based on the decomposition of the velocity field (or the vorticity field) into eigenfunctions, called POD modes. Each mode represent a different amount of kinetic energy associated with the flow, i.e. a different coherent structure. By using this approach, the above mentioned studies have shown that it is possible to quantify the effects of swirl on the energy redistribution. In particular, Mak and Balabani (2007) have calculated that the energy associated with the first mode contains the 91.86% of the total kinetic energy for the non-swirling case, while with S = 0.17 this value decreases to 83.32%. At the same time, the energy associated with the second and third mode is higher in the case of swirling flow.

In conclusion, further experimental investigations are required to fully understand the unstable mechanisms associated with swirling flows, in combination with the numerical models that will be presented in next sections. The use of intrusive methods, such as Hot-Wire Anemometry, can result in flow distortion and thus provide inaccurate quantitative results. On the other hand, the use of non-intrusive methods, such as Particle Image Velocimetry, allow a better analysis of the flow structures, without altering the flow properties during the experiment, but it is more complex and time consuming (e.g. for data collection and processing).

Swirl generators

Different methods exist for generating swirling motion in experimental studies and applications. The use of swirl generators to generate and control the swirl level in experiments is widely documented. Different types of swirl generators have been used

in research facilities, aiming to reproduce the swirling flows in real case applications. Three ways of introducing swirl into the flow can be identified from literature (Gupta et al., 1984):

1. *active* methods, in which the generator presents an axial and one or multiple tangential entries;
2. *passive* methods, in which the flow is forced to pass through guide vanes, helical strips or blades;
3. direct rotation.

A schematic view of several swirl generators used in experimental studies, reported by Alekseenko et al. (2007), is shown in Figure 2.5, in which two types of swirl generators can be identified: active swirl generators (a-d) and passive swirl generators (e-f). Alekseenko et al. (2007) also distinguish between *tangential* type swirl generator devices (a-e) and *axial* type swirl generator devices (f).

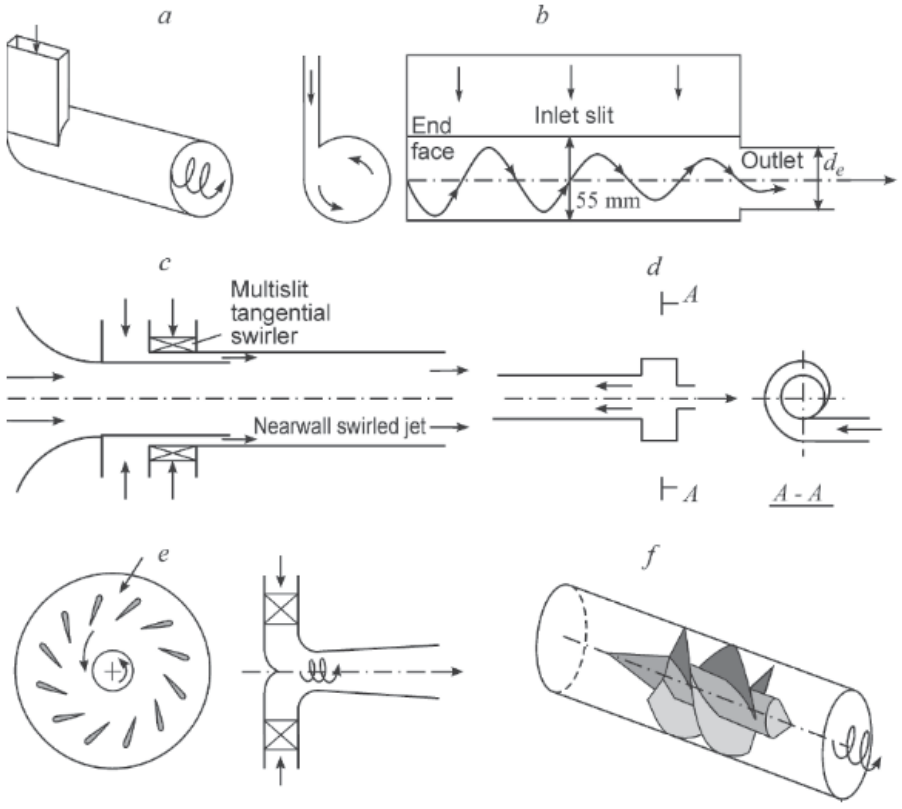

Figure 2.5 Schematics of devices used to generate swirling flows. Source: Alekseenko et al. (2007)

Active methods to generate swirl have been used intensively in experimental studies (e.g. in Dellenback et al. (1988)) because they provide uniform stable jets, in which the ratio between swirl and axial components can be controlled by adjusting the flow rate ratios in the axial and tangential entries. These devices are efficient for low swirl level, but one drawback of these systems is the high total pressure requirement to generate high swirl level, as reported in Gupta et al. (1984).

The use of *passive* methods, such has guide vanes or moving blocks devices allows to obtain stable swirling flows, with a reduced pressure requirement compared to the active methods to generate high swirl. High swirl levels can be obtained, depending on the vane angle. Swirl is generated by deflection of the axial flow injected upstream through the guide vanes, thus obtaining higher swirl levels by increasing the vane angle.

The use of the *direct rotation* devices can be applied only to generate low swirl levels. Alternatives have been proposed by using a perforated rotating disk (or a porous material inside the rotating tube, generating solid body rotation type swirl (Gupta et al., 1984).

Farokhi et al. (1988) have demonstrated, at the NASA-Lewis Research Center, that the way in which the swirl component is generated affects the evolution of the flow. The authors compared the evolution of two nominally similar swirling jets, modifying only the way of generating the tangential component of the flow, keeping the same initial conditions. The conditions imposed were a mass flow rate $\dot{m} = 0.59$ g/s, a swirl number S = 0.48 and a Mach number M = 0.14. In their first test, a solid body rotation was applied to the jet, while in the second case a free-vortex distribution was used to generate the swirl. The resulting flow patterns were different in the two cases. The near field, up to x/D=5 from the inlet, was extremely sensitive to the initial swirl distribution, resulting in a different evolution of the flow downstream. With the first jet, the flow was evolving as predicted from the theoretical results. In the second case the vortex breakdown phenomenon was observed that should occur at higher swirl levels. The authors have explained this effect as a consequence of the reduced size of the vortex core in the initial distribution, compared to the other case. For this reason, a higher swirl number effect on the mean flow could be observed. The experiments by Farokhi et al. (1988) give a clear example of how a swirling flow is dominated by the tangential velocity component distribution given by the swirl generator.

In the current thesis a moving block type swirl generator has been used (described in section 3.1.1). The swirl generator is similar to the one used in the study of Skusiewicz (2012). The characterisation of the swirl generator made by Skusiewicz (2012) was based on the theoretical study made by Leuckel (1973) on a similar device and shows a good agreement with the results from Leuckel (1973). It has been shown that the flow

exiting the swirl generator is characterised by the *axial* and *tangential* components only, with the *radial* component negligible, compared to the other two.

Wall pressure measurements

The study of confined flows can limit the use and application of some fluid dynamics measurement techniques due to limited access inside the test section. The use of pressure measurements is common to a wide range of applications and it is used as a direct or indirect measurement of flow quantities (e.g. in wind tunnels). In the current study, wall static pressure measurements have been used to get insight into flow features and validate Computational Fluid Dynamics (CFD) studies.

Static wall pressure is commonly measured using a pressure tapping mounted to the wall and connected to the manometer. The design of the pressure tap is usually based on the study by Shaw (1960). The research presented more recently by McKeon and Smits (2002) and by Furuichi and Terao (2015) has allowed some improvement in understanding of the effect of pressure tapping geometry and quality on the pressure reading, but there are still many unanswered questions.

The International Standard Organisation provides only general guidance on the topic, stating in ISO (2003a) that a wall pressure tap should be a

> *annular slot or circular hole drilled in the wall of a conduit in such a way that the edge of the hole is flush with the internal surface of the conduit*

There are several pressure tapping parameters that can affect pressure readings and cause errors in static pressure measurements as described in Schetz et al. (1996). The most common problems identified in practice are:

1. misalignment between the pressure tap and the flow (*yaw* angle effect);
2. pressure tap protrusion inside the wall;
3. size of hole-tap configuration.

The effect of the parameters listed above on the measurement accuracy for fully developed axial flows have been investigated in several studies (Chue, 1975; Ducruet and Dyment, 1984; Franklin and Wallace, 1970; Livesey et al., 1962; Rayle, 1949). Corrections and best-practice guidelines have been developed to minimise the errors due to tap protrusion and misalignment. A hole-tap configuration (Figure 2.6) similar to the one reported in Arter and Meier (1990) is commonly adopted to minimise the

static pressure measurement error. The aim of this kind of pressure tap configuration is to minimise the disturbance introduced to the flow, by using a hole as small as possible towards the inner wall. The use of a tap larger then the hole is preferred to facilitate the connection with the instrumentation and minimise the effects of obstruction due to dust or dirt.

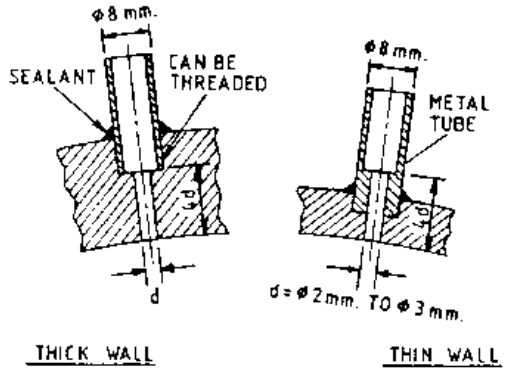

Figure 2.6 Tap-hole configuration proposed in Arter and Meier (1990) for *thick* or *thin* walls.

The presence of the hole-tap introduces a disturbance to the flow, which is well known since the study of Shaw (1960). The effect on the streamline curvature proposed by Shaw (1960) is shown in Figure 2.7.

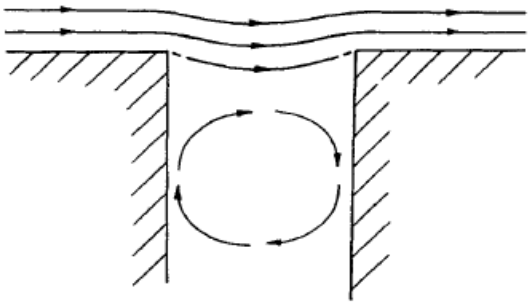

Figure 2.7 Flow behaviour around the hole from Shaw (1960)

The study of Shaw (1960) and, more recently, the work of McKeon and Smits (2002) have shown that for a fully turbulent axial flow the error in the static pressure measurement is lower than 1% of the dynamic pressure on the pipe centreline, for a Reynolds number $Re = 14 \cdot 10^6$. In both studies, the authors have observed that the error decreases when reducing the hole diameter. The effect of the hole depth has also been investigated in both studies, establishing that the ratio between diameter and depth of the hole should be higher then 1.5. It is important to emphasise, however, that both studies (McKeon and Smits, 2002; Shaw, 1960) were focused on the effects of hole

burrs and surface defects near the hole, meaning that high precision instrumentation has been adopted in both studies, which is not commonly available in standard applications.

In addition, the above mentioned studies were focused on the investigation of a single hole. It is not clear if the presence of multiple holes and the distance between them affects the results of static pressure measurements. Another aspect to consider is the effect of the radial component of the velocity. In case of flows with a strong streamline curvature, such as swirling flows, the pressure readings can be modified, as pointed out by Wang et al. (2017). A really limited number of studies have investigated these two problems.

In the study by Moulden et al. (1974) it has been observed that for wind tunnel testing the interference between two consecutive pressure orifices can induce distortion in the downstream boundary layer. It has been observed by Somers et al. (1982) that the presence of static orifices affects the natural transition on a laminar airfoil, with an increased adverse effect on transition when the orifices are aligned with the flow in a chord-wise row. Few years later, Roach and Turner (1988) have observed a similar effect testing the flow around a circular cylinder. The authors state that the *static pressure tappings behave in a similar manner to trip wires*, thus promoting the boundary layer transition. As a consequence, the error in the calculation of the integrated pressure drag based on the static pressure measurements can be as high as 25%.

It can be inferred that the distance between two consecutive static holes could influence the measurements when pressure taps are used to sample the static pressure of confined flows. A CFD study from Vercauteren et al. (2010) suggests that the disturbance caused by the presence of the pressure tap is more complex than the streamline curvature proposed by Shaw (1960). It is possible to see from Figure 2.8 that the presence of the hole can alter the flow around the edges of the hole and the disturbance can be transferred downstream.

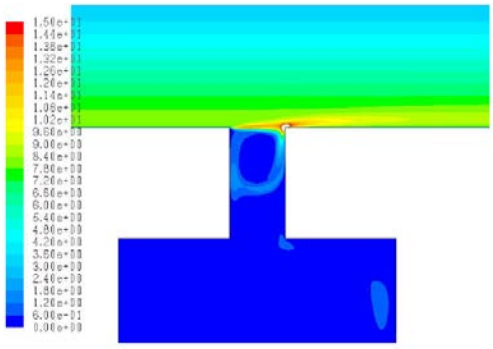

Figure 2.8 Turbulence kinetic energy for a 8 mm pressure tap in a 50 mm channel. Airflow of 30 m/s. From Vercauteren et al. (2010).

2.2 Computational Fluid Dynamics

Because of the limitations and costs of the experimental studies, Computational Fluid Dynamics (CFD) simulations are routinely used to get insight into the properties of complex flows. However, in complex turbulent 3-dimensional flows modelling also presents a number of challenges.

2.2.1 Governing equations

Most Computational Fluid Dynamics codes are based on solving momentum equations derived using the *continuum* hypothesis. Fluids are considered as continuous media, in which the molecular scales are not relevant for the motion. The continuum hypothesis has been confirmed to be a reasonable approximation by several experiments for a wide range of flows, so that the length and time scales involved in the fluid motion are larger then the molecular ones (Pope, 2000). Such hypothesis is verified through the calculation of the Knudsen number (Kn), defined as

$$Kn = \frac{\lambda}{l_s} \tag{2.2}$$

in which λ is the mean free path and l_s is the smallest geometric length scale of the domain. The fluid can be considered as a continuum medium if $Kn < 0.01$. The mean free molecule path in air is $\approx 8 \cdot 10^{-8}$ m, so for the scales involved in the current project, for which the length scales are of the order of mm, the hypothesis is valid.

The equations describing the motion of a viscous fluid are derived applying the principle of conservation of the extensive property considered (e.g. mass, momentum and energy) in a fixed control volume (Pope (2000), Ferziger and Perić (2002)). The properties of the fluid particles change continuously with both time (t) and space ($\underline{x}$), e. g. the velocity field is represented by the vector $\mathbf{U}(\underline{x},t)$. The *governing* equations describing the fluid motion can be derived from physical principles.

The *continuity* equation represents the conservation of mass in the control volume. Under the hypothesis of constant density (ρ), it expresses the *solenoidal* nature of the velocity field $\mathbf{U}$

$$\nabla \cdot \mathbf{U} = 0 \tag{2.3}$$

The forces acting on a fluid can be external (also know as *body* forces, e.g. gravity) or *surface* forces (e.g. shear forces). By applying Newton's Second Law to the forces acting on the fluid, it is possible to derive an expression for the acceleration of the fluid particles (Pope, 2000)

$$\rho \frac{DU_j}{Dt} = \frac{\partial \tau_{ij}}{\partial x_i} - \rho \frac{\partial \Psi}{\partial x_j} \tag{2.4}$$

In Equation 2.4 Ψ is the gravitational potential and τ_{ij} is the stress tensor. Under the hypothesis of Newtonian fluids, the stress tensor can be expressed as

$$\tau_{ij} = -P\delta_{ij} + \mu \left(\frac{\partial U_i}{\partial x_j} + \frac{\partial U_j}{\partial x_i} \right) \tag{2.5}$$

in which μ is the dynamic viscosity of the fluid and P is the pressure. By substituting the stress tensor Eq. 2.5 into Eq. 2.4 an introducing the kinematic viscosity ($\nu \equiv \mu/\rho$) and the *modified* pressure

$$p = P + \rho\Psi \tag{2.6}$$

the *momentum* equation (Equation 2.4) becomes

$$\rho \frac{D\mathbf{U}}{Dt} = -\frac{1}{\rho}\nabla p + \nu\nabla^2\mathbf{U} \tag{2.7}$$

Equation 2.7 is referred to as the *Navier - Stokes* equations (N-S) and represent a complex and strongly coupled system (Pope (2000), Bailly and Comte-Bellot (2015)). The analytical solution of the complex system represented by the Navier-Stokes equations has been obtained under strong restrictive hypothesis only for a limited number of flows, e.g. Scheffel (2001). The problem of finding a unique and smooth analytical solution to the Navier - Stokes equations is listed among the millennium problems of the Clay Mathematics Institute and represents the last unsolved problem of the classical physics (Fefferman, 2000).

2.2.2 Turbulence modelling

Turbulent flows

Fluid flows can be classified using different criteria, based on their global features. It is a standard approach to introduce non-dimensional parameters to identify the flow characteristics. A fundamental distinction between classes of flows is usually made by using the Reynolds number, which is defined as

$$Re = \frac{\rho \overline{U} L}{\mu} \tag{2.8}$$

where $\overline{U}$ is the mean velocity, L is a typical length of the system, ρ is the air density and μ is the air dynamic viscosity of the working fluid. The Reynolds number represents

the ratio between the inertial and viscous forces acting on the fluid particle. For a fixed geometry, the change of velocity corresponds to a change in the flow regime. In a pipe, the flow regimes can be classified as

- *creeping* (or *Stokes*) flow for $Re \to 0$;
- *laminar* flow for $Re < 2300$;
- *transitional* flow for $2300 < Re < 4000$;
- *turbulent* flow for $Re > 4000$.

At very low velocities (creeping flow) the inertial terms can be neglected if compared to the viscous ones. In a laminar flow, the flow particles tend to move on a smooth trajectory, with the viscous terms still predominant on the inertial ones. If the velocity further increases the motion of the fluid particles becomes unstable (transitional flow) until transitions to turbulent, characterised by chaotic and random motion of the particles.

For the majority of turbulent flows, i.e. the ones of interest in engineering applications, the Navier - Stokes equations cannot be solved analytically , therefore numerical methods have been developed and widely used, e.g. Chorin (1968). This problem led to the development of the Computational Fluid Dynamics (CFD), a branch of fluid mechanics dedicated to the numerical simulation of the motion of fluids. The progress made in CFD during the recent years, together with the increased computational power of modern computers, has allowed the use of complex techniques, increasing the accuracy of the numerical simulation of many flows (Pope (1999), Gatski (2004), Zingg and Godin (2009)).

The numerical solution of the Navier-Stokes equations for turbulent flows has been obtained using different methods. Depending on the scale of motion resolved, it is possible to identify three main categories: *Reynolds Averaged Navier Stokes* (**RANS**), *Large Eddy Simulation* (**LES**) and *Direct Numerical Simulation* (**DNS**). The RANS, the LES and the hybrid method of the Detached Eddy Simulation (DES) use statistical data about the turbulence in the whole or parts of the domain, therefore reducing the need for highly resolved mesh everywhere (Spalart et al., 1997), while the DNS solves all the scale of motions. Each model has been formulated under restrictive hypothesis on the behaviour of the flow, which affects the accuracy and fidelity of the results. In general, as highlighted by Pope (2004), *"there is not one 'right' approach"* to model

turbulent flows. A brief discussion of the hypothesis under each approach is presented in the next paragraphs.

RANS modelling approach

RANS models are intensively used in industry and engineering to simulate several turbulent flows, due to their low computational requirements. The crucial hypothesis at the base of RANS models is the decomposition of the velocity field $\mathbf{U}(\underline{x},t)$ in two parts: mean value $\langle \mathbf{U}(\underline{x},t) \rangle$ and fluctuation $\mathbf{u}(\underline{x},t)$, which leads to

$$\mathbf{U}(\underline{x},t) = \langle \mathbf{U}(\underline{x},t) \rangle + \mathbf{u}(\underline{x},t) \tag{2.9}$$

By substituting the hypothesis in 2.9 into the continuity equation (Equation 2.3), it becomes

$$\nabla \cdot \mathbf{u} = 0 \tag{2.10}$$

while the momentum equation (Equation 2.7) becomes

$$\rho \frac{\bar{D}\langle U_j \rangle}{\bar{D}t} = -\frac{1}{\rho}\frac{\partial \langle p \rangle}{\partial x_j} - \frac{\partial \langle u_i u_j \rangle}{\partial x_i} + \nu \nabla^2 \langle U_j \rangle \tag{2.11}$$

In Equation 2.11 the *Reynolds stresses* are expressed by the term $\langle u_i u_j \rangle$. This term adds more unknown terms to the equations, leading to the *closure problem* for RANS equations. The solution can be obtained only by modelling the Reynolds stresses, i.e. adding additional equations for the unknown terms considered. The choice of the closure equations is crucial to correctly simulate a turbulent flow. The Reynolds stresses are functions of the velocity fluctuations, since if $\langle u_i u_j \rangle = 0$ then $\mathbf{U}(\underline{x},t) = \langle \mathbf{U}(\underline{x},t) \rangle$. In tensorial form the Reynolds stress tensor is expressed as

$$\langle u_i u_j \rangle = \begin{bmatrix} \langle {u_1}^2 \rangle & \langle u_1 u_2 \rangle & \langle u_1 u_3 \rangle \\ \langle u_2 u_1 \rangle & \langle {u_2}^2 \rangle & \langle u_2 u_3 \rangle \\ \langle u_3 u_1 \rangle & \langle u_3 u_1 \rangle & \langle {u_3}^2 \rangle \end{bmatrix} \tag{2.12}$$

The diagonal terms in the tensor 2.12 represent the normal stresses, while the other terms are called shear stresses. The turbulent kinetic energy is defined as

$$k \equiv \frac{1}{2}\langle u_i u_i \rangle \tag{2.13}$$

The model of the stress tensor 2.12 led to the definition of several RANS turbulence models, which can be divided in two main categories: a first group of models is based on

the *Boussinesq* hypothesis and its modifications, the second group contains the models in which the Reynolds stress components are directly computed.

Eddy viscosity models The Boussinesq hypothesis is based on the assumption that the deviatoric part of the Reynolds stress tensor 2.12 is proportional to the mean rate of strain

$$-\rho\langle u_i u_j\rangle + \frac{2}{3}\rho k\delta_{ij} = \rho\mu_T\left(\frac{\partial\langle U_i\rangle}{\partial x_j} + \frac{\partial\langle U_j\rangle}{\partial x_i}\right) \tag{2.14}$$

in which μ_T is defined as *eddy* (or *turbulent*) viscosity. By including Eq. 2.14 into the momentum equation 2.11

$$\frac{\bar{D}\langle U_j\rangle}{\bar{D}t} = \frac{\partial}{\partial x_i}\left[\nu_{eff}\left(\frac{\partial\langle U_i\rangle}{\partial x_j} + \frac{\partial\langle U_j\rangle}{\partial x_i}\right)\right] - \frac{1}{\rho}\frac{\partial}{\partial x_j}\left(\langle p\rangle + \frac{2}{3}\rho k\right) \tag{2.15}$$

in which the *effective* viscosity $\nu_{eff}(\underline{x},t) = \nu + \nu_T(\underline{x},t)$ has been introduced.

The eddy viscosity can be expressed as

$$\nu_T(\underline{x},t) = u^*(\underline{x},t)\cdot l^*(\underline{x},t) \tag{2.16}$$

in which $u^*(\underline{x},t)$ and $l^*(\underline{x},t)$ are respectively a characteristic velocity and a characteristic length-scale of the flow.

Under the Boussinesq hypothesis several models have been derived, known as *Eddy Viscosity Models* (EVMs), introducing a strong approximation in the numerical simulation. The restrictions associated with the choice of the Boussinesq hypothesis have been intensively discussed among the researchers, e.g. in Pope (1975), Pope (2000), Schmitt (2007) and Bailly and Comte-Bellot (2015). The models have been derived under the assumption of Equation 2.16, which has led to the development of models in which additional transport equations are used to calculate u^* and l^*.

The first RANS eddy viscosity models introduced were *Algebraic* or *zero equation* models, for which the solution of the velocity field does not require additional equations (e.g. Smith et al. (1967) and Baldwin and Lomax (1978)). Improved accuracy in the calculation of the flow field can be obtained using the turbulent kinetic energy models, such as the two equation $k-\varepsilon$ model introduced by Launder and Spalding (1974). These models are based on the solution of two additional transport equations, from which it is possible to reconstruct the Reynolds stress components. As a consequence, they can provide only the so called first order results, such as the mean values of the

velocity and pressure field, with an accuracy that can be increased by tuning the model's coefficients.

More complex methods have been developed to overcome this problem, modifying the choice of the transport equations, e.g. in the $k-\omega$ model (Wilcox, 2008) or introducing non-linear models, such as the $\bar{v}^2-f$ model and its derivations (Durbin, 1995). The range of applicability of this class of models has been increased with the use of additional equations aiming to introduce a correction, such as the curvature correction proposed by Spalart and Shur (1997) and Shur et al. (1998), or with the Shear Stress Transport $k-\omega$ model from Menter (1994) and its modifications (e.g. Smirnov and Menter (2009)). Additional, more complex and accurate models have been derived including high order terms for the eddy viscosity formulation, under the modification suggested by Pope (1975), at cost of increased computational requirements.

Reynolds Stress Models (RSMs) The direct calculation of the components of the Reynolds Stress tensor has led to the formulation of the Reynolds Stress Models (RSMs) (Shih and Lumley, 1993; Taulbee, 1992). The solution is obtained from the transport equations of each Reynolds stress component, introducing high order correlations for the velocity fluctuations. Therefore, the number of equations that need to be solved and the computational cost of the simulation increase. The use of the Reynolds Stress models has improved the accuracy of the calculation of the stress components, overcoming the problem of the forced isotropy of the Reynolds stress tensor (Hanjalić and Launder, 2009). The Algebraic Stress Model (ASM) Gatski and Speziale (1993) is based on the same equations, but the transport equations for the correlations are assumed proportional to the transport of the kinetic energy, reducing the number of equations that need to be solved.

Large Eddy Simulation and Detached Eddy Simulation

The statistical description of turbulence introduced by the two Russian mathematicians Kolmogorov and Obukhov lead to the development of new modelling techniques. The theory behind the Large Eddy Simulation (LES) can be dated back to the similarity hypotheses presented in the studies of Kolmogorov (1941) and Kolmogorov (1962). Kolmogorov and Obukhov observed that the large scale of the turbulent flows varies with the geometrical features, while the smallest scale is independent and it is possible to describe it with universal laws.

Few years later, Smagorinsky developed the first model that introduced the LES in the turbulence modelling for the weather prediction (Smagorinsky, 1963). In the LES description, the flow is mathematically described by the resolved field (the large scale)

and the sub-grid scale (Pope, 2000). Based on these hypotheses, the Navier Stokes equations can be rewritten in a formal way that recalls the RANS decomposition (Pope (2000), Ferziger and Perić (2002) and Bailly and Comte-Bellot (2015)).

Detached Eddy Simulation (DES) is an hybrid approach that combines RANS modelling near the wall and LES in the far field. It allows to considerably reduce the computational cost of a pure LES simulation, since the grid resolution can be increased. This can be achieved by splitting the domain, in order to obtain two zones in the domain. By doing that, turbulence will be modelled with RANS where the large eddies are dissipated, i.e. near the wall, and with the LES modelling approach in the remaining part of the domain. Problems can raise at the interface between the two parts of the domain, where appropriate conditions to switch between the two models are required. The coupling between the two models at the interface represents one of the challenges to overcome to correctly use this approach (Girimaji et al., 2012).

Direct Numerical Simulation

The solution of all the scales of motion is obtained with the DNS method, which represent the most accurate method, since it does not require turbulence modelling. The level of details obtained from a DNS solution can be higher than those obtained from experiments in the estimation of the Reynolds stresses and DNS solutions are often used to get more insight into the turbulence scales of motion (Le et al., 1997; Lee and Moser, 2015; Moin and Mahesh, 1998). The main drawback of this method is the very high computational cost to calculate the solution, which makes the application to highly turbulent flows with complex geometries still prohibitive, despite the recent availability of more powerful computers (Anantharamu and Mahesh, 2020; Win Naung et al., 2020).

2.2.3 Numerical studies of swirling flows

All of the methods described in the above section have their advantages and disadvantages, and have been applied to various swirling flows with different degrees of success. Swirling flows are particularly challenging turbulent flows, due to the high turbulence level, the high anisotropy of the Reynolds stress tensor and the strong streamline curvature of the flow. As a consequence, the numerical simulation of this particular category of flows is a *perpetual challenge*, using the words of Jakirlić et al. (2002).

The use of RANS models to simulate swirling flows has been described in the detailed review by Sloan et al. (1986). The RANS models based on the eddy viscosity

hypothesis have been proven to be acceptable for low swirl levels, being able to capture the main characteristics of the flow field (Sloan et al., 1986). With increasing swirl levels (S > 0.6) the complexity of the simulation raises, due to the strong coupling between the governing equations. The influence of the rotational terms becomes higher, increasing the anisotropy of the Reynolds stress tensor. As a consequence, a strong effort has been made to model highly swirling flows with more complex techniques, such as LES or DES. The complex, unsteady behaviour of high swirl flows associated with the vortex breakdown and the precessing vortex core, has prompted some authors to use the LES to correctly predict the swirling flow characteristics. On the other hand, the use of LES and DES increases the complexity of the numerical simulation.

Some of the numerical studies of swirling flows have been applied to axial-symmetric cases. This assumption has been supported by the experimental studies inside annular pipes and/or circular pipes, e.g. in the study by Escudier et al. (1980) and in Dellenback et al. (1988). Under the above assumptions, the Navier-Stokes equations can be re-written in cylindrical coordinates, as reported in the study of Hogg and Leschziner (1989).

Steady RANS models

A comparison between the RSM and the $k-\varepsilon$ model has been presented by Hogg and Leschziner (1989) inside an annular pipe with a swirl level S = 2.25. The authors have observed that, by comparing with experimental data, the $k-\varepsilon$ model predicted an excessive turbulence diffusion. On the other hand, with the RSM model the shear stress was better predicted, leading to a consequent better velocity prediction. An interesting result of this study is that the main difference in the predictions between the two models is linked to the influence of the pressure-strain on the shear stress, rather than to the anisotropy of the stress tensor. A weak point of the model proposed by Hogg and Leschziner (1989) is the boundary condition formulation. The definition of the outlet boundary condition was found to be a challenging problem, due to the high sensitivity of the models, in particular the RSM, to the downstream conditions. The authors have decided to impose the experimental velocity profiles at the outlet to overcome this problem, limiting the applicability of the models used for a more general case. This choice has been justified stating that the main purpose of the study was the assessment of the turbulence model used.

A similar study was conducted by Sharif and Wong (1995), in which a non-linear $k-\varepsilon$ model was compared with a RSM and an ASM for four different types of an annular confined swirling flow. The results of the numerical simulations were compared with experimental data previously published. The authors have simulated high swirl jets,

with S = 2.25 and the $Re = 5.49 \cdot 10^4$ (comparing with the experimental results from So et al. (1984)) and medium swirl with S = 0.58 (comparing with the experimental results from Vu et al. (1982). The flow was assumed to be axisymmetric and incompressible. One important assumption made by the authors is the decomposition of the Reynolds stress into its isotropic and deviatoric part, useful to avoid numerical instabilities. The inlet and outlet boundary condition formulation was adopted using the same hypothesis as in the previously mentioned paper by Hogg and Leschziner (1989). A strong influence of the inlet boundary condition formulation on the results has been reported in both papers. In particular, the correct prescription of the turbulence dissipation ε was crucial to obtain a good agreement with the experimental data. The RSM and ASM give a better qualitative agreement with the experiments, compared to the non-linear $k-\varepsilon$ model. For the lower swirl case, the prediction of the mean flow properties, i.e. velocity and pressure, is in good agreement with the experiments for both the RSM and the ASM, while the non-linear $k-\varepsilon$ model under predicts the pressure components. The non-linear $k-\varepsilon$ predicted higher values of the shear stress compared to the RSM and the ASM, resulting in a worse agreement with the centreline velocity values obtained from experiments. However, the azimuthal velocity component was not predicted correctly by any of the models considered in the study. The authors have partially attributed this discrepancy to the high experimental error, estimated between 20% and 50% for the high turbulence regions, i.e. where the discrepancy between the numerical solution and the experiments was higher. The authors conclude that the non-linear $k-\varepsilon$ model is not suitable for prediction of the rotational shear stress flows, while the RSM and the ASM models give acceptable agreement with the experimental data, at least for the mean flow properties. The slightly better results obtained with the RSM model do not justify the increased CPU requirements (estimated about 1.5 times higher than the ASM). However, the authors warn that a definitive conclusion about the model performance cannot be made, since the turbulence quantities were not available from the experiments, so they compared only the first moment properties.

An interesting model has been presented by Shih et al. (1997). A cubic Reynolds stress strain model is validated for a rotating pipe flow and a swirling flow with recirculation. An explicit expression for the Reynolds stress terms was proposed by the authors, based on a tensorial polynomial expression of the mean velocity gradients. The advantage of this formulation is the inclusion of up to the sixth power of the velocity gradient in the formulation. The quadratic formulation of this kind of models has been proved to be suitable for complex flows, including separation. However, it is not sufficient for swirling flows, as highlighted by Launder and Spalding (1974). Therefore, Shih et al. (1997) used a cubic term for the Reynolds stress formulation, modelling

the transport equations of the $k-\varepsilon$ model. The model correctly predicted the effects of the axial rotation in the rotational pipe flow test case, showing a good agreement with the experimental data for both axial and tangential velocity profiles, published in literature. The second comparison presented by Shih et al. (1997) has been made with the experimental data for a confined annular swirling flow ejected in a sudden expansion, which is similar to the one encountered in aircraft engines, published by Roback and Johnson (1983). The recirculation bubble was correctly predicted by the cubic model developed by Shih et al. (1997), with an improved prediction of the rear stagnation point when compared to the results of a standard $k-\varepsilon$ model. The comparison of the numerical results with the mean velocity profiles from the experiments is good for both models, however, the cubic model was able to better evaluate the tangential velocity components, correctly predicting the non-solid body rotation observed in experiments. The authors observed that for the 2D case considered their model caused an increased CPU cost of about the 15% within respect to the $k-\varepsilon$ model.

As mentioned in section 2.2.2, an improvement to the eddy viscosity models can be achieved by introducing additional equations to account for curvature corrections. An interesting solution is presented by Alahmadi and Nowakowski (2016), used to investigate the swirling flow in a cyclone separator. The model has been identified by the authors as Shear Stress Transport with Curvature Correction Modification (SSTCCM) and it has been implemented in Open-Foam. The curvature correction adopted in this study is a modification of the one proposed by Smirnov and Menter (2009) . A series of numerical simulations of the flow in a U-duct has been used as benchmark. The model proposed can correctly estimate the velocity profiles in the duct and the recirculation zone, proving an interesting enhancement on the classic EVMs (Figure 2.9).

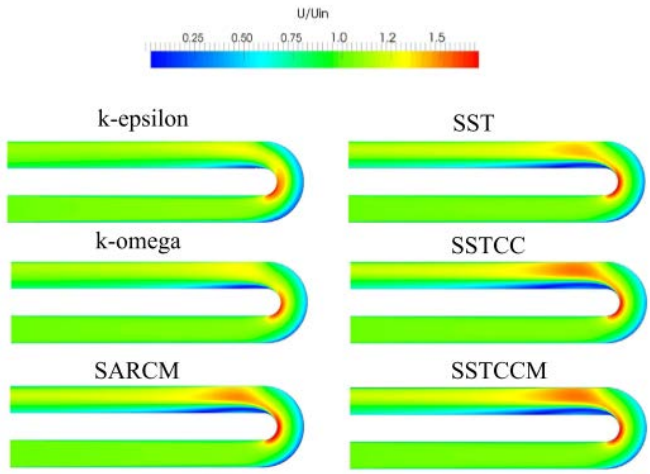

Figure 2.9 Mean velocity contours plots in the U-duct, for different EVMs. Source: Alahmadi and Nowakowski (2016).

The second part of the paper by Alahmadi and Nowakowski (2016) presents the results of the simulation of the swirling flow in a cyclone separator. Alahmadi and Nowakowski (2016) observed a strong impact of the boundary conditions on the solution. The authors have shown that the results are affected by the inlet and outlet boundary conditions. To overcome the problem, an extended domain has been adopted to reduce the impact of both velocity inlet and pressure outlet conditions. Interestingly, both the normal and the extended domain capture with good agreement the velocity values in the separation region, Figure 2.10b (bottom). But only with the extended domain the simulation can reproduce the experimental inverted W pattern in the cylindrical region, as shown in Figure 2.10b (bottom). A weak point of the formulation, compared to the experiment, was found in the prediction of the flow near the wall.

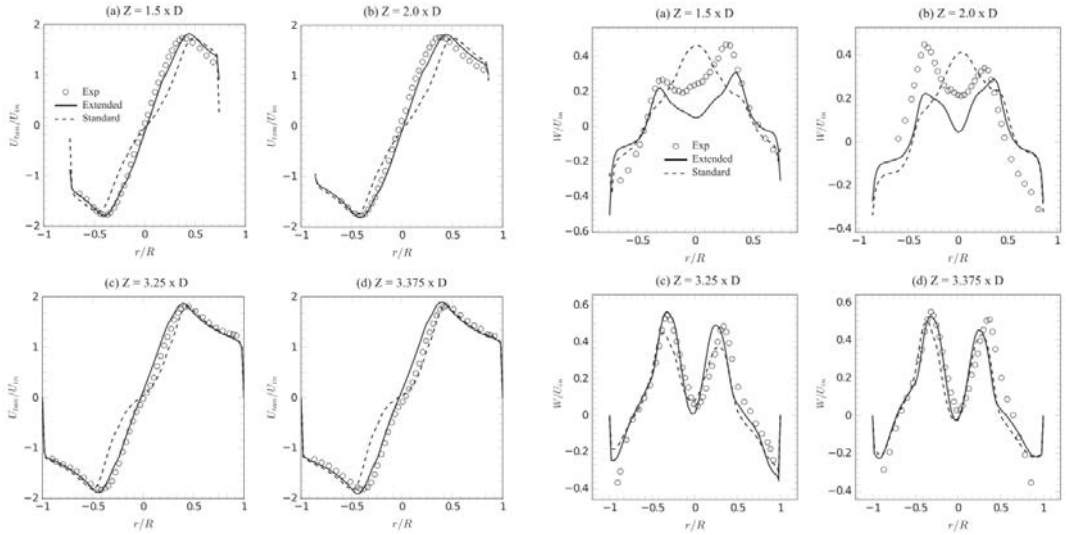

(a) U/U_m **(b)** W/U_m

Figure 2.10 Comparison of the velocity profiles at different stations along the cyclone separator. U/U_m (a) and W/U_m (b) are presented as a comparison between experiments (circles), the standard inlet size (dashed line) and the extended inlet size (solid line). Source: Alahmadi and Nowakowski (2016).

The application of the SSTCCM by Alahmadi and Nowakowski (2016) to swirling flow has shown that high accuracy predictions could be achieved with the curvature correction modifications. In particular, the proposed correction improved the prediction of the Rankine vortex pattern of the tangential component and the inverted W pattern of the axial velocity component inside the cyclone separator compared to a standard $k-\omega$ SST model.

URANS and LES/DES models

The models presented so far were based on the hypothesis of steady flow, with which the unsteady characteristics of swirling flows, e.g. the precessing vortex core, cannot be predicted. To overcome this limitation some authors have used an Unsteady RANS (URANS) formulation, such as in Wegner et al. (2003) and Wegner et al. (2004).

The URANS formulation is suitable to predict the precessing vortex core, since the Reynolds averaging does not correspond to a temporal averaging (Wegner et al., 2003). By using an RSM model Wegner et al. (2004) have been able to predict the behaviour of an unconfined swirling flow with S = 0.75 and Re ranging between 10000 to 42000, Wegner et al. (2003) have evaluated the performance of the URANS formulation in the prediction of the precessing vortex core in an unconfined swirling jet. A comparison between URANS and LES for the same case has shown that the experimental mean velocity profiles were captured by both approaches with good agreement. The authors have observed a better agreement with the experimental results near the swirler exit with the RSM model, compared to the LES. However, this aspect has been attributed to the use of the wall function used in the RSM and the poor grid resolution of the mesh used for the LES simulations. The URANS model was able to capture the qualitative behaviour of the total kinetic energy, but under-predicted the energy levels. The authors noticed a negative effect of the low flux-blending parameters, suggesting that the numerical schemes adopted can highly influence the results. The evaluation of the precessing core frequency was obtained from the Fourier analysis of the velocity time series. The authors show a good prediction of the core frequency, proving that the URANS method based on the RSM is suitable to capture the PVC in a swirling flow. The computational cost of this modelling approach is significantly increased if compared to the steady state simulation, but it is still low if compared to LES. Further investigations are needed to better clarify the problems identified by Wegner et al. (2004), such as the instability of the numerical solution and the effects of the numerical schemes adopted. However, the use of the unsteady formulation of RANS models seems to be a promising way to predict the unstable behaviour of swirling flows (in particular the precessing vortex core) with reduced computational requirements compared to LES.

Additional confirmation of this aspect has been recently given for low swirling flow in the work of Zhang and Vanierschot (2021). The numerical study performed using URANS with a RSM model for turbulence has confirmed reasonably accuracy of both temporal and spatial properties in the prediction of the coherent structures in an annular swirling jet at S = 0.39. Zhang and Vanierschot (2021) have demonstrated that the precessing vortex core could be predicted with good agreement with the experimental data.

García-Villalba et al. (2006) have investigated unconfined swirling flows generated by an annular jet that discharges into a domain that contains the same fluid at rest. The authors used the in-house code LESOCC2 to perform the simulations. The configuration was based on the experimental setup used by Hillemanns: the annular swirling jet is discharged in a cylinder with a diameter that is 10 times greater than the outer diameter (D) of the annulus. The authors imposed a free slip condition for the external boundary of the cylinder and a convective outflow boundary condition at 12 D downstream the annulus. To avoid the un-physical recirculation zone in the outer region of the annulus, the authors imposed a co-flow stream at the boundary of the cylinder used to extend the domain, with 5% of the bulk velocity $U_b = 25.5m/s$. By varying the co-flow between 2% and 10% the authors did not observe major differences in the near field of the annular jet. The inlet boundary condition was imposed far upstream the outlet of the annulus, using flat top-hat velocity profiles for both the radial and the azimuthal components. This strategy is not common in LES simulations, since they usually require unsteady inlet conditions. However, the authors report that the turbulence is rapidly developed in the annular duct upstream the jet exit, so the inlet condition adopted does not affect the computations. The swirl level at the inlet was adjusted to match the experimental value of S = 0.9 at the outer section of the annulus. The results are presented for the simulation run for 150 time steps, in order to eliminate the effects of the initial conditions. This was not enough to let the convergence of the statistical quantities near the symmetry axis far downstream the annulus exit, but does not affect the results in the near field, that is the area of interest for the authors.

The length of the recirculation zone generated downstream the annulus varies from 1 R for the no swirl case up to 6 R for the high swirl case, in accordance with previous experimental observations from Gupta et al. (1984). García-Villalba et al. (2006) observed the presence of two shear layers: the inner one, wider, is at the border between the swirling flow and the recirculating flow, while the outer one is at the border between the annular flow and the co-flow. The authors observed that the inner layer presents a larger change in velocity, since a negative velocity is present in the recirculation zone. The swirling jet was spreading radially faster than the non-swirling case. The comparison with the experimental data for the mean flow shows that the tangential and axial velocity components are correctly predicted with this model, while the radial component shows a good agreement only in the near field zone, up to 1R downstream the annulus exit. However, the authors argue that the experimental data are affected by a systematic error, showing that it is possible to achieve a good agreement for the radial component at 2 R, as well. In fact, re-evaluating the continuity equation using a central

difference scheme based on the experimental values the numerical results are in good agreement with the experimental data.

A similar trend is observed for the velocity fluctuations, with a better agreement with the experiments only for the first two components. The overall behaviour is qualitatively correct, even though the LES simulations under-predict the fluctuations. The instantaneous flow analysis allows to identify the flow structures characteristic of the swirling flow. It is possible to see the evolution of the vortices for half a rotation time period (Figure 2.11) in which three different instants show the iso-surface of the pressure fluctuations. Figure 2.11 shows two structures with elongated helical vortices: the outer region vortices (O in figure) have a larger angle than the inner ones (I1 and I2). In particular, the inner structures represent the PVC observed in experimental studies. The vortices are rapidly damped downstream, while the effect of inner structures extends upstream into the annulus outlet section. The authors state that both inner and outer shear layers are prone to Kelvin-Helmholtz instability. In particular, they observe that the instability of the inner shear layer is at the origin of the PVC. The authors correlate the origin of the flow structures with the frequencies of the flow, through the power spectral analysis.

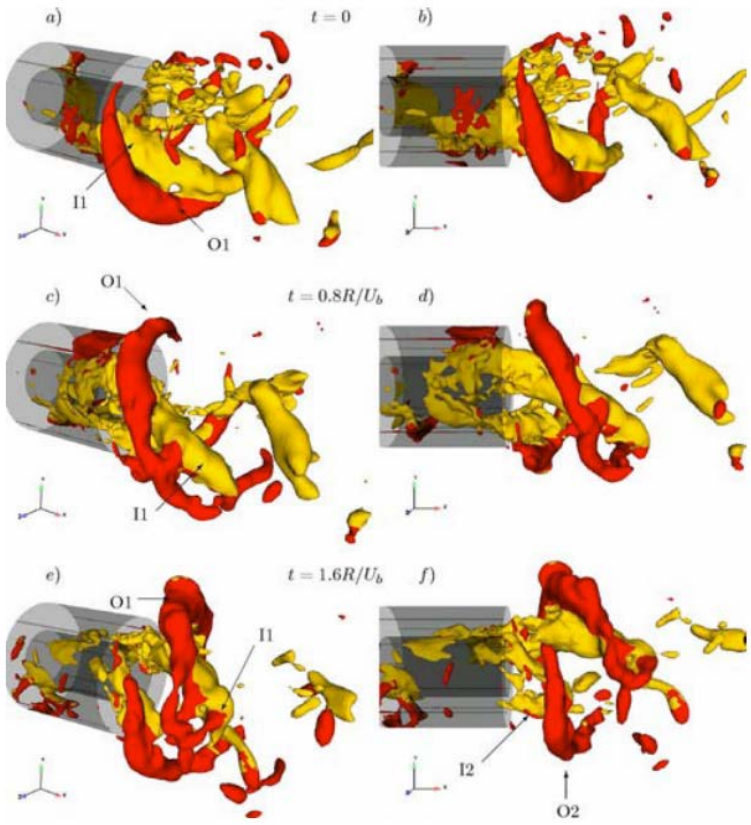

Figure 2.11 Isosurface of filtered pressure fluctuations, at three instants in time. Swirl is clockwise when looking upstream in axial direction. Source: García-Villalba et al. (2006).

As previously mentioned, the use of pure LES models increases the computational cost of the simulations. Some hybrid models, such as the one presented by De Langhe et al. (2006) are suitable to reduce the computational time requested. The hybrid RANS/LES model presented in De Langhe et al. (2006) is based on a re-normalization group (RG) procedure. The domain consists of a cylindrical pipe with a sudden 1:2 expansion that reproduces the experimental test section used by Dellenback et al. (1988). The model is implemented in the commercial CFD code Fluent, using a one-equation sub-grid model in the LES regions and a $k-\varepsilon$ model in the RANS regions. The authors compared the results of the hybrid model with an unsteady RANS simulation. In particular, a Second Moment Closure model (SMC) is used to define which approach lead to the best quality/cost ratio. The flow was initialized using a RANS solution, without superposed initial perturbations on the velocity field. The turbulence develops itself because of the unstable mixing layer behind the separation point. The mesh resolution adopted by the authors is fine enough to get mesh independence with the SMC model. The same grid is fine enough to solve the LES in the core region. The RANS model is activated near the wall, since the wall effect is of minor importance according to the authors. Occasional switches to RANS in one or two cells near the wall, which should not influence the results, have been observed. The authors determined the inlet conditions for the velocity in a particular way, since they do not imposed directly the experimental data. The experimental mean velocity profiles were used to calculate the production convection and diffusion terms for the sub-grid turbulent model. An interesting assumption made in the paper is that the simulated flows were not sensitive to the details of the fluctuations, therefore the authors did not investigate the effects of inlet conditions.

The results presented by De Langhe et al. (2006) show that with increased swirl levels, the agreement with the experimental results is better than the no-swirl case. In particular, a good prediction of the mean axial velocity profile is achieved, with a visible discrepancy only behind the expansion near the symmetry axis. In the same way, the turbulence fluctuations are well predicted with increasing swirl level, showing the same discrepancy observed for the axial velocity, with over-predicted values near the centreline axis in the region near the expansion. The same simulations, performed with the SMC model, show that the results for the axial velocity profile are comparable, but the SMC under-predict the turbulence fluctuations. The authors report that the hybrid model requires three to four mode time steps to reach the same statistical convergence of the SMC model. A further comparison with DES and LES models was performed by the authors. They found that the solution obtained with the DES was sensitive to

the choice of the model constants, especially for the centreline velocity. The LES simulations with wall functions, give results comparable with the hybrid model.

The LES and DES model of a swirling flow thorough a suddenly expanding pipe has been performed by Javadi and Nilsson (2015) for various levels of swirl, ranging from 0.6 and 1.23. The study has identified anisotropy immediately after the sudden expansion, with isotropy rapidly recovered due to the redistribution between the velocity fluctuations. The use of hybrid URANS - LES simulations has been proven to be effective, however finer grid refinements near the wall were needed in the simulations performed by Javadi and Nilsson (2015) to achieve the same accuracy of LES.

In conclusion, the studies presented in this section have shown that RANS models, under the hypothesis of steady flow, are able to capture the mean flow properties of rotational and swirling flows. The use of the Reynolds Stress Models and the implementation of curvature corrections can give some improvement in the prediction of velocity and pressure fields, compared to the classic Eddy Viscosity Models, but can still result in non-realistic decay of turbulence and swirl. In addition, the complexity of the simulation increases, thus resulting in increased computational requirements.

It is necessary to remark that, as highlighted by the authors of the works above mentioned, additional studies to extend the validity of the modifications proposed in the models are required. In addition, a strong effect on the solution of the boundary conditions has been observed for all the models above mentioned, as will be explained in section 2.2.3.

The use of LES is proven to give high order results for the turbulent flows, such as velocity and pressure fluctuations. It has been shown in several studies that LES used to model swirling flows has given a better insight of some unsteady flow features. Thus, LES is a promising technique to better understand the unsteady behaviour of vortex breakdown and precessing vortex core. However, the implementation of the LES model and its application to complex geometries is more computational demanding then RANS models. In addition, the definition of the boundary conditions has been reported to be more complicated if compared to the RANS models.

Impact and definition of boundary conditions

The problem of the definition of both inlet and outlet conditions for the swirling flow models has been reported in the majority of studies. More or less complex definitions and/or strategies to overcome the issue have been proposed and a brief review is presented in the next paragraphs.

Inflow boundary condition It has been reported in several experiments that depending on how the swirl is introduced in the test section, i.e. depending on the swirl generator used in the experimental facilities, different structures could be present in the downstream flow (section 2.1.3).

The problem of the inflow condition is even more crucial in the numerical simulations, since inevitably approximations are introduced. It has already been mentioned in the above section 2.2.3 that in the majority of numerical studies applied to swirling flows, the authors have encountered the problem of the definition of the inlet boundary condition. In most of the cases, this has resulted in the inclusion of the swirl generator assembly in the computational domain, to overcome the issues associated with the definition of the inlet condition. For example, in the study of Wegner et al. (2004) the authors have stated that imposing the experimental results directly at the pipe inlet made the simulation unstable. To overcome the problem, the authors have been forced to include the swirl generator in the computational domain. Realistic results have been achieved by imposing the experimental velocity components or from the numerical simulation of the swirl generator far upstream of the domain of interest (e.g. Alahmadi and Nowakowski (2016)).

In the study by Xia et al. (1997) the effect of the inlet boundary condition on the flow downstream has been investigated using a standard $k-\varepsilon$ model. The velocity components for the inlet boundary have been obtained using a separate simulation of the swirl generator assembly and several tests to evaluate the influence of the boundary conditions have been reported. Two approaches have been used by Xia et al. (1997) to vary the velocity inlet conditions. The baseline simulation has been obtained by substituting the velocity profiles computed from the swirl generator simulation, while other two cases have been considered, replacing the computed velocity profiles with a constant and then with a linear shape, keeping the same average values of the three velocity components obtained from the swirl generator simulation. With this approach the results slightly change only near the inlet region, up to 1 x/D. Xia et al. (1997) have then considered other two cases, for which only the total mass flow rate has been preserved, thus obtaining different values of the average velocity components. The results obtained with this second approach show a completely different behaviour of the flow downstream. According to Xia et al. (1997), the differences could be explained not only by the change in the swirl level at the inlet (i.e. the change of the ratio between the tangential and axial momentum), but can be attributed to the increased ratio between the radial and axial velocity components. In analogy with the swirl level, Xia et al. (1997) have introduced a *radial* number to express the influence of the radial component,

suggesting that the hypothesis of negligible radial component is not always valid and further analysis are needed.

The problem of the inlet boundary definition has been found to be more problematic with the LES modelling approach (García-Villalba et al. (2006), Luginsland and Kleiser (2015)), for which, in general, the definition of the boundary condition is a non-trivial task.

Pierce and Moin (1998) proposed a method based on the azimuthal body force technique for the definition of the inflow boundary conditions for swirling flows modelled with LES. According to Pierce and Moin (1998), while the axial body force is physically represented by the mean pressure gradient, *"the azimuthal body force used to drive the swirl component is not physically producible and should be thoughtof as existing only to overcome drag from the walls*. By modifying the forcing profile in the momentum equations, the authors have obtained a good agreement with experimental data for a stationary fully developed confined swirling flow.

An interesting approach to improve the inlet boundary condition implementation with LES is reported in the paper of Palm et al. (2006). The authors have modelled, with the commercial CFD code Fluent, the flow inside an annular cylinder. They have seen that the velocity profiles at the outlet of the annulus were extremely sensitive to the swirl level. The increased swirl number caused the loss of axial symmetry of the flow in the annulus. They have shown that the simulation of the entire swirl generator, using a RANS model with a Second Moment Closure (SMC) is in good agreement with the experiments. The application of LES to the full geometry is not practical, so the authors have used a different approach to obtain the inlet conditions. They have imposed a fictitious pressure gradient into the momentum equation for the circumferential equation to create the swirl motion, assuming fully developed flow conditions. Then, they have adjusted the magnitude of the pressure gradient to get the experimental swirl magnitude. They have seen that the axial component is not predicted correctly. A better correlation with the results has been obtained with the use of the method described by Pierce and Moin (1998), i.e. introduction of a body force into the axial component of the velocity, based on the specification of its experimental statistical properties. In practice, the axial velocity component, at each time step, was modified, by subtracting the mean value in the non streamwise directions. This technique allows a better prediction of the Reynolds shear stress, but it is still dependent from the experimental characterization of the flow. As Palm et al. (2006) conclude, further investigations to understand the nature of this phenomenon and propose appropriate corrections are needed.

In conclusion, it has been found that the problem of the definition of the inlet boundary condition is a non-trivial task and that, in general, better agreement between

experimental data and numerical results can be obtained when the swirl generator assembly is included into the computational domain.

Outflow boundary condition The definition of the outlet boundary conditions has been proven to be problematic, given the elliptical nature of the flow field.

Some authors (e.g. Hogg and Leschziner (1989) or Sharif and Wong (1995)) have imposed the experimental velocity profiles at the outlet to overcome the problem and focused on the prediction of the flow features in the near field.

In the study by Xia et al. (1997) the effect of the outlet boundary condition on the flow upstream have been shown to be significant up to $\approx 1.3x/D$ upstream the outlet boundary. The extent of the central recirculation zone predicted for both conditions is similar. The flow downstream has shown a monotonic increase of the axial velocity with the mass flow rate condition imposed at the outlet, while with the pressure boundary condition a weak recirculation zone has been observed, suggesting that a radial pressure gradient at the outlet is still present. According to Xia et al. (1997), the constant pressure boundary condition should be used when the flow discharges in a larger volume (i.e. it is unconfined downstream the test section), while a mass flow rate condition is more appropriate when the flow is still confined downstream.

A general trend observed in the study of swirling flow is that in order to reduce the impact of the outflow boundary condition, the computational domain is extended far downstream. As already mentioned in the previous section, (Alahmadi and Nowakowski, 2016) have found that by extending the computational domain of the cyclone separator the computational model is in better agreement with the experimental data. Moving the zero-velocity gradient outflow condition far downstream the computational domain has a significant impact on the results, so that only with the extended domain the simulation can reproduce the experimental inverted W pattern in the cylindrical region, as shown in Figure 2.10.

The outflow boundary can be even more detrimental in presence of unsteady phenomenon, such as precessing vortex core. In order to predict the unconfined swirling flow Wegner et al. (2004) have imposed a free slip boundary condition at the lateral boundaries of the cylinder downstream the swirl generator and a zero gradient outflow condition at the outlet.

The outflow boundary condition has a strong impact in LES simulations, as shown by Schluter and Pitsch (2001). A large domain downstream has been used by García-Villalba et al. (2006) for the numerical simulation of the unconfined swirling flow generated by an annular jet that discharges into a domain that contains the same fluid at rest. The annular swirling jet is discharged in a cylinder with a diameter that is 10 times

greater than the outer diameter (D) of the annulus. The authors imposed a free slip condition for the external boundary of the cylinder and a convective outflow boundary condition at 12 D downstream the annulus (12 times the length of the annulus).

In the study of Javadi and Nilsson (2015) the authors report that a series of outlet boundary conditions was investigated, with a zero gradient condition for the velocity (with limitation for the back-flow) and a homogeneous Dirichlet condition for pressure *"found to have the least effect on the upstream flow"*, without providing details about the comparison. The study confirms that a reduction of the effect of the outlet boundary conditions on the flow upstream can be achieved by extending the domain further downstream, since the author extend the domain at 10 pipe diameters downstream the expansion to reduce the impact of the outlet boundary.

In conclusion, the outflow boundary condition problem can be partially mitigated by extending the domain far downstream. However, in presence of swirling flow discharging into a domain in which fluid is at rest, unsteady flow phenomena arise and the computational domain should become significantly larger then the test section, to minimise the effects of the boundary condition.

2.3 Diffusers and high resistance devices

2.3.1 Swirling flows in diffusers

When pipe flow undergoes a sudden expansion, flow usually separates from the expansion walls, which is detrimental to flow uniformity (e.g. Durst et al. (1993)) and causes extra flow losses. However, expansions often feature in many engineering applications - for example, where an increase in residence time is required within catalytic converters (Bella et al., 1991). On the other hand the introduction of swirl in a diffuser can reduce the size of the separation zone McDonald et al. (1971).

In the study by Okhio et al. (1983) it has been found that in presence of swirl in a diffuser with a 16.5° angle, the onset of separation moved downstream, and it is completely eliminated with increasing swirl level. According to Okhio et al. (1983), an optimal swirl level exists to reduce the losses through the diffuser. A study of flow in a diffuser with downstream resistance by Rusli et al. (2017) further demonstrated that low and moderate swirl can be beneficial for flow uniformity, at the cost of increased pressure loss when compared to the axial case.

When swirling pipe flow enters a sudden expansion (finite or infinite), new complex global flow structures are often observed, such as vortex breakdown and precessing vortex core phenomena. These are of particular interest as they affect flow uniformity,

stability and mixing, factors important for efficiency of the flow device placed downstream (Lilley, 1977). Conversely, adding a high resistance device in the flow path makes the problem easier to study as development of time-dependent flow instabilities is limited.

As shown by Rusli et al. (2017), swirling flows in sudden expansions with a high resistance device feature high axial inertia, pressure build up at the front face of the monolith, flow separation at the sudden expansion point, high radial inertia (so-called centrifugal force), accompanied by high radial pressure gradients, and adverse axial pressure gradients causing the appearance of the central recirculation zone.

Therefore, introducing swirl into flows in sudden expansions can be beneficial to the overall performance of the system, since the swirl may prevent flow separation and produce a more uniform flow. However, high swirl may result in formation of the central recirculation zone with extra losses, and adverse axial gradient at the diffuser axis may result in reverse flow in the device placed downstream, as is often the case in applications.

2.3.2 High resistance device modelling

Devices with high resistance to the flow are commonly modelled using a distributed resistance through the domain. Where the resistance is proportional to the flow velocity and/or its square, the equivalent porous medium approach can be used. This assumption is generally valid in many multi-channel devices such as catalysts, filters and heat exchangers. The analogy between the high resistance device and the flow model of a porous medium is often made in numerical studies of automotive catalysts (e.g. in Benjamin et al. (2001)) and heat exchangers (e.g. in Prithiviraj and Andrews (1998)). The full geometry of high resistance devices is usually constituted by complex flow passages which are impractical to include in the computational domain due to the high computational cost, since they require multiple scales to be modelled. For example, in a catalytic converter, the scales range from the molecular scale of the catalyst to the full converter scale (Cornejo et al., 2018a). Gao et al. (2011) have observed that the heat transfer inside packed beds, in which the catalyst particles are modelled using a porous medium model, is influenced by the transition from laminar to turbulent regime, confirming the impact of the geometry on high resistance device modelling.

A good prediction of the velocity distribution downstream high resistance devices modelled using a distributed resistance approach has been achieved in several studies, e.g. in Benjamin et al. (2001) and Porter et al. (2014). A significant reduction of the computational time requirements compared to the complete scale model of the channels has been shown in the Ph. D. thesis of Porter (2016). The definition of the resistance

coefficients of the porous medium is based on experimental data or semi-empirical laws, such as the pressure drop law proposed by Shah (1978) for single channels. The approach has been successfully applied to 2D (Abu-Khiran et al., 2003) or 3D models (Hayes et al., 2012).

The prediction of turbulence and related quantities (i.e. mass and heat transfer) downstream the high resistance device modelled as a porous medium represents a drawback of the formulation. As an example, downstream a catalytic converter monolith, the individual jets exiting the channels can not be predicted with the porous medium model. The small jets downstream the monolith can be unstable and generate turbulent structures, as observed using more complex modelling approaches (Cornejo et al., 2018a; Hettel et al., 2020).

Different approaches have been proposed to overcome this problem, ranging from the inclusion of the full scale geometry inside the domain to modified RANS models approaches to simulate multiple scales (Kuwata et al., 2014) or artificially generated turbulence downstream the porous region used by Cornejo et al. (2018a). The use of such methods inevitably increases the computational requirements of the simulation and limit the possibility to extend the model to a wide range of devices and configurations.

In addition, during the design phase of a high resistance device, it is often required to test the flow in several geometries, in order to optimise their performance. Recently, prototypes of catalysts produced using 3D printing techniques have been presented by Thakkar et al. (2016) and Ruiz-Morales et al. (2017). The use of 3D printing widens the possibilities in the definition of the geometries of the monolith, allowing even the definition of channels with variable dimensions. It is possible to infer that once the technology will be more robust, it will be possible to create customised geometries for the monolith, optimising the distribution and the size of the channels to achieve high uniformity indices. This creates the need for more flexible models representing multi-channel devices.

2.4 Asymmetric swirling flows

The overwhelming majority of existing studies of swirling and non-swirling flows in sudden expansions have focused on symmetrical configurations, and the effect of the asymmetry (often encountered in practical applications) on such flows is not fully understood. Only a limited number of studies have demonstrated an effect of the asymmetry on swirling flows, often as the result of flow instability.

In the study by Farokhi et al. (1988) it has been found that when an asymmetric swirling jet has been generated from an axisymmetric nozzle, the swirling flow would

self-centre downstream, with a rapid recovery of the axisymmetric character (within 1 nozzle diameter). A similar behaviour has been observed by Parchen (1993) for pipe flow subject to rotation. The presence of low swirl in the flow can lead to unstable non axisymmetric structures. Parchen (1993) observed experimentally that non symmetrical structures can be seen downstream the swirl generator. However, in the downstream pipe the symmetric character of the flow is recovered for both velocity components (along the axis and along the circumference). This behaviour has been attributed by Parchen (1993) to the swirl decay that occurs downstream.

Escudier et al. (2006) have investigated the influence of the outlet geometry offset for low (S = 0.3) and high swirl flows (S = 0.6) in water. The use of an orifice plate has allowed the creation of a stable vortex breakdown structure also for the low swirl case. A comparison between 5 outlet geometries at 6 pipe diameters downstream the inlet has been reported by Escudier et al. (2006): straight and fully open, concentric circular tube (2.2 contraction ratio between inlet and outlet), eccentric circular tube (2.2 contraction) with eccentricity of 0.24 (compared to the inlet diameter), annular contraction, double bend geometry (two 90° elbows). In general, none of the configurations explored in the study by Escudier et al. (2006) has shown the precessing vortex core or periodicity. A complex flow has been observed for the high swirl case for all the outlet sections. The presence of the downstream contraction has shown a strong impact on the velocity field upstream, which becomes more significant and complex in presence of the eccentric outlet. The asymmetry introduced downstream affects both velocity components upstream, causing a distortion of the vortex core. Escudier et al. (2006) observe that the vortex core axis twists in the opposite direction of the swirl, i.e. for clockwise swirl around the vortex core, the vortex axis is twisted in the opposite direction (anticlockwise).

The study of asymmetric planar diffuser with axial inflow condition has been successfully used by several authors to benchmark turbulence models (Obi et al., 1993), due to the presence of flow separation and adverse pressure gradients, both challenging for the turbulence models.

Buice and Eaton (2000) have observed that in the asymmetric diffuser with 10° expansion the separation zone typical of the expansion region can be significantly larger in asymmetric configuration than that in an axisymmetric case, with a consequent increased acceleration of the flow in the mid-plane region. The study by Gullman-Strand et al. (2004) has shown that the introduction of asymmetry can significantly alter the flow distribution in the planar diffuser, with a weaker pressure gradient observed for the 8.5° diffuser, compared to the 10° diffuser. Both studies accounted for unidirectional flow only, it is therefore reasonable to expect that introducing asymmetry into swirling flows will result in a considerable flow redistribution in both axial and radial directions.

2.5 Chapter summary

The reviewed literature highlighted the challenges associated with the experimental and numerical studies of swirling flows. In particular, such flows present a complex flow field and exhibit high radial and axial pressure and velocity gradients, especially inside sudden expansions with downstream resistance.

Confined swirling flows are highly sensitive to disturbances introduced by measuring probes, thus limiting the accuracy of the measurements obtained using intrusive techniques, such as Hot Wire Anemometry. The use of more complex non-intrusive laser measurement techniques (i.e. Particle Image Velocimetry) have been shown to provide significant improvement in the understanding of swirling flows. Wall pressure measurements are commonly used to study confined flows and gain some insight into the flow features. The use of hole-taps at the wall has been well established for application to axial flows. However, some questions remain about the error induced in pressure measurements in presence of flows with high curvature, such as swirling flows. Additionally, it has been shown that the presence of multiple holes at the wall causes disturbances inside the boundary layer. Thus, it is possible that the presence of multiple holes and the distance between them affects the results of static pressure measurements.

The numerical modelling of swirling flows presents several challenges due to their high radial pressure and velocity gradients and their turbulence anisotropy. All the CFD models applied to the study of swirling flows have been proven to be highly sensitive to the choice of the boundary condition for both inlet and outlet of the computational domain. The choice of the appropriate turbulence model for swirling flows is non trivial and the balance between accuracy of the results and computational cost of the simulation remains an open question. The use of LES models has been proven to give accurate results for the calculation of velocity and pressure fluctuations in presence of swirling flows. However, some additional challenges in the definition of the boundary conditions have been identified, compared to RANS models. In addition, they have been proven to be more computational demanding then RANS models. The use of hybrid RANS/LES models appears to be a promising compromise in terms of accuracy, but presents additional unsolved challenges to overcome, in particular for the coupling of the two models. Therefore, RANS models still remain attractive for their more robust implementation and their lower computational cost. RANS models have been proven to give reasonable results in some applications to swirling flows and their performance is still not well investigated for such flows.

Practical applications are rarely symmetrical, but not many studies have been carried out to evaluate the effect of asymmetry on the flow structures. In order to understand the changes caused by the asymmetry in confined swirling flows it is crucial to develop

a robust experimental and numerical methodology to appropriately study flows under such conditions.

High resistance devices (such as catalysts used in aftertreatment systems) often present complex flow passages. The presence of small scale structures exiting such devices has been shown to promote turbulence, beneficial for heat and mass transfer. Porous medium models have been successfully applied to catalysts exhibiting reasonable predictions of the high level distribution of velocity and pressure, but can not provide details about the local flow structures. The inclusion of the full scale device into the computational domain increases the computational requirements. Therefore, new strategies are needed to provide low computationally demanding, yet reasonably accurate modelling tools for the prediction of the small scale structures downstream high resistance devices.

2.6 Aims and objectives

The aim of this work is to experimentally and numerically investigate the fundamental flow features of confined swirling flows (including the effect of inlet asymmetry) found in automotive emission aftertreatment configurations to enable the development of robust simulation methodologies that will facilitate the design of future, and optimised, emission systems.

In order to achieve the above aims the following objectives have been identified:

1. Assess existing experimental and numerical methodologies suitable for the study of confined swirling flows and for high resistance device models.

2. Develop an experimental programme (combining PIV, HWA and pressure measurements) to gain better understanding of fundamental swirling flow properties (in a simple annular pipe configuration), and understand the development of the swirling flow structures inside a sudden expansion with downstream resistance, with and without asymmetry. Thus, providing also a set of experimental data for setting inflow conditions and for validation of complex CFD models, such as LES and DES.

3. Develop a robust numerical methodology for internal swirling flow modelling, by assessing the performance and limitations of RANS-based models in the prediction of confined swirling flows.

4. Develop a novel porous medium modelling approach for high flow resistance devices (monoliths, heat exchangers, etc.) to improve the prediction of the downstream flow, and facilitate computationally efficient optimisation of the multichannel device geometry.

Chapter 3

Methodology

This chapter provides a review of the experimental and numerical methods used in the current study. A combination of experimental techniques and numerical modelling has been used to characterize the evolution of confined swirling flows for various inflow and outflow conditions. The experimental data collected in the current study have provided further insight on the flow features and represent a database for the numerical model validation.

The experimental techniques used are critically analysed to identify their advantages and limitations. Similarly, the method adopted for the CFD study is presented highlighting the modelling capabilities and its approximations, which are the result of the constant balance between accuracy and computational cost of the simulation.

3.1 Experimental methodology

The experimental characterization of confined swirling flows is a non-trivial task, as discussed in the review subsection 2.1.1. A combination of Hot Wire Anemometry (HWA) and static pressure measurements has been used to study the properties of the confined swirling flows in a pipe with annular cross section (described in section 3.1.1), while Particle Image Velocimetry (PIV) has been used to determine the flow distribution inside a diffuser with sudden expansion and downstream resistance (described in section 3.1.1).

Although the techniques adopted in the present study have been widely used in fluid-dynamics, some limitations are known when applied to swirling flows and have been highlighted in the following sections. The strategies adopted to process the data collected are described for each measurement technique. The effects of some post processing choices are shown, where relevant, in the respective results chapter.

3.1.1 Experimental apparatus

The experiments have been conducted in the Flow Research Laboratory at Coventry University. A schematic view of the main components of the experimental apparatus, common to all the experimental activities, is shown in Figure 3.1.

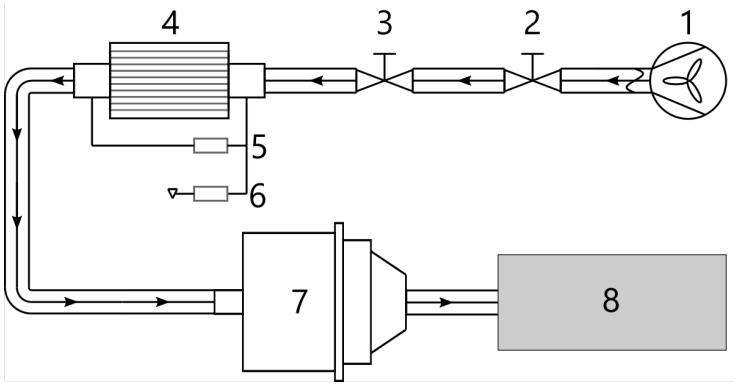

Figure 3.1 Diagram of the experimental apparatus components. Air compressor (1), flow rate control valves (2-3), Viscous Flow Meter (4), Digital pressure transmitters (5-6), Swirl generator assembly (7) and test sections location (8).

The experimental activities included in this thesis use air as working fluid, supplied from the University air compressor, part 1 in Figure 3.1. The amount of air supplied has been manually adjusted using two control valves, (2-3) in Figure 3.1. The mass flow rate has been controlled by imposing differential pressure through the Viscous Flow Meter (VFM), (4) in Figure 3.1. The swirl generator (part 7 in Figure 3.1) has been connected downstream the VFM using a flexible reinforced plastic hose (more details in section 3.1.1). The test sections (part 8 in Figure 3.1) have been attached to the swirl generator using a flange connector and sealed by interposing a ring gasket. For the PIV study, an extractor pipe has been placed downstream the test section, to remove the atomised seeding used in the experiments.

The viscous flow meter, swirl generator and the test sections used are described in more detail below.

Viscous flow meter

The Viscous Flow Meter (VFM) is used to measure the air flow rate upstream the test section. It is a differential pressure flow meter (Miller, 1996; Tropea et al., 2007), with a honeycomb monolith enclosed in a stainless steel pipe providing resistance to the flow.

The differential pressure across the VFM monolith is measured through a digital pressure transmitter (Model 318 - Furness Controls, part 5 in Figure 3.1) and it is

regulated through two manual air valves placed upstream (parts 2 and 3 in Figure 3.1). A second pressure value is measured and recorded using a similar pressure transmitter (part 6 in Figure 3.1), to measure the difference between the pressure upstream the VFM device and the ambient pressure. This pressure is defined as *VFM backpressure* (p_{back}).

A correlation between the differential pressure measured at the VFM (p_{VFM}) and mass flow rate ($\dot{m}_{emp}$) entering the test section has been established. Since differential pressure flow meter measurements depend on the air density, large changes in air temperature and the absolute pressure need to be taken into account. This is usually done by applying a correction to the actual measurements when the temperature and/or line pressure deviate from those standard conditions (Miller, 1996). Since the temperature in the pressure line is relatively stable and close to the ambient temperature ($\approx 20°$ C), the changes in the air density due to the temperature are very small. However, the back pressure in the test sections can be high, which results in high back pressure at the VFM, thus causing a considerable change in the air density.

Therefore, separate experiments have been performed to get a semi-empirical correlation to account for the high back pressure from the downstream resistance devices, which result in an increased p_{back} and temperature variations. During the calibration, the mass flow rate downstream of the VFM has been calculated from the differential pressure measured through an orifice plate device. More details about the experiment and the calibration procedure are given in Appendix B. The experimental data have been fitted and interpolated using high orders polynomial to link the pressure measured at the VFM (p_{VFM}) with the mass flow rate ($\dot{m}_{emp}$). The resulting correlation is described in Appendix B. For clarity, the VFM calibration curve obtained using the orifice plate in the current study (blue line) and the correlation from a previous study (red line, calibration carried out using HWA) are shown in Figure 3.2 for the region of interest of the current study.

A good agreement between the previous calibration curve with the ratio correction (red line with squares in Figure 3.2) and the orifice plate measurements (blue line with dots in Figure 3.2) has been found for the mass flow rate of interest in the current thesis (up to 100 g/s). The ratio correction is discussed in Appendix B, together with a new formulation proposed with the current thesis. The correction needs to be applied to account for the high back-pressure values, which occur at high mass flow rates and in presence of downstream resistance. More details about the effects of the back-pressure and about the correction to apply are given in Appendix B.

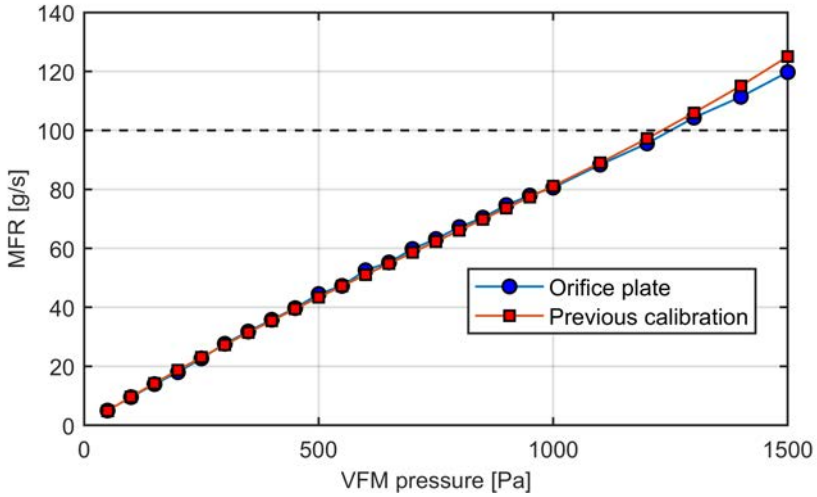

Figure 3.2 Mass flow rate correlation through the Viscous Flow Meter (VFM). Comparison between orifice plate calibration (blue dots) and previous calibration (red squares).

Swirl generator

A moving block swirl generator has been used to generate swirling flow at the test section inlet for all the experimental activities. The swirl generator used for the current thesis is similar to the swirl generator described and characterised in Skusiewicz (2012). As discussed in section 2.1.3, the swirl level and velocity profile at the entrance to the test section has a significant effect on the flow features. Therefore, the assessment of the flow exiting the swirl generator used in the current project has been performed to assess the swirl level and velocity profile at the exit from the swirl generator. The effects of the swirl generator on the flow distribution are presented in Chapter 4 by comparing the experimental data collected with the CFD model. The flow structures generated by this type of swirl generator have been discussed in section 2.1.3. The flow exiting the swirl generator blocks consists with good approximation of only two components (in the *axial* and *tangential* direction), as explained in section 2.1.3.

The main parts of the swirl generator assembly used for the experimental study are shown in Figure 3.3. The tangential component of the inlet flow is modified by changing the relative angle between the *fixed* blocks (Figure 3.3a) and the *moving* blocks (Figure 3.3b). The rotation of the moving blocks allows to change the angle θ_s (Figure 3.3c) from a minimum of $\theta_s = 0°$, which is identified in the following sections as *axial* flow when no swirl is introduced in the test section, to a maximum of $\theta_s = 18°$, which corresponds to the maximum swirl level imposed. The swirl generator features a converging nozzle at the exit (Figure 3.3d) which provides the attachment for the test sections. A detail of the inner insert of the nozzle is shown in Figure 3.3e.

The same geometry has been used in the CFD simulations, to closely reproduce the inflow conditions, keeping the dimensions within 1%.

(a) Fixed blocks **(b)** Moving blocks **(c)** Angle θ_s

(d) Nozzle (ext.) **(e)** Nozzle (int.)

Figure 3.3 Swirl generator: fixed blocks plate (a), moving blocks plate (b), angle (θ_s) between the blocks (c), nozzle view (external) (d), detail of the nozzle insert (e).

Test sections

The test sections used throughout the current thesis are:

1. pipe with annular cross section;
2. diffuser with sudden expansion and downstream resistance;
3. planar diffuser with downstream resistance.

The first two test sections (pipe with annular cross section and diffuser with a sudden expansion) have been used in both numerical and experimental studies, while the third one (planar diffuser) has been used for a numerical study only. A description of the geometry of each test sections and of the experiments carried out, including the motivation of the choice of the configuration, is presented in the next paragraphs.

Differences between the dimensions of the experimental test rigs and the computational domains reproduced for the CFD models are within 1%.

Pipe with annular cross section The pipe with annular cross section has been used to study a confined swirling flow, without downstream resistance (Figure 3.4). The

presence of the annular insert acts as a blunt body around which the flow is forced to move. It is often introduced in the studies of confined swirling flows, because in this case the formation of the central recirculation bubble (discussed in subsection 2.1.1) is avoided. It is therefore convenient to use this configuration to study the effect of swirl on a simple pipe flow. Short annular pipes are also relevant in several engineering applications, such as jet burners and combustion chambers.

The test section used for the current study is shown in Figure 3.4. The pipe has been used in both experiments and CFD model to analyse the effects of the inflow conditions, swirl level and Reynolds number, on the flow distribution.

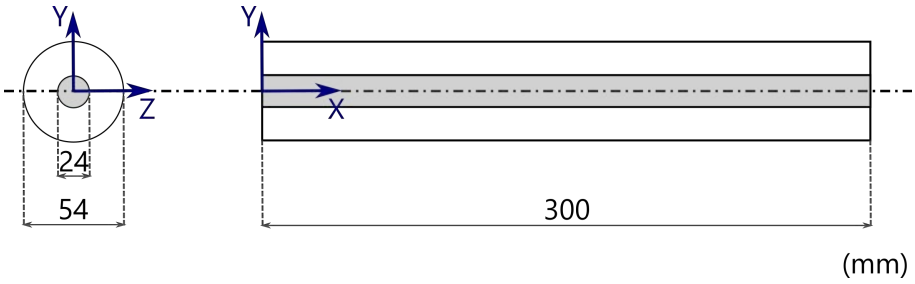

Figure 3.4 Pipe with annular cross section. Dimensions in mm.

The pipe has a nominal length of 300 mm, with an outer diameter of 54 mm and an inner diameter of 24 mm, resulting in a ratio of 2.25. The presence of the flanges and the ring gasket used to connect the pipe to the upstream swirl generator increase the overall length by up to 6 mm. The external cylinder has been manufactured in aluminium, with a thickness of 10 mm, to allow the positioning of the pressure tap-holes. The position and design of the tap-holes are discussed in the next section, when the static pressure measurements are described (subsection 3.1.3).

A *cylindrical* coordinate system for the pipe with annular cross section is introduced here and used throughout the thesis (Figure 3.5b).

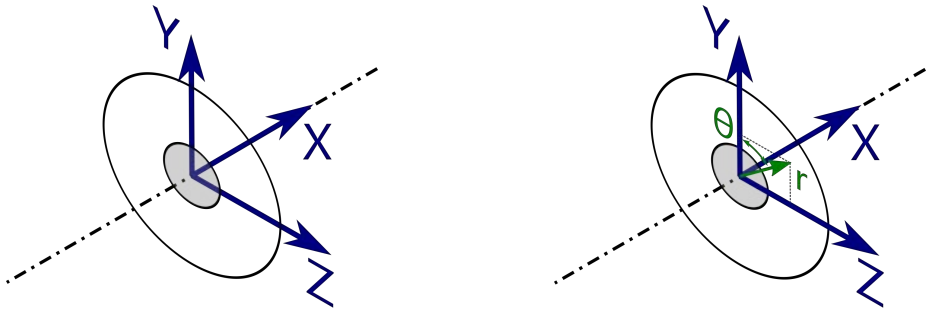

(a) Cartesian **(b)** Cylindrical

Figure 3.5 Transformation from Cartesian coordinate system [X,Y,Z] to cylindrical coordinate system [X, r, θ] used for the pipe with annular cross section (Figure 3.4).

This pipe geometry has been used in both experiments and CFD model to analyse the effects of the inflow conditions, swirl level and Reynolds number, on the flow distribution.

Diffuser with a sudden expansion The dimensions of the diffuser with a sudden expansion are given in Figure 3.6.

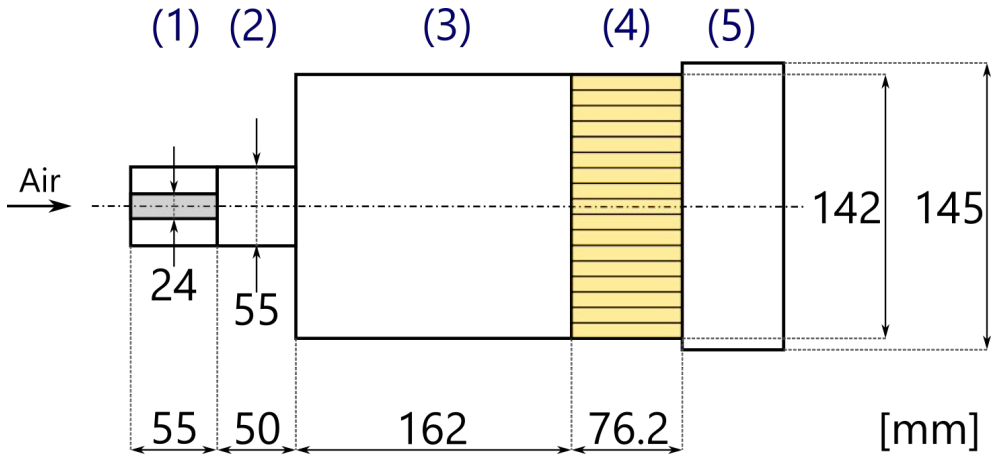

Figure 3.6 Diffuser with a sudden expansion: experimental rig, schematic view (not to scale). Left to right: annular pipe insert (1), diffuser inlet (2), sudden expansion (3), monolith (4) and outlet sleeve (5). Dimensions in mm.

The annular pipe insert (1) is placed downstream the swirl generator. The flow enters the diffuser inlet (2), before expanding in the sudden expansion section (3), with an area ratio of 2.58. A 400-cpsi ceramic honeycomb monolith substrate (4) is fitted downstream the sudden expansion. An outlet sleeve (5) is used downstream, to hold the monolith in place and provide shielding to facilitate downstream flow measurements (Skusiewicz, 2012).

The diffuser has been manufactured in borosilicate glass, to provide optical access inside the sudden expansion for laser measurements. The isometric view of the CAD model used to design the asymmetric glass diffuser with 20 mm displacement is shown in Figure 3.7a, while the view of the experimental test section is shown in Figure 3.7b. The diffuser has been assembled from three separate components (Figure 3.7a). The three components identified as *inlet pipe* (1), *expansion disk* (2) and *sudden expansion* (3) have been glued together and sealed at the external surface, to avoid air leaks. Black non reflective paint has been applied at the inner surfaces (inlet and diffuser half bottom and disk) to minimise the light reflections.

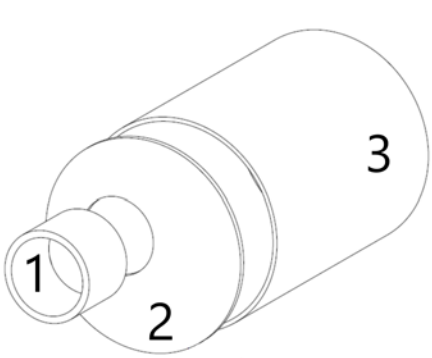

(a) Sudden expansion CAD

(b) Test section view

Figure 3.7 Diffuser with downstream sudden expansion (non symmetric rig). CAD isometric view (a): inlet (1), expansion disk (2), sudden expansion (3). View of the experimental test section (b).

Two different glass diffusers have been used for the PIV study presented in this thesis:

1. *axisymmetric*: used as a baseline to further investigate the flow structures and validate the CFD model;
2. *asymmetric*: used to explore the flow structures of confined swirling flows with asymmetry and for model validation.

A schematic representation of the relative position of the inlet pipe and the sudden expansion is shown in Figure 3.8: on the left the axisymmetric diffuser (a), on the right the asymmetric one (b). Asymmetry has been introduced by shifting the expansion axis by 20 mm relative to the inlet pipe axis.

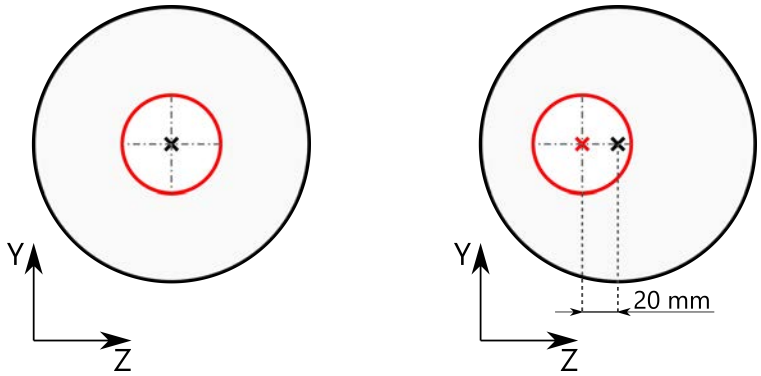

(a) D = 0 mm

(b) D = 20 mm

Figure 3.8 Displacement between inlet pipe (red) and sudden expansion (black): D = 0 mm (a), D = 20 mm (b)

Planar diffuser In this study, the planar diffuser test section (Figure 3.9a) has been used for numerical modelling purposes only. A brief description of the experimental apparatus used in the study performed by Porter (2016) is presented here, as the results of the experiments are used for the numerical model validation in Chapter 7. Air is supplied to the inlet and enters a diffuser section, which features an angle of 30° with respect to the axis, section (1) in Figure 3.9b.

The diffuser part of the experimental rig used in the study by Porter (2016) is shown in Figure 3.9a. The nozzle section upstream the glass diffuser was designed to provide a uniform velocity profile at the diffuser inlet and it has not been included in the CFD model. A monolith was fitted downstream the glass diffuser and held into position by an outlet sleeve. The schematic representation and the dimensions of the geometry reproduced for the computational model are shown in Figure 3.9b. Only half geometry is shown here, since the flow has proved to be 2-dimensional and symmetrical within respect to the axis, as shown in Porter (2016).

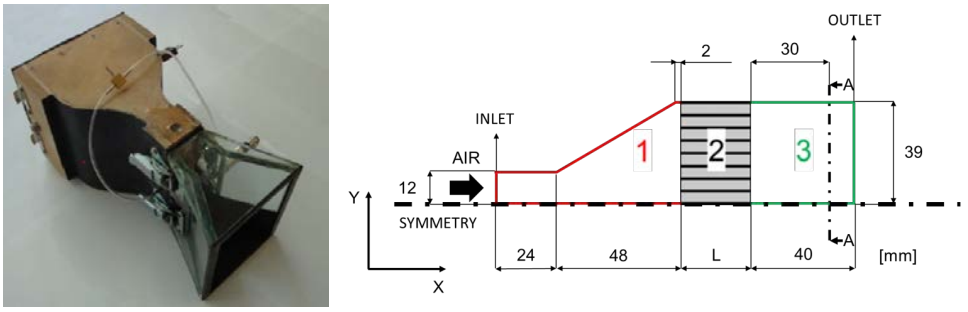

(a) Experimental rig **(b)** Dimensions

Figure 3.9 Planar diffuser with downstream resistance. Experimental apparatus view (a) used in (Porter, 2016). Test section dimensions used for the CFD model (b): diffuser section (1), monolith section (2) and outlet sleeve (3).

3.1.2 Hot-Wire Anemometry

The velocity measurements using Hot Wire Anemometry (HWA) have been made downstream the swirl generator and at the outlet section of the pipe with annular cross section, Figure 3.10. The sampling section downstream the swirl generator has been identified as *Section 1* (Sec.1) and the sampling section downstream the pipe has been identified as *Section 2* (Sec.2).

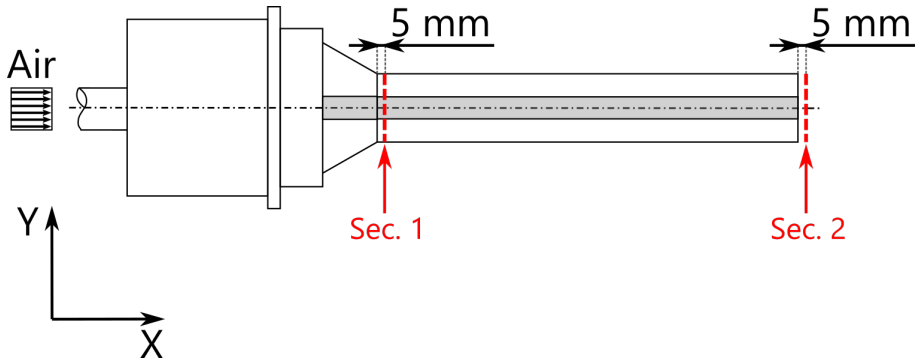

Figure 3.10 Pipe with annular cross section: HWA measuring sections. Section 1 (Sec. 1) at 5 mm downstream the swirl generator, Section 2 (Sec. 2) at 5 mm downstream the pipe outlet.

As HWA is an intrusive measurement technique and because of the difficulty of the access, no velocity measurements were carried out inside the pipe. However, due to the simplicity of the annular configuration, knowledge of the inlet and outlet velocity profiles combined with the wall pressure measurements still allows to get a good insight into the flow properties, and provides sufficient data for CFD validation studies.

The velocity measurements in the upstream section (Sec. 1 in Figure 3.10) have been carried out without the pipe attached to allow probe access. Although the presence of the test section can change the flow at the swirl generator exit, this effect was judged to be negligible as the pipe with annular cross section provides negligible back pressure and no flow instabilities (such as precessing vortex core) were expected and indeed observed for the flow parameters considered in this study.

Measurements at both sections have been made using a single-wire Dantec 55P11, connected to a Constant Temperature Anemometer system IFA 300 (TSI, 2010). The probe calibration and the data acquisition have been made using the TSI software ThermalPro (TSI, 2010). The probe calibration and the sampling points are described in the following paragraphs.

Single wire calibration

The probe has been calibrated using a TSI 1129 calibrator (TSI, 2010). The calibration has been repeated several times during the experimental activities to reduce the uncertainty. An example of the plot obtained during the calibration is shown in Figure 3.11. The velocity range for the calibration has been chosen from 0 m/s to 150 m/s, in order to have the same calibration for all the inflow conditions. The calibration file gives an estimate of the error for each calibration point, which has been used to estimate the uncertainty of the HWA measurements in subsection 3.4.2.

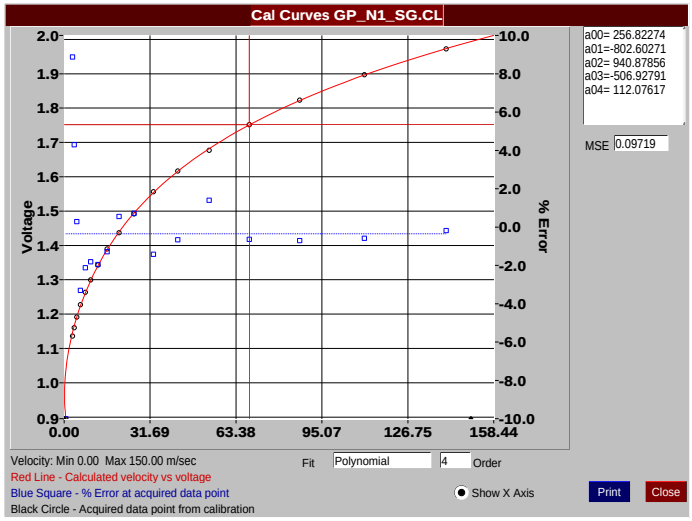

Figure 3.11 HWA calibration plot from ThermalPro (TSI, 2010). Calibration curve (red), relative error at data points (blue squares).

Sampling points

A programmable 2D transverse has been used to vary the probe position at both sections (e.g. at the outlet section in Figure 3.12a). The transverse has been connected to an Isel Schrittmotor-Controller C142-4 and controlled with the TSI ThermalPro software (TSI, 2010).

The sampling points in the cross section are shown in Figure 3.12b. The velocity has been sampled along the two perpendicular diameters Y and Z, using a total of 14 points for each radius, spaced every 1 mm, starting at $\approx$ 1 mm from the wall.

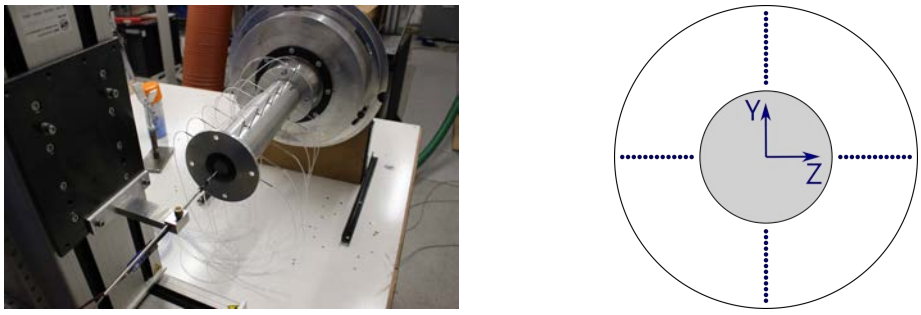

(a) Experimental view **(b)** Sampling points

Figure 3.12 View of the experimental apparatus for the HWA measurements at the pipe outlet (a). Sampling points (a) used for the HWA measurements at both sections shown in Figure 3.10.

Velocity component decomposition

The directional sensitivity of single wire probes has been investigated in multiple studies (Adrian et al., 1984; Di Mare et al., 2017; Figliola and Beasley, 2011; Jørgensen,

2002; Tropea et al., 2007). A single wire probe can not measure multiple velocity components, but only the velocity normal to the hot-wire probe. In presence of swirling flows, the flow stream is not parallel to the pipe axis, but features a certain angle that varies with the swirl level and the position. It is, consequently, not possible to align the probe with the flow direction *a priori*.

The heat transfer for ideal sensors (wire only) varies with the "cosine law", meaning that the heat transfer depends on the cosine of the angle between the probe and the flow (Jørgensen, 2002). The presence of the prongs support (brown in Figure 3.13) modifies this behaviour, since heat is transferred to the prongs. This effect is accounted for in the measurements (Jørgensen, 2002) by including a *yaw* factor coefficient (k). The increased heat transfer due to out of plane effects in 3D flows (Jørgensen, 2002) is accounted for including a *pitch* factor coefficient (h). All the above results in the following expression for the effective cooling velocity (U_{eff}) in 3D flows

$$U_{eff}^2 = U_x^2 + k^2 U_y^2 + h^2 U_z^2 \tag{3.1}$$

In Equation 3.1, the terms U_x, U_y, U_z are the three velocity components in the local probe reference system (shown in Figure 3.13), while k is the yaw factor and h is the pitch factor.

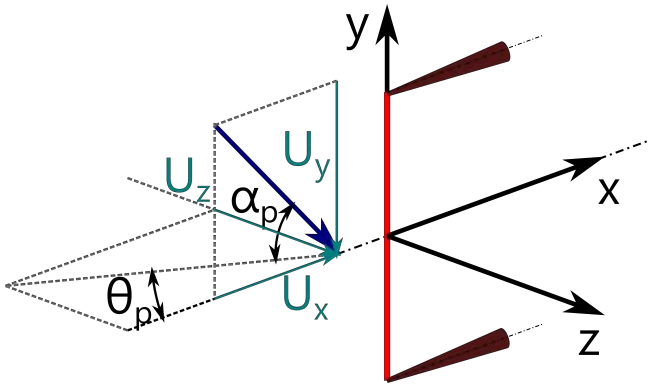

Figure 3.13 Single wire probe: *effective* velocity decomposition in the local probe reference frame.

The yaw and pitch factors for the probes used in the current study were not given by the manufacturer. Wagner and Kent (1988) performed a study on the single wire probes used in the current study aiming to evaluate the angular response of the single HWA probe. The angular response in Wagner and Kent (1988) has been made repeating the same experiments on 5 Dantec 55P11 probes. The pitch coefficient has been found to decrease with the velocity, with the maximum for h between 1.09 and 1.16 for the velocity range between 10 m/s to 30 m/s. In the same study (Wagner and Kent, 1988) the yaw coefficient is calculated from experiments for the same probes. High variability

of the coefficient has been observed between the 5 probes used ($0.01 < k^2 < 0.10$) exhibiting a linear dependence with the velocity. Wagner and Kent (1988) have observed a high variability of the yaw coefficient ($\approx 0.20 \pm 50\%$) and a low impact of its use for flow angles up to 45° if pitch effects are accounted for. For the above reasons, in the current study, the pitch coefficient has been assumed to be $h = 1$, while the yaw coefficient has been neglected ($k = 0$).

The main approximation made in the current study is that the "third" velocity component (in the θ direction, Figure 3.5) is negligible with respect to the other two components, given that the swirl generator is of the moving blocks type, as discussed in section 3.1.1. Therefore, only two velocity components have been assumed to be measured: the *axial* velocity component (U_x) in the direction of the pipe axis (X) and the *tangential* velocity component (U_y), in the direction of the pipe radius (r). Thus, two measurements have been made in each sampling point (Figure 3.12b), orienting the probe as shown in Figure 3.14: the probe has been positioned *parallel* to or *normal* to r.

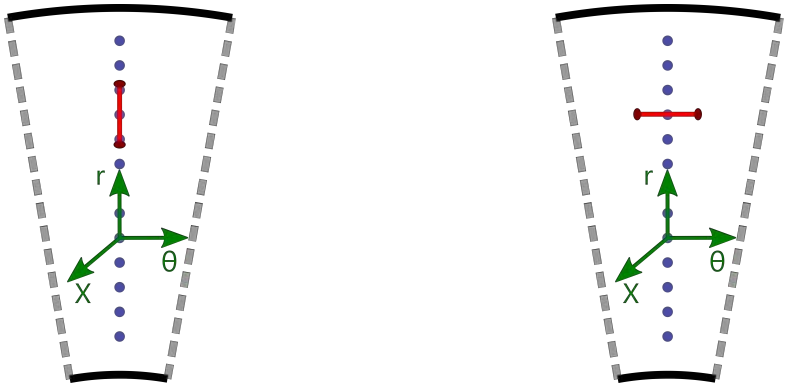

(a) Parallel **(b)** Normal

Figure 3.14 Single wire probe (red) orientation: *parallel* (a) or *normal* (b) to r.

Introducing the above approximations, the effective cooling velocity with the probe in the *parallel* position is

$$U_{eff_p}^2 = U_x^2 + h^2 U_y^2 \tag{3.2}$$

while the effective cooling velocity with the probe in the *normal* position is

$$U_{eff_n}^2 = U_x^2 \tag{3.3}$$

Combining Equation 3.2 and Equation 3.3, the tangential velocity component is

$$U_y = \sqrt{U_{eff_p}^2 - U_{eff_n}^2} = \sqrt{(U_x^2 + U_y^2) - U_x^2} \tag{3.4}$$

The flow angle (γ_s) has been extracted from the calculated velocity components as

$$\gamma_s = \arctan\left(\frac{U_y}{U_x}\right) \tag{3.5}$$

An example of the application of the velocity decomposition is presented in section 4.1.1, while an assessment of the results is presented in section 4.3.

Turbulence intensity and frequency

The time signal acquired with the hot-wire can be used to calculate some turbulence quantities. The estimation of turbulence using a hot-wire system is advantageous over other techniques (e.g. LDA) for multiple reasons, including lower cost, lower noise/signal ratio and high frequency response (Bruun, 1996).

The turbulence intensity T_i (Bailly and Comte-Bellot, 2015) is defined as

$$T_i = \frac{u'}{\bar{U}} \tag{3.6}$$

in which $\bar{U}$ is the mean velocity and u' is the root-mean-square of the turbulent velocity fluctuations.

In addition to the turbulence intensity other information about the turbulent character of the flow can be extracted by performing a frequency analysis. The signal acquired experimentally from the velocity measurements, is known to combine a range of frequencies originating from different sources. Frequencies associated with the fluid flow can be used to analyse flow instabilities, behaviour of different flow structures and turbulent properties. The flow frequency has a crucial role in the definition of the inlet boundary conditions for complex modelling approaches, such as LES and DES, as described in subsection 2.2.2. However, the presence of multiple components in the test rig, such as the compressor, the swirl generator assembly and the actual test section, can cause the presence of peak frequencies not directly associated with the flow structures typical of swirling flows. While signal analysis can be successfully used to get extra insights into the flow properties (e.g. turbulence characteristics (Bailly and Comte-Bellot, 2015; Pope, 2000), it is important to ensure that other frequencies (e.g. natural frequency of the experimental rig) and noise are eliminated (Figliola and Beasley, 2011). The results of the analysis applied in the current study is presented in section 4.1.1.

In order to establish the validity of the frequency analysis carried out on the signals acquired, different sampling frequencies have been used for the Hot Wire Anemometry measurements. The sampling frequency is not crucial when determining the mean properties of the flow, but can be important if it is necessary to capture a wide range of

frequencies in the experiment. The typical frequencies for the flows considered in the current study were not known *a priori*. For this reason, during the data acquisition of the HWA velocity three different sampling frequencies have been used, for all inflow conditions: 200 Hz, 600 Hz and 1000 Hz.

It is known from data analysis theory (Figliola and Beasley, 2011) that if the frequency of interest is f_t, in order to satisfy the *Nyquist-Shannon* theorem, the sampling frequency f_s should satisfy the condition

$$f_s > 2f_t \tag{3.7}$$

Consequently, the maximum frequency values that was possible to capture are half of the ones imposed (i.e. frequencies up to 500 Hz with the maximum sampling frequency of 1000 Hz).

The analysis of the time signal has been performed using MATLAB. The Discrete Fourier Transform (DFT) has been calculated using the Fast Fourier Transform (FFT) algorithm. The built-in MATLAB function *fft* has been used to calculate the amplitude spectrum of the signal, which has been reduced to a single-side spectrum in the positive frequency domain (MATLAB, 2019), thus obtaining the power spectral density of the signal. The energy density spectrum has been calculated using the definition presented in El-Gabry et al. (2014). The energy ($E(f)$) can be determined as

$$E(f) = \frac{P(f)}{f} \tag{3.8}$$

where $P(f)$ is the power spectral density calculated as

$$P(f) = \frac{\left|fft(U)\right|^2}{L_s} \tag{3.9}$$

in which L_s is the length of the signal. An example of the procedure is given in section 4.1.1. The effects of the sampling frequency have been analysed for all the inflow conditions (Table 3.3) and a discussion is presented in section 4.1.1.

3.1.3 Pressure tap size and spacing study

Due to the intrusive nature of most pressure measurement techniques, only static wall pressure is usually measured in confined flows. This is done using pressure taps (holes) in the walls. In order to establish the best configuration for wall pressure measurements in the confined swirling flows, an experimental study has been carried out with different pressure tap geometries and positions. The study has been carried out on the pipe with annular cross section (Figure 3.4).

The static pressure measurements have been carried out using a classic pressure-tap configuration (Shaw, 1960), which is shown in Figure 3.15. It has been discussed in section 2.1.3 that the tap-hole configuration can affect the flow properties and possibly lead to incorrect measurements. The majority of studies (as described in section 2.1.3) have shown that the errors for the single hole-tap configuration can be attributed to the following 4 sources:

- inner hole size (d_h in Figure 3.15a);
- hole depth (L_h in Figure 3.15a);
- hole-tap axis alignment;
- protruding tap;

The use of a configuration similar to the one shown in Figure 3.15a allows to eliminate the error due to tap protrusion (as discussed in section 2.1.3). The inner hole can be carefully polished to reduce the material residual due to the manufacturing process and minimise the effects of the protrusion inside the flow. The alignment of the tap-hole axis can be minimised during the manufacturing process and it is considered negligible in the current study. This study aims to investigate the effects of the hole-tap geometry in presence of flows with high streamline curvature, such as swirling flows.

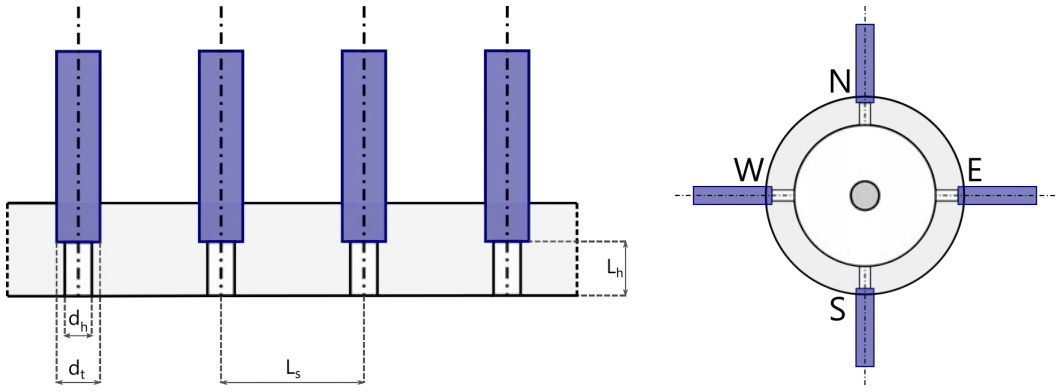

(a) Tap-hole topology **(b)** Section view

Figure 3.15 Tapping-hole topology for the static pressure measurements (a): hole diameter (d_h), tap diameter (d_t), distance between two consecutive pressure tappings (L_S), hole depth measured from the inner wall (L_h). Spacing of the pressure taps in a section on the external pipe (b). Figures are not to scale

The main aspect that has not been clarified in the available literature, as pointed out in section 2.1.3, is the impact of the distance L_S between two consecutive pressure tappings

on the flow distribution. In order to assess the quality of wall pressure measurements in this project, an experimental study has been performed focused on the effect of the geometry of the pressure taps and the distance between pressure taps (Chapter 4).

Hole-tap study

The pressure taps used for the current study are bulged stainless steel tubulations manufactured by Scanivalve. The TUBN-063 type has been used, with nominal internal diameter (d_t) of 0.063 inch, corresponding to 1.59 mm and a nominal length of 2.0 inch, corresponding to 50.8 mm.

Two external cylinders for the pipe have been used, which are referred in the text as *Cylinder 1* and *Cylinder 2*. A detailed CAD drawing for both configurations is included in Appendix A, together with the positions of each pressure tap. The first one (*Cylinder 1*) has been used to investigate the effects of hole size (d_h) and hole depth (L_h), while the second (*Cylinder 2*) has been used to investigate the effects of the distance between two consecutive pressure tappings (L_S).

The distance between the pressure tappings on *Cylinder 1* has been fixed to 50 mm. The pressure tappings on Cylinder 1 have been mounted along the external wall, in order to get 4 tappings in each cross section, as shown in Figure 3.15b. The hole depth (L_h) has been fixed 6 mm on the North line, 4 mm on the South line, 2 mm on the East line and 0 mm on the West line (Figure 3.15). For the line with the flush pressure tapping (West, $L_h = 0$ mm) the hole diameter d_h has been fixed equal to the pressure tapping diameter $d_t = 1.59$ mm. For the other three lines (North, South and East), the hole diameter has been fixed to 1 mm.

The second external cylinder (*Cylinder 2*) has been manufactured to evaluate the influence of the axial spacing between two consecutive pressure hole-taps on the pressure readings, which is still not well understood. The use of the second cylinder had also the purpose to increase the spatial resolution of the measurements (as a consequence of the increased number of points) and to test the repeatability of the experiments. For all the pressure tappings used in *Cylinder 2*, the hole diameter has been fixed to $d_h = 1$ mm and the hole depth has been fixed to $L_h = 6$ mm.

The distance between individual pressure tappings (L_S in Figure 3.15a) has been varied on *Cylinder 2* from 40 mm down to 5 mm, aiming to capture the effects of the interference between two consecutive probing points. Similarly to the previous configuration, 4 pressure lines have been used, keeping the same topology shown in Figure 3.15b. The pressure tappings along the North (L_S = 40 mm) and South (L_S = 20 mm) lines have been equally distributed along the axial direction, with the first tapping at 10 mm from the inlet and the last one at 10 mm from the inlet. For the other two

lines (East - L_S = 10 mm and West - L_S = 5 mm) the pressure tappings have been fitted in the central portion of the pipe (90 mm up to 210 mm). For the remaining length, in both cases, the distance has been left equal to 40 mm. By using this configuration, the pressure taps every 40 mm (red in Figure 3.16) are common to all the pressure lines.

A schematic view of the central portion of *Cylinder 2* (90 mm up to 210 mm from the pipe inlet) is shown in Figure 3.16, to visualise the differences between the taps positions.

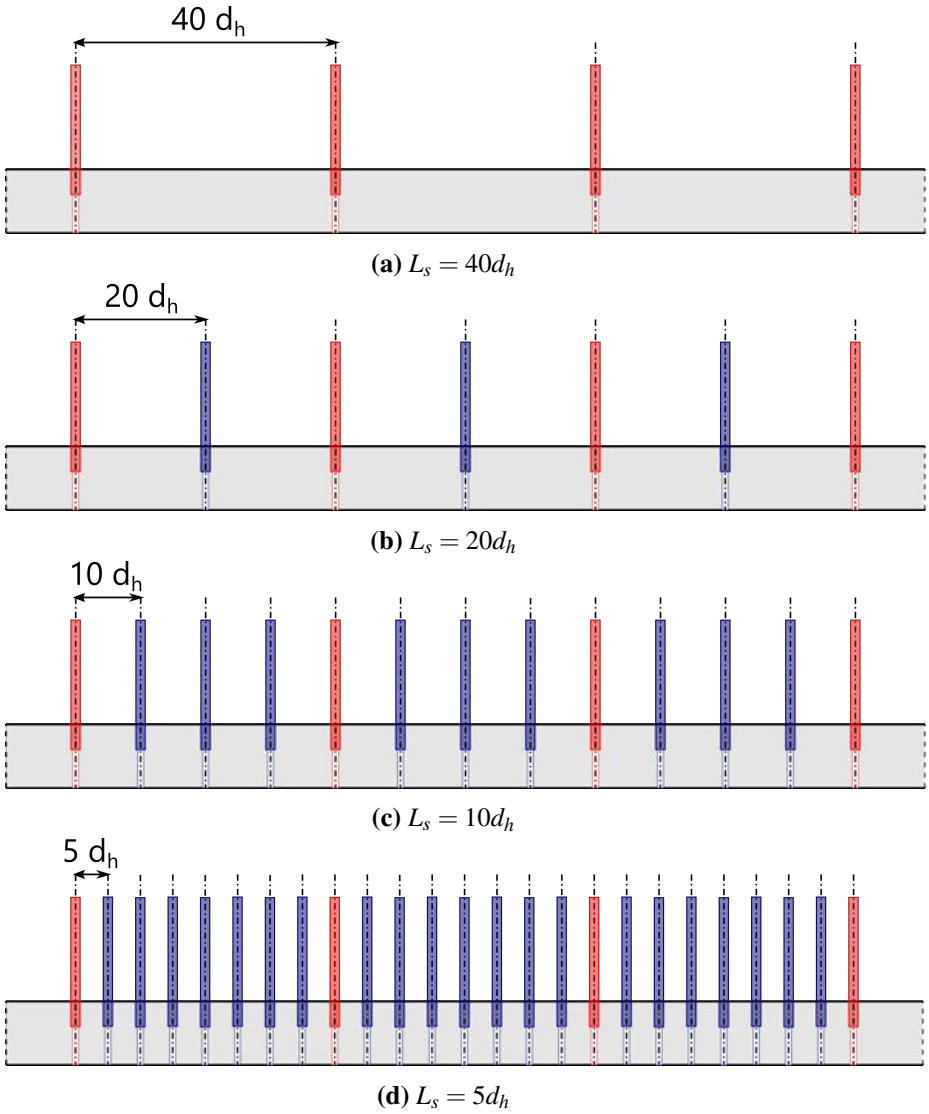

(a) $L_s = 40d_h$

(b) $L_s = 20d_h$

(c) $L_s = 10d_h$

(d) $L_s = 5d_h$

Figure 3.16 Details of the pressure tappings distance (L_s) for *Cylinder 2* (from 90 mm to 210 mm). North line, $L_s = 40mm$ (a), South line, $L_s = 20mm$ (b), East line $L_s = 10mm$ (c) and West line $L_s = 5mm$ (d). Red pressure tappings are common to all the pressure lines, blue ones are specific of the line.

The methodology used to analyse the effects of the pressure tappings distance is presented in the following section 3.1.3, while an example of the procedure and the results of the analysis are discussed in section 4.1.2.

Pressure sampling and data analysis

The tappings have been connected to the electronic pressure scanning module *ZOC 33/64* by Scanivalve Corp. using vinyl tubing of fixed length, with an inner diameter of 0.063 inch. The ZOC33 module incorporates 64 individual piezoresistive pressure sensors, linked through plastic tubes of fixed length to a round pneumatic connector. The module is connected to the RAD4000 Ethernet Pressure measurement system, linked via Ethernet to the Workstation, to get real time readings through the acquisition software ScanTel (Scanivalve, 2016). For the majority of pressure tappings, the model *ZOC33-20* has been used, with a range of $\pm$5 kPa and accuracy rated at $\pm$ 0.15 % full scale. For 5 pressure tappings close to the outlet on Cylinder 2 the model *ZOC33-10*, with a range of $\pm$2.5 kPa and accuracy rated at $\pm$ 0.20 % full scale has been used.

The pressure measured at each location is a differential pressure between the local value and the reference pressure acquired during the calibration. The calibration of the Scanivalve has been performed before each measurement without flow entering the pipe, using ambient pressure as reference for the calibration. The results have been post processed using MATLAB.

In order to smooth the effect of the asymmetry due to connections and manufacturing, that could alter the results, 4 measurement sets have been acquired for each inflow condition, by rotating the position of the external cylinder. In practice, the first measurement set has been obtained with the North line up (Figure 3.15b), the second with the East line up, the third with the South line up and the fourth one with the West line up. The final values used for the analysis have been obtained by averaging the data from the 4 measurement sets, obtaining a smoothing effect on the manufacturing asymmetry.

The effects of the hole depth have been analysed by comparing the standard error of the mean associated with the measurement (as defined in subsection 3.4.5, Equation 3.39). The effects of the pressure tappings distance (L_s) has been investigated by performing a linear regression analysis in the central portion of the pipe, between 0.3 X and 0.7 X (Figure 3.16). A linear interpolation for each separate pressure line has been made using the built-in MATLAB function `polyfit` (MATLAB, 2019). An estimate of the 95% prediction interval ($\pm\delta_{L_s}$) has been made using the error estimation structure of the function `polyfit` (MATLAB, 2019). The average value of δ_{L_s} for each line has been used to evaluate the data scattering due to the pressure tappings distance. The

analysis of the results and examples to clarify the methodology adopted are included in section 4.1.2.

Similarly to the HWA frequency analysis (presented in section 3.1.2), three sampling frequencies have been used for the pressure sampling (200 Hz, 600 Hz and 1000 Hz). The acquisition data rate (f_s) for the Scanivalve cannot be set directly, but it can be calculated (Scanivalve, 2016) from

$$f_s = \frac{1}{N_{ch} \cdot T_s} \tag{3.10}$$

Here, N_{ch} is the number of channels used (which is equal to the number of pressure tappings) and T_s is the sampling period specified by the user (in μs). Since N_{ch} is fixed and it is equal to the number of pressure tappings, in order to obtain a specific sampling frequency (f_s), Equation 3.10 can be reversed as

$$T_s = \frac{1}{f_s \cdot N_{ch}} \cdot 10^6 \tag{3.11}$$

The sampling period (Equation 3.11) is limited between $20\mu s$ to $65535\mu s$ (Scanivalve, 2016). For this reason, when the *Cylinder 2* configuration was used, the maximum available frequency for the simultaneous acquisition of the data from all the 69 channels was limited to 600 Hz, corresponding to $\approx 24\mu s$. The time duration of the sampled signal has been adjusted by varying the number of samples captured for each pressure tapping (Scanivalve, 2016). The number of samples for each pressure tapping has been fixed to 10000 for all the measurements.

3.1.4 Particle Image Velocimetry

Particle Image Velocimetry has been used to determine the flow structures inside the diffuser with sudden expansion and downstream resistance. The data collected constitute a database for model validation.

PIV Equipment

The view of the experimental test section and of the experimental components used for the PIV measurements is shown in Figure 3.17. A schematic representation of the components used for the PIV experiments and the relative positions between them is presented in Figure 3.18. The camera has been mounted on the top of the sudden expansion (Y direction in Figure 3.18a) perpendicular to the section XZ. The height of the camera (B) has been adjusted manually to include the inlet and the expansion in each frame. When the non symmetric diffuser has been used, the camera has been

shifted by 20 mm (as the sudden expansion displacement) and re-aligned with the sudden expansion axis. The laser has been mounted on a stand at the right hand side of the test section when seen from upstream (Figure 3.18b). The distance between the laser and the sudden expansion (A) has been adjusted to ensure that the entire diffuser was illuminated (inlet and sudden expansion). The height of the laser has been regulated to generate the light sheet in the XZ plane at Y = 0. More details about the alignment procedure are given in the next paragraphs.

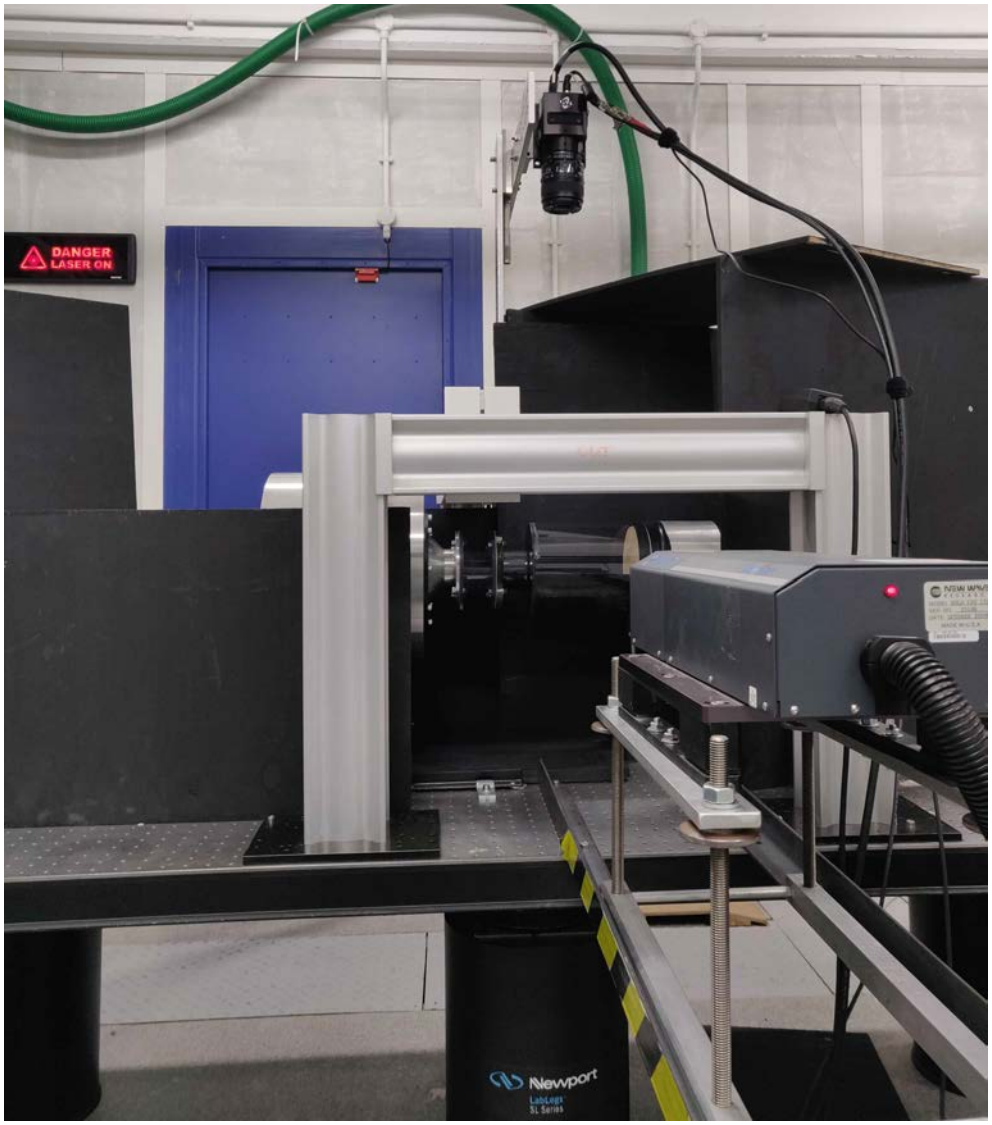

Figure 3.17 View of the experimental apparatus used for the PIV experiments

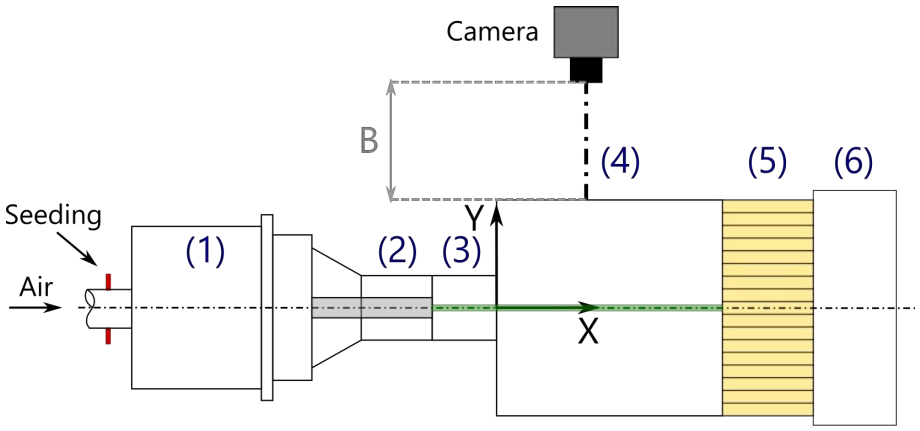

(a) Side view

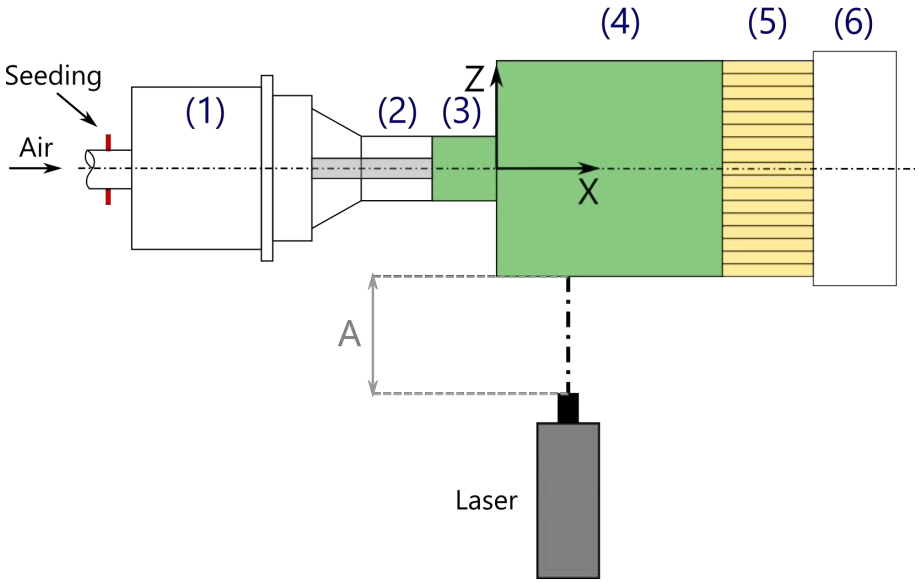

(b) Top view

Figure 3.18 PIV test section: relative position between components, side view (a) and top view (b). Swirl generator assembly (1). Annular pipe extension (2). Diffuser test section: inlet (3) and sudden expansion(4). Ceramic monolith (5). Outlet sleeve (6). Camera mounted on top of the sudden expansion section (a). Laser beam coming from the right hand side (b).

Camera and lens The TSI PowerView Model 630094 camera with 29 MP resolution has been used for the acquisition of the images, with the Nikon AF Micro Nikkor 60 mm f/2.8D lens attached to the camera sensor. The camera has been mounted on a frame stand, to regulate the height, the relative angle between the camera and the test section and adjust the positioning relative to the expansion axis (Figure 3.18a).

The lens with focal length of 60 mm has been selected to capture the entire test section. The aperture was manual-controlled for adjustments between f/2.8 and f/32 and was fixed to f/11 for all the experiments. The camera has been connected to a LaserPulse

Synchronizer Model 610063 and to a frame grabber installed on the Workstation used for the image capturing.

Laser and light sheet The laser used to generate the illumination sheet for the PIV plane is a SOLO PIV Nd:YAG Laser by New Wave Research. The laser has been positioned on a stand located at the right hand side of the diffuser (Figure 3.18b). The laser height has been adjusted manually using an in-house made support, which has also allowed the alignment of the laser with the sudden expansion axis (Y = 0 mm). The distance between the laser and the test section has been calibrated manually in order to capture the inlet pipe and the sudden expansion section.

The laser beam sheet plane has been obtained using a combination of three lenses to transform the beam emitted by the laser from a cylindrical cross-section (with a diameter of 4 to 5 mm) to a light sheet (Raffel et al., 2007). The first two lenses, with a focal length of -15 mm and -25 mm respectively, have been used to spread the light in the width direction (X in Figure 3.18b), while the third lens with 500 mm focal length has been used to reduce the beam thickness (l_t). The resulting laser thickness of 1 mm has been estimated to be sufficient for the swirling flow measurements carried out, using the approximation proposed in Giannadakis et al. (2008). The relative alignment between the laser sheet and the diffuser has been carefully verified step by step using a calibration target. The procedure is explained in the following section.

Calibration targets A reference target is fundamental to convert the pixel dimensions into standard units, as will be clarified in the results processing section. The conversion factor between pixels and SI units can be extracted in first approximation from known dimensions of the test section, but the use of a target with fixed positions and dimensions increases the accuracy of the calibration procedure (Raffel et al., 2007). A basic calibration consists in the extraction of the distance between two points, assuming that the conversion factor is the same for all the points of the image, in both directions. In addition, the images captured by the PIV camera are subject to distortion caused by several factors, such as camera lens curvature, light refraction from the test section, light path distortion due to materials reflections and curvature of the test section. To account for this effect, the acquired images should be corrected by using a reference target with know dimensions.

In this study, three different reference targets have been used, shown in Figure 3.19. The targets have been printed on non-reflective paper with a high resolution laser printer and glued on aluminium plates with 3 mm thickness. This step has been necessary

to adapt the dimensions of the target to the test section. Prior to each experiment 10 images of each target have been acquired and stored.

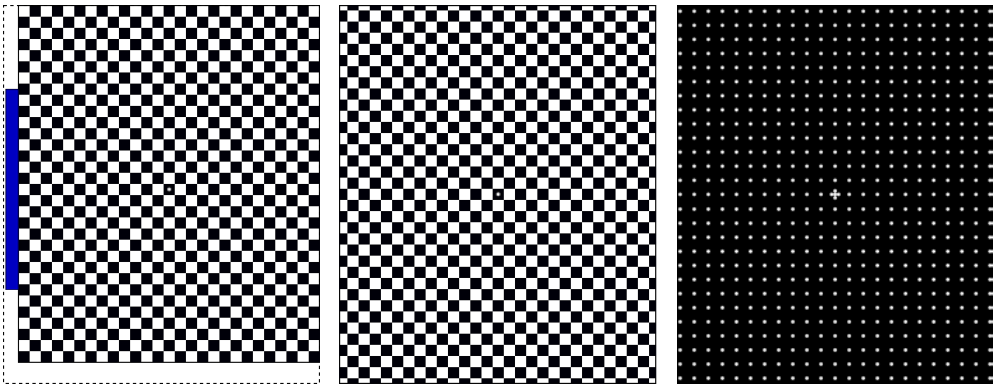

(a) Target #1 **(b)** Target #2 **(c)** Target #3

Figure 3.19 PIV target plates

The dimensions of Target #2 and Target #3 are the same (140 mm x 170 mm), while Target #1 is smaller then the other two targets, since it features a mirror on the side (blue insert in Figure 3.19a). The chequered board used for the first two targets (Target #1 and Target #2) consists of black and white squares of 5 mm side. The squares have been distributed along the two directions starting from the central black square for both targets identified by the white dot. The third target (Figure 3.19c) consists of white dots with a diameter of 1.6 mm (6 px), equally distanced every 6.4 mm (24 px). The targets have been used for different purposes during the configuration of the experiment and in the post-processing phase. The Target #1 has been used to facilitate the laser alignment, using the mirror on the side. The Target #3 has been used during the set-up phase to refine the camera focus on the plane and regulate the lens aperture. The lens aperture has been manually optimised to ensure image clarity, reducing the overexposure which could damage the camera sensor and fixed to f/11 for all the experiments. The adjustments have been verified prior to each experiment, to account for the presence of the monolith, which modifies the luminosity distribution inside the test section. The calibration and the estimation of the image distortion has been made by using the reference target #2 (Figure 3.19b). More details are given in section 3.1.4.

Relative alignment between the components The procedure for the alignment between the different components is a non-trivial task in PIV experiments. As mentioned in the previous section, the alignment of camera and laser relative to the test section has been made in a multi-step approach. The initial alignment has been made using a spirit

level to ensure that each component was aligned vertically and horizontally (along the X and Y directions shown in Figure 3.18).

A separate alignment has been made for the camera stand, aiming to align the axis of the camera to the axis of the sudden expansion (Figure 3.18a). The camera position has been refined by adjusting its position using as reference the image acquired using the Target #1 inside the glass diffuser, with the laser turned off.

The laser alignment has been more critical. The laser has been mounted on an aluminium frame, for which it was possible to regulate the height and pitch angle of the laser. Similarly to the camera alignment, the final laser positioning has been determined using the Target #1. The adjustment has been performed with the power set to *Low* to reduce the risk of injury. The laser sheet has been adjusted in both height and angle using the mirror placed on Target #1.

Seeding Glycerol and similar compounds are advantageous for PIV applications over other compounds (e.g. olive oil) because of easiness in cleaning and maintenance of the impacted surfaces and the low impact on human health. In the current study, a glycerine-water solution has been chosen to generate the particle seeding, using a TSI 9306A Six-Jet atomizer (TSI, 2015). In this section, the properties of the seeding material are summarised to demonstrate the suitability of the seeding for the current application. It is necessary to remark that a complete study on the properties of the seeding particles used for the PIV experiments is beyond the purpose of this study.

The seeding has been fed to the text section through the swirl generator hose (red connectors in Figure 3.18). This choice has been made to provide uniform mixing between air the the glycerol solution at the test section.

It has not been possible to atomise the pure glycerol (vegetable glycerine pure at 99.9%) using the atomiser adopted in the study, since no particles were visible inside the test section.

The atomisation of liquids is a complex phenomenon, analysed for a wide range of applications and fluids. A discussion about the physics involved in the atomisation process is not included here, since it goes beyond the purpose of this work and can be found in literature, e.g. Ashgriz (2011); Hinze (1955); Lefebvre and McDonell (2017). In extreme synthesis, the droplet formation in a liquid can occur if the external forces (due to inertial force and surface tension) are able to overcome the internal viscous forces. A measure of the relative importance between those forces acting on a liquid is given by the Onhesorge number (Oh)

$$Oh = \frac{\mu_l}{\sqrt{\rho_l \sigma_l d_p}} \tag{3.12}$$

where μ_l is the dynamic viscosity of the liquid, ρ_l its density, σ_l its surface tension and d_p the particle diameter (used as reference length). If the Onhesorge number is small, the viscous forces can be overcome by the surface tension and the atomisation can occur (Andersson and Andersson, 2006). From Equation 3.12 it can be seen that the viscosity of the liquid has a primary role in the formation of the droplet particles. In the current study, it has been chosen to dilute the glycerol with water, in order to reduce its dynamic viscosity, to facilitate the aerosol generation and the droplets formation.

A study from Li et al. (2013) has shown that the surface tension of a diluted solution of industrial glycerine with water is comparable to the one of pure industrial glycerine. From the experimental activities by Li et al. (2013), the measured surface tension for pure industrial glycerine at 11° C is estimated to be $57.5 \pm 0.03 mN/m$, while the surface tension for a 62% glycerine - 38% water solution is $61.3 \pm 0.03 mN/m$. In addition, the refractive index of the pure glycerine is comparable with the one of the 62% glycerine - 38% water solution, respectively 1.48 and 1.42. In the study by Legrand et al. (2017) it has been shown that for a similar compound (propylene glycol) the water solution at 60% has a surface tension comparable to the pure propylene glycol and the mean particles diameter is not affected substantially by the reduced viscosity of the water solution. A similar behaviour for the glycol used in the current study can, therefore, be inferred. The dilution with water reduces the dynamic viscosity, but has low impact on surface tension and density, allowing to reduce the Ohnesorge number.

The density (ρ) and the dynamic viscosity (μ) of pure glycerol and of the 60% Glycerol - 40% Water solution used in the current study have been estimated using the formulation proposed in the study of Volk and Kähler (2018) and are given in Table 3.1. It can be seen that the drop in dynamic viscosity for the glycerol water solution is of about two order of magnitudes, while the density is comparable.

Table 3.1 Glycerol properties comparison: estimation made at $25°C$, based on the formulation proposed by Volk and Kähler (2018)

	100% **Glycerol**	60% **Glycerol** 40% **Water**
Density (ρ)	1257.7 kg/m^3	1165.4 kg/m^3
Dynamic viscosity (μ)	0.9057 $Pa \cdot s$	0.01276 $Pa \cdot s$

The value estimated for the dynamic viscosity of the 60% Glycerol - 40% Water solution is of the same order of magnitude of the olive oil (0.074 $Pa \cdot s$ at $23°C$, from Sahasrabudhe et al. (2017)) and higher then the 0.0064 $Pa \cdot s$ of the 60% propylene glycol solution used in Legrand et al. (2017). For this reason, it is expected that the particle size diameter (d_p) is around 1 μm, which is between the value of 0.9 μm

measured by Legrand et al. (2017) and within the range of 1 μm to 2 μm declared by TSI for oil particles generated with the atomiser model used in the current study.

The value of $d_p \approx 1\mu$m satisfies the two main requirements of the particle seeding for PIV applications: particles should be as small as possible, in order to follow the flow stream without altering its features, but, on the other hand, larger particles reflect more light from the laser sheet, resulting in more visibility at the camera sensor (Raffel et al., 2007). The first criterion can be assessed by estimating the particle settling velocity (u_p) under gravity, assuming that the particles have a spherical shape from Stoke's drag formula reported in Raffel et al. (2007)

$$u_p = {d_p}^2 \frac{(\rho_p - \rho_f)}{18\mu_f}\mathbf{g} \tag{3.13}$$

in which ρ_p is the particle density, ρ_f is the density of the fluid, μ_f its viscosity and $\mathbf{g}$ is the acceleration due to gravity. In the current study, the fluid is air and substituting its properties (Table 3.4) into Equation 3.13, the estimated gravitationally induced velocity of the particles is $3.42 \cdot 10^{-5} m/s$, which is significantly lower then the expected flow velocities. The relaxation time (Raffel et al., 2007) for the particles can be calculated from

$$\tau_s = {d_p}^2 \frac{(\rho_p)}{18\mu_f} \tag{3.14}$$

For seeding obtained from the 60% Glycerol - 40% Water solution in air, the relaxation time estimated from Equation 3.14 is 3.49μs. Both estimated values, u_p and τ_s, are satisfying, so it can be concluded that the particles generated using the 60% Glycerol - 40% Water solution tend to *attain velocity equilibrium with the fluid* (Raffel et al., 2007).

Although this investigation cannot be considered conclusive for the complete characterisation of the seeding particles generated (since a more sophisticated apparatus should be used), the properties of the compound have been considered satisfactory for the current application.

The atomiser used allows to vary the number of jets used to atomise the seeding material and the input pressure (TSI, 2015). The input pressure has been fixed to 40 psi, which is within the range suggested in the manual (20 psi to 50 psi). For a fixed input pressure, the number of particles generated is directly proportional to the number of jets used in the atomiser (TSI, 2015).

A satisfying number of particles in the test section, meeting the rule of thumb proposed by Adrian (1991), has been achieved using the configuration with 3 jets, so

this setting has been used to carry out the experiments presented in Chapter 5 and in Chapter 6.

Image acquisition

The image pairs for each inflow condition have been acquired by using the TSI Insight 4G software (TSI, 2017). The time step was fixed to 10 μs for all the cases analysed. With the time step chosen the in-plane displacement is less then 1/4 of the interrogation window size (Adrian, 1991), as verified inside the TSI software prior to each experiment. Prior to each run, the camera aperture and the camera focus, described in section 3.1.4, were double checked to minimise the overexposure due to the laser light. A total of 1000 image pairs was captured for all the inflow conditions for both the axisymmetric and the asymmetric configuration.

The configuration of the camera and lens, with aperture fixed at f/11 has enabled a particle image diameter of ≈ 2 px, which is desired to avoid pixel locking (Raffel et al., 2007).

Image processing

The raw images acquired with Insight 4G have been exported and post-processed in PIVlab (Thielicke and Stamhuis, 2014), which is a GUI based open-source tool for performing Digital PIV flow analysis in MATLAB. The PIVlab tool (v 2.36) has been used to pre-process the images, calculate the cross-correlation to obtain the velocity vectors and validate the velocity field. Further analysis on the data, e.g. convergence study, image distortion evaluation and velocity plots, have been made using in-house MATLAB codes.

The images have been processed in a selected region of interest (ROI) inside the sudden expansion section, in order to reduce the computational requirement of the analysis. A preliminary analysis of the data inside the inlet has revealed that only a small portion of the region could have been investigated, therefore no data have been extracted in that region for the current study.

Image pre-processing The images acquired had a non-uniform luminosity, caused by the presence of the monolith block, which has reflected part of the laser light inside the domain. In order to minimise this effect and to enhance the quality of the images, two pre-processing techniques have been applied: histogram equalisation and intensity filtering.

A constant limited adaptive histogram equalisation (CLAHE) algorithm has been used, since it allows to equalise the histogram locally, dividing the images in multiple

regions. The algorithm is integrated in PIVlab using the standard MATLAB function `adapthisteq` (Pizer et al., 1987; Zuiderveld, 1994). A window of 60 pixel has been chosen for the correction, leading to a subdivision of the region of interest in 141 x 173 tiles (MATLAB, 2019).

The intensity of the particles has been enhanced using a low-pass gaussian filter with 15 px kernel size, chosen after empirical test on a selected number of cases. The filter preserves the particle information, suppressing the low frequencies associated with background noise and low frequency displacement (Thielicke and Stamhuis, 2014).

Image cross-correlation The image cross correlation has been calculated using the Fast Fourier Transform (FFT) window deformation technique, which is considerably faster then the Direct Cross Correlation (DCC), as shown in Thielicke and Stamhuis (2014).

A two pass approach has been used, to improve the accuracy of the results (Thielicke and Stamhuis, 2014). The first pass of the cross-correlation has been obtained with a 256 px window (with step of 128 px). The second pass has been used to refine the analysis and reduce the loss of information due to particle displacement. The interrogation window has been refined, reducing the size to 128 px (with a step of 64 px). This approach results in a higher spatial resolution of the vector field and in the optimisation of the signal to noise ratio (Thielicke and Stamhuis, 2014). The Gaussian 2-3 point fit has been selected as peak finding method, resulting in sub-pixel accuracy (Thielicke and Stamhuis, 2014).

Calibration and vector validation The two-point calibration mentioned in the previous section has been applied for the conversion from pixel units to standard units, using the calibration Target #2 (Figure 3.19b). The reference distance has been manually selected on the target starting from the centre of the image (white dot) up to the second last row of black squares, in the width direction (i.e. the sudden expansion diameter). The resulting nominal distance extracted from the synthetic image is 67.5 mm.

The velocity vector field has been initially limited using the scatter plot of both velocity components, defining the boundary limits for both components between ± 100 m/s. The limit is higher than the expected velocities in the domain and it has been used to eliminate the most evident outliers detected. The vectors have been validated using a median filter (Westerweel and Scarano, 2005), imposing a fluctuation threshold of 5 and a normalisation level of 0.1 px. The rejected vectors have been interpolated from the neighbouring values, using the built-in tool in PIVlab (Thielicke and Stamhuis, 2014).

The mean vector field has been extracted for each inflow configuration and smoothed using a spline interpolation to further reduce the noise, based on the algorithm proposed by Garcia (2011), which is implemented in PIVlab.

Convergence analysis The running average from the image pairs has been extracted to evaluate the convergence to a mean value in selected points. It is a standard practice in PIV measurements to evaluate the convergence at multiple locations of the domain, which correspond to particular features of interest of the flow field (Cavazzini et al., 2013).

A practical criterion to evaluate the convergence has been presented in the study by Wernert and Favier (1999). The estimation of the convergence proposed by Wernert and Favier (1999) is based on the ratio between the running average $\bar{U}_N$ obtained using N frames and the global average $\bar{U}_{Nmax}$ obtained using all the available frames

$$1-\varepsilon < \frac{\bar{U}_N}{\bar{U}_{Nmax}} < 1+\varepsilon \tag{3.15}$$

where ε is a small quantity.

Based on that consideration, a more quantitative approach has been used in Cavazzini et al. (2013). The convergence has been evaluated not only using the running average $\bar{U}_N$, but also using its standard deviation ε_{piv_N}. The standard deviation ε_{piv_N} is defined as

$$\varepsilon_{piv_N} = \sqrt{\frac{1}{N-1} \cdot \sum^{N} \left(\bar{U}_N - \bar{U}_{Nmax}\right)^2} \tag{3.16}$$

Both quantities, running average ($\bar{U}_N$) and standard deviation ε_{piv_N}, are calculated at each iteration, which corresponds to the image frame N. This implies that the iteration number includes the time variation, since the frames are captured with a fixed time step interval (section 3.1.4). The convergence criterion suggested by Cavazzini et al. (2013) is based on the asymptotical behaviour of both functions ($\bar{U}_N$ and ε_{piv_N}), but a practical algorithm to establish the convergence has not been presented. The transition to asymptotic behaviour in both functions has been used in Cavazzini et al. (2013) to determine the minimum number of images required to achieve convergence. This number corresponds to the minimum number of instantaneous flow fields to average in order to obtain a meaningful flow field.

In this study, a similar analysis has been performed, calculating $\bar{U}_N$ and ε_{piv_N} at each iteration, but a convergence criterion has been introduced to evaluate the minimum number of images. The asymptotic behaviour of the standard deviation ε_{piv_N} has been established based on its first derivative $\partial\varepsilon_{piv_N}$, calculated numerically as difference

between adjacent values for the increasing number of iterations. The convergence has been considered to be satisfactory when $|\partial \varepsilon_{piv_N}| < 0.05$. The algorithm has been implemented in a MATLAB script and applied to all the cases considered. The results are summarised for all the inflow conditions in section 5.1.1 and section 6.1.2 for the axisymmetric case and non symmetric case respectively.

Distortion estimation The image distortion has been estimated in MATLAB, based on the calibration image acquired with Target #2. Standard techniques have been used to normalise the image and center it (Gonzalez and Woods, 2004). The presence of a chequered board in the image has allowed the use of the built-in MATLAB function `detectCheckerboardPoints`. The function detects the corners of the black and white checker-board and their position in the image (MATLAB, 2019).

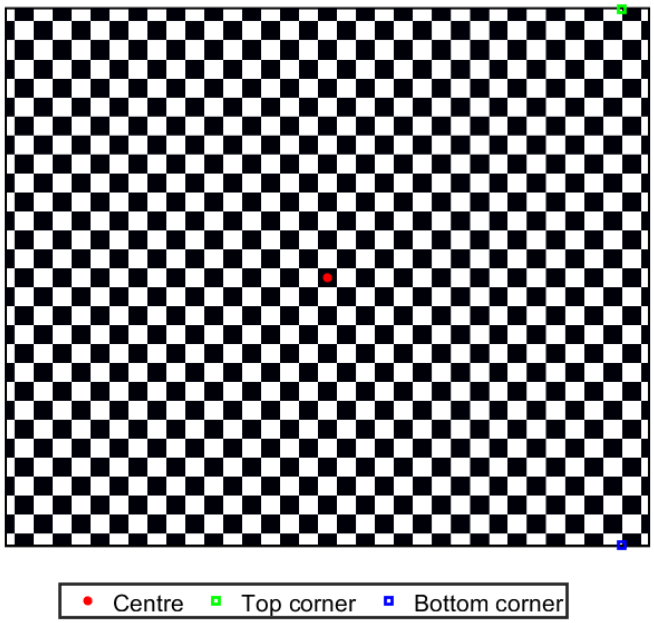

Figure 3.20 Synthetic target image with indication of the points used for the centering and normalisation operations. Red dot represents the target centre, the distance between the green square and the blue square represents the target diameter

The *synthetic* image used to print the target has been used as reference image to sample the undistorted positions of the corners of each square. The *real* image of the target has been obtained as mean of the 10 images acquired for the Target #2. The positions of the corners of each square has been determined for both images, obtaining two separate sets of pixel coordinates. In order to bypass the problem of the image sizes, a scaling operation has been applied to both, using the reference points shown in Figure 3.20. The position of the center dot in the target (red circle) has been

used to determine the center in both images and the positions of the top right corner (green square) and the bottom left corner (blue square) have been used to calculate the distance in pixel corresponding to the expansion diameter. A scaling factor has been calculated for both images, thus obtaining a normalisation of the pixel coordinates with the expansion diameter.

The distance between each corner of the checker-board has been used to determine the distortion of the image target and estimate the general distortion in the data. A map of the relative distances has been created to visualise the impact of the distortion on the data. The procedure has been applied to both configurations, axisymmetric and non symmetric cases, obtaining that higher distortion is present towards the edges, where the data were discarded. The resulting distortion maps are presented in the respective chapters, respectively in section 5.1.1 and section 6.1.2.

Vorticity component calculation The vorticity component (ζ_Y) perpendicular to the sampling plane has been calculated from the two velocity components.

In the case of the XZ section, for the two velocity components U (along X) and V (along Z), the vorticity ζ_Y is

$$\zeta_Y = \frac{\partial U}{\partial z} - \frac{\partial V}{\partial x} \tag{3.17}$$

The vorticity ζ_Y has been calculated in MATLAB using the built-in function `curl` and treated as a scalar field for the representation of the contours.

3.1.5 Experimental procedure

The methodology adopted for the experimental study carried out in the current thesis has been presented in the above sections. The instrumentation and the sampling methods used have been described for each measurement technique, together with the procedure adopted to process the data. The results of the processing choices have been included in the respective chapters to highlight the effects of the post-processing technique and validate the experimental data.

The experimental procedure is common to all the different activities presented in the thesis (HWA, pressure and PIV measurements). The set-up and calibration of each system used for the measurements has been discussed in detail in the respective sections.

For each test section and measurement techinque, the following steps have been used:

1. connect the test section to the swirl generator assembly;

2. prepare and connect the relevant instrumentation for the measurements;
3. initialise measurements instrumentation and software;
4. calibrate the instrumentation;
5. fix the angle of the swirl generator;
6. log ambient pressure and ambient temperature;
7. run the VFM pressure and back pressure application log (Appendix C);
8. calculate the VFM pressure for the target mass flow rate (Appendix B);
9. fix the VFM pressure to the target value;
10. run the experiment;
11. save data and logs.

A summary of the experimental activities carried out on the different test sections is shown in Table 3.2, with the reference to the respective chapter in which the data are discussed and analysed.

Table 3.2 Summary of the experimental activities. Inflow conditions for each test section are summarised in Table 3.3.

Test section	**Experimental technique**			**Chapter**
	Pressure	HWA	PIV	
Annular pipe	✓	✓	-	4
Axisymmetric sudden exp.	-	-	✓	5
Asymmetric sudden exp.	-	-	✓	6

A summary of the experimental inflow conditions used for the pipe with annular cross section and for the diffuser with sudden expansion and downstream resistance is given in Table 3.3.

Table 3.3 Inflow conditions adopted for the experimental study of swirling flows using the pipe with annular cross section (Figure 3.4) and the diffuser with sudden expansion (Figure 3.6).

Test section	$\dot{m}$ (g/s)	**Swirl generator angles** θ_s (°)					
Annular pipe	25 63 100	0	4	7	10	14	18
Axisymmetric sudden exp.	63	0	4	7	10		18
Asymmetric sudden exp.	63	0	4	7	10		18

During each experiment, the VFM differential pressure measured by both manometers has been monitored and logged using a in-house built LabView interface. The purpose of the monitoring has been duplex: verify the stability of the mass flow rate and identify cycling variations that could bias the flow frequency analysis. A brief description of the LabView interface used is given in Appendix C.

A sample recorded pressure signal (p_{VFM}) of the length of 100 seconds is shown in Figure 3.21, normalised with the mean value recorded. The peak to peak cycle is estimated to be 8 seconds, while the fluctuation from the mean value is within $\pm 2\%$. The effect on the global mass flow rate can be therefore neglected for the duration of the experimental activities, since it can give a fluctuation of about ± 0.2 g/s around the mean value.

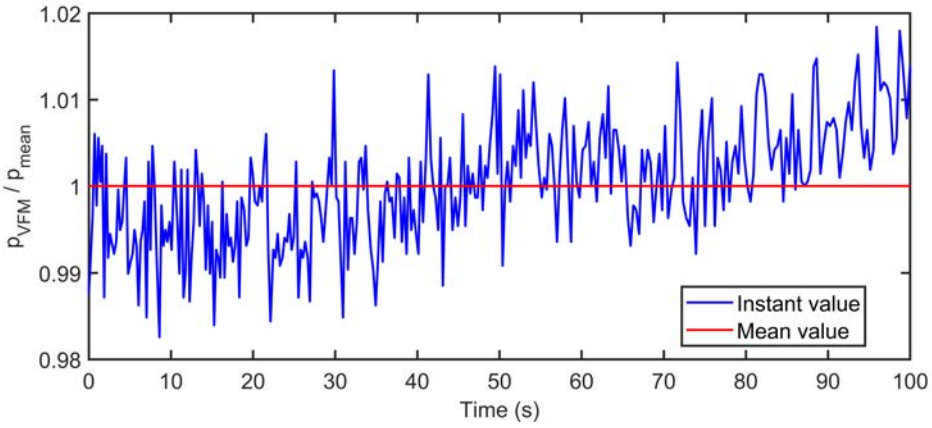

Figure 3.21 Viscous Flow Meter (VFM) pressure log example

3.2 Numerical methodology

Computational Fluid Dynamics (CFD) has been widely used in several engineering applications as part of the design process. One of the advantages of a validated CFD model over the experimental design is the possibility to easily change some parameters of interest, such as initial conditions and geometry, with reduced time and cost when compared to experimental activities.

In this project, CFD has been used for multiple purposes. The combination with the experimental activities has allowed a critical assessment of the model, identifying its potential and limitations. The use of a 3D modelling approach has allowed to gain more insight of the flow features for multiple inflow conditions to complement the experimental data available. In addition, the CFD model has been used for the design optimisation and to explore a new approach for modelling high resistance devices. The lowest Reynolds number, based on the mean axial velocity at the nozzle, entering the test section analysed in the current study is 21720. This corresponds to the lowest mass flow rate (25 g/s) used in the experiments (pipe with annular cross section, Table 3.5). Therefore, the flow is expected to be turbulent for all the cases analysed.

Several methods to obtain a numerical solution that captures the effects of turbulence have been applied to study swirling flows, as discussed in subsection 2.2.3. Despite the limitations of the RANS turbulence modelling to predict some features of complex flows their use is still preferred in applications, for its robustness and its computational efficiency. In addition, the use of more complex approaches to model swirling flows, such as LES and DES, is still limited by the problem of the boundary condition closure, as already discussed in subsection 2.2.3. In the current thesis, the assessment of some RANS turbulence models commonly adopted in a wide range of applications has been made. The objective of the comparison is to give some indications on the reliability of such models when applied to swirling flow modelling.

The CFD modelling approach adopted in this project is described in the following sections, focusing on the key steps involved in the process:

- creation of the geometrical domain;
- discretization of the domain and mesh preparation;
- formulation of the model equations and definition of the boundary conditions;
- numerical solution of the equations.

The three computational domains used for the CFD modelling part of the current thesis are a reproduction of the ones used in the correspondent experimental study, presented in section 3.1.1. Air has been used as working fluid for all the cases, using the properties shown in Table 3.4 and it is assumed to be an incompressible Newtonian fluid with constant properties.

Table 3.4 Air properties defined used for the CFD model

Variable	Value
Temperature (T)	$20°C$
Density (ρ)	$1.18415\ kg/m^3$
Dynamic viscosity (μ)	$1.85508 \cdot 10^{-5} Pa \cdot s$
Ambient pressure (p_{amb})	$101325.0\ Pa$

The following sections will briefly present the modelling steps adopted in the current study. The specific choices made for each test section will be specified and motivated in the relative chapter.

3.2.1 Meshing strategy

The domain discretization can be obtained using several strategies, which will result on a wide range of possible grids that can be used to obtain the solution. The grid has a primary role for the *reliability* of the solution. In general, a good computational grid (often simply referred as *mesh*) reduces the numerical errors linked to the approximations introduced by the discretization. The use of *structured grids*, in which the grid lines do not cross each other, are often preferred from a theoretical point of view, since the neighbour connectivity is simple and the algebraic solution of the equations can be obtained more efficiently. In addition, structured grids are preferred since they reduce the discretization errors in the computation of fluxes. Those errors arise if the cells are not aligned with the flow direction, since the computation of fluxes depends on the orientation of the cell faces and their normal direction, in particular for the diffusive terms. However, it is impractical to use regular grids when complex geometries need to be modelled, when the domain presents curvature or when the flow does not present a preferred direction (e.g. swirling flows). In the current thesis, a structured grid has been used for the case of the planar diffuser (Figure 3.9b), for which hexahedral cells have been used. More details are given in Chapter 7.

The use of *unstructured* grids, in which the more complex shapes for the control volumes (CVs) are used offers more flexibility for the discretization of such cases.

Many algorithms have been introduced to generate meshes using tetrahedra, hexahedra or, more in general polyhedra cells (Perić, 2004), which have been applied to a wide range of complex geometries and applications (Sosnowski et al. (2017); Spiegel et al. (2009)). The possibility to create a mesh with polyhedral cells has been introduced in the past decade in commercial CFD codes and it is available in StarCCM+, exhibiting several advantages over less complex tetrahedral cells (Peric and Ferguson, 2005). The numerical accuracy increases, when compared to pure tetrahedral cells, and a reduction of the number of cells by about a factor of 6 can be achieved. In parallel, new algorithms for the numerical solution and improved accuracy of the numerical schemes applied to polyhedral discretization have been developed (e.g. Brezzi et al. (2007)). For the above reasons, polyhedral cells have been used for the cases of the pipe with annular cross section and for the diffuser with sudden expansion.

The numerical simulation of internal flows requires more attention for the cells close to the walls, in particular when wall functions are used in the model. It is known from literature that more regular cells, such as prisms, can improve the solution accuracy in the boundary layer region. The methodology adopted to define the prism layers distribution in the current study is explained in section 3.2.3.

As a result, it is often necessary to combine different cell types to improve the solution accuracy. This aspect is important also in the presence of regions in the computational domain with specific properties, such as a porous medium region, for which a particular mesh treatment might be required. The impact of the cells type on the porous medium region modelling has been investigated in subsection 5.2.1.

An example of a mesh layer is shown in Figure 3.22a. The cells inside the core region are *polyhedral* cells, while the cells close to the wall are *prismatic* cells, which are commonly adopted in the near wall region (as discussed in subsection 2.2.3). A mesh sensitivity study has been carried out separately for each domain and it is included in the relative chapters. The sensitivity test had the scope to evaluate the independence of the solution from the mesh chosen, evaluate the effects of local refinement in zones of particular interest (e.g. the sudden expansion) and find a balance between solution accuracy and computational cost.

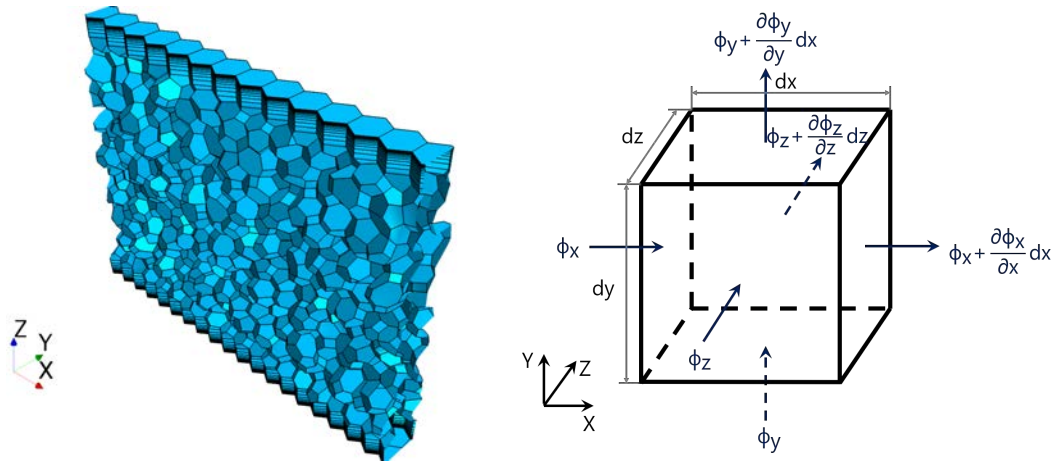

(a) Mesh layer **(b)** Control volume

Figure 3.22 Example of polyhedral mesh with prism layers near the wall (a). Control volume schematic (b).

3.2.2 Equation discretization

The Navier-Stokes equations, presented in section 2.2, represent the mathematical model to be solved in Computational Fluid Dynamics and require a numerical solution. The computational domain needs to be discretised in order to approximate the set of differential equations into an algebraic system. The variables are consequently solved in discrete locations of time and space (Ferziger and Perić, 2002).

Finite Volume Method

The equation discretization can be obtained using different methods, e.g. finite volume (FV) and finite difference (FD), which theoretically converge to the same solution. The discretization introduces a numerical approximation, which can be reduced with a correct grid resolution. In the current thesis, the finite volume approach has been used, since it is the method implemented in StarCCM+ (CD-Adapco, 2018).

In order to apply the finite volume method, it is necessary to "split" the computational domain into smaller volumes (e. g. Figure 3.22a), which are defined *control volumes* (CV) and constitute the computational cell. The equations are derived in integral form and applied to each CV for the generic variable ϕ (Figure 3.22b). The computational node is represented by the centroid of each cell, at which each variable associated with the control volume is computed. The solution at each node is linked to the neighbour ones through the calculation of the convective and diffusive fluxes. Those fluxes are calculated from the surface integrals over the cell surfaces. This aspect represent a main advantage over the other formulations: the continuity equation is respected in each

CV, since the surface integrals cancel out. The use of a finite volume method allows the definition of arbitrary shapes for the CVs, e.g. polyhedral volumes (Figure 3.22a), which means that the method can be applied to model complex geometries.

Numerical schemes

Several flow models are available in StarCCM+, which can be used for the numerical solution of the governing equations (section 2.2) in a wide range of fluid properties (CD-Adapco, 2018). For the current study, the flow is incompressible and the *segregated flow* model has been applied to all the cases, so only this method is described here.

The solution of the momentum equations is obtained separately for the three directions and linked with the continuity equation using a predictor-corrector approach. The overall solution is calculated using the SIMPLE algorithm, which allows the coupling between pressure and velocity (Ferziger and Perić, 2002). The final solution is calculated using an iterative method, in which each equation is solved separately. At each iteration, an estimated value and a correction are calculated for both pressure and velocity. The solution of the remaining flow variables is then calculated and the process iterated up to convergence.

The second order upwind scheme has been used for the convective terms, which has an accuracy of at least the first order. The numerical gradients are used to calculate the variable value at the cell face (Figure 3.22b). The calculation of the gradients has been made using a Hybrid Gauss-LSQ method, for which higher accuracy can be achieved (Mishriky and Walsh, 2017). A standard Venkatakrishnan limiter (Venkatakrishnan, 1993) has been used, to improve the convergence and the stability of the solution. On the other hand, limiters can introduce numerical dissipation, thus reducing the accuracy of the solution (Ferziger and Perić, 2002).

It is known from literature that the calculation of the gradients on the cell faces in presence of swirl can lead to numerical instability and solution convergence problems, e.g. Hogg and Leschziner (1989) and Jakirlić et al. (2002). This aspect has been observed in presence of flow oblique to the grid lines, often referred as *false diffusion* problem (Patankar, 1980). The numerical schemes used for the calculation of gradients should, consequently, be carefully selected to reduce this effect.

In some of the cases analysed in the current thesis numerical instability has been observed, in particular for low swirl levels with the diffuser with sudden expansion test section. After excluding non-desired mesh effects, by comparing the solution on different meshes, the effects of the numerical schemes have been considered to eliminate the solution instability. The solution obtained changing the scheme used for the convective terms from a 2^{nd} order to a lower 1^{st} order upwind scheme was still

affected by instability. A second comparison has been made by changing the scheme to a central differencing (CD) scheme and then a third solution was obtained using a hybrid 3^{rd} order - CD scheme, obtaining similar results.

A stable solution has been obtained by changing the accuracy of the numerical scheme used for the gradient computation to a 1^{st} order. The overall accuracy of the solution is still of at least the 2^{nd} order, as reported in Sozer et al. (2014) and Syrakos et al. (2017). From the analysis, it has been concluded that the instability can be attributed to the computation of the velocity gradients on the cell faces. More details are given in subsection 5.2.3. Swirling flows are more sensitive to the choice of some numerical parameters used to help the convergence, such as the under-relaxation factors (Jakirlić et al., 2002; Sloan et al., 1986). The under-relaxation factor used for the velocity equation is 0.3 and for the pressure equation is 0.1.

3.2.3 Boundary conditions

The critical aspects of both inflow and outflow conditions for the swirling flow modelling have been highlighted in section 2.2.3. The choices made for the definition of the boundary conditions (B.C.) in the current study are presented in the next sections.

Inlet boundary

The choice of the inflow boundary condition can significantly alter the formation of the flow structures downstream, as discussed in section 2.2.3. To reduce the impact of the inlet boundary condition on the flow in the pipe, the swirl generator assembly has been included in the computational domain, Figure 3.23. The introduction of the tangential velocity component into the test section is, therefore, driven by the flow path, rather then by a numerical input. The relative angle between the blocks has been varied as in the experimental case Table 3.3. A uniform velocity profile has been imposed normal to the inlet section boundary of the swirl generator, red section in Figure 3.23, and varied to match the experimental mass flow rate imposed Table 3.3.

When a velocity inlet B.C. is specified, reconstruction gradients are used to extrapolate the pressure at the boundary from the adjacent cell (CD-Adapco, 2018). A low turbulence value has been assigned at the inlet in all configurations, specifying a turbulence intensity of 0.01 and a viscosity ratio of 10. The choice has been made since the properties of the flow at the inlet are unknown for all the cases analysed. Since the inlet is far from the test section, the effects of the choice are negligible for all the cases.

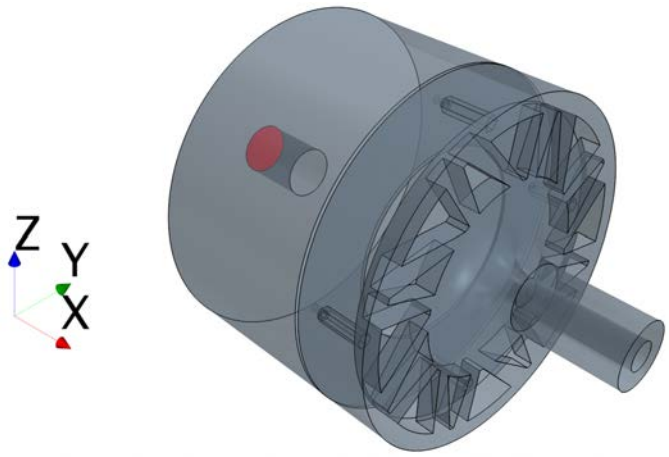

Figure 3.23 Swirl generator assembly used at the inlet for the swirling flow simulations. Red section represent the numerical inlet for the model.

The Reynolds number has been estimated at two cross sections: the swirl generator inlet and the swirl generator nozzle section. The Reynolds number has been calculated at both sections using the equation

$$Re = \frac{\rho \overline{V} L}{\mu} \tag{3.18}$$

where $\overline{V}$ is the mean velocity at the section, L is the reference length, ρ is the air density and μ is the air dynamic viscosity, as defined in the air properties Table 3.4.

The mean velocity at both sections has been calculated from the continuity equation

$$\dot{m} = \rho \bar{V} A \tag{3.19}$$

where ρ is the air density and A the cross sectional area. From Equation 3.19, the mean velocity is

$$\bar{V} = \frac{\dot{m}}{\rho A} \tag{3.20}$$

The Reynolds number (Re) calculated from Equation 3.18 is reported in Table 3.5. The Reynolds number at the swirl generator inlet (Re_{in}) has been calculated using as reference length the inlet diameter, while the Reynolds number at the nozzle section has been calculated using the hydraulic diameter at that section ($D_{noz} = D_{out} - D_{in}$). The Reynolds number at the nozzle section (Re_{noz}) is representative of the Reynolds number entering the test sections (pipe with annular cross section and diffuser with sudden expansion) and it is used as reference throughout the thesis. The values used for each case are summarised in Table 3.5. The table includes a comparison between the

mean velocity estimated at the swirl generator inlet ($\overline{V}_{in}$), which has been used for the inlet B.C., and the mean velocity estimated at the swirl generator nozzle section ($\overline{V}_{noz}$).

Table 3.5 Reference values used for the inlet boundary condition for each mass flow rate considered for the swirling flows modelling. Values at the swirl generator inlet (subscript *in*) and nozzle outlet (subscript *noz*) are given.

	Swirl generator inlet L_{in} = 44 mm		**Swirl generator nozzle** L_{noz} = 31 mm	
$\dot{m}$ (g/s)	$\bar{V}_{in}$ (m/s)	Re_{in}	$\bar{V}_{noz}$ (m/s)	Re_{noz}
25	13.88	38997	10.98	21720
63	34.99	98273	27.66	54374
100	55.54	155989	43.91	86880

A uniform velocity profile has been imposed at the inlet for the numerical study of the planar diffuser (Figure 3.9). As explained in section 3.1.1, the domain is a reproduction of the experimental apparatus (Figure 3.9a) used in the study of Porter (2016). The plenum nozzle upstream the test section has been designed in order to prescribe uniform flow in the test section. Consequently, a uniform velocity profile has been imposed at the planar diffuser inlet, as summarised in Table 3.6. The reference length used for this case is the hydraulic diameter of the test section inlet.

The flow entering the section is turbulent for both inflow conditions, since the lowest Reynolds number is 22000.

Table 3.6 Reference values used at the inlet boundary for the planar diffuser modelling.

Planar diffuser inlet		
$\overline{V}_{in}$ (m/s)	L_{in} (mm)	Re_{in}
8.98	38.4	22000
24.48	38.4	60000

Outlet boundary

Different types of outlet conditions are used in CFD simulations, the most common ones being *mass flow* outlets (where the mass flow at the outlet section is defined) and *pressure* outlets (where the pressure is known, and is usually set as ambient pressure).

A *pressure outlet* boundary condition has been used for all the domains considered in the study. The pressure variable (p) in StarCCM+ is defined as *working* pressure, expressed relative to a reference pressure (p_{ref}) for computational convenience in the

code (CD-Adapco, 2018). The reference pressure has been imposed equal to the ambient pressure (p_{amb}, specified in Table 3.4) for the cases analysed in the current thesis. At the outlet section, a constant *working* pressure has been imposed, setting its value to $p = 0$ Pa, thus obtaining that the pressure at the outlet boundary is equal to the ambient pressure. The velocity at the outlet boundary is extrapolated from the interior cells, in order to satisfy the continuity equation (CD-Adapco, 2018).

The outlet boundary condition can significantly alter the flow distribution near the outlet boundary in presence of swirling flows, as discussed in section 2.2.3. Although it has generally less impact on the formation of the main flow structures if compared to the inlet boundary condition, the outlet boundary condition affects the redistribution of the velocity components upstream (Xia et al., 1997). Therefore, it is a common practice in complex flows to move the outlet boundary further downstream of the area of interest if possible. This effect is more critical in the case of the annular pipe, since the flow exiting the pipe, especially at high swirl level, has a non uniform pressure distribution across the section. The approximation introduced placing the outlet boundary near the test section outlet would result in flow distortion near the outlet, with a possible effect on the upstream flow (Xia et al., 1997).

In case of the diffuser with a sudden expansion, the outlet flow is nearly unidirectional because of the honeycomb monolith presence. This means that the pressure downstream is nearly uniform in each cross section perpendicular to the flow, and introducing a constant pressure boundary would not result in significant flow and pressure redistribution upstream. Therefore, the outlet sleeve present in the experimental activities, Figure 3.6, has been reproduced in the computational model. The length of the outlet sleeve has been set equal to twice the outlet diameter, to alleviate the effect of the outlet boundary on the flow upstream, Chapter 5. Similarly to the diffuser with a sudden expansion, an outlet sleeve has been included in the model of the planar diffuser, Chapter 7.

Symmetry boundary

In presence of symmetry inside the domain, it is possible to simplify the computational model and reduce the size of the domain, defining a *symmetry* boundary at the appropriate section. When a symmetry condition is imposed the parallel component of the velocity at the boundary is calculated from the adjacent cells and the shear stress at the boundary is set to zero (CD-Adapco, 2018). The pressure at the boundary is extrapolated from the adjacent cell. Consequently, the use of a symmetry boundary condition can alter the flow near the boundary and should be carefully assessed.

A symmetry boundary condition has been used in the preliminary study carried out for the domain of the axisymmetric diffuser with a sudden expansion, Chapter 5. By modelling 1/8 of the entire domain, a 45° wedge, the computational effort has been reduced. Consequently, the configuration has been used to rapidly assess some of the modelling choices, as explained in Chapter 5. The symmetry boundary condition has been imposed at the two sides of the wedge.

A symmetry B.C. has been imposed at the axis of the planar diffuser (Figure 3.9). In that case, the flow at the axis is almost uni-directional, parallel to the boundary, so the condition imposed has a low impact on the flow features. More details are given in Chapter 7.

Wall treatment

The boundary condition used at the external solid boundaries for all the configurations is a *no-slip wall* boundary condition. The velocity at the wall is forced to zero. The model adopted for all the cases analysed in the current thesis is based on the low y+ formulation for the boundary layer, meaning that the viscous sub-layer is resolved.

As mentioned in subsection 3.2.1, prism layers have been used near the wall, in order to obtain a structured mesh and refine the width of the cells close to the wall. The first layer thickness has been chosen aiming to a y+ value lower then 1, based on the boundary layer theory.

Interface treatment

The use of regions with different properties requires a specific boundary condition treatment to connect the two regions. The solution in the upstream region needs to be transferred to the downstream region. This is achieved in StarCCM+ by defining an *interface* boundary condition at the connecting surface between the two regions (CD-Adapco, 2018).

This condition has been used for the sudden expansion with downstream resistance and for the planar diffuser cases, in which two different region types have been used: a *porous* region for the monolith section and *fluid* regions for the other sections (Figure 3.6 and Figure 3.9). Therefore, a first interface between the expansion region and the porous region has been created and a second one between the porous region and the outlet sleeve region. In this way, the solution quantities between the two connected regions have been transferred.

The impact on the solution of the mesh at the interface has been investigated for the diffuser with a sudden expansion and it is discussed in subsection 5.2.1.

3.2.4 Turbulence modelling

The assessment of different RANS turbulence models has been made using the pipe with annular cross section. The model has been validated against the experimental data collected using the flow rig described in section 3.1.1. Although most turbulence models have a number of constants that can be calibrated for specific flows, in this study the models constants have not been modified. The coefficients used for each model formulation are the standard coefficients implemented in StarCCM+ (CD-Adapco, 2018). It is known that some improvements in the solution for swirling flows can be obtained, as discussed previously in section 2.2.2. However, one of the objectives of this study is to assess the performance of standard turbulence models for a wide range of swirl levels and provide more insight in the turbulence models capabilities for industrial applications. The models tested on the pipe with annular cross section are the following:

- Standard $k-\varepsilon$;
- Realizable $k-\varepsilon$;
- Standard $k-\omega$;
- $k-\omega$ SST;
- $\overline{v}^2-f$;
- Reynolds Stress Transport (RSM).

It was expected that RSM model would perform best because of the better prediction of the turbulence anisotropy. However, the RSM model carries much higher computational costs, therefore for the larger geometry of the diffuser with sudden expansion the $\overline{v}^2-f$ model has been used. The $\overline{v}^2-f$ model has been proven to provide better results for separated flows (Iaccarino et al. (2003); Porter et al. (2014); Salehi et al. (2017)).

3.2.5 Porous medium modelling

The monolith used for the current study, as already mentioned in section 3.1.1, is a 400-cpsi ceramic honeycomb monolith substrate, shown in Figure 3.24a. The monolith consists of multiple channels with a hydraulic diameter of approximately 1 mm (Figure 3.24b) typically used as a catalyst in automotive aftertreatment systems (Koltsakis et al., 1997) and (Benjamin et al., 2001). The monolith represents a high resistance device for the flow, since the air is forced to enter the small channels of the

monolith. The flow impinges on the monolith as if there is a wall, with a consequent redistribution of the flow in the radial direction of the monolith face, to allow the passage through the small channels. The flow inside the single channels becomes laminar, even if the flow upstream is turbulent. The single jets exiting the channels merge downstream the monolith, re-enhancing the formation of turbulent structures, while keeping a mainly axial direction.

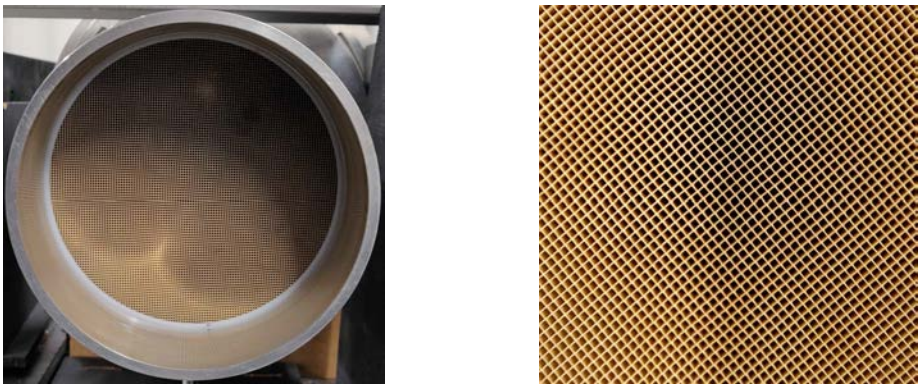

(a) Monolith downstream view **(b)** Front surface detail

Figure 3.24 400-cpsi ceramic honeycomb monolith substrate. Downstream view of the monolith used for the diffuser with sudden expansion (a). Detail of the channels on the front surface (b).

The numerical simulation of the full scale model, which means including all the small channels in the computational domain, can be prohibitive for the computational requirements (Porter et al., 2014). Simplified models, such the porous medium approach, are proven to give a good prediction of the pressure losses due to the presence of the resistance, but fail to correctly predict the redistribution of the flow due to the mixing of the jets exiting the channels Benjamin et al. (2003) and Porter et al. (2014). As a consequence, the accuracy of the CFD model is reduced, as observed for several applications, from after-treatment systems, e.g. Bertrand et al. (2012) and Cornejo et al. (2018b) to heat exchangers Wang et al. (2014).

Since the focus of this study is mostly on the features of the swirling flow upstream of the monolith, the porous medium approach used in Benjamin et al. (2003) is sufficient and is used in all configurations considered in Chapter 5 and Chapter 6. A modification to this approach is proposed in Chapter 7. The formulation adopted in the current study is based on Benjamin et al. (2003). The monolith has been modelled as a porous medium, computing the pressure drop across the region as

$$\frac{\Delta p}{L} = \alpha u + \beta u|u| \tag{3.21}$$

where u is the axial velocity upstream the porous medium entrance, L is the monolith length, while α is the viscous coefficient and β is the inertial coefficient in the axial

direction. The resistance coefficient have been calculated from experiments (Skusiewicz, 2012) carried out on a monolith with length of 76.2 mm, through polynomial fitting of the experimental data Figure 3.25, obtaining $\alpha = 684.37 kg/m^3 s$ and $\beta = 28.28 kg/m^4$. Since the flow in the monolith is only allowed to have the axial component, the viscous and inertial coefficients in the other two directions perpendicular to the expansion axis are set to 10^6, to ensure very high resistance in those directions.

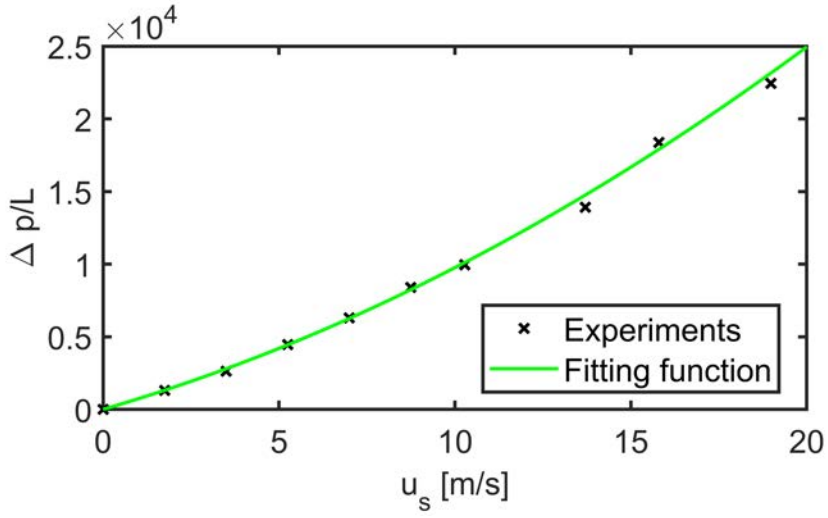

Figure 3.25 Experimental data fitting for the estimation of the porous medium coefficients for the monolith used for the diffuser with sudden expansion.

The flow may enter the catalyst channel at a certain angle relative to the axial direction. This results in additional pressure loss caused by the flow separation at the channel entrance, as shown in Benjamin et al. (2003) and Persoons et al. (2008). Since the channels are not actually modelled in the porous medium approach, this extra pressure loss is introduced into the simulation artificially by adding an extra pressure loss into the Equation 3.21. Different approximations exist for the oblique entrance loss, the one used in this study is (Benjamin et al., 2003), using a momentum source term

$$\Delta p_{oblique} = \pm \frac{\rho v^2}{2} \tag{3.22}$$

where ρ is the air density and v is velocity tangential to the monolith front face sampled upstream the monolith entrance. The resultant force is opposing the flow, so the sign is chosen accordingly. More details about the implementation in StarCCM+ are given in Appendix D.

Since at the front face of the monolith the flow is already unidirectional, the entrance angle needs to be evaluated upstream of the monolith where the flow has not changed direction yet (Benjamin et al., 2003). For this purpose, the velocity v used in Equation 3.22 is calculated at a cross-section located just upstream of the monolith. The

distance from this upstream plane to the monolith can significantly change the predicted pressure loss, since the tangential velocity component (and consequently the entrance angle) can vary with location of the plane. As shown in the study by (Haimad, 1997), the agreement with the experimental results can be improved by choosing as sampling plane the section at 1 mm upstream the porous region front face.

One of the main limitations of this porous medium approach is its inability to predict the mixing of the jets exiting the channels downstream the monolith. Since the flow in the monolith is not separated into individual channels, the porous medium model does not account for the turbulence kinetic energy recovered downstream the monolith caused by the jet mixing, that can significantly modify the redistribution of the flow downstream. An investigation of this effects has been performed on a planar diffuser (section 3.1.1) and a new formulation of the porous medium modelling has been proposed. The novel approach, together with the comparison with previous experimental and numerical data, is presented in Chapter 7.

3.2.6 Flow structure visualization

The visualisation of the 3D structures in presence of swirl has been made using several post-processing tools available in StarCCM+ (CD-Adapco, 2018).

The zero velocity areas inside the domain are most likely representative of the borders of a recirculation zone, since it can be assumed that the change in flow direction occurs where the flow reaches 0 m/s inside the domain. For this reason, the iso-surfaces of zero axial velocity (U = 0 m/s) have been used to visualise the recirculation zones inside the domain. In presence of swirling flow, it has also been possible to visualise the central recirculation bubble formed with high swirl levels (as discussed in subsection 2.1.1).

The flow direction has been visualised using streamlines calculated using a Runge-Kutta integration over the vectorial velocity field. To complement the visualisation of the flow direction, arrows have been added to the stream tubes.

The visualisation of the vortices is of particular interest in fluid dynamics, in order to identify the rotating structures (Haller, 2005; Kolář, 2007). In presence of asymmetry, it is difficult to correctly define the vortex core, so, it has been chosen to use the *vortex core line*, in combination with the streamlines. The vortex core line identifies the axis along which the flow is rotating (Roth, 2000), so it can be used to visualise the vortical structures inside the domain, such as the central recirculation bubble that is created with swirling flows.

3.3 Global flow parameters calculation

Global flow parameters are commonly defined to identify the main characteristics of the problem of interest. These global parameters are often used in engineering applications and can give a rapid estimation of the characteristics of the flow considered.

The definition of swirl level (S) has been discussed in section 2.1.3 and it is commonly adopted to classify swirling flows. Flow uniformity inside the monolith or other high resistance device is important in many applications, resulting in better heat transfer characteristics, consistent residence time and better utilisation of the device. It is common practice to calculate the flow uniformity using a uniformity index (UI). The energy loss through the domain can be determined by calculating the pressure drop (Δp) between two test sections.

The calculation of swirl level, uniformity index and pressure drop is similar between the experiments and the simulations. The definitions used for each parameter are discussed in the next sections.

3.3.1 Swirl level calculation

The swirl level in both experimental and numerical activities has been calculated using the definition from Lucca-Negro and O'Doherty (2001).

$$S = \frac{G_\Theta}{G_x r_o} \tag{3.23}$$

in which G_Θ the tangential momentum flux and G_x is the axial momentum flux, calculated respectively as

$$G_\Theta = \int_{r_i}^{r_o} \rho U W 2\pi r^2 \, \mathrm{d}r \tag{3.24}$$

$$G_x = \int_{r_i}^{r_o} \rho U^2 2\pi r \, \mathrm{d}r \tag{3.25}$$

In equations from 3.23 to 3.25 r is the radial distance from the centre of the cross section, r_o is the outer radius, r_i is inner radius, U is the axial velocity, W is the azimuthal velocity and ρ is the air density.

3.3.2 Uniformity index

The uniformity index (UI) at the outlet section has been estimated from the CFD data as follows

$$UI = 1 - \frac{\sum_f \left| U_f - \bar{U} \right| A_f}{2 \left| \bar{U} \right| A} \tag{3.26}$$

where U_f is the local velocity in the cell area, $\bar{U}$ is the mean velocity at the section, A_f is the cell area and A is the area of the section (CD-Adapco, 2018).

3.3.3 Pressure drop

The pressure drop has been calculated as the difference between the total pressure between the sections considered (section 1 and section 2)

$$\Delta p = p_{tot2} - p_{tot1} \tag{3.27}$$

Since the flow is incompressible, the total pressure (p_{tot}) has been calculated as

$$p_{tot} = p_s + \frac{1}{2}\rho v^2 \tag{3.28}$$

where p_s is the static pressure at the section and the additional term represents the dynamic pressure, in which ρ is the flow density and v is the velocity.

3.4 Uncertainty analysis

The reliability and quality of the measurements can be quantified using the uncertainty analysis, which aims to identify the range of acceptance of the measured quantity. Uncertainty is widely recognised as a measure of the *correctness* of the results (JCGM, 2008). The methods to evaluate the uncertainty in experimental data are described in several reports and handbooks (Coleman and Steele, 2009; JCGM, 2008; Moffat, 1988; NEL, 2010).

The definitions used for the calculation and the analysis of the experimental uncertainty in the current study are based on the report *Guide to the expression of Uncertainty in Measurements (GUM)* JCGM (2008). These guidelines have been published with the support of seven international committees, including the Bureau International des Poids et Mesures (BIPM) and the International Organization for Standardization (ISO), therefore, the same methodology can be found in ISO (2009).

3.4.1 Uncertainty definitions

The measured quantity (in an experiment) X_i is defined as

$$X_i = x_i \pm \delta x_i \tag{3.29}$$

in which x_i is the measured value and δx_i its associated *standard uncertainty*.

The calculation of the standard uncertainty depends on how the quantity is sampled. Two classifications are commonly adopted, referred as *Type A* and *Type B* (JCGM, 2008).

Briefly, if the quantity X_i has been obtained as the average of n independent observations the uncertainty is expressed by the standard deviation of the mean (*Type A*).

From JCGM (2008), the mean value can be expressed as

$$\bar{X} = \frac{1}{n}\sum_{k=1}^{n} X_k \tag{3.30}$$

The experimental standard deviation is expressed by the statistical variance of the n observations, with respect to the mean value

$$s_{\bar{X}}{}^2 = \frac{1}{n-1}\sum_{j=1}^{n}(X_j - \bar{X})^2 \tag{3.31}$$

The variance $s_{\bar{X}}$ for Type A quantities is defined as the positive square root of the statistical variance (Equation 3.31)

$$s_{\bar{X}} = \sqrt{s_{\bar{X}}{}^2(\bar{X})} \tag{3.32}$$

If the measured quantity is not obtained from independent measurements, but it represents a single value, the estimation of the uncertainty is more complex (*Type B*). The Type B uncertainty is usually derived from calibration certificates, manufacturer's specifications, handbooks and experience.

For quantities calculated from other variables using a *functional relationship* f ($Y = f(X_1, X_2, ..., X_N)$) it is possible to calculate the *combined standard uncertainty* (δy). The calculation of the combined standard uncertainty depends on the complexity of the function f, and it is a combination of the uncertainty of each variable X_i. The *law of propagation of uncertainty* is derived in JCGM (2008) from the Taylor series approximation of the variables. The results presented in the guide (JCGM, 2008) to link the uncertainty of the derived quantities are used for the analysis presented here.

The measurements included in the current thesis have one or both types of uncertainties, and the sources and quantifications are presented in the next sections.

3.4.2 Instrumentation accuracy

The range and accuracy of the instrumentation used for the measurements reported in the current thesis are summarised in Table 3.7. The data have been extracted from the manufacturers datasheets and/or manuals.

The cases for which the accuracy varies proportionally to the measured value (i.e. the *reading*) the abbreviation *rdg* is used in Table 3.7. If the uncertainty is reported as a fixed percentage of the instrument range, the abbreviation *FS* is used (Full Scale).

Table 3.7 Instrumentation range and accuracy

Variable	Instrument	Range	Accuracy
VFM Δp (Pa)	FCO318	$\pm$ 20 kPa	$\pm$ 0.25 % rdg
VFM Δp_{back} (kPa)	FCO318	0-1 bar	$\pm$ 0.25 % rdg
Ambient pressure (Pa)	GE PACE 1000	0 - 1150 bar	$\pm$ 0.005 % FS
Temperature (° C)[a]	TM-747DU	-100 to 200°C	$\pm$0.1°C
Wall pressure (Pa)	ZOC33-20	$\pm$5 kPa	$\pm$ 0.15 % FS
(Scanivalve)	ZOC33-10 [b]	$\pm$2.5 kPa	$\pm$ 0.20 % FS

[a] Used for ambient and VFM temperatures with a K-Type Thermocouple

[b] Limited to 5 pressure tappings (subsection 3.1.3)

3.4.3 Mass flow rate uncertainty

The uncertainty associated with the mass flow rate through the VFM (section 3.1.1) is the primary source of uncertainty in the experiments carried out in the thesis.

The VFM calibration curve (Figure 3.2) has been obtained using an orifice plate device (Appendix B). The estimation of the uncertainty has been made using the equation for uncertainty reported in ISO (2003b).

The procedure used to calculate the mass flow rate through the orifice plate is discussed in Appendix B. For clarity, the equation used for the mass flow rate calculation has been reported here

$$q_m = \frac{C}{\sqrt{1-\beta^4}} \varepsilon \frac{\pi}{4} d^2 \sqrt{2\Delta p \rho_1} \tag{3.33}$$

in which C is the discharge coefficient, β the diameter ratio of the orifice plate, ε is the expansibility factor, d is the throat diameter of the orifice plate, Δp is the differential pressure though the device and ρ_1 is the fluid density.

The variables in Equation 3.33 are interdependent, e.g. the discharge coefficient is a function of geometry and flow rate (Equation B.2). The ISO (2003a) suggests that the combined uncertainty for Equation 3.33 can be calculated for practical applications assuming that the relative standard uncertainties of those variables are independent. This approximation leads to the calculation of the combined uncertainty for the mass flow rate through the orifice plate with the equation proposed in the standard ISO (2003a)

$$\frac{\delta q_m}{q_m} = \left\{ \left(\frac{\delta C}{C}\right)^2 + \left(\frac{\delta \varepsilon}{\varepsilon}\right)^2 + \right. \\ + \left(\frac{2\beta^4}{1-\beta^4}\right)^2 \left(\frac{\delta OD}{OD}\right)^2 + \left(\frac{2}{1-\beta^4}\right)^2 \left(\frac{\delta ID}{ID}\right)^2 + \\ \left. + \frac{1}{4}\left(\frac{\delta \Delta p}{\Delta p}\right)^2 + \frac{1}{4}\left(\frac{\delta \rho_1}{\rho_1}\right)^2 \right\}^{1/2} \tag{3.34}$$

Here OD is the outer diameter of the orifice plate, ID is the throat diameter of the orifice plate (more details in Appendix B).

The uncertainty associated with ε is not accounted for (Baker, 2016), since the incompressible approximation has been made for the flow, fixing $\varepsilon = 1$ (more details in Appendix B). The relative uncertainty for β is given by the manufacturer of the orifice plate (Dwyer, 2009). The relative uncertainty for the discharge coefficient has been calculated from the ISO (2003a) and it is a function of β

$$\frac{\delta C}{C} = 1.667\beta - 0.5\% \tag{3.35}$$

The relative uncertainty of the measured Δp (Type B uncertainty) has been calculated from the instrumentation manual (Table 3.7). The uncertainty associated with the orifice plates diameters (OD and ID) has been assumed to be the maximum value from ISO (2003a), since no data were available in the manufacturer datasheet (Dwyer, 2009). The uncertainty of the density (ρ_1) has been calculated using the ideal gas law from the uncertainty of pressure and temperature, which are Type B quantities, with relative uncertainties reported in Table 3.7. The ideal gas law, reformulated using the molar mass M (more details in Appendix B), becomes

$$p \cdot M = \rho R T \tag{3.36}$$

Therefore the density ρ is proportional to pressure and inversely proportional to the temperature

$$\rho \propto \frac{p}{T} \tag{3.37}$$

Thus, the uncertainty associated with ρ can be calculated as

$$\frac{\delta\rho}{\rho} = \sqrt{\left(\frac{\delta p}{p}\right)^2 + \left(\frac{\delta T}{T}\right)^2} \tag{3.38}$$

The standard uncertainty associated with each term is reported in Table 3.8. By substituting each quantity from Table 3.8 into Equation 3.34, the uncertainty associated with the mass flow rate trough the orifice plate is $\delta q_m/q_m = 0.75\%$.

Table 3.8 Relative standard uncertainty of the terms in Equation 3.34

Variable	Relative standard uncertainty
$\delta C/C$	0.67% [a]
$\delta\beta/\beta$	$\pm$0.7% [b]
$\delta OD/OD$	$\pm$0.4% [a]
$\delta ID/ID$	$\pm$0.1% [a]
$\delta\Delta p/\Delta p$	$\pm$ 0.25 % rdg
$\delta\rho_1/\rho_1$	$\pm$0.27% [d]

[a] From Equation 3.35 ISO (2003a)

[b] From Dwyer (2009)

[c] From instrumentation manual (Table 3.7)

[d] Expanded uncertainty from ambient pressure and temperature

3.4.4 Velocity measurement uncertainty (HWA)

The uncertainty in velocity measurements obtained using a constant temperature anemometer depends on the instrumentation, the calibration and the experimental conditions (Jørgensen, 2002). In the current thesis, the analysis of the HWA uncertainty is based on the guidelines presented in Jørgensen (2002). The hypothesis made on the current study are described in the next paragraphs.

The calibration has been made using a TSI 1129 calibrator (as explained in subsection 3.1.2) and the calibration curve (Figure 3.11) has been obtained with the ThermalPro software (TSI, 2010). From Jørgensen (2002), the relative uncertainty for the calibration

is $\pm 1\%$. The curve fitting errors are calculated from the ThermalPro software and for the velocity range of interest are estimated within $\pm 2\%$ (Figure 3.11).

The accuracy for the signal conditioner (*A/D board* source in Table 3.9) has been taken from the manufacturer manual and it is equal to 0.15% (TSI, 2010).

The uncertainty of the probe positioning is associated in Jørgensen (2002) only to the probe alignment and it is considered negligible, given that the probe can be positioned with a small uncertainty. The same approximation is considered valid in the current thesis, since the probe positioning has been controlled using the traverse controller described in subsection 3.1.2.

The temperature variations from calibration to experiments have been corrected by the ThermalPro software. A type T thermocouple has been positioned close to the HWA sensor to obtain the real time temperature correction (frequency response of $\approx 1s$). Therefore, only the uncertainty associated with the thermocouple accuracy has been considered here ($\pm 1^\circ$ C from TSI).

The uncertainty due to ambient pressure variations (consequently the associated density variation) is considered to be small for the duration of the experiments and it has not been applied. The variations due to gas composition and humidity have been neglected, since their contribution to heat transfer changes is small, according to Jørgensen (2002).

A summary of the HWA experimental uncertainty for each source is given in Table 3.9. The combined standard uncertainty for the HWA velocity measurements is estimated to be $\pm 2.7\%$.

Table 3.9 Error sources and relative standard uncertainty for the HWA velocity sample

Source	**Relative standard uncertainty**
Calibrator	$\pm 1\%$
Curve fitting	$\pm 2\%$
A/D board	$\pm 0.15\%$
Probe positioning	≈ 0
Temperature variations	$\pm 1^\circ$ rdg
Ambient pressure	≈ 0
Humidity	≈ 0

3.4.5 Pressure measurement uncertainty

The uncertainty for the pressure measurements is considered a Type A (Equation 3.32) for each sampling point, since the pressure is sampled n times (the number of frames) and then averaged (subsection 3.1.3). The uncertainty around the estimate of the mean (Biau, 2011) has been calculated using the *standard error* of the mean ($\sigma_{\bar{X}}$), using

$$\sigma_{\bar{X}} = \frac{s}{\sqrt{n}} \tag{3.39}$$

in which s is the variance calculated from (Equation 3.31). The confidence interval ($\delta_{\bar{X}}$) at 95% for the standard error has been calculated as $\delta_{\bar{X}} = 1.96 \cdot \sigma_{\bar{X}}$.

The relative uncertainty due to changes of ambient pressure and temperature variations has been neglected for these measurements. This approximation has been made since the changes in ambient conditions are negligible for the duration of the experiment and the calibration procedure has been repeated before each experimental run, thus reducing the impact of the ambient conditions.

3.4.6 CFD uncertainty

The estimation of the uncertainty from the CFD simulations is more difficult to assess, given the lack of standard procedures reported in many studies (e.g. Karniadakis (2002); Roache (1997); Stern et al. (2006)).

A basic definition of the CFD uncertainty (δ_s) from Stern et al. (2006) is given by the expression

$$\delta_S = \delta_{SM} + \delta_{SN} \tag{3.40}$$

in which δ_{SM} is defined as *modelling error* and δ_{SN} is defined as *numerical error*.

The modelling error is related to the formulation of the model, including the mathematical approximations introduced with the choice of the boundary conditions. The numerical error includes the uncertainty and errors associated with the numerical approximation of the equations, e.g. round-off error, grid error and numerical schemes.

In this study, the impact of the numerical convergence of the solution is considered small, since strict convergence criteria have been adopted for each variable modelled (subsection 3.2.2). The impact of the mesh discretisation has been estimated for each test section through a mesh independence study and it is reported in the relative chapter. The verification and validation of the CFD simulations, as suggested by Stern et al. (2006), has been made using the comparison with experiments.

3.5 Chapter summary

The three test sections used throughout the thesis (annular pipe, diffuser with a sudden expansion and planar diffuser) have been described and presented, identifying and motivating the objectives of their use in the study.

The advantages and limitations of the experimental techniques used for the study of swirling flows have been presented for the HWA and pressure measurements carried out on the pipe with annular cross section (Chapter 4) and for the PIV applied to the study of the diffuser with a sudden expansion (Chapter 5 and Chapter 6).

The methodology used for the CFD study has been described in detail, aiming to highlight and motivate the modelling strategy chosen for each test section.

The global quantities used throughout the thesis have been defined in accordance to the engineering applications for which they are relevant, giving a motivation of their use, based on the current literature.

The uncertainty analysis has been presented in the last section, giving an overview of the challenges to overcome when dealing with the experimental and numerical uncertainty. The sources of uncertainty have been identified and discussed based on the published standards procedure.

The methodology described in the current chapter covers the general aspects of the experimental and numerical activities carried out in the current thesis. More details about the specific choices made for the three test sections investigated are given in the respective chapters.

Chapter 4

Swirling flow in a pipe with annular cross section

An experimental and numerical study of the flow inside a pipe with annular cross section has been used to investigate the effects of confined swirling flows and characterise important flow statistics such as turbulence level, which can be used for high fidelity flow simulations such as LES.

The experimental study presented here includes an assessment of the pressure measurement accuracy in confined swirling flows, which was used to evaluate the effects of the sampling techniques and of the processing methodology on the analysis of swirling flows. In particular, the impact on the measurements of the HWA probe orientation and sampling frequency have been investigated and the effects of pressure tappings geometry and spacing on the measurements error have been analysed.

The performance of six RANS turbulence models in simulating high swirl flows have been investigated and analysed.

4.1 Experiments

The aim of this section is to provide some guidelines to assess the advantages and disadvantages of the measurement techniques used, identifying and clarifying their potential and limitations before the analysis of the results, which is presented in conjunction with the results of the CFD model in section 4.3.

The methodology used for the two experimental activities performed on the current test section, *HWA* measurements and *static pressure* measurements, has been described in section 3.1.2 and section 3.1.3 respectively. The experimental dataset acquired with both techniques includes measurements for a range of Reynolds numbers and swirl levels. The inflow conditions used for all the measurements are summarised in Table 3.5.

4.1.1 Hot-Wire Anemometry measurements

Calculation of mean velocity components

The use of two probe orientations to sample the data has allowed the extraction of two velocity components, as explained in section 3.1.2. The measurements downstream the swirl generator are shown for the two cases of $\theta_s = 0°$ and $\theta_s = 18°$. The velocity for both swirl generator angles is shown at one sampling radius for the three inflow Reynolds numbers ($Re_1 = 21720$, $Re_2 = 54374$ and $Re_3 = 86880$). The data sampled with the probe oriented in the direction *parallel* to the pipe radius are represented with dots, while the data sampled with the probe oriented in the direction *normal* to the radius (azimuthal direction) are represented by crosses.

The axial flow case ($\theta_s = 0°$) has been used to verify that the velocity sampled without swirl is independent from the probe orientation. It can be seen from Figure 4.1 that the differences between the velocity measured with the two probe orientations are within $\approx 2\%$. Higher differences (up to 30%) can be observed towards the outer wall ($r/r_o = 0.92$ and $r/r_o = 0.96$). Since the same trend has been observed for both probe orientations (i.e. for data sampled non simultaneously) and that the trend is consistent for the all the 3 inflow Reynolds numbers, it can be concluded that the changes observed between $r/r_o = 0.46$ (pipe insert wall) and $r/r_o = 0.88$ can be mainly attributed to asymmetry of the experimental rig, while the changes observed towards the outer wall are attributed to the flow expanding (and therefore non-negligible radial velocity component present) and probe positioning, since the measurements have been made without the annular pipe attached (as described in section 3.1.2).

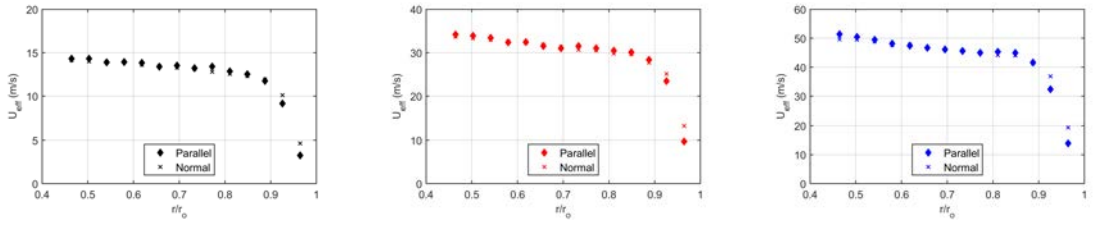

(a) $\theta_s = 0°$ - $Re_1 = 21720$ **(b)** $\theta_s = 0°$ - $Re_2 = 54374$ **(c)** $\theta_s = 0°$ - $Re_3 = 86880$

Figure 4.1 HWA velocity sampled downstream the swirl generator for $\theta_s = 0°$ along one sampling radius. Diamonds represent the data sampled with the probe oriented along the *parallel* direction, crosses represent the data sampled with the probe oriented along the *normal* direction. $Re_1 = 21720$ (a) in black, $Re_2 = 54374$ (b) in red and $Re_3 = 86880$ (c) in blue.

Similarly to the axial case (Figure 4.1) the results for the highest swirl case are shown in Figure 4.2. Higher velocity is measured with the probe oriented in the *parallel* direction compared to the velocity measured with the probe oriented in the *normal* direction. It is caused by the HWA capturing two different effective cooling velocities

(Figure 3.13), depending on the probe orientation. Thus, the two velocities can be transformed to estimate the *axial* velocity (U_x along X) and the *tangential* velocity (U_y along r), as described in section 3.1.2.

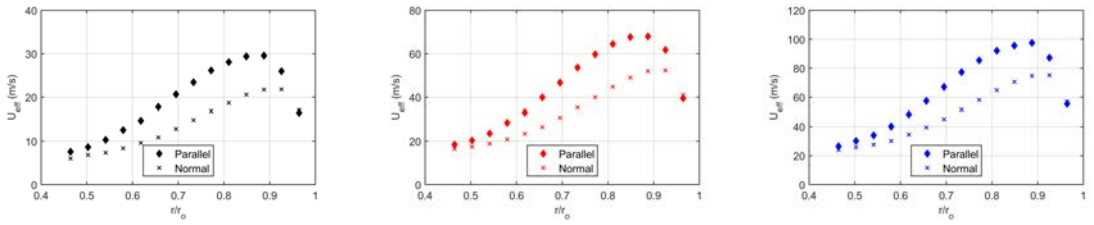

(a) $\theta_s = 18°$ - $Re_1 = 21720$ **(b)** $\theta_s = 18°$ - $Re_2 = 54374$ **(c)** $\theta_s = 18°$ - $Re_3 = 86880$

Figure 4.2 HWA velocity sampled downstream the swirl generator for $\theta_s = 18°$ along one sampling radius. Diamonds represent the data sampled with the probe oriented along the *parallel* direction, crosses represent the data sampled with the probe oriented along the *normal* direction. $Re_1 = 21720$ (a) in black, $Re_2 = 54374$ (b) in red and $Re_3 = 86880$ (c) in blue.

The decomposition from Equation 3.2 and Equation 3.3 has been applied to the HWA data for $\theta_s = 18°$ (Figure 4.2), obtaining the two velocity components shown in Figure 4.3.

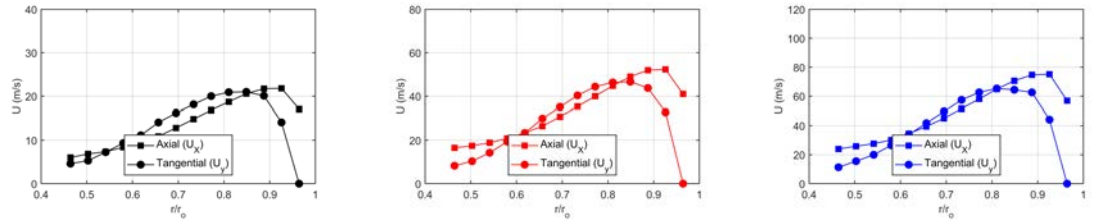

(a) $\theta_s = 18°$ - $Re_1 = 21720$ **(b)** $\theta_s = 18°$ - $Re_2 = 54374$ **(c)** $\theta_s = 18°$ - $Re_3 = 86880$

Figure 4.3 HWA velocity components extracted from HWA data for $\theta_s = 18°$ along one sampling radius. Squares represent the axial velocity component, dots represent the tangential velocity component. $Re_1 = 21720$ (a) in black, $Re_2 = 54374$ (b) in red and $Re_3 = 86880$ (c) in blue.

The flow angle γ_s (i.e. the angle between the pipe axis and the velocity vector) for $\theta_s = 18°$ has been calculated from the velocity components using Equation 3.5. It can be seen from Figure 4.4 that the angle is barely changing with the Reynolds number. The flow angle calculated for all the inflow conditions is reported in Figure E.1, confirming the low dependence from the Reynolds number observed for the maximum swirl case.

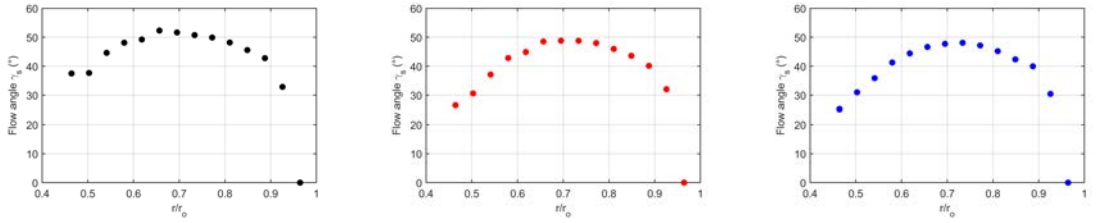

(a) $\theta_s = 18°$ - $Re_1 = 21720$ **(b)** $\theta_s = 18°$ - $Re_2 = 54374$ **(c)** $\theta_s = 18°$ - $Re_3 = 86880$

Figure 4.4 Flow angle (γ_s) extracted from the velocity components for $\theta_s = 18°$. $Re_1 = 21720$ (a) in black, $Re_2 = 54374$ (b) in red and $Re_3 = 86880$ (c) in blue.

As discussed in section 3.1.2, velocity decomposition accuracy depends on several assumptions (negligible radial velocity component, small yaw coefficient and pitch coefficient close to 1). In order to estimate this accuracy, the calculated axial velocity component has been used to calculate the mass flow rate and compared with the prescribed mass flow rate. The mass flow rate has been calculated by integrating numerically the axial velocity along the radius, from

$$\dot{m}_{HWA} = \int_{r_i}^{r_o} \rho U_x 2\pi r \, \mathrm{d}r \tag{4.1}$$

The difference between the calculated mass flow rate and the nominal mass flow rate has been calculated and is shown in Figure 4.5.

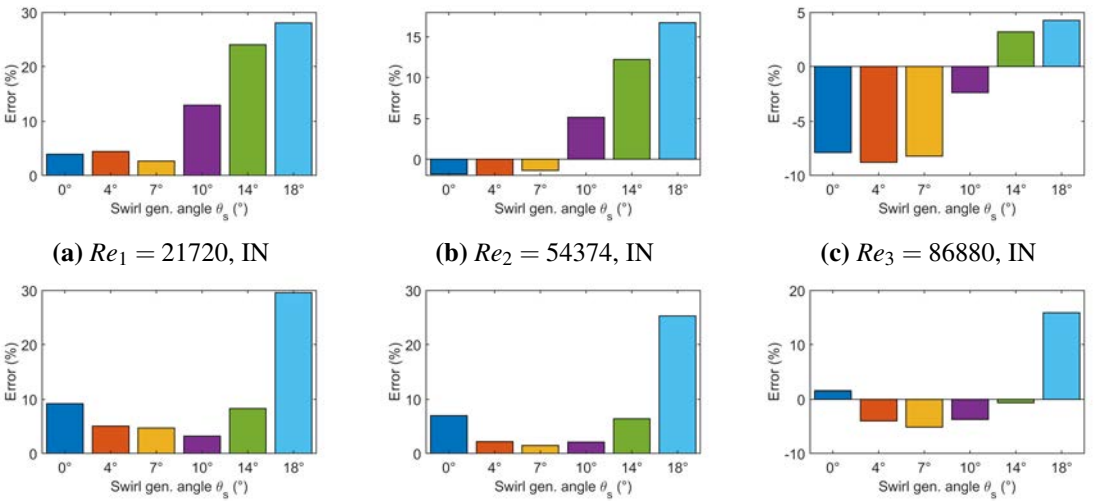

(a) $Re_1 = 21720$, IN **(b)** $Re_2 = 54374$, IN **(c)** $Re_3 = 86880$, IN

(d) $Re_1 = 21720$, OUT **(e)** $Re_2 = 54374$, OUT **(f)** $Re_3 = 86880$, OUT

Figure 4.5 Error in the MFR calculation from the *axial* velocity component. Difference at the pipe inlet section (Section 1, Figure 3.10) on top (a,b,c). Difference at the pipe outlet section (Section 2, Figure 3.10) on the bottom (d,e,f). Mass flow rate increasing from left to right: 25 g/s (a,d), 63 g/s (b,e) and 100 g/s (c,f)

It can be seen that the difference between the flow rates is consistently higher with the increasing swirl level, confirming the strong coupling between the axial and

tangential components for high swirl, that can not be captured with the technique used (Skusiewicz, 2012).

Turbulence intensity and frequency analysis

The data sampled using the HWA have been used to extract some turbulence properties, as explained in section 3.1.2. In order to establish if the sampling frequency is sufficient to resolve fluctuations of interest for different Reynolds numbers and swirl levels, several measurements have been performed using different sampling frequencies. Here, the initial comparison between measurements with different frequencies and the motivations of the study on the frequency analysis are presented for the two limiting swirl levels ($\theta_s = 0°$ and $\theta_s = 18°$) for all three mass flow rates.

The turbulence intensity calculated from the HWA data for $\theta_s = 0°$ is shown in Figure 4.6 for the three Reynolds numbers $Re_1 = 21720$, $Re_2 = 54374$ and $Re_3 = 86880$. Note that the fluctuations recorded by the hot wire probe are the signal fluctuations in the calculated cooling velocity. In isotropic turbulence scenario, these would be sufficient to characterise the turbulence. Since the turbulence in swirling flows is known to be highly anisotropic (Gupta et al., 1984), the results presented here only represent turbulence intensity in one (normal measurements) direction.

It can be seen that the turbulence intensity sampled with the lowest frequency $f_s = 200Hz$ is lower then the turbulence intensity sampled with the other two sampling frequencies ($f_s = 600Hz$ and $f_s = 1000Hz$), which are in good agreement (within 3%).

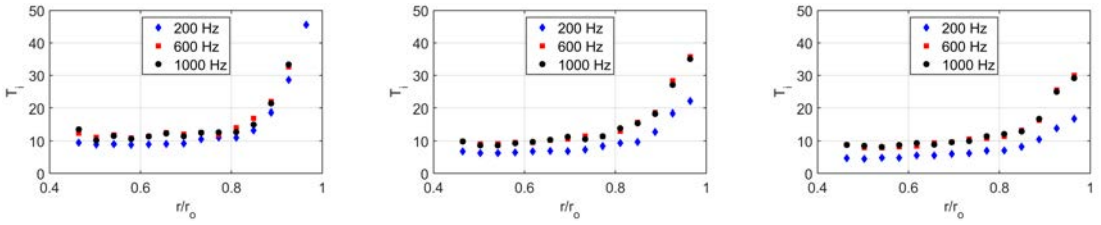

(a) $\theta_s = 0°$ - $Re_1 = 21720$ **(b)** $\theta_s = 0°$ - $Re_2 = 54374$ **(c)** $\theta_s = 0°$ - $Re_3 = 86880$

Figure 4.6 Turbulence intensity extracted from HWA data for $\theta_s = 0°$ along one sampling radius. $Re_1 = 21720$ (a), $Re_2 = 54374$ (b) and $Re_3 = 86880$ (c). Sampling frequency: $f_s = 200Hz$ (blue diamonds), $f_s = 600Hz$ (red squares), $f_s = 1000Hz$ (black dots).

A similar trend can be observed for the turbulence intensity for $\theta_s = 18°$ (Figure 4.7). Similarly to the axial flow case ($\theta_s = 0°$) the turbulence intensity sampled with the lowest frequency $f_s = 200Hz$ is lower then the turbulence intensity sampled with the other two sampling frequencies ($f_s = 600Hz$ and $f_s = 1000Hz$), which are in good agreement (within 3%).

For both cases presented here ($\theta_s = 0°$ in Figure 4.6 and $\theta_s = 18°$ in Figure 4.7) the same trend is confirmed for all the three Reynolds numbers $Re_1 = 21720$, $Re_2 = 54374$ and $Re_3 = 86880$. The same trend has been observed for all the other swirl levels and downstream the pipe outlet.

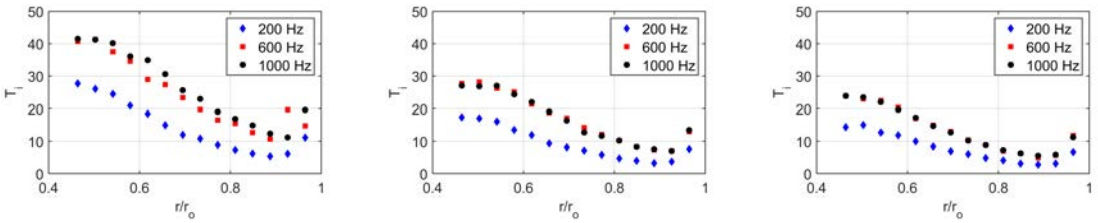

(a) $\theta_s = 18°$ - $Re_1 = 21720$ **(b)** $\theta_s = 18°$ - $Re_2 = 54374$ **(c)** $\theta_s = 18°$ - $Re_3 = 86880$

Figure 4.7 Turbulence intensity extracted from HWA data for $\theta_s = 18°$ along one sampling radius. Effect of the sampling frequency: $f_s = 200Hz$ (blue diamonds), $f_s = 600Hz$ (red squares), $f_s = 1000Hz$ (black dots). $Re_1 = 21720$ (a), $Re_2 = 54374$ (b) and $Re_3 = 86880$ (c).

The difference in the turbulent intensity obtained using $f_s = 200Hz$ indicates that a significant part of the turbulent energy is carried by fluctuations with higher frequency, since no changes in the mean velocity component have been observed with the sampling frequency. The fact that no significant changes have been observed with the two higher sampling frequencies of (600 Hz and 1000 Hz), suggests that the frequencies associated with the flow structures typical of the flows studied in the current thesis are in the range between 100 Hz and 500 Hz. In order to isolate frequencies associated with the swirling flow, one needs to eliminate oscillations not associated with the flow structures, as mentioned in section 3.1.2. Here, some of the possible factors influencing the results are investigated:

1. upstream flow frequency (associated with the compressor supplying air line);
2. periodic motion of the flow upstream (*vortex shedding*);
3. structural frequency of the swirl generator;

The analysis of the characteristic frequencies associated with the 3 sources is presented in the next paragraphs.

Upstream flow frequency The flow entering the test section is supplied by the air compressor (Figure 3.1), which is known to produce air supply fluctuations in the air line, causing the presence of extra peak frequencies in the measurements. In order

to evaluate the order of magnitude of these frequencies, the pressure logged at the VFM (Appendix C) has been used to evaluate any periodicity associated with the flow supplied to the test section.

A log sample has been presented in Figure 3.21 to show the low impact of the unsteady flow supplied on the mass flow rate. As mentioned in subsection 3.1.5, the peak to peak cycle T_{VFM} is estimated to be 8 seconds, with a fluctuation of the pressure from the mean value within $\pm 2\%$. The frequency associated with this periodic motion (f_{VFM}) can be calculated as

$$f_{VFM} = \frac{1}{T_{VFM}} \tag{4.2}$$

For $T_{VFM} = 8$ s, the associated $f_{VFM} = 0.125$ Hz.

Thus, the influence of the compressor on the HWA data can be excluded also because the duration of the sampling signal in each point is as high as 5.12 s, which is lower than the fluctuation period associated with the air compressor.

Vortex shedding The presence of the blocks in the swirl generator assembly can cause the presence of a periodic motion in the flow downstream, in similarity with the *vortex shedding* phenomenon. In presence of a blunt body, such as the blocks inside the swirl generator, the flow wake downstream could exhibit an oscillating behaviour, similarly to the flow past a cylinder (Matsumoto, 1999). The non-dimensional parameter used to characterise the oscillating flow mechanism is the Strouhal number (St), defined as

$$St = \frac{f_{St} L_{St}}{U_{St}} \tag{4.3}$$

where f_{St} is the frequency associated with the vortex shedding, L_{St} is the characteristic length and U_{St} is the flow velocity.

The shedding of the vortices has been observed at intermediate Strouhal numbers ($St \approx 0.2 - 0.3$) in numerous experimental studies over different geometries (e.g. in Matsumoto (1999); Nikolaos D. Katopodes (2019); Sobey (1982); Tropea et al. (2007)).

The value of the characteristic frequency associated with the vortex shedding can be estimated by reversing Equation 4.3, under the hypothesis that $St \approx 0.2 - 0.3$. Thus, the frequency associated with the vortex shedding f_{St} can be calculated as

$$f_{St} = \frac{St U_{St}}{L_{St}} \tag{4.4}$$

Because of the complexity of the swirl generator geometry, there are several length scales that can be used to estimate the vortex shedding frequency. Here, different

characteristic lengths L_{St} are used, in order to establish the range of frequencies that could be associated with the vortex shedding. The characteristic length has been assumed to be equal to the dimensions on the blocks of the swirl generator, which varies with the swirl generator angle. In particular, the two extreme cases of no swirl and maximum swirl have been examined, corresponding to $\theta_s = 0°$ and $\theta_s = 18°$. For clarity the schematic view of the swirl generator blocks for each position is given in Figure 4.8. The characteristic length used for the calculation is indicated in Figure 4.8 and it has been used to evaluate the effects of the swirl generator blocks positions on the frequency.

(a) $\theta_s = 0°$ **(b)** $\theta_s = 18°$

Figure 4.8 Characteristic lengths extracted from the swirl generator for $\theta_s = 0°$ (a) and $\theta_s = 18°$ (b). The dimensions indicated are used in Table 4.1.

The characteristic velocity U_{st} reported in Table 4.1 has been extracted for the three Reynolds numbers, assuming that uniform flow passes through the cross section of the swirl generator blocks. The results presented in Table 4.1 show that the frequencies associated with the vortex shedding should be lower than 100 Hz, therefore smaller then the range of interest in the current study.

Table 4.1 Frequencies associated with the vortex shedding (Equation 4.4), assuming $0.2 \leq St \leq 0.3$ for the three different inflow Re (Table 3.5). Characteristics lengths for the swirl generator blocks (Figure 4.8): $L_0 = 41$ mm, $L'_0 = 50$ mm and $L_{18} = 38$ mm.

St	Re	U_{St} (m/s)	**Characteristic lengths L_{St} (mm)**		
			$L_0 = 41$	$L'_0 = 50$	$L_{18} = 38$
				f_{St} (Hz)	
0.2	21720	2.94	14.35	11.77	15.49
	54374	7.42	36.17	29.66	39.03
	86880	11.77	57.42	47.08	61.95
0.3	21720	2.94	21.53	17.66	23.23
	54374	7.42	54.26	44.49	58.54
	86880	11.77	86.12	70.62	92.92

Structural frequency The swirl generator resembles an Helmholtz resonator assembly. The corresponding *structural* frequency (f_H) has been calculated from theory (Mechel, 2008) as

$$f_H = \frac{a}{2\pi}\sqrt{\frac{A}{V_0 L_{eq}}} \tag{4.5}$$

where a is the speed of sound, A is the cross sectional area of the nozzle section, V_0 is the static volume of the cavity and L_{eq} is the equivalent length of the nozzle, calculated from

$$L_{eq} = L_n + 0.3D_n \tag{4.6}$$

in which $L_n = 88$ mm is the nozzle length and $D_n = 31$ mm is the hydraulic diameter of the nozzle.

The volume of the cavity ($V_0 = 1.42^{-2}m^3$) has been extracted from the CAD used for the CFD model, while the other dimensions have been directly measured. The speed of sound, extracted from the standard atmospheric conditions assuming a temperature $T = 20°C$, is equal to 343.21 m/s. The effect of the moving blocks does not need to be accounted for in calculating with the Helmholtz frequency, since the volume of the cavity is not changing with the relative position of the blocks.

Under the above hypothesis, the Helmholtz frequency calculated from Equation 4.5 for the swirl generator assembly is estimated to be around 64 Hz.

Frequency peaks and power spectra From the above analysis, all the frequencies that could be attributed to the upstream rig components have been estimated to be below 100 Hz, which is the maximum frequency that could be captured with the sampling frequency of $f_s = 200Hz$. Therefore, the power spectra obtained with the two higher frequencies should contain relevant information about the flow analysed.

The Fast Fourier Transform (FFT) analysis on the case corresponding to $\theta_s = 7°$ and $Re_3 = 86880$ is presented here as an example of the data processing described in the methodology section 3.1.2. The FFT has been applied to the time signal acquired for all the 56 sampling points (Figure 3.12). The results are shown in Figure 4.9 for the 3 sampling frequencies. It is possible to identify a very distinguished primary peak in all the plots: with the lower sampling frequency used (200 Hz, Figure 4.9a), the peak is at a frequency of $\approx 16Hz$, while for the other two sampling frequencies (600 Hz, Figure 4.9b and 1000 Hz, Figure 4.9c) the peak is at $\approx 180Hz$. The FFT peak position is independent from the sampling point position for all the sampling frequencies, as shown in Figure 4.9d.

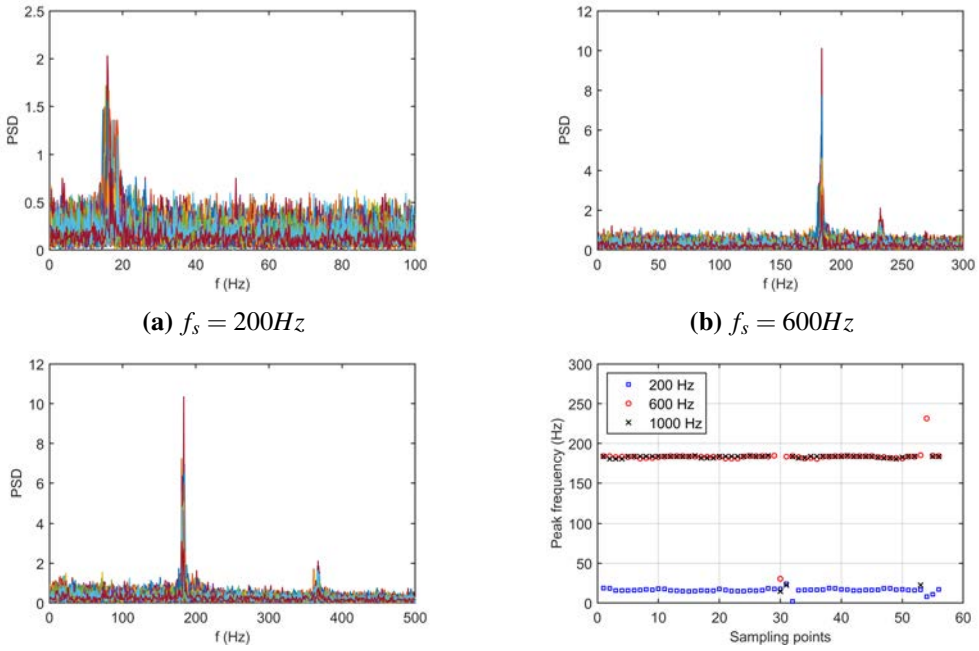

(a) $f_s = 200Hz$ **(b)** $f_s = 600Hz$

(c) $f_s = 1000Hz$ **(d)** Peaks

Figure 4.9 Example of the FFT power spectral density for the case of $\theta_s = 7°$ and $Re_3 = 86880$. Effect of the sampling frequency: $f_s = 200Hz$ (a), $f_s = 600Hz$ (b), $f_s = 1000Hz$ (c). Maximum peak for each sampling point (d).

From the above analysis, it can be concluded that the dominant flow frequency is captured with a minimum sampling frequency of 600 Hz and that the frequency analysis in the configuration considered here does not depend on the probe position along the pipe radius. For these reasons, the energy power spectra for all the cases have been plotted only at one point ($r/r_o = 0.73$ in the upper quadrant) using the data sampled with the highest sampling frequency of 1000 Hz. An example of the energy power spectra calculated using Equation 3.8 for the case presented $\theta_s = 7°$ and $Re_3 = 86880$ (Figure 4.9) is shown in Figure 4.10. The results for all the cases are included in Appendix E as an additional dataset.

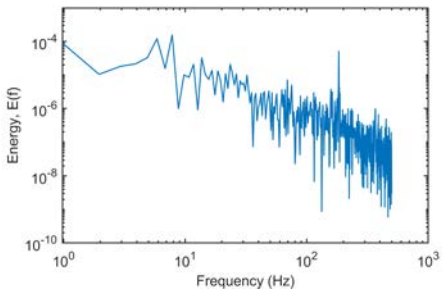

Figure 4.10 Energy spectrum for $\theta_s = 7°$ and $Re_3 = 86880$ at $r/r_o = 0.73$ mm in the upper quadrant (positive Y in Figure 3.12b).

4.1.2 Static pressure measurements

The pressure measurements made at the outer wall of the pipe have allowed further analysis of the flow and more data for the CFD model validation. The methodology presented in subsection 3.1.3 has been applied to the data to smooth the effects of the manufacturing asymmetry. This section provides examples of the methodology presented in subsection 3.1.3 and includes the analysis of the pressure-taps effects.

Standard error of the mean

The uncertainty for the pressure measurements is a *Type A* uncertainty (subsection 3.4.5). Although the scatter of the measurements is considerable, the high number of measurements allowed to use standard error to estimate the average pressure reading at each point with high confidence. The standard error of the mean for each measuring location (pressure tapping) has been calculated using Equation 3.39. The maximum error determined for the data is 0.2% of the mean value, for all the pressure tappings, which is within the instrumentation accuracy.

No significant effects of the sampling frequency on the measured mean pressure values have been identified, in agreement with the velocity measurements. The frequency analysis for pressure signal has confirmed that the presence of tubing used to connect the pressure tappings to the pressure transducer has significantly altered the frequency response of the system, as described in Pemberton (2010). Therefore, no results of the pressure signal frequency analysis are presented here.

Pressure-taps effect

The pressure measurement accuracy depends not only on the instrumentation, but also on the pressure tapping geometry and spacing, as discussed in 3.1.3. The effects of the pressure tappings geometry on the result accuracy (using the methodology described in section 3.1.3) are presented here. The disturbances introduced by pressure tappings in the flow have been discussed in section 2.1.3.

Hole depth and diameter The results obtained using *Cylinder 1* (with constant distance between the tappings fixed at $L_s = 50d_h$) have been used to establish the effects of the hole depth (L_h) and of the hole diameter (d_h) on the measurement accuracy, as described in subsection 3.1.3 for different swirl levels and Reynolds numbers. The comparison has been made calculating the standard error of the mean associated with each pressure tap, following the procedure described in section 4.1.2.

The results shown in Figure 4.11 represent the standard error of the mean ($\sigma_{\bar{X}}$) for the the two extreme cases analysed in the thesis, corresponding to the axial (no swirl) case of $\theta_s = 0°$ and to the maximum swirl case of $\theta_s = 18°$, for all the 3 inflow Reynolds numbers. The histogram plots shown in Figure 4.11 include the results for all the 6 pressure tappings used for *Cylinder 1* and for all 4 pressure lines. It can be seen that for the results obtained for $\theta_s = 0°$ - $Re_1 = 21720$ (Figure 4.11a) the error is higher compared to all the other cases and present higher scattering. This result is attributed to the small pressure measured in this case, which is near the lower limit of the instrumentation scale. Therefore, the analysis presented here is focused on the remaining cases.

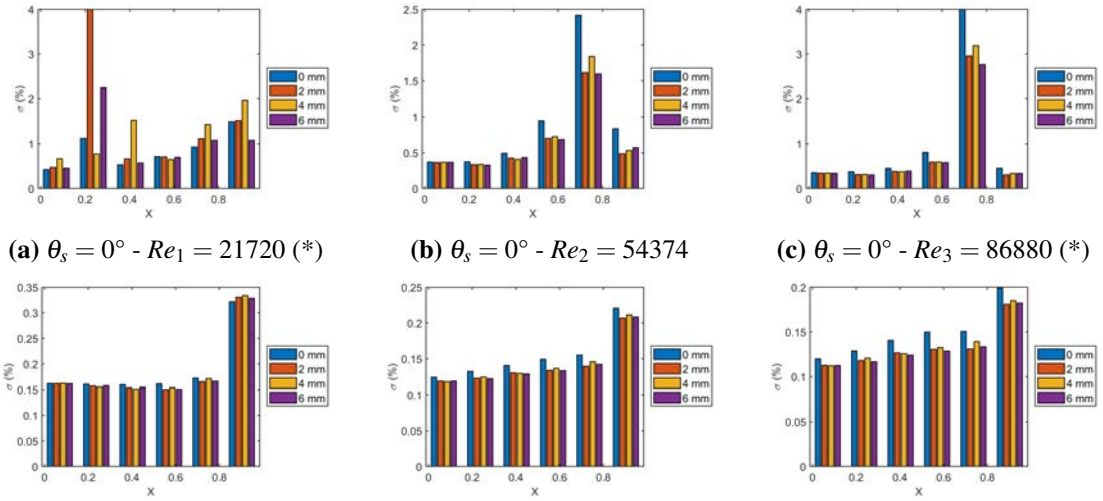

(a) $\theta_s = 0°$ - $Re_1 = 21720$ (*) **(b)** $\theta_s = 0°$ - $Re_2 = 54374$ **(c)** $\theta_s = 0°$ - $Re_3 = 86880$ (*)

(d) $\theta_s = 18°$ - $Re_1 = 21720$ **(e)** $\theta_s = 18°$ - $Re_2 = 54374$ **(f)** $\theta_s = 18°$ - $Re_3 = 86880$

Figure 4.11 Standard error of the mean ($\sigma_{\bar{X}}$) for each pressure tapping on *Cylinder 1*. Comparison between the 4 pressure lines with hole depths of 0 mm, 2 mm, 4 mm and 6 mm. No swirl case ($\theta_s = 0°$) on top (a,b,c), maximum swirl case ($\theta_s = 18°$) below (d,e,f). Inflow Reynolds increasing from left to right: $Re_1 = 21720$ (a,d), $Re_2 = 54374$ (b,e) and $Re_3 = 86880$ (c,f). (*) Scale limited to improve visualisation.

The general trend confirms the known fact that the pressure tappings mounted flush to the surface lead to a higher sampling error (blue bar in Figure 4.11). The highest error observed is $\sigma_{\bar{X}} = 25\%$, in the case $\theta_s = 0°$ and $Re_3 = 86880$ (blue bar in Figure 4.11c, please note that the axis range has been limited to improve the visualisation). It can be seen that the the error associated with $L_h = 0$ mm, for which $d_h = 1.6$ mm is higher than all the other cases, for which $d_h = 1$ mm. Thus, these results confirm that the effect of the hole diameter is significant also for high swirl levels and high mass flow rates, for which the local pressure measured is high. The error $\sigma_{\bar{X}}$ can be further reduced by using a hole depth $L_h = 6$ mm, for the majority of the cases. A reduction of the error can be observed for the maximum swirl level, confirming that the effects of the pressure

tapping configuration become more significant for lower pressures (which can be linked to the accuracy of the instrumentation).

Pressure tappings distance Another important factor that can impact pressure measurements is the distance between pressure taps. Here we use the fact that the swirling flow in an annular pipe should have a linear pressure profile along the wall (Clayton and Morsi (1985); Denton (1963); Yowakim and Kind (1988)). Therefore, the deviation of the measured pressure from a linear "base" pressure distribution obtained from the highest tapping distance data using linear regression is calculated. This "non-linearity" associated with each pressure line (North, East, South and West in Figure 3.15) has been calculated for all the inflow conditions.

A linear regression analysis has been used to quantify the effect of the pressure taps distance, for all the inflow conditions (as described in section 3.1.3). The analysis has been made on the tappings fitted in the central part of the pipe (X = 90 mm up to X = 210 mm, Figure 3.16), where the swirling flow is expected to be fully established, and the effect of the pipe entrance and exit on the pressure distribution is negligible. An example of the linear regression analysis is shown for the axial (no swirl) case ($\theta_s = 0°$ in Figure 4.12) and for the maximum swirl case ($\theta_s = 18°$ in Figure 4.13). The results for all the other inflow conditions are given in Table 4.2.

More data scattering has been observed for the lower Reynolds number, in particular for $\theta_s = 0°$. This aspect, as mentioned in the previous paragraph, is attributed to the resolution of the instrumentation, since the pressure sampled is small. Higher deviation from the linear trend has been observed in all the cases with the tapping distance of $L_s = 10$ mm, which exhibit the highest estimate of the standard errors.

The general trend observed is that with the highest $L_s = 40$ mm, the standard error is lower, meaning that the data preserve the expected linearity. It is interesting to notice that the patterns observed with decreasing distance between the pressure tappings are changing with Reynolds number and swirl level.

It is necessary to remark that the analysis presented here is assuming a linear decay of pressure in the sampling area (known from previous studies, e.g. Clayton and Morsi (1985); Denton (1963); Yowakim and Kind (1988)). The use of more tappings to increase the data resolution might be required by the application, but might lead to inaccurate estimates of the pressure law.

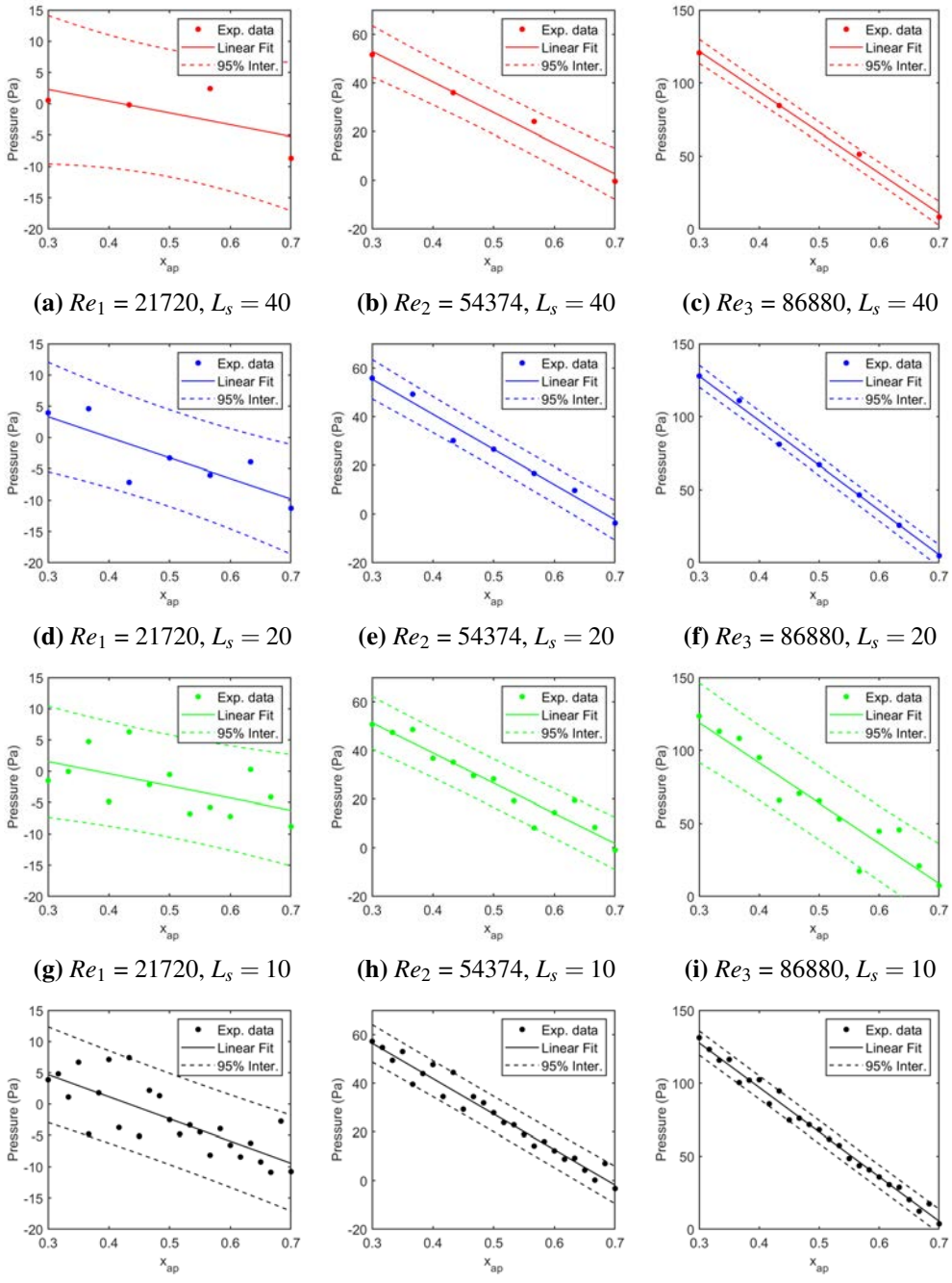

(a) $Re_1 = 21720$, $L_s = 40$ **(b)** $Re_2 = 54374$, $L_s = 40$ **(c)** $Re_3 = 86880$, $L_s = 40$

(d) $Re_1 = 21720$, $L_s = 20$ **(e)** $Re_2 = 54374$, $L_s = 20$ **(f)** $Re_3 = 86880$, $L_s = 20$

(g) $Re_1 = 21720$, $L_s = 10$ **(h)** $Re_2 = 54374$, $L_s = 10$ **(i)** $Re_3 = 86880$, $L_s = 10$

(j) $Re_1 = 21720$, $L_s = 5$ **(k)** $Re_2 = 54374$, $L_s = 5$ **(l)** $Re_3 = 86880$, $L_s = 5$

Figure 4.12 Pressure measurements for *Cylinder 2*: axial flow case ($\theta_s = 0°$). Experimental value (plain circles), linear fitting (continuous line) and confidence interval at 95% (dotted line).

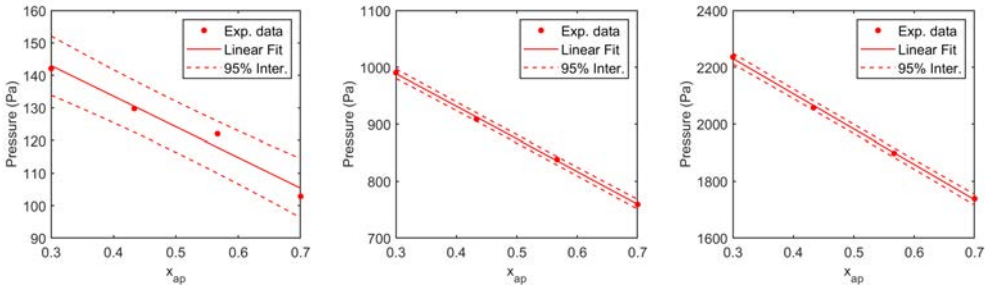

(a) $Re_1 = 21720$, $L_s = 40$ **(b)** $Re_2 = 54374$, $L_s = 40$ **(c)** $Re_3 = 86880$, $L_s = 40$

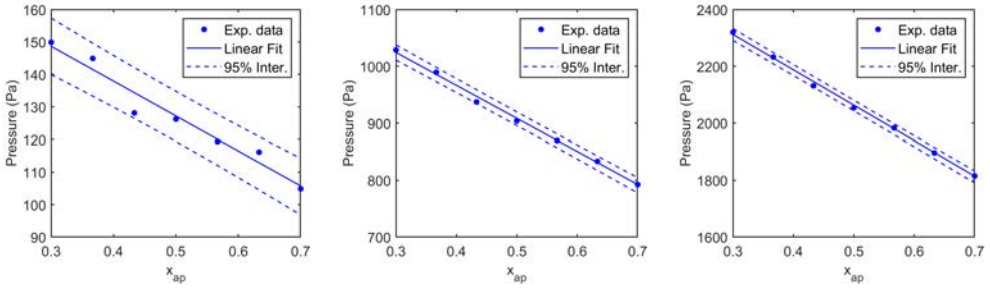

(d) $Re_1 = 21720$, $L_s = 20$ **(e)** $Re_2 = 54374$, $L_s = 20$ **(f)** $Re_3 = 86880$, $L_s = 20$

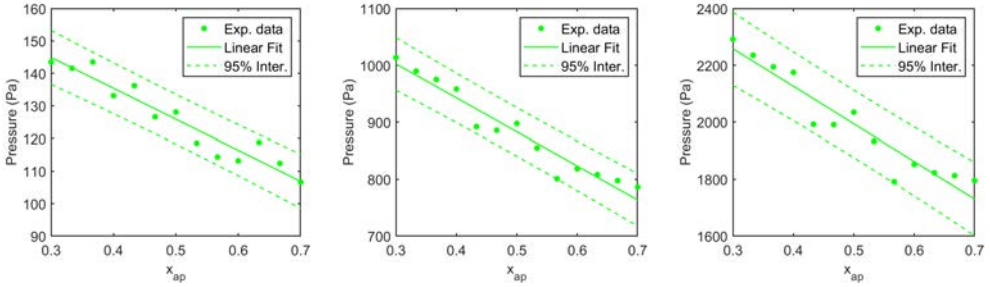

(g) $Re_1 = 21720$, $L_s = 10$ **(h)** $Re_2 = 54374$, $L_s = 10$ **(i)** $Re_3 = 86880$, $L_s = 10$

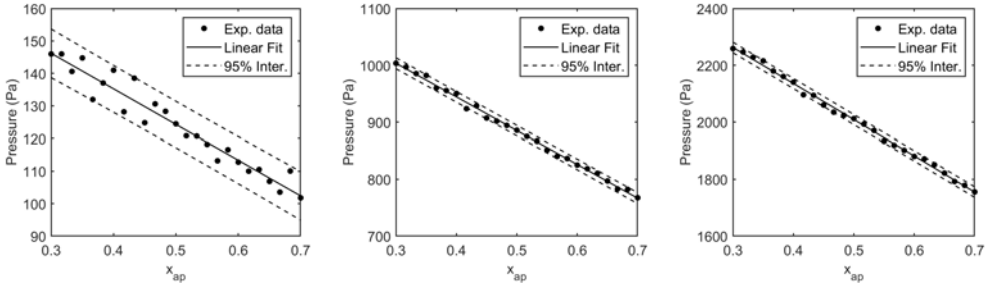

(j) $Re_1 = 21720$, $L_s = 5$ **(k)** $Re_2 = 54374$, $L_s = 5$ **(l)** $Re_3 = 86880$, $L_s = 5$

Figure 4.13 Pressure measurements for *Cylinder 2*: high swirl case ($\theta_s = 18°$). Experimental value (plain circles), linear fitting (continuous line) and confidence interval at 95% (dotted line).

Table 4.2 Error estimate table

Swirl angles	**Re**	**Tap distance (L_s)**			
θ_s (°)		40	20	10	5
		Estimate of standard error			
0	21720	±5.38%	±4.04%	±4.21%	±3.71%
	54374	±4.78%	±3.75%	±5.12%	±3.72%
	86880	±3.76%	±3.48%	±12.94%	±4.01%
4	21720	±5.32%	±4.08%	±4.16%	±3.63%
	54374	±4.47%	±3.87%	±6.01%	±3.70%
	86880	±2.84%	±3.76%	±17.88%	±3.99%
7	21720	±5.07%	±3.65%	±4.00%	±3.29%
	54374	±3.87%	±3.45%	±7.46%	±3.43%
	86880	±2.84%	±3.59%	±22.93%	±4.05%
10	21720	±4.75%	±3.61%	±3.85%	±3.52%
	54374	±3.61%	±3.49%	±8.40%	±3.65%
	86880	±2.57%	±3.67%	±25.84%	±4.25%
14	21720	±4.59%	±3.81%	±3.84%	±3.57%
	54374	±4.01%	±4.18%	±11.39%	±3.76%
	86880	±2.01%	±5.34%	±34.36%	±5.12%
18	21720	±4.14%	±4.03%	±3.94%	±3.63%
	54374	±3.89%	±6.22%	±21.95%	±4.67%
	86880	±8.60%	±9.80%	±61.06%	±9.02%

4.2 CFD simulations

The CFD simulations have been implemented in StarCCM+, following the methodology described in section 3.2. The flow has been assumed to be steady and incompressible for all the inflow conditions used for this test section (Table 3.5). The inlet boundary condition has been specified at the swirl generator hose, since the entire geometry of the swirl generator has been included in the computational domain, as described in section 3.2. A constant pressure boundary condition has been specified at the pipe outlet.

Mesh independence study The case with maximum swirl generator angle ($\theta_s = 18°$) and maximum inlet $Re_3 = 86880$ ($\dot{m} = 100g/s$) has been chosen as benchmark for the assessment of the mesh quality, since it represents the most challenging flow configuration with high velocity and pressure gradients.

Here, the mesh independence study carried out for this case is presented. A polyhedral mesh has been used for the entire domain up to the walls, where 10 prism layers have been used to apply the log-wall scaling (as described in subsection 3.2.1). The mesh independence has been assessed by comparing the results obtained on 4 different grids, which are referred to in the following text as *Grid 1*, *Grid 2*, *Grid 3* and *Grid 4* from the coarser to the finer respectively. The total number of cells is shown in Figure 4.14a for each grid.

The mesh independence of the results has been assessed by comparing the solution obtained for relevant quantities at various locations: velocity downstream the swirl generator (Figure 4.14b), swirl number downstream the swirl generator (Figure 4.14c), pressure at the outer pipe wall (Figure 4.14d).

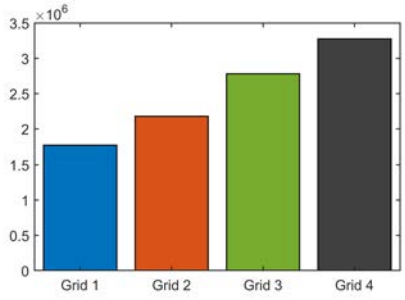

(a) Number of cells

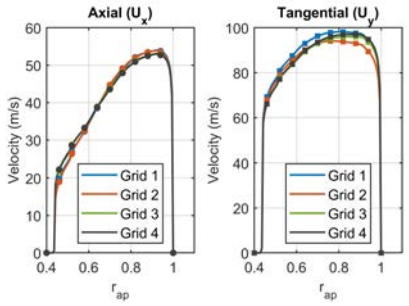

(b) Velocity at X = 0

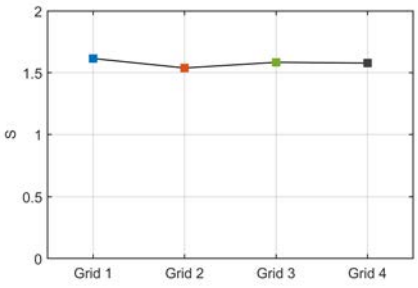

(c) Swirl number at X = 0

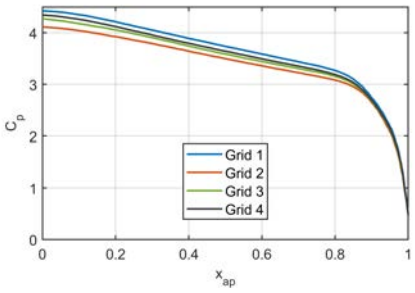

(d) Wall pressure

Figure 4.14 Comparison between the solution obtained with different grids: *Grid 1* (blue), *Grid 2* (red), *Grid 3* (green) and *Grid 4* (black). Total number of cells (a). Axial (dash-dot line, left) and tangential (dotted line, right) velocity components at the pipe inlet (b). Swirl number (c) and static pressure distribution at the outer pipe wall (d).

The difference between Grid 3 and Grid 4 is within 1% for the axial component and within 1.5% for the tangential component. The convergence of the swirl level can be seen from Figure 4.14c, with a difference between the solution obtained with the Grid

3 and Grid 4 of 0.4%. The convergence of the solution for the pressure at the wall is shown in Figure 4.14d and the difference between Grid 3 and Grid 4 is within 2%.

The convergence obtained is satisfying for the inflow condition analysed ($Re_3 = 86880$, $\theta_s = 18°$), therefore the meshing strategy used for Grid 3 has been applied to all the other inflow conditions, since a reduction of the number of cells of about 15% can be obtained compared to the Grid 4, with a consequent reduction of the computational cost of the simulation.

4.3 Results and analysis

The results of experiments and numerical simulation are presented and discussed in this section. The results are presented as follows:

1. flow velocity at the pipe inlet and outlet;
2. turbulence intensity at the inlet and the outlet;
3. static pressure at the outer wall (comparison between experiments and CFD);
4. comparison between the results from simulations with turbulence models.

4.3.1 Flow velocity at the inlet and outlet

The HWA measurements (velocity components, swirl number, turbulence intensity and energy spectra) at the two sections *Section 1* and *Section 2* (Figure 3.10) are used here to determine the changes in the flow due to changes in swirl and Reynolds number.

As has been discussed in subsection 4.1.1, the accuracy of the calculation of velocity components from HWA measurements is affected by the assumptions made about the flow direction and decomposition coefficients, however the results still allow to get an insight into the qualitative properties of the flow, and the effect of increasing swirl level and mass flow on the flow properties.

Because of the way the velocity components are calculated, the axial velocity component (U_x) is overestimated with increasing swirl generator angle, while the tangential velocity component is underestimated. However, the analysis presented here aims to investigate the effect of Reynolds number (Re) and Swirl number (S) on the velocity profiles.

Figure 4.15 shows axial and tangential velocity components at the annular pipe inlet for all mass flow rates and swirl levels. it can be seen for both velocity components

calculated in Section 1 (pipe inlet, IN), the profiles are similar for increasing Reynolds numbers. The same is true for both velocity components calculated at Section 2 (pipe inlet, OUT), which is at 5 mm downstream the pipe outlet, shown in Figure 4.16. Therefore, it can be concluded that the changes in the flow distribution are driven by the swirl level, rather than by the Reynolds number.

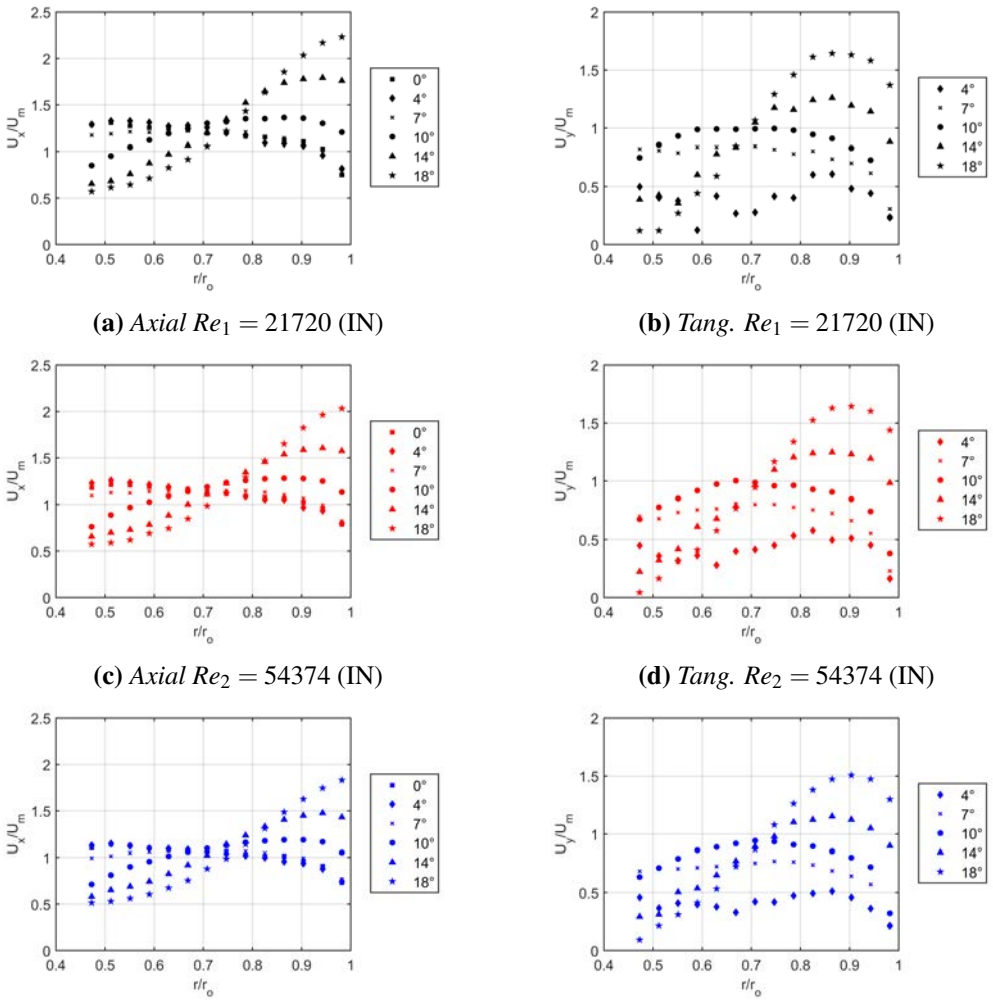

(a) *Axial* $Re_1 = 21720$ (IN)

(b) *Tang.* $Re_1 = 21720$ (IN)

(c) *Axial* $Re_2 = 54374$ (IN)

(d) *Tang.* $Re_2 = 54374$ (IN)

(e) *Axial* $Re_3 = 86880$ (IN)

(f) *Tang.* $Re_3 = 86880$ (IN)

Figure 4.15 Comparison between velocity components calculated at the pipe inlet. Axial component on the left (a,c,e), tangential component of the right (b,d,f). Re increasing from top to bottom: $Re_1 = 21720$ in black ($\bar{U} = 10.98$ m/s), $Re_2 = 54374$ in red ($\bar{U} = 27.66$ m/s), $Re_3 = 86880$ in blue ($\bar{U} = 43.91$ m/s). $\theta_s = 0°$ squares, $\theta_s = 4°$ diamonds, $\theta_s = 7°$ crosses, $\theta_s = 10°$ dots, $\theta_s = 14°$ triangles, $\theta_s = 18°$ stars.

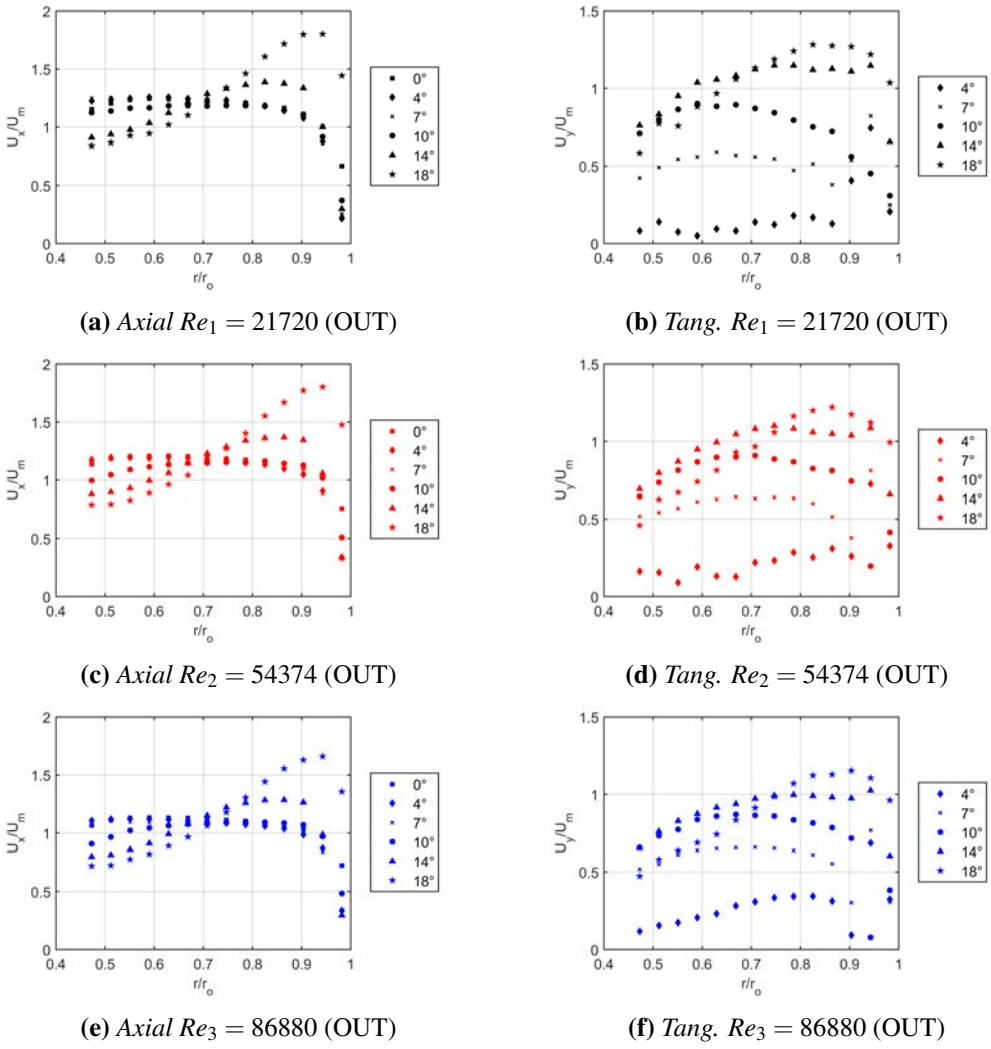

(a) *Axial* $Re_1 = 21720$ (OUT)

(b) *Tang.* $Re_1 = 21720$ (OUT)

(c) *Axial* $Re_2 = 54374$ (OUT)

(d) *Tang.* $Re_2 = 54374$ (OUT)

(e) *Axial* $Re_3 = 86880$ (OUT)

(f) *Tang.* $Re_3 = 86880$ (OUT)

Figure 4.16 Comparison between velocity components calculated at the pipe outlet. Axial component on the left (a,c,e), tangential component of the right (b,d,f). Re increasing from top to bottom: $Re_1 = 21720$ in black ($\bar{U} = 10.98$ m/s), $Re_2 = 54374$ in red ($\bar{U} = 27.66$ m/s), $Re_3 = 86880$ in blue ($\bar{U} = 43.91$ m/s). $\theta_s = 0°$ squares, $\theta_s = 4°$ diamonds, $\theta_s = 7°$ crosses, $\theta_s = 10°$ dots, $\theta_s = 14°$ triangles, $\theta_s = 18°$ stars.

By comparing the velocity components at the two sections, one can see a redistribution of the axial velocity between the two sections, with the maximum shifting towards the inner wall for all the cases. For $\theta_s = 4°$ and $\theta_s = 7°$ cases, the profile becomes more characteristic of a pipe flow without swirl, while the tangential velocity magnitude reduces considerably for all cases. This suggest that a swirl decay occurs between the two sections, in agreement with previous studies (e.g. (Clayton and Morsi, 1985)). The swirl level at both sections has been estimated using Equation 3.23. It can be seen from Figure 4.17 that the swirl level decay between Section 1 (pipe inlet) and Section 2 (pipe outlet) is more pronounced with the increasing swirl generator angle (θ_s), up to 20%. The same trend can be observed for all the Reynolds numbers.

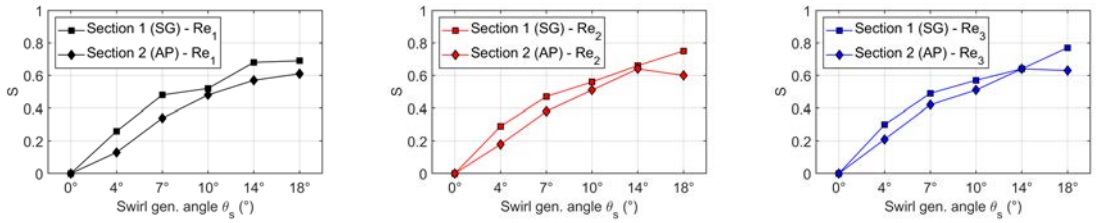

(a) $Re_1 = 21720$ **(b)** $Re_2 = 54374$ **(c)** $Re_3 = 86880$

Figure 4.17 Swirl level comparison between pipe inlet section (Section 1, Figure 3.10, squares) and pipe outlet section (Section 2, Figure 3.10, diamonds). Reynolds number increasing from left to right: $Re_1 = 21720$ in black (a), $Re_2 = 54374$ in red (b), $Re_3 = 86880$ in blue (c).

The classification of the swirling flows considered here is based on the criteria suggested by Gupta et al. (1984). The HWA data suggest that the case corresponding to $\theta_s = 4°, S = 0.28$ can be considered a *low* swirl case, since $S < 0.5$. The case corresponding to $\theta_s = 7°$ is considered as the threshold between low swirl and high swirl cases, since $S = 0.49$. The other 3 cases ($\theta_s = 10°, 14°, 18°$) correspond to *high* swirl. From the previous considerations, it has been concluded that the axial component is overestimated with increasing swirl, while the tangential component is underestimated. It can be, consequently, inferred that the swirl level is underestimated for the high swirl cases.

A comparison between the swirl level from the CFD simulations and the swirl level calculated by Rusli (2019) at the annular insert upstream the sudden expansion is given in Table 4.3. The velocity has been measured by Rusli (2019) using a more complex HWA technique (rotating cross-wire probe, briefly descried in subsection 5.1.2). The results shown in Table 4.3 show a reasonable agreement between the experiments and the simulations, with high swirl cases corresponding to swirl generator angles higher then $\theta_s = 7°$.

In general, the swirl level with $Re_1 = 21720$ is lower than that calculated for the other two Reynolds numbers (in both experiments and simulations), while for the two highest Reynolds numbers ($Re_2 = 54374$ and $Re_3 = 86880$) the swirl level calculated are similar. This trend is confirmed for the HWA data shown in Figure 4.16 and from the CFD and experimental data presented in Table 4.3.

Table 4.3 Inlet swirl level, comparison between CFD and experimental data for a confined flow downstream a similar swirl generator (Rusli, 2019) for each swirl generator angle considered (θ_s).

θ_s	Swirl number S					
	$Re_1 = 21720$		$Re_2 = 54374$		$Re_3 = 86880$	
	CFD	Exp. [a]	CFD	Exp. [a]	CFD	Exp. [a]
4°	0.23	0.25	0.25	0.27	0.25	0.23
7°	0.43	0.48	0.46	0.50	0.47	0.50
10°	0.66	0.68	0.69	0.71	0.70	0.70
14°	1.00	n.a.	1.03	n.a.	1.04	n.a.
18°	1.42	1.64	1.50	1.51	1.56	1.60

[a] From Rusli (2019) (confined flow in a sudden expansion)

4.3.2 Turbulence intensity

The turbulence intensity calculated from the HWA data at inlet and outlet cross-sections are presented here. Only the turbulence intensity profiles sampled with the probe in *normal* orientation are presented, which are representative of the axial component of the flow.

The turbulence intensity (T_i) at both sections (Figure 4.18) reflects the changes in the flow distribution observed with the velocity components. The changes are driven by the increasing swirl level, rather then by the Reynolds number.

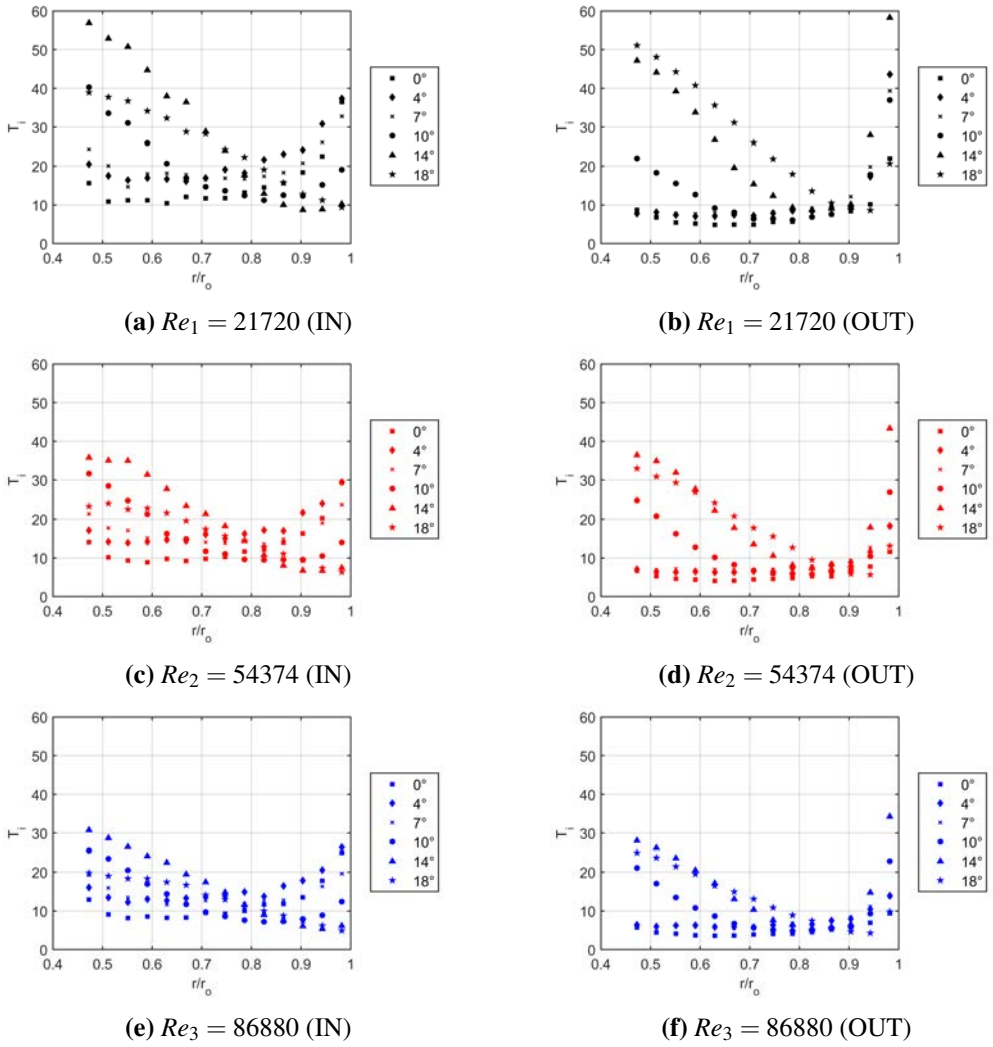

(a) $Re_1 = 21720$ (IN) **(b)** $Re_1 = 21720$ (OUT)

(c) $Re_2 = 54374$ (IN) **(d)** $Re_2 = 54374$ (OUT)

(e) $Re_3 = 86880$ (IN) **(f)** $Re_3 = 86880$ (OUT)

Figure 4.18 Comparison between turbulence intensity calculated at the pipe inlet (a,c,e), left column and at the pipe outlet, right column (b,d,f). Re increasing from top to bottom: $Re_1 = 21720$ in black ($\bar{U} = 10.98$ m/s), $Re_2 = 54374$ in red ($\bar{U} = 27.66$ m/s), $Re_3 = 86880$ in blue ($\bar{U} = 43.91$ m/s). $\theta_s = 0°$ squares, $\theta_s = 4°$ diamonds, $\theta_s = 7°$ crosses, $\theta_s = 10°$ dots, $\theta_s = 14°$ triangles, $\theta_s = 18°$ stars.

4.3.3 Pressure

The pressure distribution at the outer wall of the pipe is presented in this section. The experimental results (dots) are shown only for the *Cylinder 2* case, for the line with the tapping spacing of $L_s = 20$ mm, which offers more axial resolution of the data and it has been shown to have the results marginally affected by the neighbouring tappings compared to the spacing of $L_s = 40$ mm. The results from the experiments are compared with the CFD model for all the inflow conditions analysed (Figure 4.19). A pressure coefficient has been introduced, defined as

$$C_p = \frac{p}{p_{ref}} = \frac{p}{0.5\rho\bar{U}^2} \tag{4.7}$$

in which ρ is the air density, $\bar{U}$ is the mean velocity at the pipe cross section estimated from the continuity equation (used to calculate the reference pressure p_{ref}) and p is the local gauge pressure, calculated as difference between the *absolute* pressure p_{abs} and the *ambient* pressure p_{amb}. The reference pressure readings for the 3 Reynolds numbers, consequently is: $p_{ref_1} = 71.33$ Pa ($Re_1 = 21720$, $\bar{U} = 10.98$ m/s), $p_{ref_2} = 452.99$ Pa ($\bar{U} = 27.66$ m/s, $Re_2 = 54374$) and $p_{ref_3} = 1141.3$ Pa ($\bar{U} = 43.91$ m/s, $Re_3 = 86880$).

The experimental pressure for the lowest Reynolds number ($Re_1 = 21720$) are more scattered, especially for the swirl generator angles up to 10°. This effect is due to the low gauge pressure measured in those cases, which is close to the instrumentation resolution (as discussed in section 4.1.2). Pressure increases with the swirl level for all the cases (Figure 4.19), while a less pronounced effect of the Reynolds number can be seen for both experiments and CFD model.

The pressure exhibits a linear decay for low and moderate swirl (up to S = 0.5) regardless of the Reynolds number. The linear trend ends at $\approx 1.3 \cdot D_H$ upstream the pipe outlet (between $X = 260$ mm and $X = 300$ mm) for the high swirl levels ($S \geq 0.7$) where the proximity of the expansion at the outlet changes the flow and pressure distribution and become more significant with the increasing swirl.

It is possible to see from Figure 4.19 that the CFD is able to capture the pressure slope at the wall in the linear part of the decay (up to $\approx X = 260$ mm) for all the inflow conditions. Higher differences between the CFD model and the experiments can be seen towards the pipe outlet, where the effects of the boundary condition are highly affecting the flow (between $X = 260$ mm and $X = 300$ mm, $\approx 1.3 \cdot D_H$). This result confirms the findings from the numerical study of Xia et al. (1997) (described in section 3.2.3).

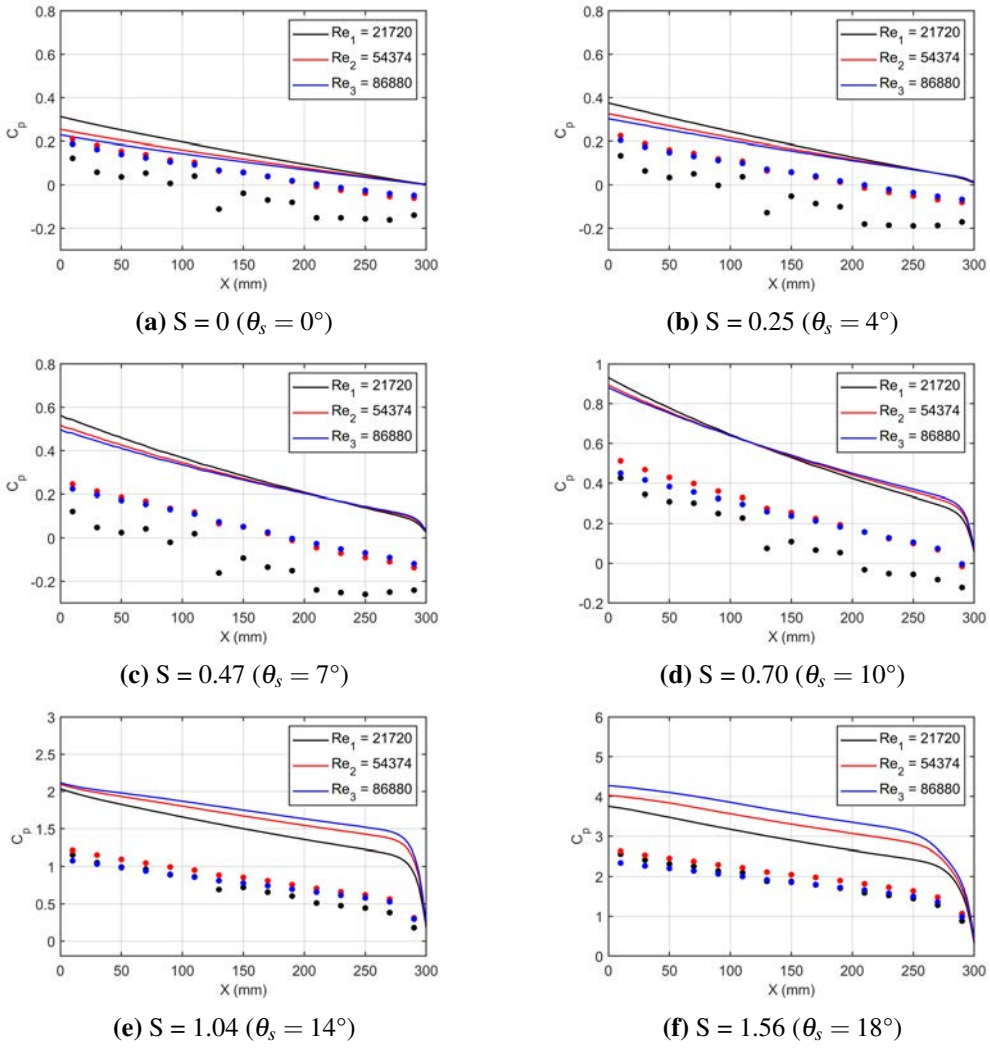

(a) S = 0 ($\theta_s = 0°$)

(b) S = 0.25 ($\theta_s = 4°$)

(c) S = 0.47 ($\theta_s = 7°$)

(d) S = 0.70 ($\theta_s = 10°$)

(e) S = 1.04 ($\theta_s = 14°$)

(f) S = 1.56 ($\theta_s = 18°$)

Figure 4.19 Pressure coefficient at the outer wall. Dots: experimental results (*Cylinder 2*, $L_s = 20$ mm). Lines: CFD model results. Swirl level increasing from a to f. $Re_1 = 21720$ in black ($\bar{U} = 10.98$ m/s, $p_{ref} = 71.33$ Pa), $Re_2 = 54374$ in red ($\bar{U} = 27.66$ m/s, $p_{ref} = 452.99$ Pa), $Re_3 = 86880$ in blue ($\bar{U} = 43.91$ m/s, $p_{ref} = 1141.3$ Pa).

4.3.4 Turbulence model comparison

A comparison between the performance of the six turbulence models presented in subsection 3.2.4 has been made for the inflow condition corresponding to the maximum swirl level ($\theta_s = 18°$) and intermediate Reynolds number ($Re_2 = 54374$).

The comparison between the velocity components at the pipe inlet is shown in Figure 4.20. Please note that the experiments have been carried out without the pipe attached, therefore the flow at the section is not confined, as discussed in the above sections. The increase in the axial velocity component towards the outer wall (r/r_o) observed in experiments (Figure 4.15c) is captured by all the models. It is difficult, however to evaluate which model is performing better. It can be observed that the none

of the models can capture the velocity gradient observed in experiments (Figure 4.15c). Similarities can be seen between the $k-\omega$ and the RST models, which exhibit a similar slope of the axial velocity. The $\bar{v}^2-f$ model preserves only partially that slope, while the two $k-\varepsilon$ models predict a smoother velocity profile. On the other hand, the $\bar{v}^2-f$ model presents a smoother gradient for the tangential velocity component, compared to the two $k-\varepsilon$ models. However, it is not possible to affirm which model performs better for the velocity prediction.

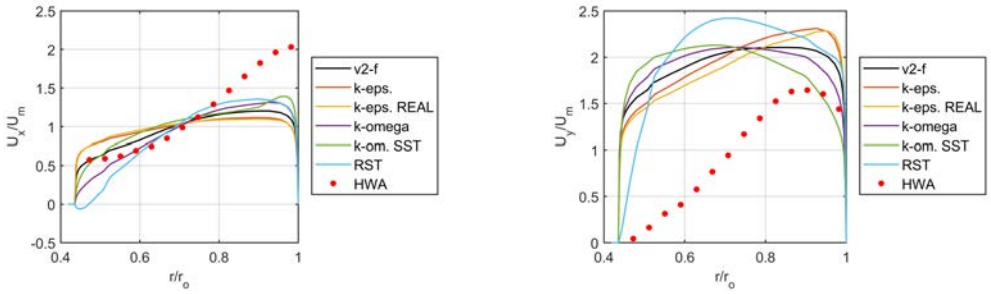

(a) Axial U_x **(b)** Tangential U_y

Figure 4.20 Velocity components from the CFD. Comparison of RANS models for the maximum swirl case ($\theta_s = 18°$) and intermediate Reynolds number ($Re_2 = 54374$). Axial velocity component on the left (a), tangential velocity component on the right (b). Both velocities have been normalise with $U_m = 27.66$ m/s

The comparison between the swirl level calculated with the 6 RANS turbulence models is presented in Table 4.4. It can been seen that with the $k-\omega$ models the swirl level is under-predicted, as expected from the comparison between the velocity components. While a more comprehensive study would be needed to establish which RANS turbulence model performs better overall in swirling flow simulations, these results indicate that k-epsilon models appear to produce mean flow velocity results close to the available experimental data in the considered configuration.

Table 4.4 Inlet swirl level calculated from CFD for each turbulence model. The reference experimental value for a similar configuration is 1.51 (Rusli (2019)).

Turbulence model	Swirl number S
$\bar{v}^2 f$	1.50
$k-\varepsilon$	1.57
Realizable $k-\varepsilon$	1.52
$k-\omega$	1.41
$k-\omega$ SST	1.42
RST	1.47

The turbulence intensity has been calculated at the pipe inlet, by using

$$T_i(\%) = \frac{u^{'}}{\bar{U}} \cdot 100 \tag{4.8}$$

where $u^{'}$ is the velocity fluctuation and $\bar{U}$ is the mean velocity at the section. The velocity fluctuation is available only with the RST, for which the Reynolds stress is calculated explicitly. For the other models, the velocity fluctuation has been extracted from the turbulent kinetic energy (k), under the assumption of isotropic turbulence

$$u^{'} = \sqrt{\frac{2}{3}k} \tag{4.9}$$

The results from the different models have been compared in Figure 4.21 with the turbulence intensity from the HWA measurements (dots).

As expected from previous studies (subsection 2.2.2), the RST model gives a better prediction of the turbulence decay towards the outer wall, compared to the other 5 models. The $\bar{v}^2 - f$ and the $k-\varepsilon$ models retain the change in the slope near the inner wall obtained with the RST. It is interesting to see that this agreement is good only near the inner wall, which can be attributed to the low y+ formulation for the boundary layer.

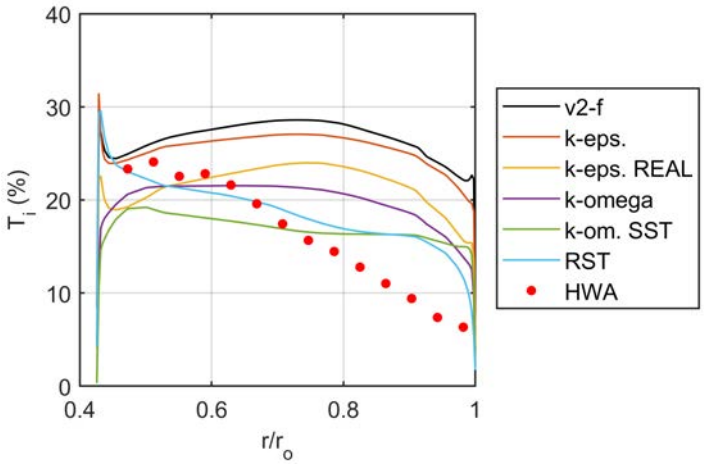

Figure 4.21 Turbulence intensity at the annular pipe inlet. Comparison of RANS models for the maximum swirl case ($\theta_s = 18°$) and intermediate Reynolds number ($Re_2 = 54374$).

The pressure coefficient calculated from the CFD simulations and experiments at the outer wall (Equation 4.7) is shown in Figure 4.22. It is possible to see that the slope of the pressure decay is well captured by the RST and the $v^2 f$ model.

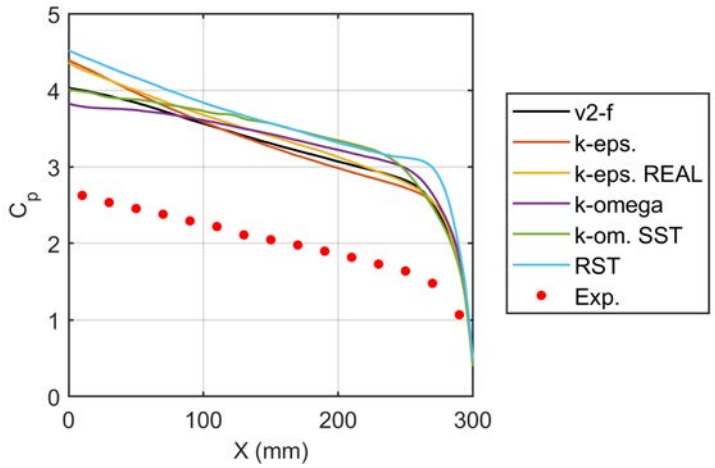

Figure 4.22 Wall pressure coefficient at the outer wall from the CFD. Comparison of RANS models for the maximum swirl case ($\theta_s = 18°$) and intermediate Reynolds number ($Re_2 = 54374$).

In conclusion, it is possible to say that, in agreement with previous studies (subsection 2.2.2), all the RANS models considered here present inaccuracies when applied to high swirl flow modelling. The RST model can improve the prediction in terms of turbulence, as expected, but does not exhibit a significant improvement over the first order quantities, such as velocity and pressure. The $\bar{v}^2 - f$ model exhibit a general better behaviour then the other two equation models considered here ($k - \varepsilon$, Realizable $k - \varepsilon$, $k - \omega$ and $k - \omega$ SST), preserving a low computational requirement.

It was expected that the RST model would perform best because of the improved prediction of the turbulence anisotropy. However, the RSM model causes a much higher computational cost. For the larger geometry of the diffuser with a sudden expansion, as already mentioned in subsection 3.2.4, the $\overline{v}^2 - f$ model has been preferred, to reduce the computational cost of the simulations. In addition, it has been proven in literature (Iaccarino et al. (2003); Porter et al. (2014); Salehi et al. (2017)) that the $\overline{v}^2 - f$ model provides good results in presence of flow separation.

4.4 Chapter summary

The experimental and numerical analysis carried out on the pipe with annular cross section has been presented in this chapter for 3 inflow Reynolds numbers ($Re_1 = 21720$, $Re_2 = 54374$ and $Re_3 = 86880$) and 6 swirl levels ($\theta_s = 0°, 4°, 7°, 10°, 14°, 18°$), aiming to identify the relative importance of Reynolds number and swirl level on the flow structure.

The methodology of obtaining and post processing experimental data has been presented in section 4.1, aiming to demonstrate the advantages and disadvantages of the experimental techniques used (HWA and static pressure measurements).

The limitations of the single wire probe measurements used to estimate the velocity components for high swirling flows have been highlighted. It has been shown that although the hot wire measurements can be used to get a qualitative picture of the confined swirling flows, the limitations associated with the accuracy of the measurements when the flow direction is not known a priori need to be considered. Despite these limitations are particularly important for high swirling flows, the method can be still applied to gather general information about the mean velocity and the turbulence.

The importance of choosing the sampling frequency for the measurements to resolve the quantities of interest has been demonstrated, showing that the effect on the mean velocity is not meaningful for the 3 frequencies considered, but the impact on the instantaneous fluctuations can be high. Under-prediction of the turbulence intensity up to 50% has been observed with the lower sampling frequency used (200 Hz), while a good agreement (within 1%) has been found for the higher frequencies of 600 Hz and 1000 Hz. The frequency analysis shows that the dominant frequency of the measured signal do not change with the two highest sampling frequencies. A frequency study has been presented, aiming to highlight the differences shown in the turbulence intensity profiles sampled with 3 sampling frequencies. The upstream frequencies due to air compressor fluctuation, vortex shedding through the swirl generator blocks and resonance frequency of the swirl generator have been analysed and discussed. It has been shown that the range

of frequencies associated with the flows considered in the current studies is between 100 Hz and 500 Hz and that with reasonable approximation, the energy associated with the flow is within 300 Hz, since the turbulence intensity is not changing between the sampling frequencies of 600 Hz and 1000 Hz. Although this requires further analysis, which goes beyond the objectives of the current study, the results can be used for the validation of complex modelling validation, such as LES or DES and setting up inflow turbulence properties. Additional data, such as the energy spectra have been therefore extracted and included in Appendix E.

The effects of the pressure tappings geometry on the accuracy of the measurements for increasing swirl level have been studied, identifying that with a hole depth which is 6 times the hole diameter it is possible to reduce the standard error of the mean. This is consistent with a similar study carried out by McKeon and Smits (2002) for a purely axial flow. This conclusion is important as it shows that the guidelines established for pressure measurements in unidirectional flows also hold for highly swirling confined flows, which are generally much more sensitive to flow disturbances and intrusive measurements. The effects of the distance between the pressure tappings have been analysed using a linear regression analysis, suggesting that the effect of the distance can alter the pressure distribution and lead to inaccurate predictions of the pressure law. It has been shown that the distance between tappings up to 20 mm did not affect the accuracy of the pressure measurements considerably. However, for distances of 10 and 5 mm, the measured wall pressure distribution featured periodic fluctuations in the axial direction, which suggests that the pressure tappings are affected by their upstream neighbours, which may produce vortex shedding or other boundary layer disturbances affecting the flow and pressure distribution in the vicinity.

The main objective of the experimental and CFD analysis presented in this chapter was to identify the relative importance of Reynolds number and swirl level on the flow structure. The results have demonstrated that the velocity distribution along the radius at both inlet and outlet of the pipe is strongly dependent on the swirl level, while the effect of of the Reynolds number on the flow is weak. For high swirl levels, the axial velocity profiles feature maxima near the outer wall of the pipe because of the centrifugal "force" and strong radial pressure gradients characteristic of the swirling flows. However, the axial velocity profile becomes more flat downstream with the maximum shifting towards the inner wall. At the same time, the azimuthal (swirl) velocity decays considerably between the inlet and outlet section. Similar results have been identified for the turbulence intensity distribution and the static wall pressure. Calculated swirl numbers at the inlet and outlet sections show swirl decay, in agreement with studies published in literature.

Overall, the experimental data provides characterisation of the swirl level, velocity distribution and turbulence properties at the pipe inlet, which will be useful for the studies in the following chapters. The wall pressure and outlet velocity measurements provided an extra insight into the properties of a swirling flow in an annular pipe, and can be used for validation of numerical models.

A numerical study of swirling flow in the same configuration has been carried out to assess different RANS models to be used in the more complex configurations considered in the following chapters. It has been shown that overall all turbulence models, including the Reynolds Stress model, are not very good at predicting the axial flow redistribution at high swirl levels where the velocities are higher near the wall due to the high radial pressure gradients. The RST and $\bar{v}^2 - f$ models were slightly better than the other 4 considered models. The RST model has been shown to perform better at predicting turbulence distribution along the pipe radius.

A reasonable prediction of the wall pressure decay in the axial direction has been observed with the $\bar{v}^2 - f$ turbulence model for all the cases analysed. The effects of the outlet boundary condition on the pressure distribution have been identified up to $\approx 1.3D_H$ upstream the outlet, in accordance with results published in literature. Overall, the $\bar{v}^2 - f$ model appears to be a reasonable choice amongst the RANS models considered in predicting the mean flow and the deficiencies in the turbulence level predictions when compared to the RST are offset by lower demands of the computational resources. Therefore, the $\bar{v}^2 - f$ model will be used for studies of symmetric and asymmetric flows in the sudden expansion geometries considered in Chapter 5 and Chapter 6.

Chapter 5

Swirling flow in a sudden expansion with downstream resistance

This chapter presents the analysis of the swirling flow inside the axisymmetric sudden expansion with downstream resistance. The aim of the study is not only the assessment of the numerical model capabilities, but also the analysis of the evolution of the flow structures with increasing swirl, combining experimental data and CFD results.

The chapter consists of three main sections: *Experiments*, *CFD simulations* and *Flow analysis*. The first section presents the experimental data used for the numerical model validation. The second section presents a review of some modelling choices made for this configuration, including the effect of the mesh topology on the model accuracy in the porous region and selection of numerical schemes.

The third section includes the analysis of both experimental and numerical results. The CFD model is used to support and interpret experimental results obtained from PIV, HWA and pressure measurements, and to provide an insight into the flow physics and the changes in the flow features with increasing swirl levels.

The results presented here constitute a baseline for the following Chapter 6, in which the effects of the asymmetry are presented.

5.1 Experiments

The experimental data used to assess the numerical model performance and gain more insight into the flow features have been collected using different techniques. The analysis of the flow structures inside the sudden expansion has been conducted using PIV, following the methodology presented in Chapter 3. The HWA data and the static pressure data have been collected in a previous study by Rusli (2019) on a similar configuration.

A schematic representation of the experimental assembly, not to scale, is shown in Figure 5.1, to show the location of the flow measurements. The PIV data have been collected in the section highlighted in green, which includes the entire glass diffuser assembly (expansion inlet (3) and sudden expansion (4) in Figure 5.1). The HWA data were sampled in two different sections (red dotted lines in Figure 5.1): 77.5 mm upstream the diffuser expansion (HWA (a) section) and 30 mm downstream the ceramic monolith (HWA (b) section). The static pressure was sampled at the wall of both expansion inlet (3) and at sudden expansion (4), identified by the blue lines in Figure 5.1. A total of 4 azimuthal lines, Figure 5.1 (b), has been used, identified as *North* (N), *East* (E), *South* (S) and *West* W. More details about each measuring technique are given in the next paragraphs.

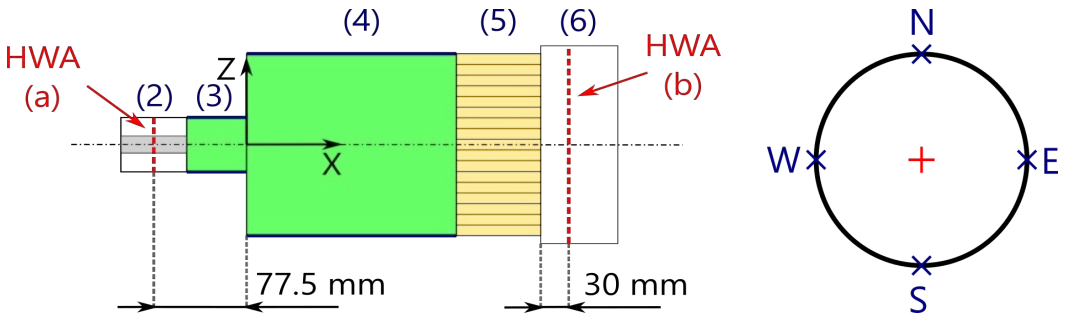

(a) Side view **(b)** Expansion section

Figure 5.1 Axisymmetric diffuser: location of experimental data used for model assessment. Left scheme (a): PIV sampling plane (green) at the sudden expansion (4); HWA measuring sections (red): HWA (a) at the annular pipe insert (2) and HWA (b) at the outlet sleeve (6); pressure measurement lines (blue) at expansion wall (3-4). Right scheme: pressure measurement lines topology, *North* (N), *East* (E), *South* (S) and *West* (W)

5.1.1 PIV measurements

The PIV data have been collected and post-processed using the methodology presented in subsection 3.1.4. The convergence analysis is presented in this section.

Data near the walls and close to the monolith entrance have been discarded, due to lower fidelity of the data in those areas. The final sampling area is shown in green in Figure 5.2, in which the distance of the sampling area from the boundaries is reported.

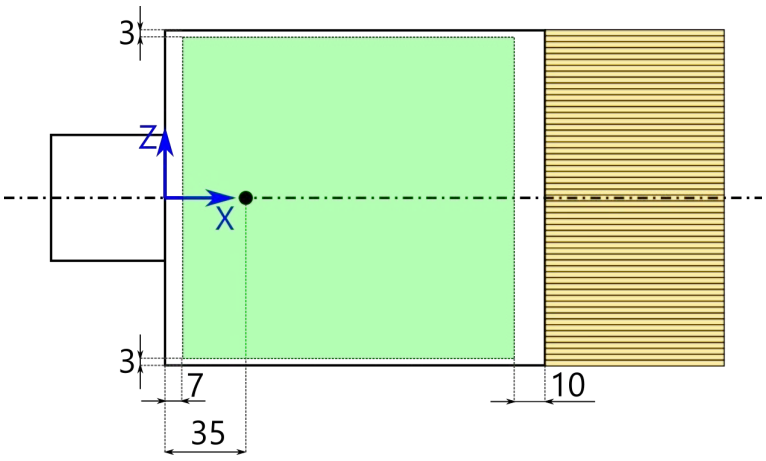

Figure 5.2 Location of the PIV data inside the sudden expansion for the symmetric case (green area). Black dot represents the sampling point used for the convergence study. Dimensions in mm.

PIV convergence

In order to ensure that sufficient number of frames has been used to accurately calculate mean flow velocity, a convergence study has been performed. For that, the flow velocity has been calculated at one reference point inside the domain (black dot in Figure 5.2) using an increasing number of frames.

The results of the convergence study applied to the maximum swirl level (corresponding to $\theta_s = 18°$) for the non-symmetric case are shown in Figure 5.3. This case is presented as an example to clarify the methodology presented in section 3.1.4. The analysis has been applied to all the inflow conditions. The minimum number of samples required for the convergence of the PIV data in the three locations (black dots in Figure 5.2) has been extracted for all the inflow conditions and it is summarised in Table 5.1.

The local mean velocity (blue line) and the relative error ε_{PIV} (red line) are shown in the top sub-plot, while $\partial\varepsilon_{piv_N}$ is shown in the bottom sub-plot for each case (black line, light blue rectangle is used to visualise the accepted deviation). The analysis carried out on the U component (in the X direction) is shown on the left column (Figure 5.3a), while the results for the V component (in the Z direction) are shown on the right column (Figure 5.2b). The convergence has been satisfactory when the asymptotic behaviour of velocity and error has been achieved, verifying that $|\partial\varepsilon_{piv_N}| < 0.05$ (as discussed in section 3.1.4). The minimum number of images has been extracted for each case, as shown in Figure 5.3, in which the convergence criterion is represented by the light blue band.

From Table 5.1 it can be seen that the total of 1000 pairs of images acquired is sufficient to obtain a meaningful representation of the average flow field (based on the discussion presented in subsection 3.1.4).

Table 5.1 Minimum number of PIV sampling images required for the axisymmetric diffuser with sudden expansion.

	Minimum number of samples	
	Point 1	
θ_s	(U)	(V)
0°	258	182
4°	630	708
7°	656	728
10°	736	309
18°	457	309

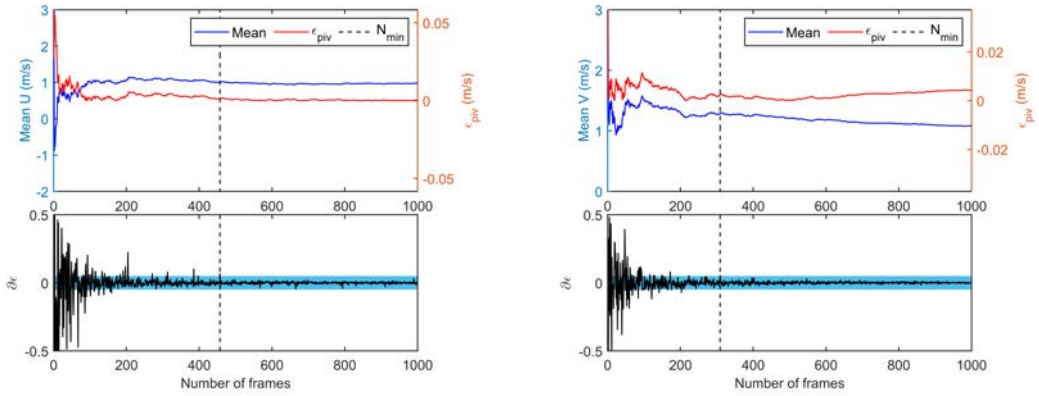

(a) Point 1 @ (35,0) mm - U

(b) Point 1 @ (35,0) mm - V

Figure 5.3 PIV convergence study: $\theta_s = 18°$, axisymmetric case (D = 0 mm). U component (X direction) on the left (a) and V component (Z direction) on the right (b).

Target deformation

As discussed in subsection 3.1.4, the accuracy of the results is also affected by the image deformation due to the camera lens curvature, light refraction from the test section, light path distortion due to materials reflections and curvature of the test section. The deformation of the images acquired has been evaluated using the procedure presented in section 3.1.4. The resulting map is shown in Figure 5.4.

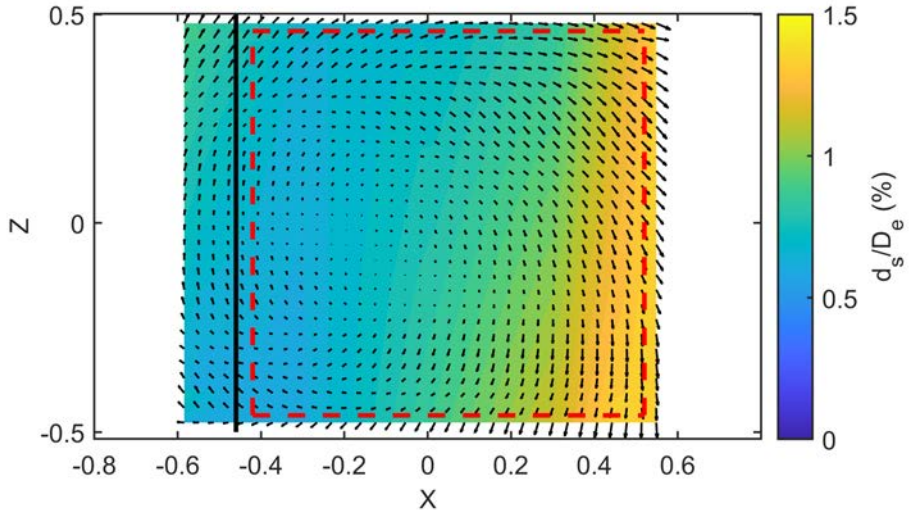

Figure 5.4 Distortion map for the axisymmetric case. Vectors represent the direction of the displacement (d_s) of the chequered board corners (used for the calibration target target) between the synthetic image and the real image (please refer to section 3.1.4 for more details). The contour map shows the displacement magnitude in percentage of the expansion diameter (D_e). Black line represents the catalyst position, red dotted rectangle indicates the final sampling area used for data analysis

Figure 5.4 shows that the effect of the distortion is higher towards the walls of the domain (edges of the map). This is expected, since the main sources of the distortion are the wall curvature and the camera lens, and both effects become more important towards the edges of the domain of interest. The maximum displacement (d_s) between the squares in the synthetic image and the squares in the real target is $\approx 1.2\%$ of the expansion diameter (D_e).

The sampled area (Figure 5.2) is the one enclosed by the red dashed line in Figure 5.4, where the average deformation is $\approx 0.5\%$ (≈ 0.7 mm). This deformation has been considered small for the purpose of the current study, so no algorithm has been applied for the data correction in the pre-processing.

5.1.2 HWA measurements

The HWA data have been collected by Rusli (2019) using different methods for the two sections. A brief review of the methodology used to collect those data is presented in this section, while a more detailed description of the techniques used can be found in Rusli (2019). A schematic representation of the position of the HWA sampling points is shown in Figure 5.5, for both the upstream section HWA (a) and the downstream section HWA (b) from Figure 5.1.

The velocity measurements at the annular pipe insert were made using a TSI 1247A X-probe, at 3 different lines at 120° along the circumference located 25 mm upstream the

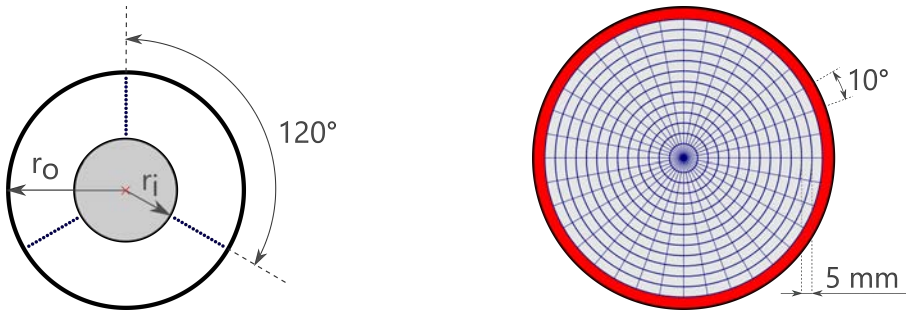

(a) Annular insert **(b)** Outlet sleeve

Figure 5.5 Positions of the HWA measurements. Locations of the cross-wire probe, blue dots, at the annular pipe insert (a). Locations of the single-wire probe at the outlet sleeve (b), measuring points at the intersection between blue lines and circumferences

sudden expansion inlet. The probe was traversed along each line every 1 mm between the outer and inner radii of the cross-section, blue dots in Figure 5.5 (a). The flow direction was estimated by rotating the probe in each point every 4°, using a rotating step-motor. The HWA data sampled in the annular pipe insert (HWA (a) section) have been used to calculate the swirl level of the flow entering the pipe. Different techniques have been applied to calculate the swirl level, resulting in considerable differences between the values, as reported in (Rusli, 2019).

The measurements downstream the monolith section have been made using a single-wire Dantec 55P11 probe, since the flow was assumed to be uni-directional. The probe was positioned at 30 mm downstream the monolith, in order to achieve a sufficient mixing between the single jets exiting the monolith channels, as reported in the study of Clarkson (1995). The measuring probe was inside the outlet sleeve, which provided shielding to the flow, as reported by Skusiewicz (2012).

The measuring points were located at the intersection between the blue circumferences and the blue lines in Figure 5.5 (b). A total of 504 locations was obtained, by varying the probe position every 5 mm radially and every 10° azimuthally. No measurements were made in the red area shown in Figure 5.5 (b), with the closest position of the probe at about 6 mm from the outlet sleeve wall.

A comparison between the CFD results and the velocity measurements downstream the monolith is used in the following section to evaluate the effects of the increasing swirl level. The uniformity index has been calculated for both CFD and experimental data, according to the methodology presented in section 3.3.

5.1.3 Static pressure measurements

The static pressure measurements were made using pressure tappings at the wall, along the directions shown in Figure 5.1 (a), blue lines. The 4 lines of pressure tappings were distributed azimuthally every 90°, identified as *North* (N), *East* (E), *South* (S) and *West* (W), as shown in Figure 5.1 (b). The measuring points for each line were distributed in the axial direction, increasing the number of pressure tappings closer to the sections at which higher gradients were expected, that is close to the sudden expansion and to the monolith entrance.

A total of 31 pressure tappings was used, with the distance between them varying from 1 mm to 20 mm. The pressure was sampled using two *Scanivalve ZOC 33* (Scanivalve, 2016) pressure scanners with different accuracy, described in Chapter 3. The pressure scanner with larger range (with accuracy rated at ±30 Pa) was used at the expansion inlet and near the monolith entrance), while the one with higher accuracy (rated at ±7.5 Pa) was used at the remaining points. The measurements were made with a frequency of 15 Hz and a total of 2000 samples was acquired for each location. The average gauge pressure measured at each location has been used in the current study.

5.1.4 Non-dimensional parameters

The results presented in the following sections have been normalised using the same reference values for both experimental data and CFD results, in order to facilitate the comparison.

The velocity data downstream the monolith have been normalized using the mean velocity at the outlet section $\bar{U} = 3.22$ m/s, which has been calculated for the mass flow rate $\dot{m} = 63$ g/s from the continuity equation

$$\dot{m} = \rho \bar{U} A \tag{5.1}$$

where ρ is the air density and A the area of the outlet section.

A pressure coefficient has been introduced to present the pressure distribution at the sudden expansion wall, defined as

$$C_p = \frac{p}{0.5\rho\bar{U}^2} \tag{5.2}$$

in which ρ is the air density, $\bar{U} = 27.66$ m/s is the mean velocity at the annular pipe insert estimated from Equation 5.1 and p is the local gauge pressure, calculated as difference between the *absolute* pressure p_{abs} and the *ambient* pressure p_{amb}

$$p = p_{abs} - p_{amb} \tag{5.3}$$

The local gauge pressure p has been directly measured in the experiments, since the pressure scanner has been calibrated with the ambient pressure p_{amb} prior to the data acquisition, while in the CFD simulations the ambient pressure has been set to 101325.0 Pa, as reported in Chapter 3.

5.2 CFD simulations

The dimensions of the experimental apparatus have been reproduced in the CFD model, within 1%. The methodology used to implement the numerical model has been presented in Chapter 3. Here, a review of the effects of some modelling choices is presented, together with the results of the mesh independence study carried out for the final model. A preliminary assessment of some modelling choices has been made using the 45° wedge domain shown in Figure 5.6, described in Chapter 3. The differences with the full 3D case will be highlighted where necessary.

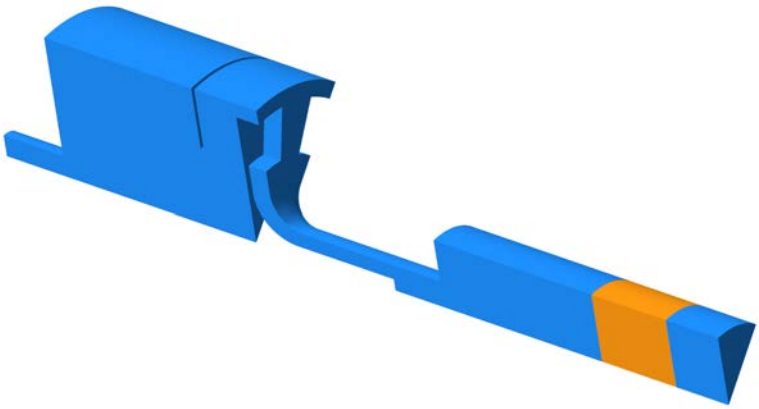

Figure 5.6 Axisymmetric diffuser - CFD model: 45° wedge geometry. *Fluid* regions (swirl generator, sudden expansion and outlet sleeve), light blue; porous medium region, orange.

5.2.1 Porous medium modelling

The impact of the mesh topology inside the porous medium has been studied on the 45° wedge domain. The porous medium region, orange in Figure 5.6, has been modelled using 3 different volume meshing approaches: a *polyhedral* mesh, an *extruded* mesh and a *trimmed* mesh. The same polyhedral mesh has been used for the regions upstream and downstream. A total of 5 different cases is presented here, depending on the mesh type used. The number of cells inside the porous region and the pressure drop through the porous region ($\Delta p_{PM}(Pa)$) are summarised in Table 5.2.

The extrusion of the sudden expansion layer face has been made using different parameters, aiming to control the number of layers, their size and their distribution inside the region (CD-Adapco, 2018). The values used for this comparison are reported in Table 5.2 and correspond to cases from 1 to 3. The mesh obtained for *Case 1* consisted of 18 layers of equal dimension in the flow direction (X), since the stretching factor was kept to 1. The effect of the stretching factor has been accounted by comparing *Case 1* and *Case 2*. It is possible to notice that the number of cells inside the region has been kept constant for the two cases, since the change in the stretching factor consists only in a change of the size of the layers in the axial direction (increasing towards the outlet of the domain). The third mesh tested, *Case 3* had a number of layers doubled, compared to the previous two. By keeping a stretching factor of 4, as in *Case 2*, it has been possible to obtain a first layer half the size of the previous one. As a result, the surface distribution at the two interfaces is not changing with the extrusion parameters.

The *trimmed* mesh generated in *Case 4* consisted of predominantly hexahedral cells, resulting in a structured mesh inside the porous medium, with a coarser size inside the core of the porous region and an almost symmetrical distribution between the entrance and the exit of the region.

The last mesh considered here, *Case 5*, consisted of polyhedral cells inside the porous region, with the same size distribution applied to the upstream and downstream regions. It is worth noticing that the highest number of cells has been obtained with the polyhedral cell, with a number that is almost 5 times larger then the first two extruded meshes, and three times larger than the trimmed mesh.

The comparison between the results obtained with the 5 cases has been carried out using as inflow condition the straight flow case ($\theta_s = 0°$), fixing the sampling plane position for the entrance effects at 4 mm upstream the monolith section for all the cases. Please note that the position of the sampling plane for this comparison is not crucial, since the investigation is focused on the mesh topology inside the porous region.

From Table 5.2 it is possible to notice that the pressure drop across the porous region Δp_{PM} is comparable for the first 4 cases, while there is a reduction of it for the polyhedral mesh. In other words, as a result of the mesh topology, the porous medium region exhibit a lower resistance in *Case 5*. This aspect has been further investigated by comparing local flow properties downstream and upstream the porous region.

Table 5.2 Meshing strategies inside the porous region

Case #	Mesh type	Layers	Stretching factor	Number of cells	$\Delta p_{PM}(Pa)$
1	Extruded	18	1	29196	2.91×10^2
2	Extruded	18	4	29196	2.87×10^2
3	Extruded	36	4	58392	2.89×10^2
4	Trimmed	-	-	37134	2.93×10^2
5	Polyhedral	-	-	106303	2.74×10^2

A comparison between the outlet velocity profile at 30 mm downstream the porous region (a) and the static pressure at the diffuser wall (b) is shown in Figure 5.7. It is possible to notice that there are no significant changes in the prediction of the outlet velocity profile with all the different extruded meshes (Cases 1 to 3) and a good agreement is shown with the trimmed mesh (Case 4). A different velocity profile has been obtained with the polyhedral mesh (Case 5), for which a smoother velocity towards the axis can be observed and a general reduction of the local maxima compared to the other cases. By comparing the static pressure at the diffuser wall, Figure 5.7 (b), it is possible to see a similar trend. A good agreement can be seen for the extruded mesh cases and the trimmed mesh, while the pressure line, although exhibiting a similar profile, is lower for the polyhedral mesh (Case 5). This result is in agreement with the smaller pressure drop through the porous region.

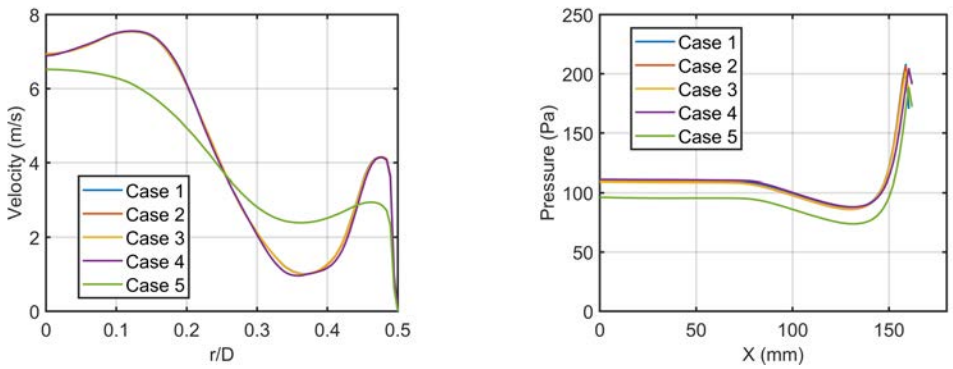

(a) Outlet velocity **(b)** Static pressure

Figure 5.7 CFD model: 45 deg wedge, axial flow. Comparison between the porous medium region meshing strategies. Cases from 1 to 3 correspond to an *extruded* mesh, Case 4 to a *trimmed* mesh and Case 5 to a *polyhedral* mesh, more details in Table 5.2. Velocity downstream the monolith (a) and static pressure at the sudden expansion wall (b)

A comparison between the velocity magnitude, the turbulent viscosity ratio and the turbulent dissipation rate at the entrance of the porous medium is shown in Figure 5.8. Only the results obtained with the extruded mesh corresponding to Case 1 have been included here, since no significant differences between the results obtained with the other two extruded mesh have been observed. A comparison between the velocity sampled at the first layer is shown in Figure 5.8 (a-c). It is possible to see that the same flow features are captured inside the extruded (a) and the trimmed (b) mesh, while the velocity distribution inside the polyhedral (c) mesh is different. Figure 5.8 suggests that the change in the flow properties has not been driven by the size of the cells inside the region, neither by their distribution. Consequently, the difference with Case 5 can be attributed to the first layer of cells inside the porous region.

It is interesting to observe that the change in velocity is reflected in a change of the turbulent quantities. In particular, the contour plots of the turbulent viscosity ratio are similar for the extruded and trimmed mesh, Figure 5.8 (d-e), while a reduction can be observed with the polyhedral mesh Figure 5.8 (f). The contour plots of the turbulent dissipation rate help to identify the change in the middle section of the flow velocity: the higher dissipation observed towards the centre of the section in the polyhedral mesh, Figure 5.8 (i), can explain why the velocity profile seen in Figure 5.7 is smoother towards the axis, compared to the other cases, in which a local minimum is observed.

In conclusion, the differences between the polyhedral mesh and the other meshes, can be attributed to the calculation of the velocity fluxes at the cell surfaces. The inclination of the surface faces with the polyhedral mesh enhances a flow diffusion towards the adjacent cells, which can be seen as an artefact of the numerical model. The results are in agreement with the results by Porter (2016). In addition, the *extruded* mesh type allows a conformal match at the interface between the sudden expansion region and the porous region, section 3.2.3. This means that the two adjacent boundaries have a perfect match between the vertex locations and the face topologies, resulting in a high quality discretization for the analysis (CD-Adapco, 2018). For the above reasons, an extruded mesh type inside the porous region has been preferred for the final model.

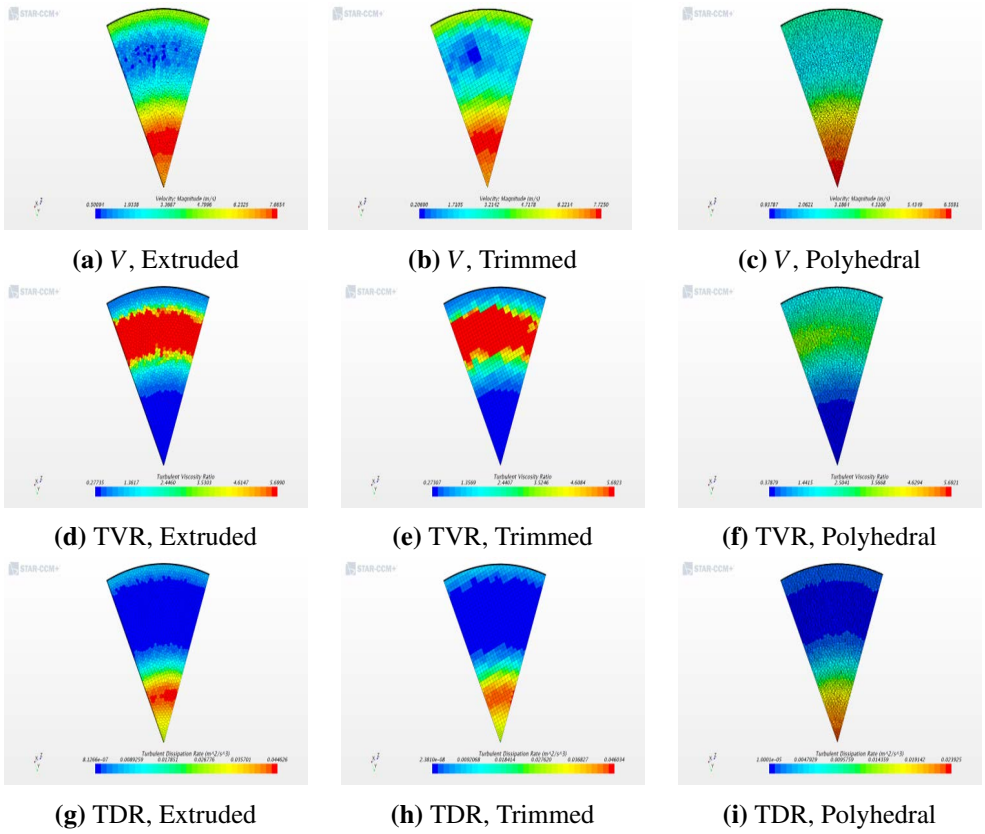

(a) V, Extruded **(b)** V, Trimmed **(c)** V, Polyhedral

(d) TVR, Extruded **(e)** TVR, Trimmed **(f)** TVR, Polyhedral

(g) TDR, Extruded **(h)** TDR, Trimmed **(i)** TDR, Polyhedral

Figure 5.8 CFD model: 45 deg wedge, axial flow. Comparison between the porous medium region meshing strategies, contours at the surface between the porous region and the diffuser. Only the extruded mesh corresponding to Case 1 has been included here. Please refer to text description and Table 5.2 for more details about the mesh. Velocity magnitude V (a-c), Turbulent viscosity ratio TVR (d-f) and Turbulent dissipation rate TDR (g-i).

5.2.2 Mesh independence study

The optimisation of the mesh parameters is a non-trivial task for swirling flows simulations, as mentioned in Chapter 2. The presence of the sudden expansion and of the downstream resistance, further complicates the choice of the mesh parameters (i.e. core size, refinements, growth rate, etc.), in order to correctly capture the flow features, balancing the computational cost.

A study of the impact of the mesh on the solution has been carried out aiming to optimise the computational cost and reduce the errors linked to domain discretization, also monitoring the symmetry of the solution. The impact of global and local volume and surface refinements has been evaluated in the regions of interest, such as the sudden expansion region and the outlet sleeve region. It has been found that the core mesh inside the sudden expansion has a great impact on the solution symmetry. A reduction of the mesh effects in terms of asymmetry has been achieved by adjusting the volume density and the growth ratio of the core mesh (CD-Adapco, 2018). This approach has

allowed a good compromise between mesh quality and mesh size. A finer mesh has been used in all the regions downstream the swirl generator, from the annular insert to the outlet sleeve, by reducing the size of the surface cells. A total of 15 prism layers has been used for all the cases, aiming to a y+ value below 5 near the wall, as explained in subsection 3.2.3. The porous region has been modelled with 9 layers, extruded from the last section of the sudden expansion, using an hyperbolic symmetrical distribution.

The impact of the mesh size on the solution has also been assessed by comparing the global parameters, listed in Table 5.3, and local variables, Figure 5.10. The results have been non-dimensionalised following the criteria presented in the first section of this chapter. The comparison between the number of cells for each region is shown in Figure 5.9, for each case summarized in Table 5.3. In this paragraph, only a selection of results is shown, aiming to present the independence of the solution from the size of the mesh chosen. The test case used for the mesh independence analysis presented here is the maximum swirl level analysed in the project, corresponding to a swirl generator angle $\theta_s = 18°$. Fewer tests were made on the lower swirl levels, confirming the results found for the maximum swirl level, but are not presented here.

Table 5.3 Axisymmetric diffuser: mesh independence study results - Global parameters

	Case 1	**Case 2**	**Case 3**	**Case 4**
Number of cells	3012593	4910119	8090874	13864360
Uniformity index	0.77	0.78	0.78	0.78
Swirl number	1.59	1.51	1.51	1.50
Total pressure drop (Pa)	5612	5209	5201	4889
Monolith pressure drop (Pa)	493	469	466	457

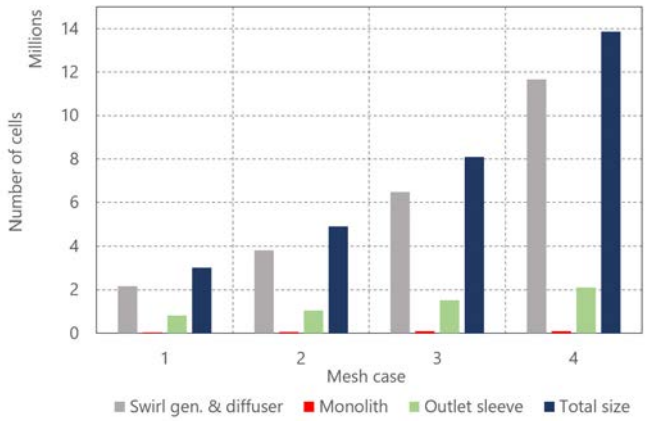

Figure 5.9 Axisymmetric diffuser: mesh independence study results - Comparison of the number of cells in each region for the 4 cases in Table 5.3. Swirl generator and diffuser region (gray bar), Monolith region (red bar), Outlet sleeve (green bar), Total number of cells (blue bar).

The velocity distribution, at the annular pipe insert Figure 5.10 (a) is presented for one diameter only, given the symmetry of the solution. Similarly, the results at the outlet section Figure 5.10 (b) are shown for one radius only. The velocity magnitude at the annular pipe insert, Figure 5.10 (a), shows that the impact of the mesh size is small for cases 2 to 4, suggesting that the solution has converged. This is further confirmed by the swirl level calculated in the same section, Table 5.3. The normalised velocity downstream the monolith is shown in Figure 5.10 (b), showing almost no impact of the mesh size for the last two cases (yellow and purple line for Case 3 and Case 4 respectively). This is confirmed by the uniformity index at the outlet section shown in Table 5.3, for which the only difference observed is of about 1% for the coarser mesh (Case 1).

The pressure coefficient, Equation 5.2, has been compared at two different locations: the wall of the inlet pipe of the diffuser, Figure 5.10 (c), and the wall of sudden expansion, Figure 5.10 (d). It can be seen that for the Cases 3 and 4, the difference in the prediction of the pressure coefficient is within 2%, at both locations. This difference is attributed to the interpolation used to extract the values in Star CCM+. It can be seen that by reducing the mesh size, there is a small impact on the location of maximum point inside the sudden expansion, Figure 5.10 (d). As it will be explained in the following section, that point can give an approximate location of the reattachment point inside the diffuser. It can be seen from Figure 5.10 (d) that the maximum is slightly shifted downstream for Case 3 and Case 4, compared to Case 1.

The pressure drop between the swirl generator inlet and the numerical outlet shows that for the last three cases shown here, the value is converging, while for the first mesh (coarser) it is over-predicted of about 7%. The pressure drop through the monolith

confirms this trend, with the coarser mesh over-predicting this value of about 6%. By comparing the pressure drop through the monolith region, Table 5.3, it can be seen that for the last three cases, the difference is within 2%. A difference in the total pressure drop can be seen between Case 3 and Case 4, but it is attributed to a change in the swirl generator assembly region, since the changes in the region of interest are not significant.

The above results have shown that the difference between Case 3 and Case 4 is within 2% in the prediction of both pressure and velocity inside the regions of interest. It has been possible to conclude that the combination of mesh parameters used for Case 3 is satisfactory in terms of quality of the solution and represent a good balance in terms of computational cost. All the other simulations carried out with the different inflow conditions have been analysed using similar settings, resulting in a mesh size of about 8M cells.

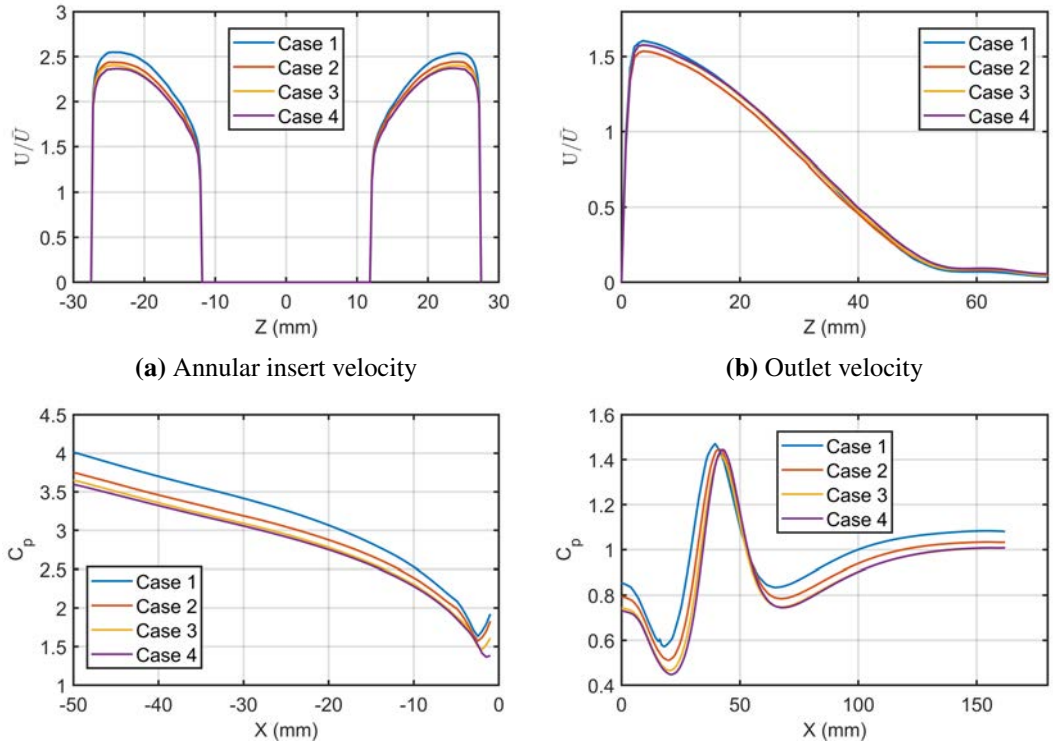

(a) Annular insert velocity

(b) Outlet velocity

(c) Expansion inlet wall pressure

(d) Sudden expansion wall pressure

Figure 5.10 Mesh independence study results: velocity at the annular insert section (a), velocity at the outlet section (b), static pressure at the wall of the diffuser inlet (c), static pressure at the wall of the sudden expansion (d). Please refer to text description for more details

5.2.3 Convergence criteria

The convergence of the solution has been first of all monitored using the solution residuals, fixing a minimum of 10^{-5} as criteria for the momentum equations and the turbulence quantities.

In addition, the solution has been monitored at 8 different locations in the 4 regions of interest: the annular pipe insert, the diffuser expansion, the porous region and the outlet sleeve. The monitoring points have been set-up in the XY section symmetrically to the domain axis X, Figure 5.11. The maximum and minimum velocity has been monitored in each point, at every iteration step.

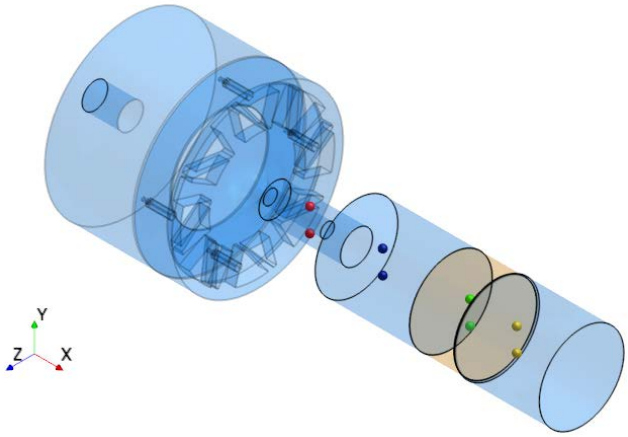

Figure 5.11 Convergence monitoring points used for the CFD model. Annular pipe region (red), sudden expansion region (blue), porous medium region (green) and outlet region (yellow).

For some inflow conditions, a slight numerical instability, resulting in flow asymmetry, has been observed. In particular, for the lower swirl level, corresponding to a $\theta_s = 4°$, an oscillation of the velocity around the mean value in the locations shown in Figure 5.11 has been observed, Figure 5.12. A maximum oscillation of $\approx 9\%$ around the mean value has been observed inside the sudden expansion points Figure 5.12b, while downstream the oscillation around the mean value was negligible ($\approx 0.2\%$). After excluding mesh related effects, the instability has been investigated by changing the numerical schemes used for the solution.

The initial solution has been calculated using a 2^{nd} order upwind scheme for the convective terms, keeping a 2^{nd} order scheme for the gradients. After changing the numerical scheme for the convective terms to a 1^{st} order and then to a 3^{rd} order scheme, the instability was still present. After excluding the effect of the turbulent model numerical scheme, the calculation of the numerical gradients has been investigated. A stable solution has been obtained by imposing a 1^{st} order scheme for the gradients,

keeping the accuracy of the solution still of the 2nd order, as shown in the study by Sozer et al. (2014).

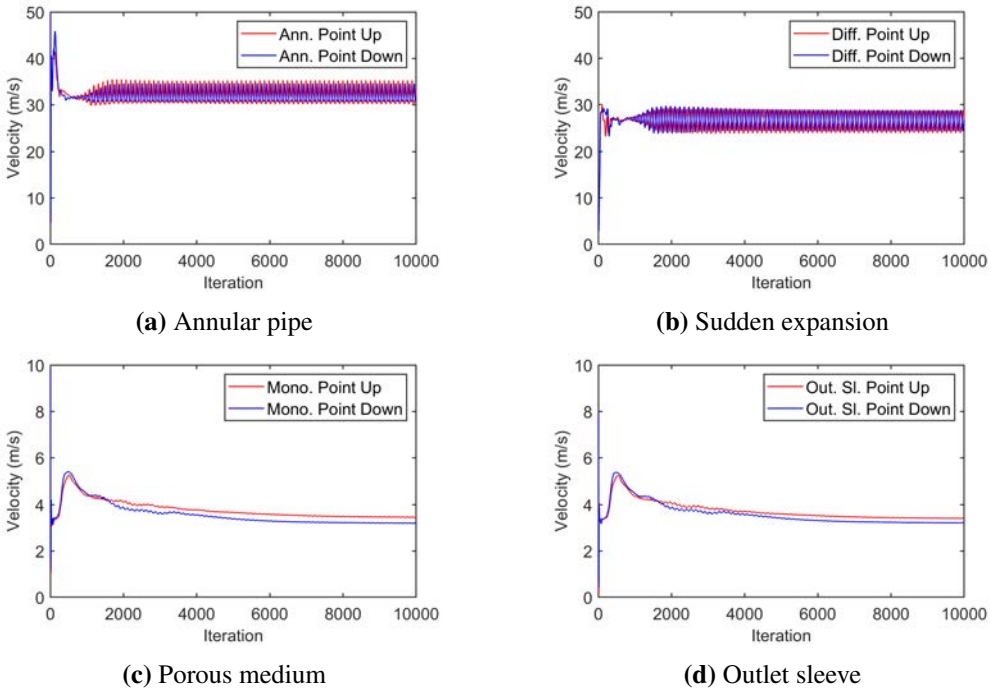

(a) Annular pipe

(b) Sudden expansion

(c) Porous medium

(d) Outlet sleeve

Figure 5.12 Velocity monitored at the several locations inside the domain, Figure 5.11. Red lines correspond to the points in the positive Y direction (*Up*), blue lines correspond to points in the negative Y direction (*Down*). Annular pipe region (a), sudden expansion region (b), porous medium region (c) and outlet sleeve region (d).

5.3 Flow analysis

The analysis of the results obtained for the axisymmetric configuration is shown in this paragraph.

The flow structures identified inside the sudden expansion plane XZ are compared between the PIV results and the CFD model. Further comparison between the CFD results and other experimental data (HWA and wall static pressure) is presented to further investigate the model capabilities. Global flow parameters are finally used to investigate the effects of increasing swirl on flow uniformity and pressure drop.

5.3.1 Inlet swirl levels

The swirl level in the annular pipe insert is representative of the swirl level entering the sudden expansion. The swirl level has been calculated using the definition shown in subsection 3.3.1.

The comparison between the values calculated from the experimental data (Rusli, 2019) and the CFD prediction is shown in Table 5.4, for each swirl generator angle considered (θ_s). It is possible to see that the highest difference between experimental estimation and CFD model can be seen for the minimum and maximum swirl levels. It is necessary to remark that in the calculation of the experimental value, several aspects can affect the evaluation, such as the sampling technique used, the number of samples, the wall treatment adopted, as confirmed by the differences shown in (Rusli, 2019) between the values estimated from single wire and cross-wire. The HWA sampling inside the annular insert is, also, an intrusive technique and the presence of the probe can significantly alter the flow distribution for swirling flows, as explained in Chapter 2. For this reasons, the values calculated by Rusli (2019) using the velocity sampled at the 3 locations inside the annular insert (Figure 5.5a) have been averaged. The standard deviation from the mean value is also included in Table 5.4.

Although the uncertainty for both model and experiment should be accounted for in the comparison, which might lead to a reduction of the differences seen in Table 5.4, the under-prediction of the swirl level from the CFD model can significantly alter the results. It is known from literature (Chapter 2) that the inlet flow prediction is critical for the numerical simulation of swirling flows, even when the swirl generator assembly is included in the domain. The analysis of the results presented in the following sections will further illustrate this point.

Table 5.4 Axisymmetric diffuser: inlet swirl level, comparison between experiments and CFD for each swirl generator angle considered (θ_s)

θ_s (deg)	Exp. value	CFD value	Difference
4	0.27 $\pm$0.03 ($\pm$9.8%)	0.25	-8%
7	0.50 $\pm$0.02 ($\pm$3.1%)	0.49	-2%
10	0.71 $\pm$0.04 ($\pm$5.1%)	0.71	0%
18	1.70 $\pm$0.21 ($\pm$12.4%)	1.51	-13%

5.3.2 Flow structures inside the sudden expansion

As discussed in Chapter 2, swirling flows are characterised by a number of complex flow features, such as reduction of wall separation and formation of the central recircula-

tion zone. Here, the flow structures inside the sudden expansion have been identified by comparing the PIV data with the CFD results in the XZ plane. The velocity components in the plane are identified as *axial* (U) and *tangential* (V). In figures from 5.13 to 5.18, the sudden expansion inlet has been added to the CFD, to visualise the incoming flow. No PIV data has been extracted at the inlet, due to reflections and glass imperfection.

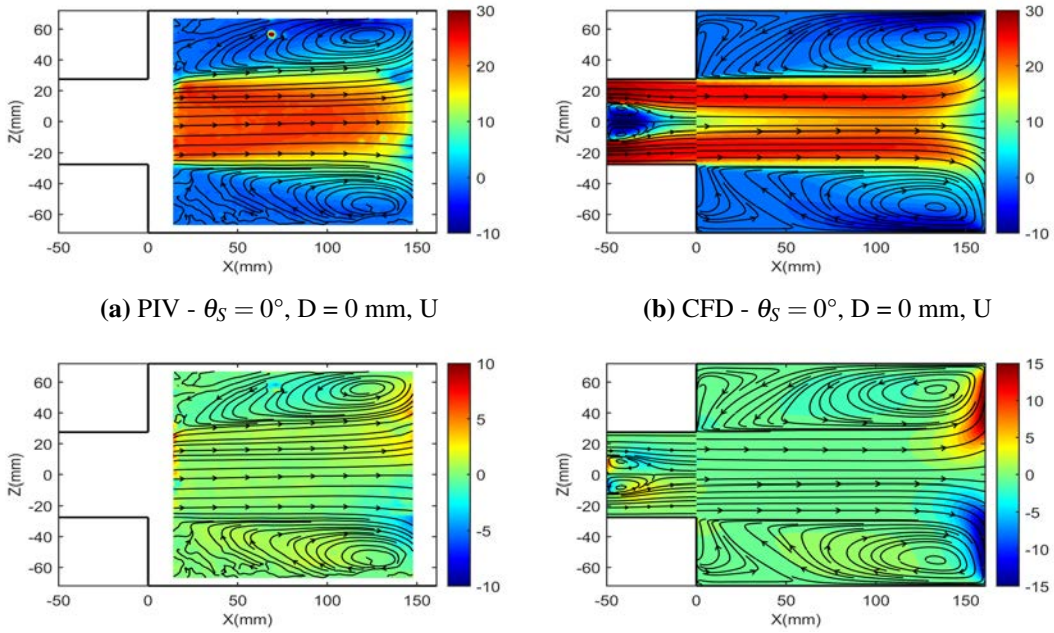

(a) PIV - $\theta_S = 0°$, D = 0 mm, U

(b) CFD - $\theta_S = 0°$, D = 0 mm, U

(c) PIV - $\theta_S = 0°$, D = 0 mm, V

(d) CFD - $\theta_S = 0°$, D = 0 mm, V

Figure 5.13 Axisymmetric diffuser: comparison between PIV and CFD data at the expansion section XZ, case: $\theta_S = 0°$. Velocity in m/s.

The straight flow condition ($\theta_s = 0°$) shows a good agreement with the PIV data for both velocity components, Figure 5.13. The CFD model is able to capture the expansion of the core jet and its redistribution towards the monolith section. The "free jet" entering the sudden expansion expands towards the walls, before impinging on the monolith surface. The radial redistribution of the flow that occurs at the monolith front face, causes the flow to turn towards the expansion wall. Part of that flow partially recirculates back towards the inlet, while the rest enters the monolith.

A good agreement between the PIV and CFD is found in the prediction of the dimensions of the separation zone close to the wall. Higher tangential velocity component can be seen from the CFD model close to the monolith front-face. A comparison with the PIV is not possible close to the monolith front face, since the experimental data close to the monolith face was only reliable up to about 10 mm upstream the monolith.

Differences between the PIV an the CFD model can be seen at the axis of the jet. The two opposite sides of the jet emerging from the inlet, as a consequence of the

annular insert, do not merge completely in the CFD model. They can be seen at the expansion inlet from the PIV data up about 40 mm from the sudden expansion section, but they merge completely after 50 mm. This is attributed to the limitations of the RANS model in predicting the radial diffusion and to the porous medium approach, which is limited in its capability of modelling the effects of the flow entering the single channels of the monolith (Padula et al., 2019).

The introduction of swirl causes a change in the velocity distribution, with the flow entering the sudden expansion passing from a "free-jet" velocity pattern to a "wall-jet" distribution. With increased swirl, the changes in the flow pattern causes a high pressure gradient in the radial direction (Gupta et al., 1984). As a consequence, the wall separation zone shrinks towards the inlet of the sudden expansion with increasing swirl level. The formation of the adverse pressure gradient at the diffuser axis can be inferred from the axial velocity components for the high swirl levels considered, starting from $\theta_S = 7°$. A central recirculation zone forms, in agreement with the observation by Gupta et al. (1984). The formation of the central recirculation bubble, as mentioned in Chapter 2, can be detrimental for the automotive aftertreatment systems, mainly because of the reversed flow entering the monolith.

The most evident difference between the PIV and the CFD model can be identified for the minimum swirl level considered, corresponding to $\theta_S = 4°$, Figure 5.14. The jet entering the sudden expansion exhibit a behaviour similar to the axial flow case in the CFD model, while from the PIV a considerable radial redistribution can be observed at about a third of the sudden expansion, starting from about 60 mm upstream the monolith section. This is more clear from the tangential component plots, from which it can be seen that the higher velocity areas from the CFD model are close to the monolith surface, similarly to the axial flow case, even if less pronounced, while from the PIV, those areas can be observed after the sudden expansion entrance, merging at about 100 mm.

This difference can be attributed to the lower inlet swirl level predicted for this case, Table 5.4. The uniform flow distribution observed in the experiments is the result of a balance between competing mechanisms (inertia in the axial direction and centrifugal force), which is expected to be very sensitive to swirl level upstream and accurate modelling of turbulent mixing. The effect of the inlet velocity has been explored for this case, by increasing the swirl generator angle in the CFD simulations to $\theta_S = 5°$.

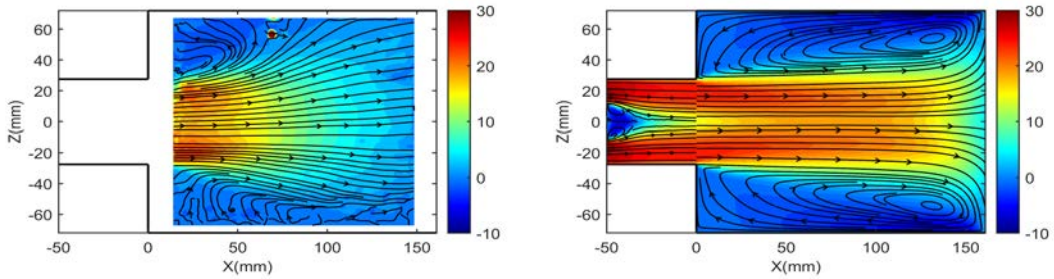

(a) PIV - $\theta_S = 4°$, D = 0 mm, U

(b) CFD - $\theta_S = 4°$, D = 0 mm, U

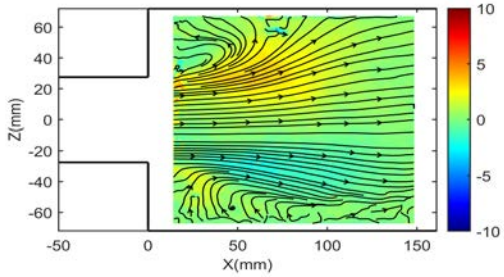

(c) PIV - $\theta_S = 4°$, D = 0 mm, V

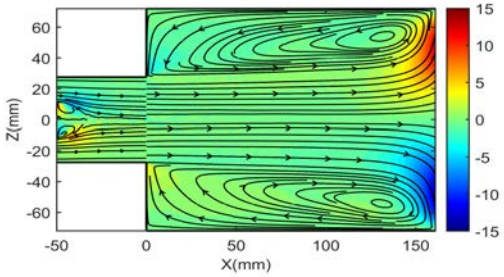

(d) CFD - $\theta_S = 4°$, D = 0 mm, V

Figure 5.14 Axisymmetric diffuser: comparison between PIV and CFD data at the expansion section XZ, case: $\theta_S = 4°$. Velocity in m/s.

Although a better prediction of the flow features has been achieved by increasing the swirl generator angle to $\theta_S = 5°$, with an increased swirl level at the inlet of 0.27, the high radial distribution observed in the PIV experiments is still not captured by the CFD model (Figure 5.15). This confirms that the under-predicted swirl level is not the only reason why the CFD cannot capture the low swirl characteristics: the RANS models, generally fail to predict the flow redistribution radially (Fadhila et al., 2020).

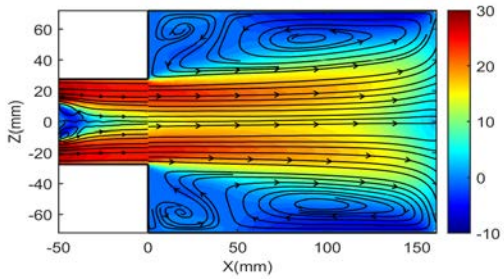

(a) CFD - $\theta_S = 5°$, D = 0 mm, U

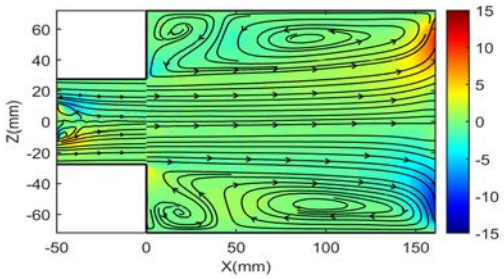

(b) CFD - $\theta_S = 5°$, D = 0 mm, V

Figure 5.15 Axisymmetric diffuser: CFD results at the expansion section XZ, case: $\theta_S = 5°$. Velocity in m/s.

The $\theta_S = 7°$ corresponds to an intermediate swirl level of about 0.5, which is identified in (Gupta et al., 1984) as the threshold between low and high swirl. The flow structures are similar to the ones identified with the higher swirl levels considered, in

both axial and tangential components. A general good agreement between PIV and CFD can be seen, Figure 5.16 to Figure 5.18. The model is able to correctly capture the increasing flow angle of the jet entering the sudden expansion for both velocity components and the size of the recirculation zone near the wall.

At the highest swirl level considered here ($\theta_S = 18°$) the central recirculation bubble spans the entire width of the sudden expansion and negative flow can be seen towards the monolith section from the PIV data. The CFD model is able to predict this behaviour, capturing the effect of the negative flow re-entering the monolith section. However, the model fails to capture the intensity of the central core redistribution, partially due to the lower swirl level predicted at the inlet. It can be seen from Figure 5.18 that the negative velocity inside the central recirculation bubble is considerably higher in the PIV than in the CFD model. As a consequence, a lower portion of negative flow is entering the monolith in the CFD model, as can be seen near the expansion axis.

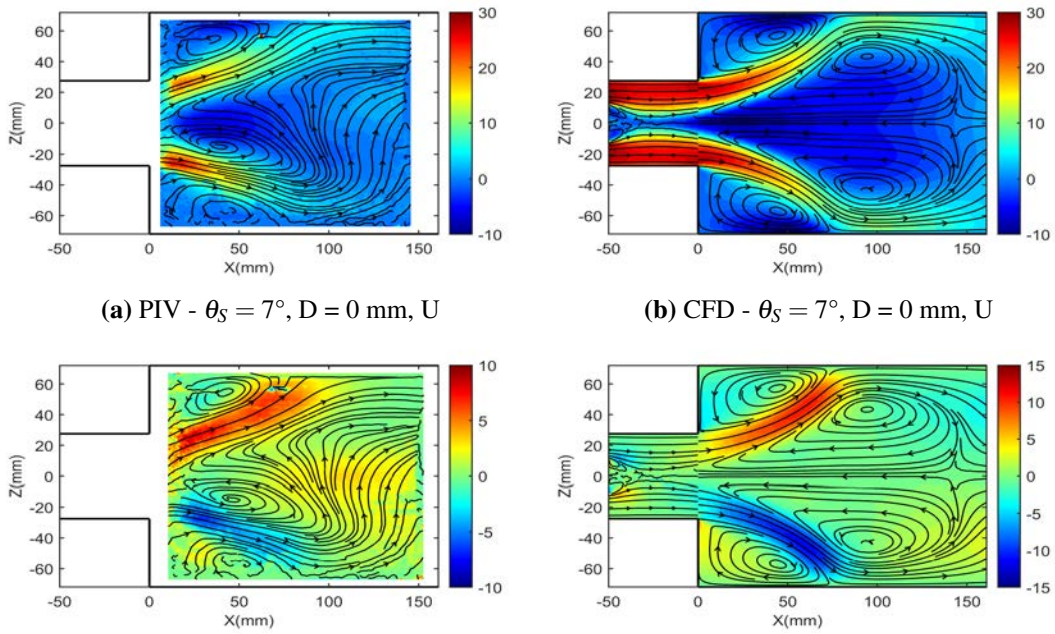

(a) PIV - $\theta_S = 7°$, D = 0 mm, U

(b) CFD - $\theta_S = 7°$, D = 0 mm, U

(c) PIV - $\theta_S = 7°$, D = 0 mm, V

(d) CFD - $\theta_S = 7°$, D = 0 mm, V

Figure 5.16 Axisymmetric diffuser: comparison between PIV and CFD data at the expansion section XZ, case: $\theta_S = 7°$. Velocity in m/s.

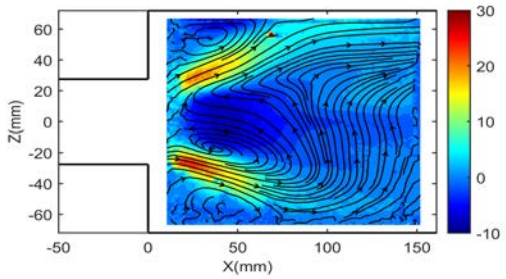

(a) PIV - $\theta_S = 10°$, D = 0 mm, U

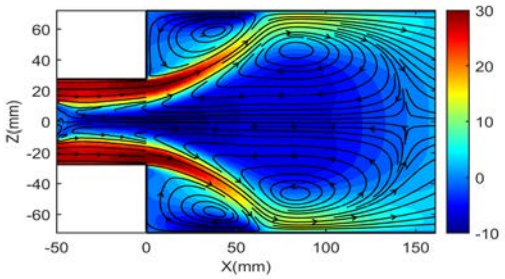

(b) CFD - $\theta_S = 10°$, D = 0 mm, U

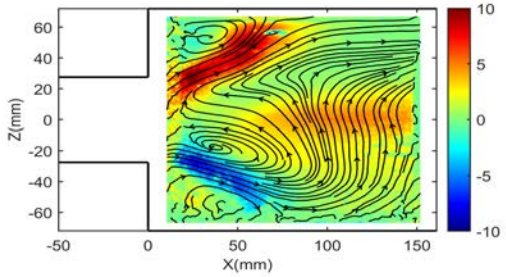

(c) PIV - $\theta_S = 10°$, D = 0 mm, V

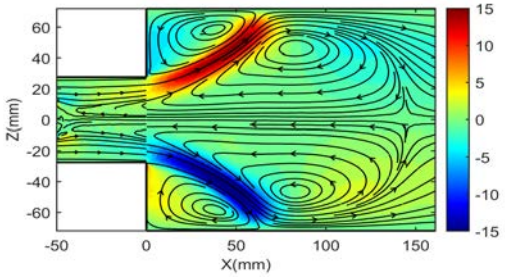

(d) CFD - $\theta_S = 10°$, D = 0 mm, V

Figure 5.17 Axisymmetric diffuser: comparison between PIV and CFD data at the expansion section XZ, case: $\theta_S = 10°$. Velocity in m/s.

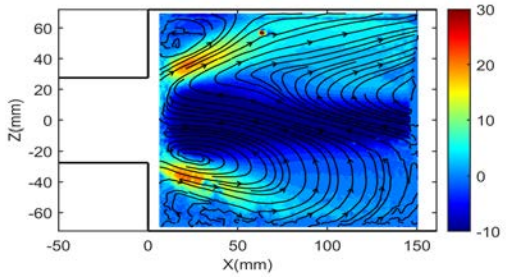

(a) PIV - $\theta_S = 18°$, D = 0 mm, U

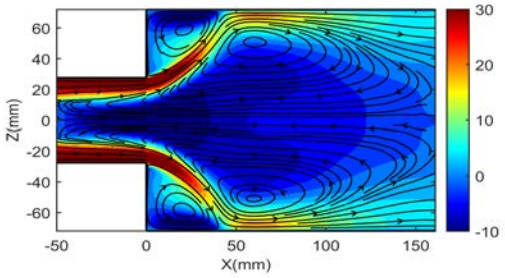

(b) CFD - $\theta_S = 18°$, D = 0 mm, U

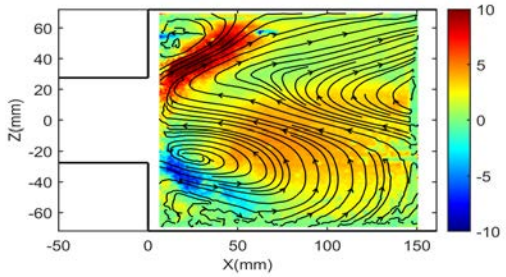

(c) PIV - $\theta_S = 18°$, D = 0 mm, V

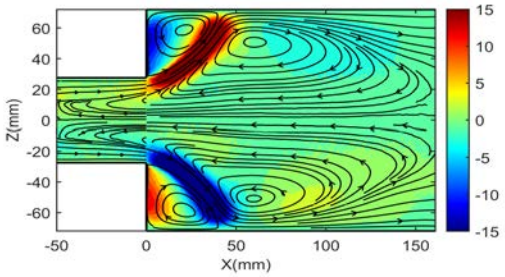

(d) CFD - $\theta_S = 18°$, D = 0 mm, V

Figure 5.18 Axisymmetric diffuser: comparison between PIV and CFD data at the expansion section XZ, case: $\theta_S = 18°$. Velocity in m/s.

In conclusion, it can be seen from Figure 5.13 to Figure 5.18 that the CFD model is able to capture the main flow structures with increasing swirl level. The formation

of the central recirculation zone starting with S = 0.49 ($\theta_S = 7°$) is well captured by the CFD, retaining the toroidal shape visible from the PIV experiments and reported in literature (e.g. Syred (2006)). The changes in the central recirculation bubble observed with increasing swirl level can be qualitatively captured, with the model being able to predict the negative flow re-entering the monolith for the highest swirl level considered. The $\bar{v}^2 - f$ model used can also correctly predict the changes of the recirculation zones towards the walls, with a good quantitative and qualitative agreement between the PIV and the CFD.

In general, it can be seen from Figure 5.13 to Figure 5.18 that flow diffusion is generally under-predicted by the CFD model. The most evident result of the under-prediction has been observed in the mixing region around and inside the annular jet, which is wider in the PIV data. This is consistent with similar studies for a planar diffuser for steady (Porter et al., 2014) and pulsating flow (Porter et al., 2015).

On the other hand, PIV measurements are a result of several spatial averaging cycles associated with the cross-correlation algorithm and averaging over a number of measurements. This is expected to result in PIV over-predicting diffusion between the jet and surroundings, in a similar way that cycle to cycle variation in transient flows causes artificial diffusion of flow structures as discussed by (Saul et al., 2015).

5.3.3 Pressure distribution

The pressure distribution in swirling flows is characterised by high radial gradients, and formation of adverse axial gradient at high swirl levels that leads to the formation of the central recirculation zone (as described in subsection 2.1.1). The experiments only allow to measure wall pressure distribution, due to the high sensitivity of swirling flows to intrusive techniques (as discussed in subsection 2.1.3) but CFD can be used to get extra insights into the pressure inside the domain. For the above reasons, further insight into the pressure distribution inside the sudden expansion is given by the static pressure contour plots. The pressure has been sampled from the CFD model at the XZ section and at three perpendicular sections inside the diffuser, respectively at the sections at 15 mm, 75 mm and 162 mm (monolith front-face) after the sudden expansion.

The wall pressure distribution at the diffuser wall (Figure 5.19 and Figure 5.20 - left column) shows a generally good agreement between the experiments and the numerical model. Note that only the *North* line is shown here for both experiments and CFD results, given the symmetry of the flow.

The results for the low swirl (S = 0.25) confirm that the radial redistribution occurs compared to the axial case (Figure 5.19), resulting in a sensible reduction of pressure build-up in front of the monolith (from $\approx$ 140 mm). The CFD model is able to capture

this effect and in general predicts the increased pressure coefficient at the wall compared to S = 0, but fails to predict the redistribution that occurs after about 60 mm, confirming the observations made in the previous subsection 5.3.2 for the velocity.

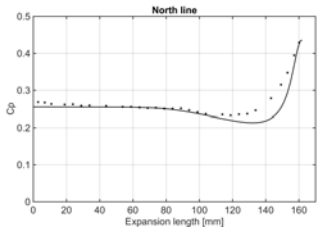

(a) $\theta_S = 0°$, D = 0 mm - Wall

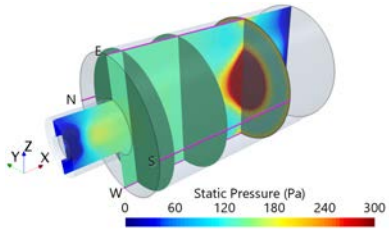

(b) $\theta_S = 0°$, D = 0 mm - Planes

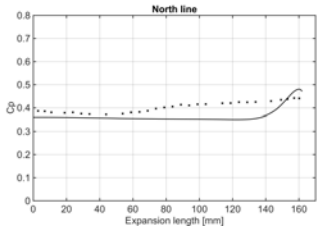

(c) $\theta_S = 4°$, D = 0 mm - Wall

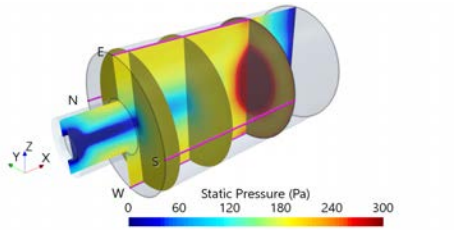

(d) $\theta_S = 4°$, D = 0 mm - Planes

Figure 5.19 Axisymmetric sudden expansion: static pressure distribution. Comparison between experimental data (dots) and CFD (line) at the sudden expansion wall (left column. CFD contours at XZ section and cross-sections at 15mm, 75 mm and 162 mm (monolith front face) after the sudden expansion. Magenta lines represent the static pressure measurements locations. Low swirl cases, corresponding to S = 0 ($\theta_S = 0°$) and S = 0.25 ($\theta_S = 4°$).

The wall pressure distribution allows to evaluate the position of the swirling jet reattachment point at the sudden expansion wall, which can be identified by the local maximum closer to the sudden expansion section. A good agreement between the CFD and the experimental data is observed (Figure 5.20a,c,e).

It has already been observed from the velocity data that for increasing swirl level that the wall separation zone shrinks towards the sudden expansion section. This is confirmed by the contour plots on the right column in Figure 5.19 and Figure 5.20.

A negative pressure area can be observed close to the wall at the sudden expansion section for the higher swirl levels considered (light blue in Figure 5.20). Immediately downstream, at the reattachment point, a high pressure zone can be seen. The flow impinging on the wall due to the swirl is then driven downstream, towards the outlet because of the pressure difference.

The adverse axial pressure gradient inferred at the axis of the diffuser from the PIV and CFD velocity distributions for the high swirl cases is confirmed by the pressure contour plots. A negative pressure area towards the axis of the XZ section can be seen even starting with the swirl level of S = 0.49 ($\theta_S = 7°$) in Figure 5.20b. With increasing swirl level, the negative pressure area extends downstream and becomes

more pronounced (Figure 5.20d-f). This is in agreement with the increased size of the recirculation zone observed for the velocity and the increased magnitude of the negative flow.

The CFD overestimates the pressure at the wall for the highest swirl level, caused by the swirling jet impingement at the wall, confirming that the flow diffusion is underestimated by the RANS model.

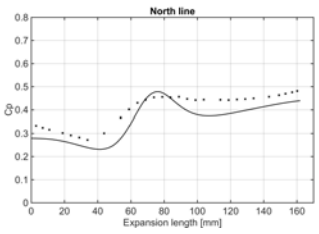

(a) $\theta_S = 7°$, D = 0 mm - Wall

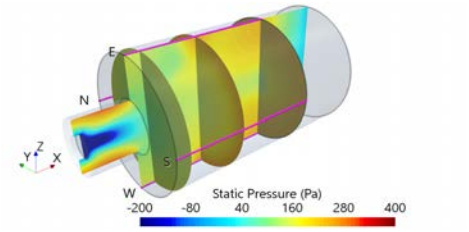

(b) $\theta_S = 7°$, D = 0 mm - Planes

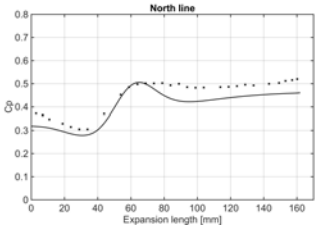

(c) $\theta_S = 10°$, D = 0 mm - Wall

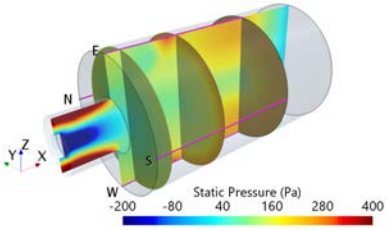

(d) $\theta_S = 10°$, D = 0 mm - Planes

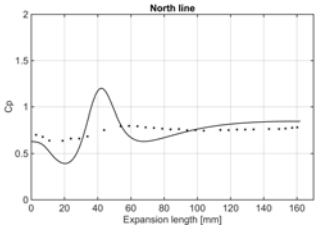

(e) $\theta_S = 18°$, D = 0 mm - Wall

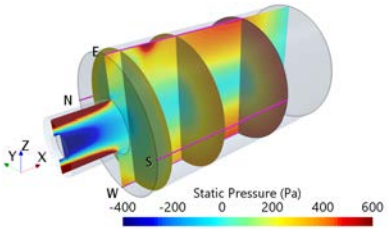

(f) $\theta_S = 18°$, D = 0 mm - Planes

Figure 5.20 Axisymmetric sudden expansion: static pressure distribution. Comparison between experimental data (dots) and CFD (line) at the sudden expansion wall (left column. CFD contours at XZ section and cross-sections at 15mm, 75 mm and 162 mm (monolith front face) after the sudden expansion. Magenta lines represent the static pressure measurements locations. High swirl cases, corresponding to S = 0.49 ($\theta_S = 7°$), S = 0.71 ($\theta_S = 10°$) and S = 1.51 ($\theta_S = 18°$).

Pressure drop

The total pressure drop between the inlet and the outlet of the domain has been extracted from the CFD data, to determine the impact of the swirl level.

The total pressure is a good representation of the energy loss due to the presence of swirl. It is a fundamental parameter for the analysis of the performance of catalysts, heat exchangers and similar devices, as discussed in Chapter 2. The high radial pressure gradients typical of swirling flows cause a pressure drop that cannot be captured by

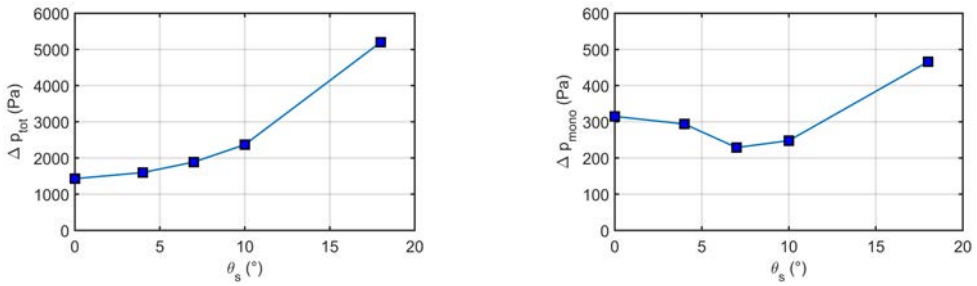

(a) δp - Inlet/Outlet **(b)** δp - Monolith

Figure 5.21 Axisymmetric diffuser: total pressure drop through the entire domain, inlet section - outlet section (a), through the monolith region (b)

the wall pressure measurements. From the good agreement at the wall pressure seen with the CFD, it can be inferred that the total pressure drop in the model, can be representative of the total head loss between inlet and outlet of the domain. It is clear from Figure 5.21 (a) that the total pressure increases between the inlet and outlet of the domain with the increasing swirl level. This is a consequence of the energy lost by the flow at the swirl generator inlet for the increasing rotation and to overcome the central adverse pressure gradient observed for the high swirl case. It can be seen, that the pressure loss between the pure axial flow ($\theta_S = 0°$) and the low swirl level ($\theta_S = 4°$) is comparable. When the air is forced to increase its tangential component by passing through the swirl generator blocks at higher angles, a more pronounced increase in the pressure loss can be seen from Figure 5.21 (a).

The effects of the monolith on the pressure loss have been evaluated with the pressure loss through the porous medium region Figure 5.21 (b). The flow entering the porous region has a certain approach angle that varies with the flow pattern upstream, resulting in a pressure loss, accounted with the entrance effects, as explained in Chapter 3. The flow entering the small axial channels of the catalyst, as observed in previous studies, e.g. (Benjamin et al., 2003) and (Persoons, 2006), loses its energy with the increasing tangential component, in addition to the pressure loss caused by flow contraction/expansion and the friction in the device channels.

The monolith pressure loss seen in Figure 5.21 (b) is not increasing with the increasing swirl level, as observed for the total pressure loss. A decreased value of the pressure loss through the monolith can be seen for the low swirl level of $\theta_S = 4°$ and the intermediate swirl level of $\theta_S = 7°$. This result is in agreement with the observations previously made on the flow redistribution at the monolith front-face, in particular for the tangential components, Figure 5.13, Figure 5.14, Figure 5.16, second row. The redistribution of the flow at the monolith front face is higher for the axial flow case. The

flow redistribution in the radial direction due to the low swirl results in a more uniform flow and is beneficial in terms of entrance losses.

5.3.4 Flow downstream the diffuser

The changes in the flow structures observed in the sudden expansion are reflected in changes of the flow pattern downstream the monolith section. The flow distribution downstream an aftertreatment device of the category considered here, the catalyst family, is representative of the flow distribution entering the device. In addition, the flow distribution downstream is important when multiple devices are used in series, since the flow exiting the first device affects the performance of the downstream ones, as already discussed in Chapter 2. This aspect is important for most of the practical applications in which high resistance devices are used. The flow exiting the monolith channels is mostly uni-directional, therefore only the axial velocity is presented in Figure 5.22 and Figure 5.23. This is true also for the CFD model, since high resistance has been imposed in the other two directions in the porous region, subsection 3.2.5.

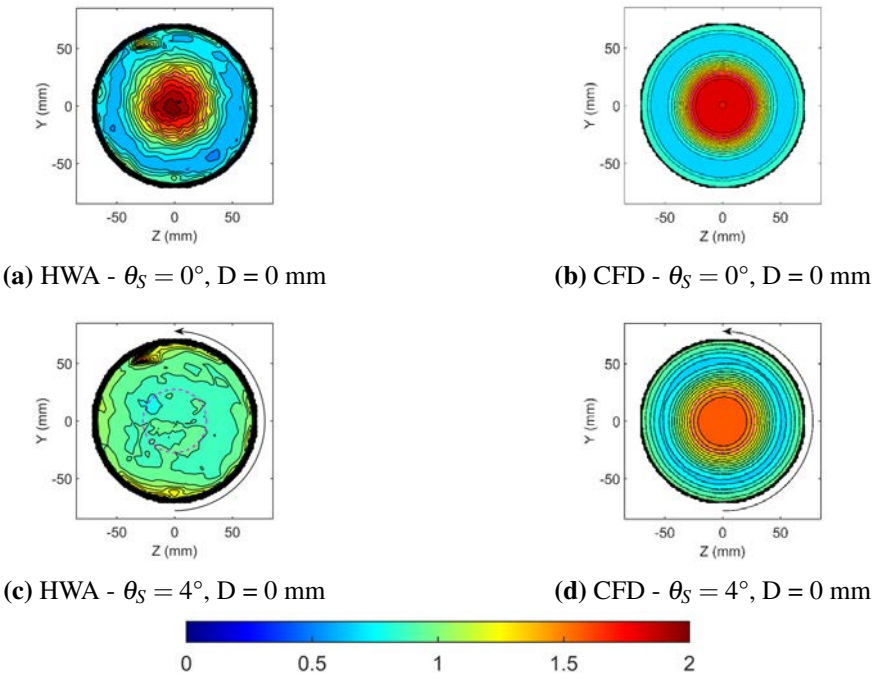

(a) HWA - $\theta_S = 0°$, D = 0 mm

(b) CFD - $\theta_S = 0°$, D = 0 mm

(c) HWA - $\theta_S = 4°$, D = 0 mm

(d) CFD - $\theta_S = 4°$, D = 0 mm

Figure 5.22 HWA and CFD data comparison downstream the monolith section. Low swirl cases, corresponding to S = 0 ($\theta_S = 0°$) and S = 0.25 ($\theta_S = 4°$). Velocity in m/s.

The axial inflow condition ($\theta_S = 0°$) causes the outlet velocity profile to have a peak in the middle, consistent with the jet impingement observed in the sudden expansion section. The effect of jet diverting towards the wall just upstream of the monolith

can be observed in the downstream velocity distribution for both HWA data and CFD model. A secondary velocity peak can indeed be observed towards the wall in both cases (Figure 5.22a, b).

The results for the low swirl level (S = 0.25, $\theta_S = 4°$) are consistent with the observations previously made for the velocity inside the sudden expansion and for the pressure distribution. The CFD model is not able to fully capture the radial flow redistribution observed in the experimental data (Figure 5.22c, d) and can not correctly predict the high uniformity observed experimentally.

The flow redistribution with increasing swirl level, causes the appearance of a velocity minimum towards the centre of the outlet section, Figure 5.23. It can be inferred from the HWA velocity distribution that the central core area for $\theta_S = 10°$ and $\theta_S = 18°$ represents a negative velocity area. The velocity pattern goes from 0 m/s to a finite value, suggesting that reverse flow was present in that area, in agreement with the presence of the central recirculation bubble. However, negative velocities cannot be captured with the single wire used in the experiments, as shown in (Skusiewicz, 2012). There is no evidence of reversed flow in the CFD model, in which only for the highest swirl level $\theta_S = 18°$ some negative flow is seen immediately downstream the porous region, but disappears at 30 mm downstream, at which the data have been sampled.

The optimal swirl level of $\theta_S = 7°$ observed in terms of pressure loss through the monolith can be attributed to the better flow distribution observed in the CFD for this case. A discussion of the optimal swirl level in terms of flow uniformity will be presented in the following Chapter 6, where the uniformity index calculated from both experiments and CFD model is presented and compared for all the cases and it is used to expand the analysis of the asymmetry effects.

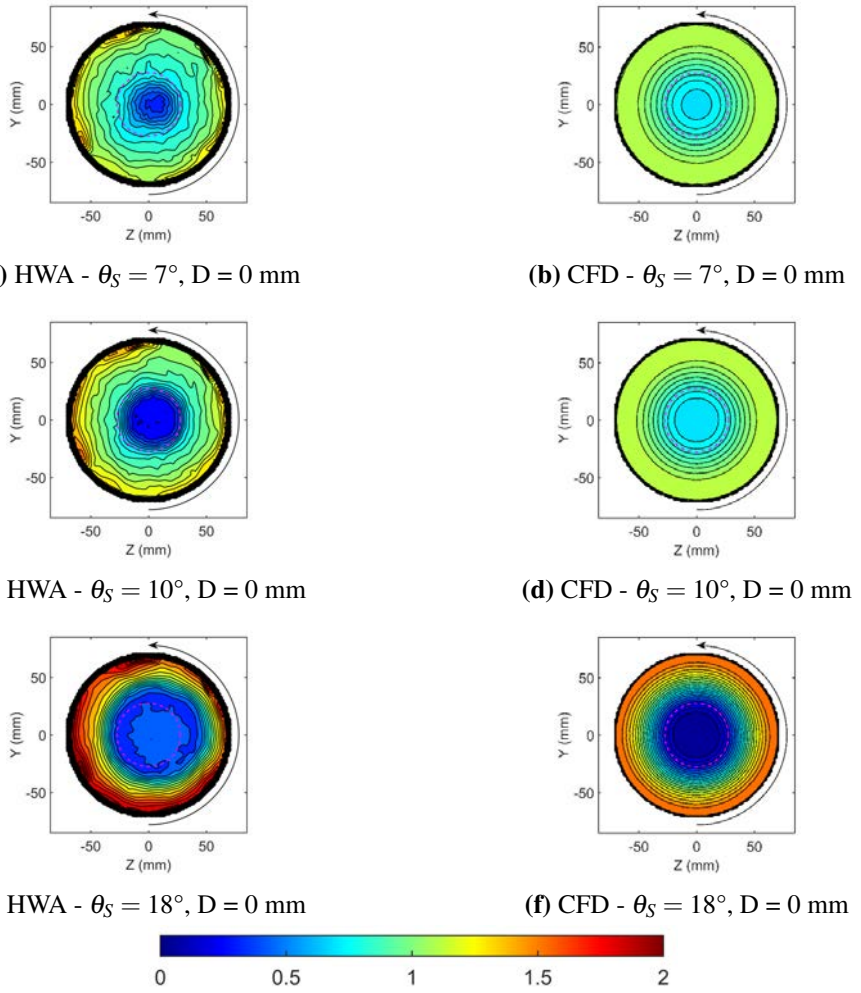

(a) HWA - $\theta_S = 7°$, D = 0 mm

(b) CFD - $\theta_S = 7°$, D = 0 mm

(c) HWA - $\theta_S = 10°$, D = 0 mm

(d) CFD - $\theta_S = 10°$, D = 0 mm

(e) HWA - $\theta_S = 18°$, D = 0 mm

(f) CFD - $\theta_S = 18°$, D = 0 mm

Figure 5.23 HWA and CFD data comparison downstream the monolith section. High swirl cases, corresponding to S = 0.49 ($\theta_S = 7°$), S = 0.71 ($\theta_S = 10°$) and S = 1.51 ($\theta_S = 18°$). Velocity in m/s.

5.4 Chapter summary

The analysis of the flow inside the axisymmetric sudden expansion has been presented for increasing swirl level. The assessment of the CFD model capabilities has been made by comparing the CFD results with experimental data.

The changes in the flow structures inside the sudden expansion can be captured by the $\bar{v}^2 - f$ model, with the model capable of predicting the formation of the central recirculation zone inside the sudden expansion with increasing swirl level and the shrinking of the recirculation zones at the sudden expansion corner. The trend observed in the PIV is qualitatively captured by the CFD model for all the cases.

The major differences between CFD and PIV have been observed with the low (S = 0.25) and high swirl (S = 1.51) cases considered here, for which the radial redistribution

of the flow due to swirl is not well captured. A combination of effects has been identified to explain the discrepancies between the CFD and the experiments. The RANS model under-predicts the flow diffusion and the turbulent mixing, in particular in the mixing region inside the annular jet. The under-prediction of the inflow swirl level has been confirmed to be only one contributing factor to the bad agreement observed with the low swirl level. Even by increasing the swirl level from S = 0.25 to S = 0.27, therefore matching the experimental data, the under-prediction of the radial redistribution still persists.

Despite these differences, the CFD model is still able to capture the effects on the pressure redistribution and gives a good prediction of the reattachment point at the diffuser wall. The $\bar{v}^2 - f$ model can be used to get some insight into the flow structures for a wide range of swirl levels (S = 0 to S = 1.51). The model can be used for practical industrial applications, for example during the design phase. It has been shown that the model can be used to identify the range of optimal swirl levels for which the pressure losses through the monolith can be reduced, compared to the axial flow case.

Chapter 6

Effects of asymmetry on swirling flow in a sudden expansion

The aim of this chapter is use experimental and numerical studies to investigate how the asymmetry changes the flow structures with increasing swirl level in a sudden expansion with an offset inlet. Two inlet offsets are considered: 10 mm and 20 mm.

The comparison fulfils three different objectives: assessment of the CFD model capabilities, understanding of the physics involved in such complex flow environment and analysis of the global flow features such as pressure loss and flow uniformity, important for engineering applications.

6.1 Experiments

6.1.1 Experimental apparatus and instrumentation

The experimental test rig has been described in section 3.1.1. The inflow mass flow rate was fixed at 63 g/s with 5 swirl levels analysed (Table 3.3). Asymmetry has been introduced into the domain by shifting the sudden expansion in the positive Z direction, thus introducing geometrical asymmetry in the domain. A schematic representation of the relative displacement between diffuser inlet (red circle) and sudden expansion (black circle) is shown in Figure 6.1. As a consequence of the displacement, the inlet axis and the sudden expansion axis are no longer the same.

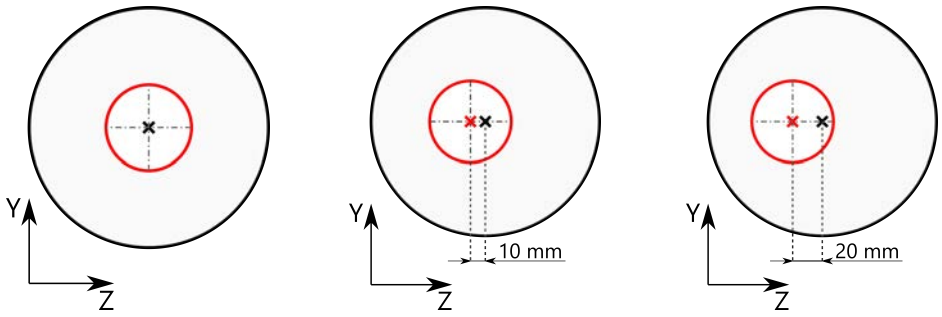

(a) D = 0 mm **(b)** D = 10 mm **(c)** D = 20 mm

Figure 6.1 Schematic representation of the relative position between diffuser inlet (red circle) and sudden expansion (black circle). Red cross marks the position of the axis of the diffuser inlet, black cross marks the axis of the sudden expansion. Axisymmetric configuration (a), relative displacement of 10 mm (b) and of 20 mm (c).

In order to build a more complete picture of the flow properties, three types of measurements have been carried out:

- PIV measurements inside the sudden expansion, carried out within this project;
- static wall pressure measurements (from the study of Rusli (2019));
- HWA measurements downstream of the test section (from the study of Rusli (2019)).

Although the HWA and pressure measurements were available for two inlet displacements, only one displacement D = 20 mm has been used in PIV measurements because a glass diffuser with a fixed displacement had to be manufactured. PIV data have been collected using the methodology presented in subsection 3.1.4.

The static pressure at the sudden expansion wall and velocity downstream the monolith have been collected on a similar configuration in a previous study (Rusli, 2019), as described in sections 5.1.2 and 5.1.3. The only difference with the axisymmetric case is in the pressure sampling positions. The spacing between the pressure tappings at the wall for the non-symmetric cases was varied between 3 mm and 10 mm (a table with tapping position is available in Rusli (2019)). The same approach used for the post-processing and the visualisation of the additional experimental data presented in Chapter 5 has been used for this chapter.

6.1.2 PIV measurements

The PIV data have been collected and post-processed using the methodology presented in subsection 3.1.4. Only the convergence analysis is presented in this section.

Data near the walls and close to the monolith entrance have been discarded, due to lower fidelity of the data in those areas, due to light refraction. The final sampling area is shown in green in Figure 6.2, in which the distance of the sampling area from the boundaries is reported.

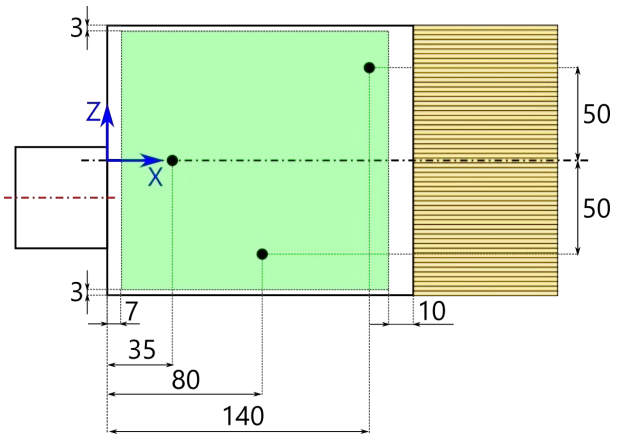

Figure 6.2 Location of the PIV data inside the sudden expansion for the non-symmetric case (green area). Black dots represent the three sampling points used for the convergence study. Dimensions in mm.

PIV convergence

In order to ensure that sufficient number of frames has been used to accurately calculate mean flow velocity, a convergence study has been performed. For that, the flow velocity has been calculated at 3 different locations inside the domain (black dots in Figure 6.2) using an increasing number of frames.

The results of the convergence study applied to the maximum swirl level (corresponding to $\theta_s = 18°$) for the non-symmetric case are shown in Figure 6.3. This case is presented as an example to clarify the methodology described in section 3.1.4. The analysis has been applied to all the inflow conditions. The minimum number of samples required for the convergence of the PIV data in the three locations (black dots in Figure 6.2) has been extracted for all the inflow conditions and it is summarised in Table 6.1. The local mean velocity (blue line) and the relative error ε_{PIV} (red line) are shown in the top sub-plot, while $\partial\varepsilon_{piv_N}$ is shown in the bottom sub-plot for each case (black line, light blue rectangle is used to visualise the accepted deviation). The analysis carried out on the U component (in the X direction) is shown on the left column

(Figure 6.3a,c,e), while the results for the V component (in the Z direction) are shown on the right column (Figure 6.2b,d,f).

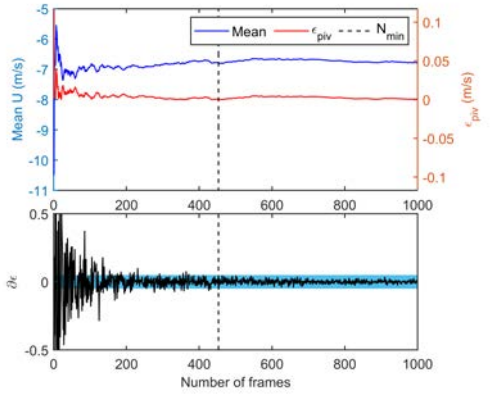

(a) Point 1 @ (35,0) mm - U

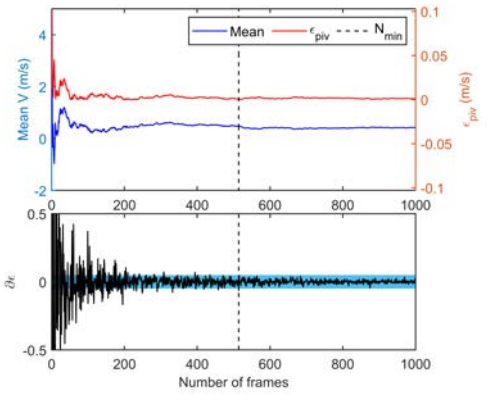

(b) Point 1 @ (35,0) mm - V

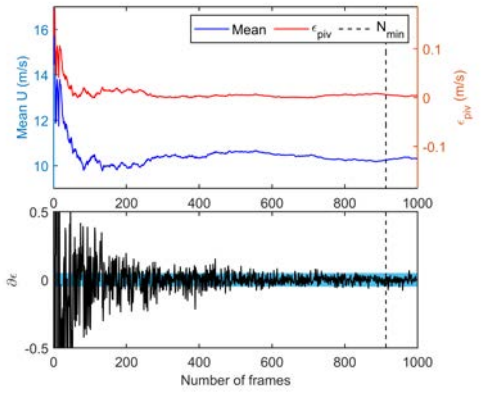

(c) Point 2 @ (80,-50) mm - U

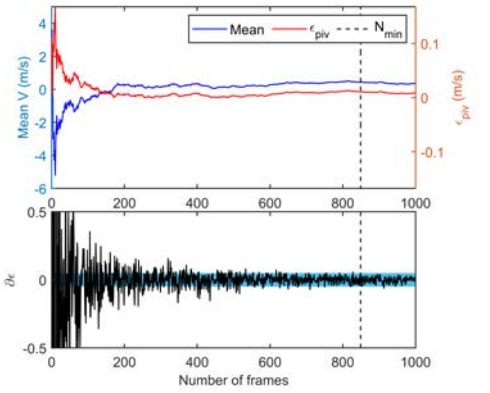

(d) Point 2 @ (80,-50) mm - V

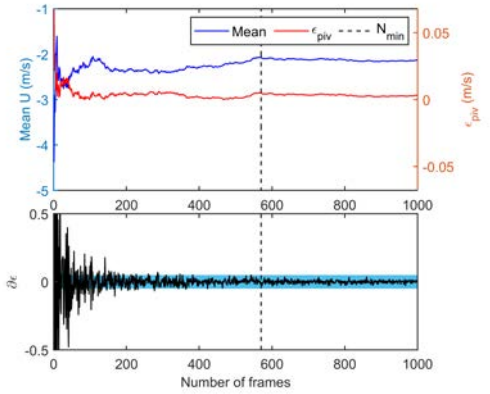

(e) Point 3 @ (140,50) mm - U

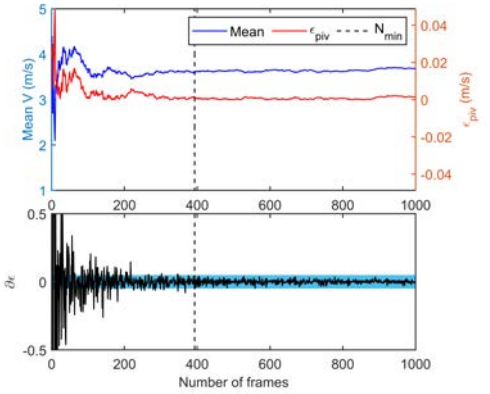

(f) Point 3 @ (140,50) mm - V

Figure 6.3 PIV convergence study: $\theta_s = 18°$, non-symmetric case (D = 20 mm). U component (X direction) on the left (a,c,e) and V component (Z direction) on the right (b,d,f).

The convergence has been satisfactory when the asymptotic behaviour of velocity and error has been achieved, verifying that $|\partial \varepsilon_{piv_N}| < 0.05$ (as discussed in section 3.1.4). The minimum number of images has been extracted for each case, as shown in Figure 6.3, in which the convergence criterion is represented by the light blue band.

From Table 6.1 it can be seen that, overall, no significant effect with increasing swirl level has been observed. Point 2 has been identified as the point in which the results are taking the longest to converge. The results in Table 6.1 show that the total of 1000 pairs of images acquired is sufficient to obtain a meaningful representation of the average flow field (based on the discussion presented in subsection 3.1.4).

Table 6.1 Minimum number of PIV sampling images required for the asymmetric diffuser with sudden expansion.

	Minimum number of samples					
	Point 1		Point 2		Point 3	
θ_s	(U)	(V)	(U)	(V)	(U)	(V)
0°	337	250	760	355	419	307
4°	390	360	753	556	427	297
7°	374	291	784	755	273	206
10°	399	314	847	828	383	237
18°	861	514	919	913	570	393

Target deformation

As discussed in subsection 3.1.4, the accuracy of the results is also affected by the image deformation due to the camera lens curvature, light refraction from the test section, light path distortion due to materials reflections and curvature of the test section. The deformation of the images acquired has been evaluated using the procedure presented in section 3.1.4. The resulting map is shown in Figure 6.4.

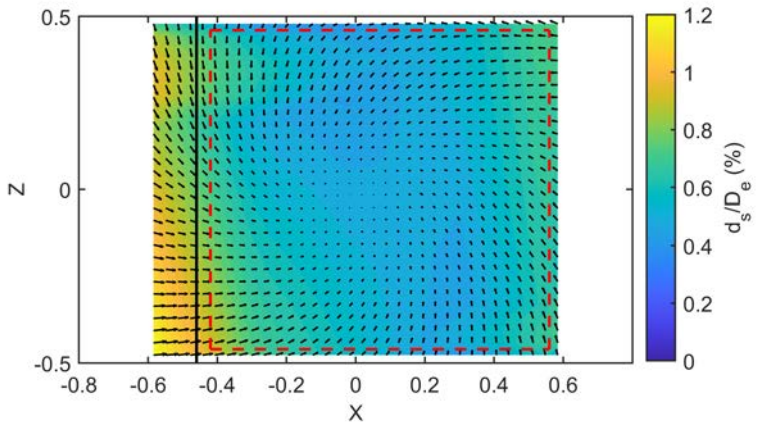

Figure 6.4 Distortion map for the non-symmetric case. Vectors represent the direction of the displacement (d_s) of the chequered board corners used for the target between the synthetic image and the real image (please refer to section 3.1.4 for more details). The contour map shows the displacement magnitude in percentage of the expansion diameter (D_e). Black line represents the catalyst position, red dotted rectangle indicates the final sampling area used for data analysis

Figure 6.4 shows that the effect of the distortion is higher towards the walls of the domain (edges of the map). This is expected, since the main sources of the distortion are the wall curvature and the camera lens, and both effects become more important towards the edges of the domain of interest. The maximum displacement (d_s) between the squares in the synthetic image and the squares in the real target is $\approx 1\%$ of the expansion diameter (D_e).

The sampled area (Figure 6.2) is the one enclosed by the red dashed line in Figure 6.4, where the average deformation is $\approx 0.5\%$ (≈ 0.7 mm). This deformation has been considered small for the purpose of the current study, so no algorithm has been applied for the data correction in the pre-processing.

6.2 CFD simulations

The aim of this section is to provide an assessment of the numerical model when the asymmetry is introduced, by comparing the PIV data with the CFD model for the highest displacement of 20 mm. The effects of the asymmetry and the analysis of the changes in the flow structures are presented in a separate section (section 6.2).

6.2.1 Implementation

The numerical model has been implemented using the methodology discussed in section 3.2. The mesh for all the non-symmetrical geometries has been created using the results from the mesh independence study carried out for the axisymmetric case

(section 5.2). In analogy with the axisymmetric case, the assumption of steady flow has been adopted also for the non-symmetric cases. It is expected that the presence of the downstream monolith dumps the instability induced by the swirling flows, such as the precessing vortex core, as confirmed by the experimental and numerical results from Chapter 5. Moreover, it has been observed by Parchen (1993), applying theoretical considerations, that turbulent swirling flows are more stable then laminar swirling flows when subject to asymmetry, as discussed in section 2.4.

6.2.2 Flow structures

Since the PIV measurements were performed in the XZ plane with the highest displacement of 20 mm, this is the case used here for CFD model validation. The velocity components extracted from both CFD and PIV will be referred as *axial* component (U, in the X direction) and *tangential* component (V, in the Z direction), in analogy with the axisymmetric case (Chapter 5). The velocity streamlines (black) have been superimposed in all the figures, to help the visualisation of the flow direction. The velocity inside the inlet section has been added to the CFD plots. More streamlines have been added in the inlet section, for a better visualisation of the symmetric character of the flow upstream the sudden expansion, thus a bit of discontinuity between streamlines at the point of expansion can be seen in Figure 6.5 to Figure 6.9.

The results obtained for $\theta_S = 0°$ are shown in Figure 6.5. A reasonable agreement between the PIV and CFD can be seen for both velocity components, with the CFD model correctly predicting the changes in the flow pattern caused by the asymmetry. Similarly to the axisymmetric case, the model fails to predict the diffusion inside the core jet (subsection 5.3.2). The radial diffusion prediction is confirmed to be one of the limitations of the RANS modelling approach, so that the wake of the annulus insert in the inlet section is seen to stretch all the way along the line Z = 0 up to the catalyst.

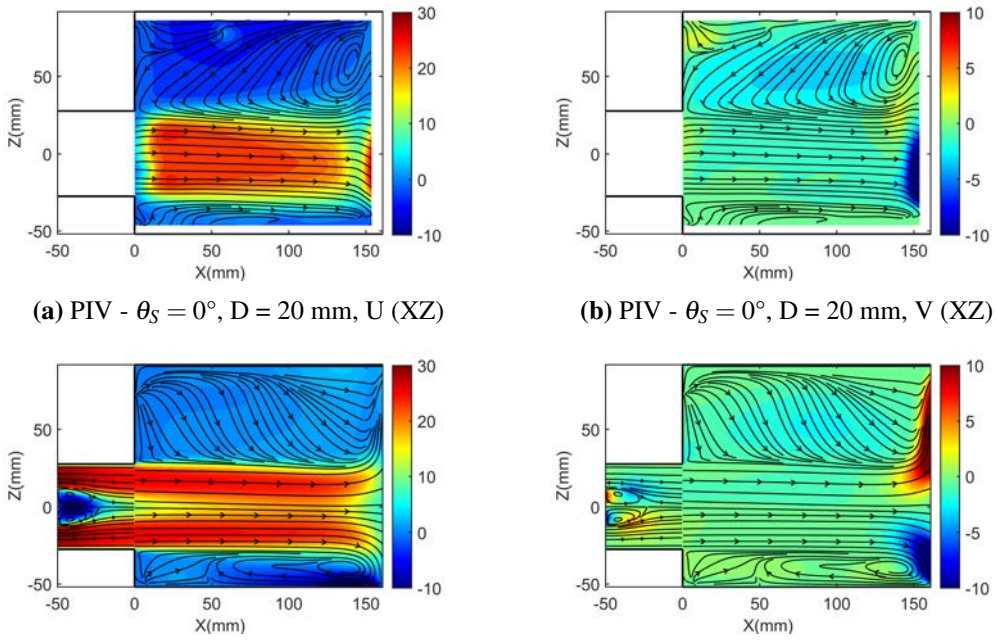

(a) PIV - $\theta_S = 0°$, D = 20 mm, U (XZ)

(b) PIV - $\theta_S = 0°$, D = 20 mm, V (XZ)

(c) CFD - $\theta_S = 0°$, D = 20 mm, U (XZ)

(d) CFD - $\theta_S = 0°$, D = 20 mm, V (XZ)

Figure 6.5 Diffuser with asymmetric sudden expansion (displacement D = 20 mm): in-plane velocity components at the expansion section XZ, comparison between PIV and CFD. Case: $\theta_S = 0°$. Velocity in m/s.

The low swirl case ($\theta_S = 4°$) was the most challenging for the modelling in the axisymmetric case, and the limitations of the model observed in the axisymmetric configuration are partially confirmed with the asymmetry. A better agreement between PIV and CFD is observed, compared to the axisymmetric case (Figure 5.14). The balance between the centrifugal "force" and inertia in the axial direction that controlled the flow in the axisymmetric case is broken in this case by the additional effect due to asymmetry, improving the comparison between experiments and model, as will be explained in the next sections.

From Figure 6.6 it is possible to see that the numerical model still over-predicts the jet penetration in the axial direction, compared to the PIV data. As observed for the axisymmetric case, it can be inferred that a partial explanation of this effect is the inlet swirl level under-prediction (Table 6.2). The model predicts the re-distribution of the flow due to the asymmetry and the radial spreading at the front of the monolith reasonably well. A secondary vortex can be observed in both PIV and CFD for $Z > 0$. The recirculation zone near the wall at $Z = -50$ mm is correctly captured by the CFD model, in both width and length (up to 60 mm in the X direction).

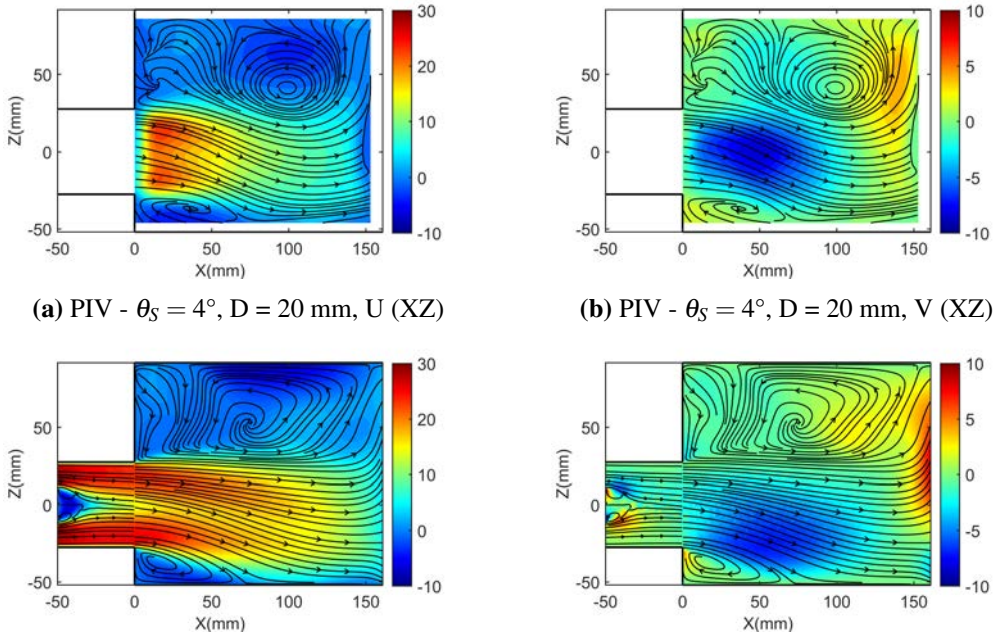

(a) PIV - $\theta_S = 4°$, D = 20 mm, U (XZ)

(b) PIV - $\theta_S = 4°$, D = 20 mm, V (XZ)

(c) CFD - $\theta_S = 4°$, D = 20 mm, U (XZ)

(d) CFD - $\theta_S = 4°$, D = 20 mm, V (XZ)

Figure 6.6 Diffuser with asymmetric sudden expansion (displacement D = 20 mm): in-plane velocity components at the expansion section XZ, comparison between PIV and CFD. Case: $\theta_S = 4°$. Velocity in m/s.

Similar to the axisymmetric case, there is a better agreement between CFD and PIV observed in Chapter 5 for the two intermediate inflow swirl levels of $\theta_S = 7°$ and $\theta_S = 10°$. As can be seen from Figure 6.7 and Figure 6.8, the flow distribution inside the sudden expansion is in good qualitative agreement between PIV and CFD for both velocity components. A qualitative comparison between the flow structures reveals that the CFD model can correctly capture the flow direction, with the central recirculation zone diverted towards the positive Z direction as the jet traverses the diffuser. The CFD model is able to capture the changes in the flow structures due to the asymmetry, but can not predict the magnitude of the velocity changes observed in the PIV. The model tends to over-predict the magnitude of the axial velocity component (similarly to the axisymmetric case).

An interesting feature can be observed with high swirl (S = 0.49 - $\theta_s = 7°$ to S = 1.49 - $\theta_s = 18°$): the jet "tilts" because of the asymmetry, exhibiting higher axial velocity in the "top jet" ($Z > 0$ half) entering the diffuser and lower velocities near the closest wall ($Z = -50$ mm). At the same time, the central recirculation bubble is no longer following the axial direction, but is diverted towards the upper wall ($Z > 0$) direction with increasing X. This is common to all the three high swirl levels analysed and will be clarified in the next sections using the 3D visualisation results from the CFD model.

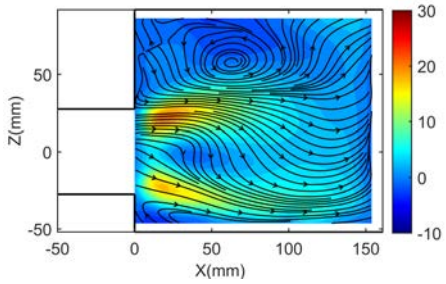

(a) PIV - $\theta_S = 7°$, D = 20 mm, U (XZ)

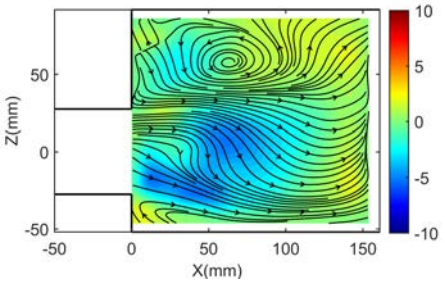

(b) PIV - $\theta_S = 7°$, D = 20 mm, V (XZ)

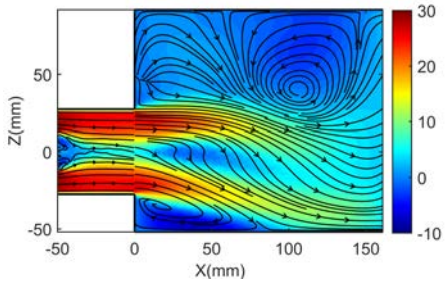

(c) CFD - $\theta_S = 7°$, D = 20 mm, U (XZ)

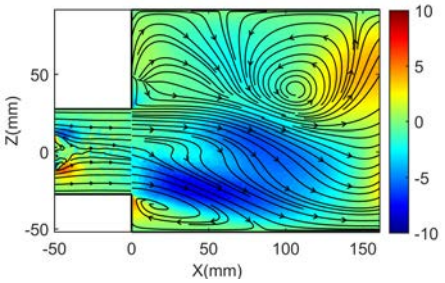

(d) CFD - $\theta_S = 7°$, D = 20 mm, V (XZ)

Figure 6.7 Diffuser with asymmetric sudden expansion (displacement D = 20 mm): in-plane velocity components at the expansion section XZ, comparison between PIV and CFD. Case: $\theta_S = 7°$. Velocity in m/s.

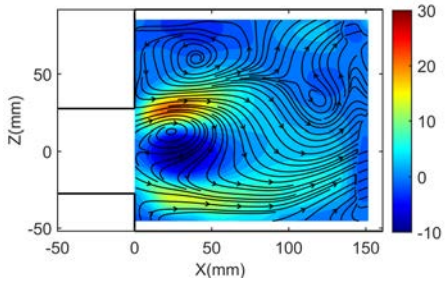

(a) PIV - $\theta_S = 10°$, D = 20 mm, U (XZ)

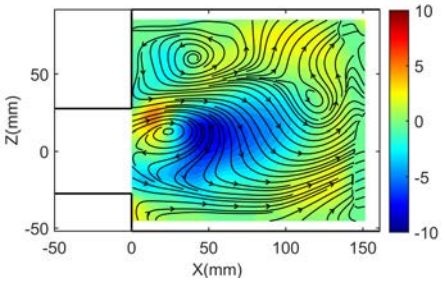

(b) PIV - $\theta_S = 10°$, D = 20 mm, V (XZ)

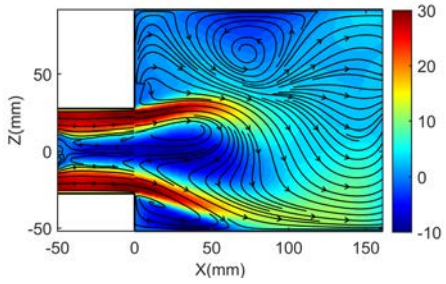

(c) CFD - $\theta_S = 10°$, D = 20 mm, U (XZ)

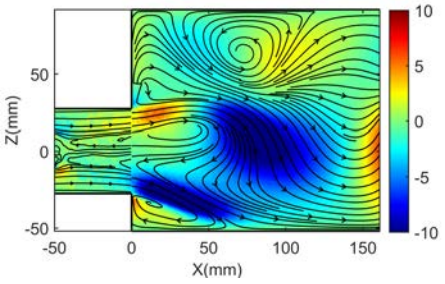

(d) CFD - $\theta_S = 10°$, D = 20 mm, V (XZ)

Figure 6.8 Diffuser with asymmetric sudden expansion (displacement D = 20 mm): in-plane velocity components at the expansion section XZ, comparison between PIV and CFD. Case: $\theta_S = 10°$. Velocity in m/s.

The centre of the separation zone near the wall at $Z = 50$ mm moves towards the expansion point with increasing swirl (compare Figure 6.6 to Figure 6.9). More details about the origin of this secondary structure are given in the analysis presented in the next sections, with the help of the 3D flow visualisation from CFD.

Similar conclusions can be drawn for the maximum swirl level considered in the current study ($\theta_S = 18°$). The comparison between CFD and PIV (Figure 6.9) confirms the trend observed for the axisymmetric case (Figure 5.18). The CFD model over-predicts the magnitude of the velocity components entering the sudden expansion, with a more pronounced flow curvature at the entrance compared to the PIV.

An interesting effect on the shape of the central recirculation zone can be observed from the PIV data in Figure 6.9. The central recirculation bubble exhibits two distinguished zones of negative flow, one closer to the inlet (from X = 0 mm up to X $\approx$ 60 mm) and a second one closer to the monolith (from X $\approx$ 100 mm up to X $\approx$ 150 mm). This feature is not entirely captured by the CFD model, which tends to smooth the flow distribution towards the monolith. This phenomenon can be attributed to the conservation of the angular momentum, which results in a vortex stretching phenomenon. Since only a slice of the flow is captured by the PIV, it is not possible to fully understand how the 3D shape is influenced by the asymmetry.

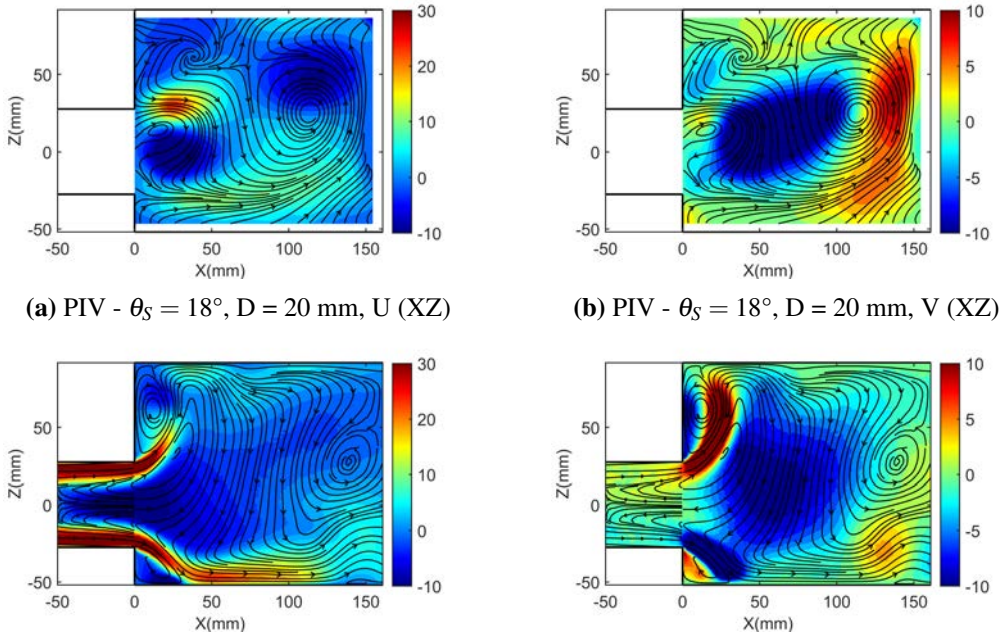

(a) PIV - $\theta_S = 18°$, D = 20 mm, U (XZ)

(b) PIV - $\theta_S = 18°$, D = 20 mm, V (XZ)

(c) CFD - $\theta_S = 18°$, D = 20 mm, U (XZ)

(d) CFD - $\theta_S = 18°$, D = 20 mm, V (XZ)

Figure 6.9 Diffuser with asymmetric sudden expansion (displacement D = 20 mm): in-plane velocity components at the expansion section XZ, comparison between PIV and CFD. Case: $\theta_S = 18°$. Velocity in m/s.

As already observed for the axisymmetric case, the model under-predicts the magnitude of the negative flow upstream the monolith area. The competing forces acting on the flow (centrifugal "force" and axial inertia) are modified by the asymmetry, resulting in a non regular shape of the central recirculation bubble. This results in high turbulence anisotropy in the shear region (between the central recirculation bubble and the surrounding swirling wall jet) which the RANS model can not correctly capture. This will be discussed in more detail in the next sections with the help of the analysis of the vorticity distribution and the 3D flow visualisation from CFD.

In conclusion, the CFD model is able to qualitatively capture the main flow features also for the highest swirl level. It is particularly interesting to see that the stronger deviation of the recirculation zone axis compared to the lower swirl cases is captured by the CFD model, confirming a strong effect of the asymmetry in terms of jet "tilting". The CFD model results, can, therefore, be trusted in the prediction of the main flow changes. However, the tangential component of the velocity and more in general the radial redistribution are not correcly predicted from the CFD, as for the axisymmetric case, suggesting that more complex models should be used.

6.3 Flow analysis

It has been shown in section 6.2 that most of the structures are captured by the CFD model, with some limitations attributed to the RANS model family in the prediction of the high anisotropic character of the flow field and to the porous medium model in the prediction of the flow redistribution and mixing upstream and downstream the monolith. The CFD model provides overall reasonable quantitative predictions for the flow velocity and pressure, although it under-predicts the effect of the centrifugal "force" and mixing in the shear layers.

With these limitations in mind, the analysis of the effects of the asymmetry is presented in this section for both displacements of 10 mm and 20 mm. The analysis has been carried out mainly using the CFD results, with the experimental data used where appropriate to support the analysis and to further assess the model capabilities.

The flow structures inside the sudden expansion have been extracted from the numerical model at the two cross section XY and XZ, as shown in Figure 6.10. The effects of the asymmetry are analysed by comparing the flow structures inside the diffuser section for both displacements of 10 mm and 20 mm, highlighting analogies and differences between the two cases with displacement and the symmetric case for increasing swirl level.

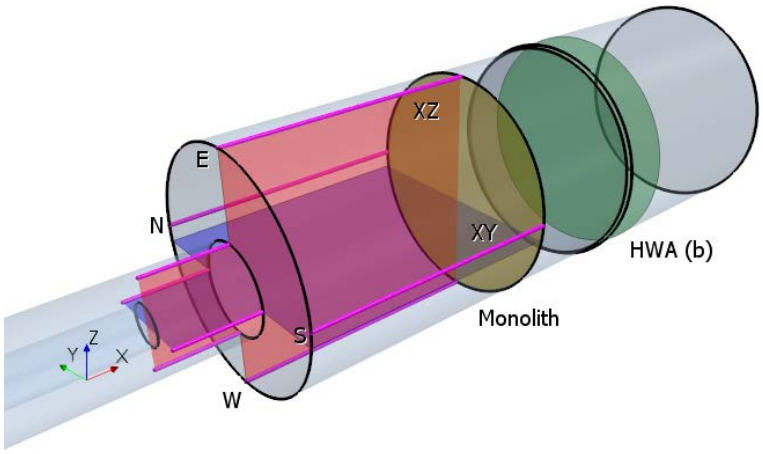

Figure 6.10 Plane sections used to extract the data from the CFD model, displacement of 20 mm. Section XY (blue plane), section XZ (red plane) inside the inlet pipe and the sudden expansion. Section HWA (b) used for the downstream velocity. Pressure lines (magenta) at the 4 azimuthal locations: North (N), East (E), South (S), West (W).

The comparison with the wall pressure and HWA velocity measurements downstream the monolith has been added to further assess the model capabilities and for gaining an insight into the properties of flow separation near the wall and the effect of swirl and offset on the flow uniformity.

The pressure at the sudden expansion wall is shown for all the cases at all the 4 azimuthal lines shown in Figure 6.10 (North, East, South, West), given that the flow is no longer symmetrical.

6.3.1 Inlet swirl levels comparison

It has been shown in section 5.3 that the swirl level is the main factor affecting the flow distribution in the axisymmetric case. Since in the simulations the swirl level is not imposed directly, but the whole swirl generator configuration is used to generate the swirling motion, it is important to compare the swirl levels between the experiments and simulations, which will allow to better assess the model performance, and the result comparison with the experiments.

The swirl number from the numerical data has been calculated using the definition described in section 3.3.1. The reference section is at 77.5 mm upstream the sudden expansion (1.5 inlet pipe diameters D_{in}) at the same location as for the axisymmetric case (presented in section 5.3.1).

A comparison with the experimental values reported in Rusli (2019) for the maximum displacement of 20 mm is presented in Table 6.2. For clarity and comparison,

the data for the axisymmetric case, already presented in Table 5.4, have been added to Table 6.2.

As explained in section 5.1.2, the velocity at the annular pipe insert has been sampled at 3 different locations. High differences have been observed in the experimental data between the velocity sampled at the 3 locations. The cause of those differences has been attributed by Rusli (2019) to the asymmetry of the experimental apparatus used. This has not been further investigated in the current thesis, since a different swirl generator (with the same design) has been used and the inflow asymmetry observed in the experimental activities carried out in the current thesis is low, as shown by the results presented in Chapter 4. To account for the differences in measurements between the three different azimuthal locations, the mean and standard deviation of the three values calculated from the experimental data have been included in Table 6.2.

Table 6.2 Asymmetric diffuser: inlet swirl level, comparison between experiments and CFD for each swirl generator angle considered (θ_s) and for each inlet pipe displacement.

θ_s	D (mm)	Experiments [a]	CFD model
4°	0	0.27 ±0.03 (±9.8%)	0.25
	10	-	0.25
	20	0.26 ±0.04 (±13.7%)	0.25
7°	0	0.50 ±0.02 (±3.1%)	0.47
	10	-	0.47
	20	0.49 ±0.03 (±6.6%)	0.47
10°	0	0.71 ±0.04 (±5.1%)	0.72
	10	-	0.71
	20	0.69 ±0.06 (±8.2%)	0.71
18°	0	1.70 ±0.21 (±12.4%)	1.51
	10	-	1.47
	20	1.68 ±0.25 (±14.8%)	1.48

[a] From (Rusli, 2019)

A higher uncertainty for the asymmetric cases can be observed, compared to the axisymmetric case. A possible explanation is the high sensitivity of the swirling flows to intrusive measurements techniques. The delicate balance between the velocity components is disturbed by the presence of the HWA probe holder used for those experimental activities. No data are available to estimate the global uncertainty, so no further analysis on those experiments are made here. The uncertainty in the experimental

values is higher for the lowest swirl ($\theta_s = 4°$) and the highest swirl ($\theta_s = 18°$) considered, confirming that those two levels are most sensitive to the perturbation of the flow. For the above reasons, a mainly qualitative comparison is made here, in similarity with the one presented in section 5.3.1.

The results from both experiments and numerical simulations confirm that, as for the axisymmetric case, only the the case corresponding to $\theta_s = 4°$ can be classified as *low* swirl, while when $\theta_s \geq 7°$ the cases correspond to *high* swirl cases, based on the classification proposed by Gupta et al. (1984).

From the comparison, it can be seen that the numerical model, as already observed for the axisymmetric case, generally under-predicts the swirl level, in particular for the lower swirl case ($\theta_s = 4°$) and for the higher swirl case ($\theta_s = 18°$).

The effect of asymmetry on the swirl level is small, with the swirl level slightly lower in the asymmetric case in experiments and most of the simulations, suggesting that the asymmetry has a low impact on the upstream flow. It can be inferred that the effects of the sudden expansion displacement on the flow is small at 77.5 mm upstream the sudden expansion, corresponding to about 1.5 times the inlet pipe diameter.

6.3.2 Flow inside the sudden expansion

To better understand the complex nature of the asymmetric swirling flow, velocity distribution in two cross-sections (XY and XZ) is first considered. The results presented in the plane sections XY and XZ (from Figure 6.11 to Figure 6.15) aim to demonstrate the complex three-dimensional interaction of the effects of swirl and asymmetry on the flow structure.

When the inlet flow is axial, velocity contours for 10 mm and 20 mm displacement are symmetrical in the XY plane (Figure 6.11 a, c). The main effect of the asymmetry in that plane is in the size and position of the recirculation zones towards the wall. The centre of rotation of the recirculation zone moves towards the expansion (X $\approx$ 80 mm) with the increasing inlet displacement.

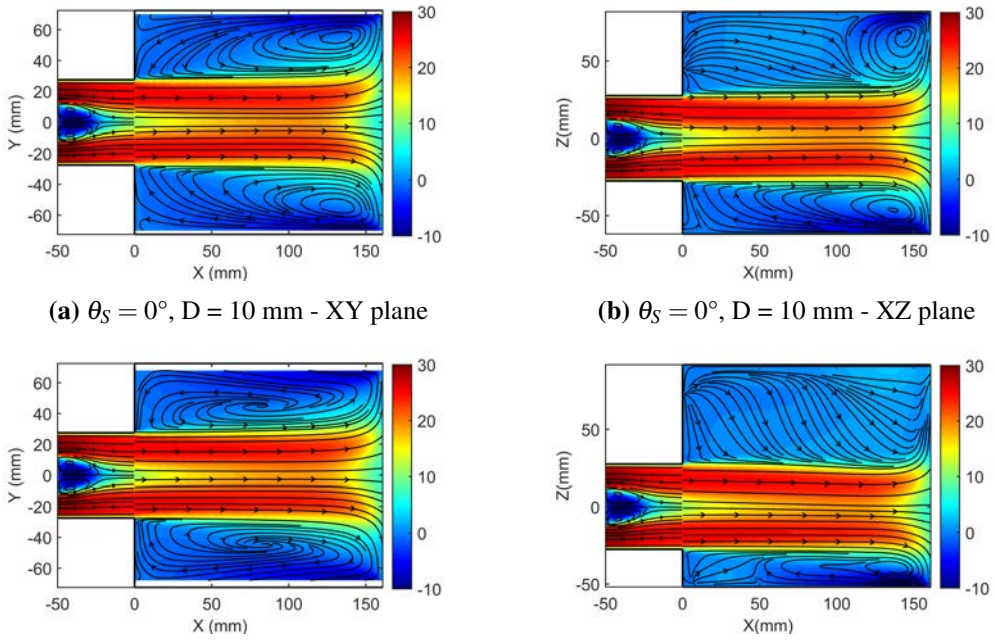

(a) $\theta_S = 0°$, D = 10 mm - XY plane

(b) $\theta_S = 0°$, D = 10 mm - XZ plane

(c) $\theta_S = 0°$, D = 20 mm - XY plane

(d) $\theta_S = 0°$, D = 20 mm - XZ plane

Figure 6.11 Axial velocity contour plot inside the sudden expansion, with superimposed vectors (black arrows). Effects of displacement on the velocity in planes XY (left) and XZ (right). D = 10 mm (a-b), D = 20 mm (c-d). Inlet swirl generator angle: $\theta_S = 0°$. Velocity in m/s.

More interesting features can be seen in the plane section XZ, for both displacements. The effect of the 10 mm displacement is shown in Figure 6.11b. The jet core is shifted in the negative Z direction, towards the nearest wall, that is the same direction of the inlet displacement. The recirculation zone at the wall is no longer symmetrical and is shrunk in both width (X direction) and height (Z direction). Near the West wall (negative Z) the wall separation zone appears more narrow. This is caused by the fact that the recirculating flow at the West wall has less space available, therefore has more intense negative velocities than the recirculation zone at the "far" (East) wall. At the opposite side, the separation zone is larger in the Z direction, but considerably smaller in the X direction. A secondary cross flow can be seen upstream the recirculation zone spanning from the sudden expansion up to X $\approx$ 100 mm.

This effect is more pronounced for the case of 20 mm displacement (Figure 6.11 d). The jet core is visibly diverted towards the West wall (negative Z), so that the wall separation zone becomes even more narrow compared to the previous case. At the opposite side (positive Z) the recirculation zone is no longer visible, while the cross flow is more robust and enters the monolith. This has been confirmed by the visualisation of the 3D structures and by the velocity sampled downstream the monolith, shown in the next sections. The effects of asymmetry in the inlet pipe are not visible in both configurations, confirming a negligible change in the flow structures upstream.

Similar to the axisymmetric case, the introduction of swirl results in the formation of the annular swirling jet flow and its redistribution towards the walls due to centrifugal "force". However, the flow is no longer symmetrical in either the XY section or the XZ section. The effect is visible starting from the lowest swirl level considered ($\theta_S = 4°$ shown in Figure 6.12) and becomes more pronounced for increasing swirl levels (Figure 6.13, Figure 6.14 and Figure 6.15). This is a manifestation of the strong coupling between axial and tangential flow components, reported for high swirling flows in several studies, such as Gupta et al. (1984) and Sloan et al. (1986). The flow becomes intrinsically 3D, exhibiting new flow structures compared to the axial inflow cases. For this reason, only the general trend is described here, while a more detailed analysis is presented in the next section, with the help of the visualisation of the 3D structures.

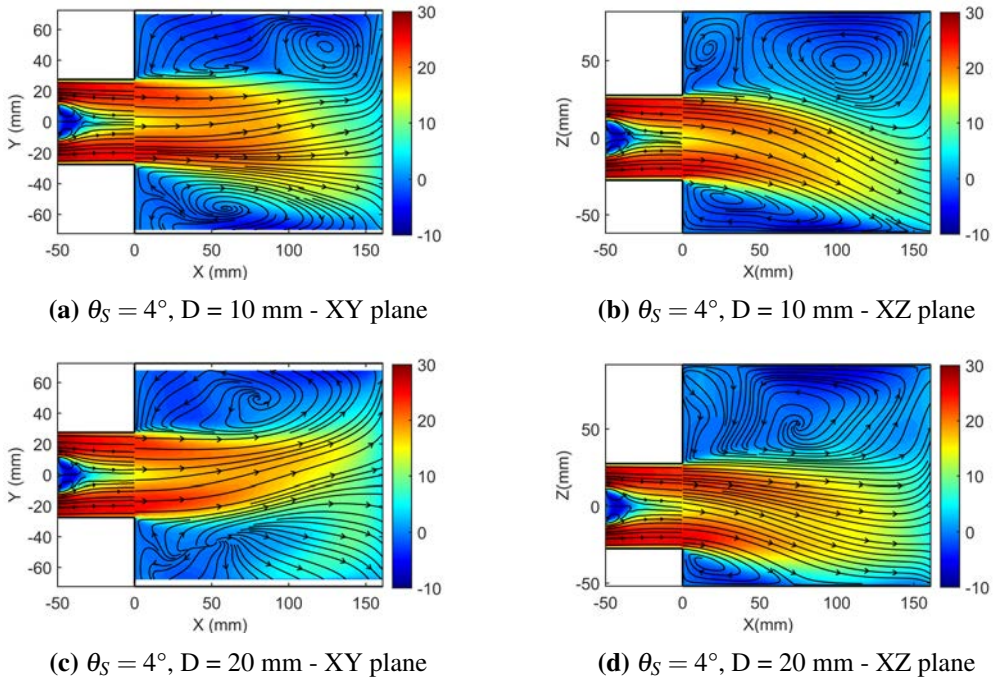

(a) $\theta_S = 4°$, D = 10 mm - XY plane

(b) $\theta_S = 4°$, D = 10 mm - XZ plane

(c) $\theta_S = 4°$, D = 20 mm - XY plane

(d) $\theta_S = 4°$, D = 20 mm - XZ plane

Figure 6.12 Axial velocity contour plot inside the sudden expansion, with superimposed vectors (black arrows). Effects of displacement on the velocity in planes XY (left) and XZ (right). D = 10 mm (a-b), D = 20 mm (c-d). Inlet swirl generator angle: $\theta_S = 4°$. Velocity in m/s.

With introduction of the displacement, the change in the flow structure is similar for all swirl levels. On one hand, the swirl causes the jet to expand upon entering the expansion (Figure 6.12 to Figure 6.15). On the other hand, similar to the no swirl case with asymmetry, the jet accelerates near the West wall, thus causing a "tilt" of the jet axis towards the West wall (Figure 6.12 to Figure 6.15, b,d). Combination of this acceleration and swirl means that the jet core also accelerates and is diverted in the

azimuthal (swirl) direction - Figure 6.12 to Figure 6.15 (a,c). Therefore, the resulting flow is no longer symmetrical in either XY nor XZ plane.

A different trend can be seen for D = 20 mm in the XY plane for the lower swirl level. The swirling core jet is slightly diverted towards the South wall (negative Y direction) with the lower displacement of 10 mm (Figure 6.12 a), while it is diverted towards the North wall with the higher displacement (Figure 6.12 c), resulting in a different flow redistribution upstream the monolith. The behaviour observed for the lower displacement is consistent with the one observed for the axial inflow condition. With increasing asymmetry, as a consequence of the reduced space towards the West direction (Figure 6.12 d), the centrifugal force causes the flow to accelerate towards the axis of the sudden expansion, resulting in the flow diverting towards the North wall in Figure 6.12 c.

At high swirl levels, starting from $\theta_S = 7°$, the tangential component of the flow is stronger (as already observed in Chapter 4 and Chapter 5).

The central recirculation bubble (present for $\theta_S \geq 7°$) is no longer symmetrical, but a similar trend compared to the axisymmetric case can be seen. The bubble becomes bigger in both width and length with increasing swirl and merges with the recirculation zone downstream the annular insert for the cases of $\theta_S = 10°$ and $\theta_S = 18°$. The asymmetry modifies the shape of the central recirculation bubble in both planes. This will be further analysed in the following section with the visualisation of the 3D flow structures.

Similar to the axisymmetric case, the wall separation zones near the wall become smaller with increasing swirl, shrinking towards the expansion corner.

The flow upstream in the inlet pipe are not influenced by the downstream asymmetry, confirming what has been inferred in section 6.3.1 from the swirl level. The flow entering the sudden expansion is still axisymmetric in both planes (XY and XZ) for both displacements.

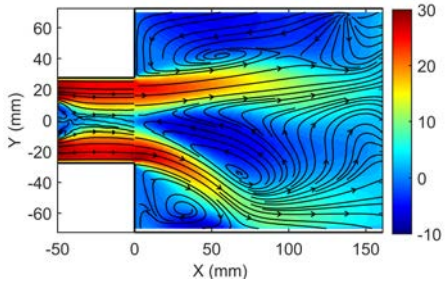

(a) $\theta_S = 7°$, D = 10 mm - XY plane

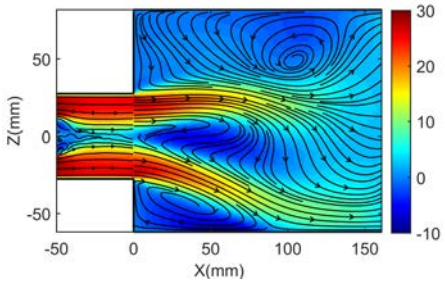

(b) $\theta_S = 7°$, D = 10 mm - XZ plane

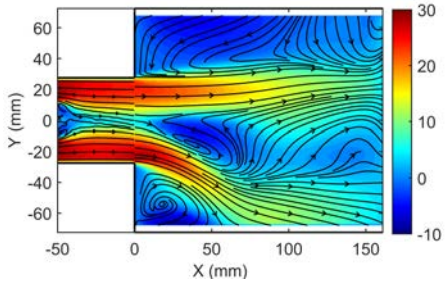

(c) $\theta_S = 7°$, D = 20 mm - XY plane

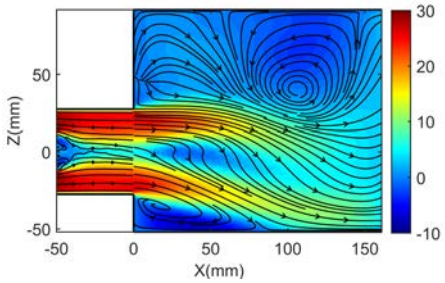

(d) $\theta_S = 7°$, D = 20 mm - XZ plane

Figure 6.13 Axial velocity contour plot inside the sudden expansion, with superimposed vectors (black arrows). Effects of displacement on the velocity in planes XY (left) and XZ (right). D = 10 mm (a-b), D = 20 mm (c-d). Inlet swirl generator angle: $\theta_S = 7°$. Velocity in m/s.

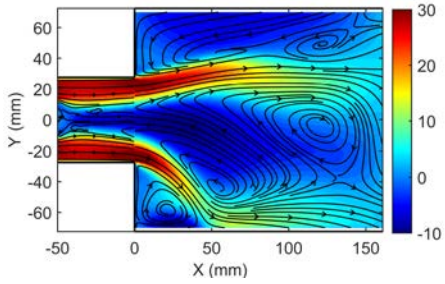

(a) $\theta_S = 10°$, D = 10 mm - XY plane

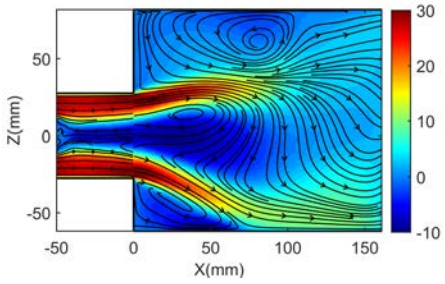

(b) $\theta_S = 10°$, D = 10 mm - XZ plane

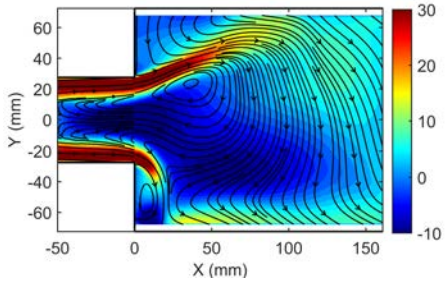

(c) $\theta_S = 10°$, D = 20 mm - XY plane

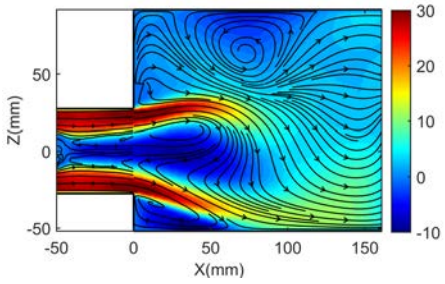

(d) $\theta_S = 10°$, D = 20 mm - XZ plane

Figure 6.14 Axial velocity contour plot inside the sudden expansion, with superimposed vectors (black arrows). Effects of displacement on the velocity in planes XY (left) and XZ (right). D = 10 mm (a-b), D = 20 mm (c-d). Inlet swirl generator angle: $\theta_S = 10°$. Velocity in m/s.

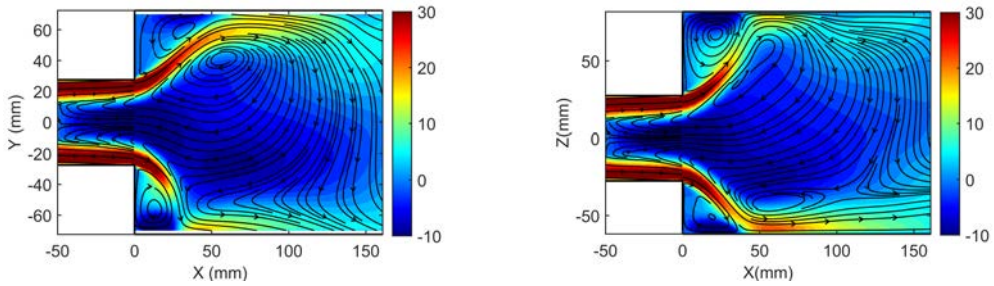

(a) $\theta_S = 18°$, D = 10 mm - XY plane

(b) $\theta_S = 18°$, D = 10 mm - XZ plane

(c) $\theta_S = 18°$, D = 20 mm - XY plane

(d) $\theta_S = 18°$, D = 20 mm - XZ plane

Figure 6.15 Axial velocity contour plot inside the sudden expansion, with superimposed vectors (black arrows). Effects of displacement on the velocity in planes XY (left) and XZ (right). D = 10 mm (a-b), D = 20 mm (c-d). Inlet swirl generator angle: $\theta_S = 18°$. Velocity in m/s.

6.3.3 3D flow structures

The complexity of the flow in asymmetric swirling flow can be appreciated better using 3D plots presented in this section (from Figure 6.16 to Figure 6.20). Three types of plots have been chosen to describe the three-dimensional structures: vortex core lines, streamlines and isosurfaces of zero axial velocity. The jet core for a swirling jet in the asymmetric case is difficult to identify. So, for the swirling flow cases (from Figure 6.17 to Figure 6.20) it is possible to identify the vortex core line, using the definition proposed by Roth (2000), as discussed in section 3.2.6. The iso-surfaces of zero axial velocity (right column in all figures) encompass the reverse flow areas, and can be used to estimate the size of the wall separation zones and the central recirculation bubble formed with swirling flow.

In the axisymmetric case with no swirl (Figure 6.16 (a-b)) the separation zone spans most of the diffuser length, with the main flow reattaching immediately upstream of the monolith. With the introduction of the displacement (Figure 6.16 (c) to (f)), the flow is no longer symmetrical.

Following the streamlines inside the diffuser (Figure 6.16 (a),(c) and (e)), one can see that when the displacement is present, the flow impinging on the monolith near the West wall does not have sufficient space to recirculate back towards the expansion.

Therefore, this returning flow is forced to divert from the axial direction (Figure 6.16 (c) and (e)). It is manifested by "tilting" of the recirculating streamlines (compare streamlines near the West and South walls in (Figure 6.16 (a), (c) and (e)). This feature causes the formation of the secondary cross-flow described in section 6.3.2 This is the purely axial flow in the XZ cross section in the Z>0 half of the diffuser clearly seen in (Figure 6.11d), where the "tilted" streamlines from the separation zone from both halves of the diffuser meet. This is a unique, fully three-dimensional effect that cannot be observed in two-dimensional studies.

The separation zone (size of which can be inferred from the isosurfaces of U - 0 in Figure 6.16b,d,f) becomes narrower along the West wall in the radial direction, while the flow accelerates in the axial direction as discussed before. At the opposite, East wall, the iso-surface becomes shorter in the axial direction, with a "split" in the iso-surface appearing along the East wall at D = 10 mm, and spanning the length of the East wall for D = 20 mm. Thus, the reverse flow part of the wall separation zone transforms from an "extruded doughnut" shape for D = 0 (Figure 6.16 (b)) into an "extruded horseshoe" shape for increasing asymmetry (Figure 6.16 (f)), with the split in the “doughnut” (seen in Figure 6.16 (d) near the East wall) propagating from the expansion point along the East line with increasing inlet displacement.

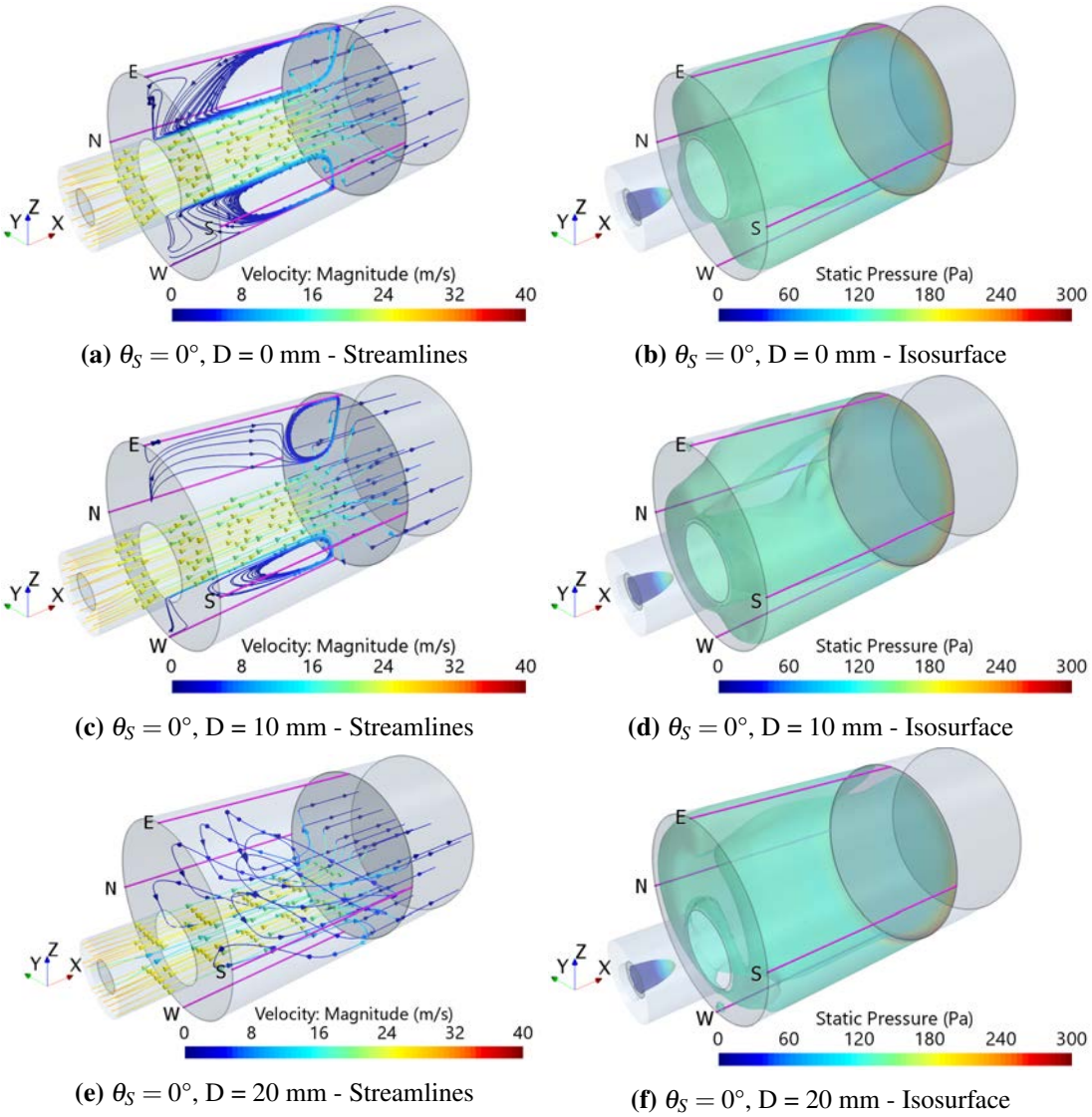

(a) $\theta_S = 0°$, D = 0 mm - Streamlines

(b) $\theta_S = 0°$, D = 0 mm - Isosurface

(c) $\theta_S = 0°$, D = 10 mm - Streamlines

(d) $\theta_S = 0°$, D = 10 mm - Isosurface

(e) $\theta_S = 0°$, D = 20 mm - Streamlines

(f) $\theta_S = 0°$, D = 20 mm - Isosurface

Figure 6.16 3D visualisation of the flow inside the sudden expansion. Streamlines on the left column, isosurface of axial velocity U = 0 m/s and vortex line (black). Effects of displacement: D = 0 mm (a-b), D = 10 mm (c-d), D = 20 mm (e-f). Inlet swirl generator angle: $\theta_S = 0°$.

For the lowest swirl level considered (Figure 6.17), the effect on the flow structures is similar to the axial inflow condition. The presence of low swirl causes the primary flow rotation around the vortex core, without the formation of the central recirculation bubble. Therefore, the flow behaviour in the axisymmetric case is similar to the axial inflow condition, as discussed in section 5.2. The reverse flow near the wall separation zone can be still described as an "extruded doughnut" shape for D = 0 (Figure 6.17 (b)) as for the axial inflow condition.

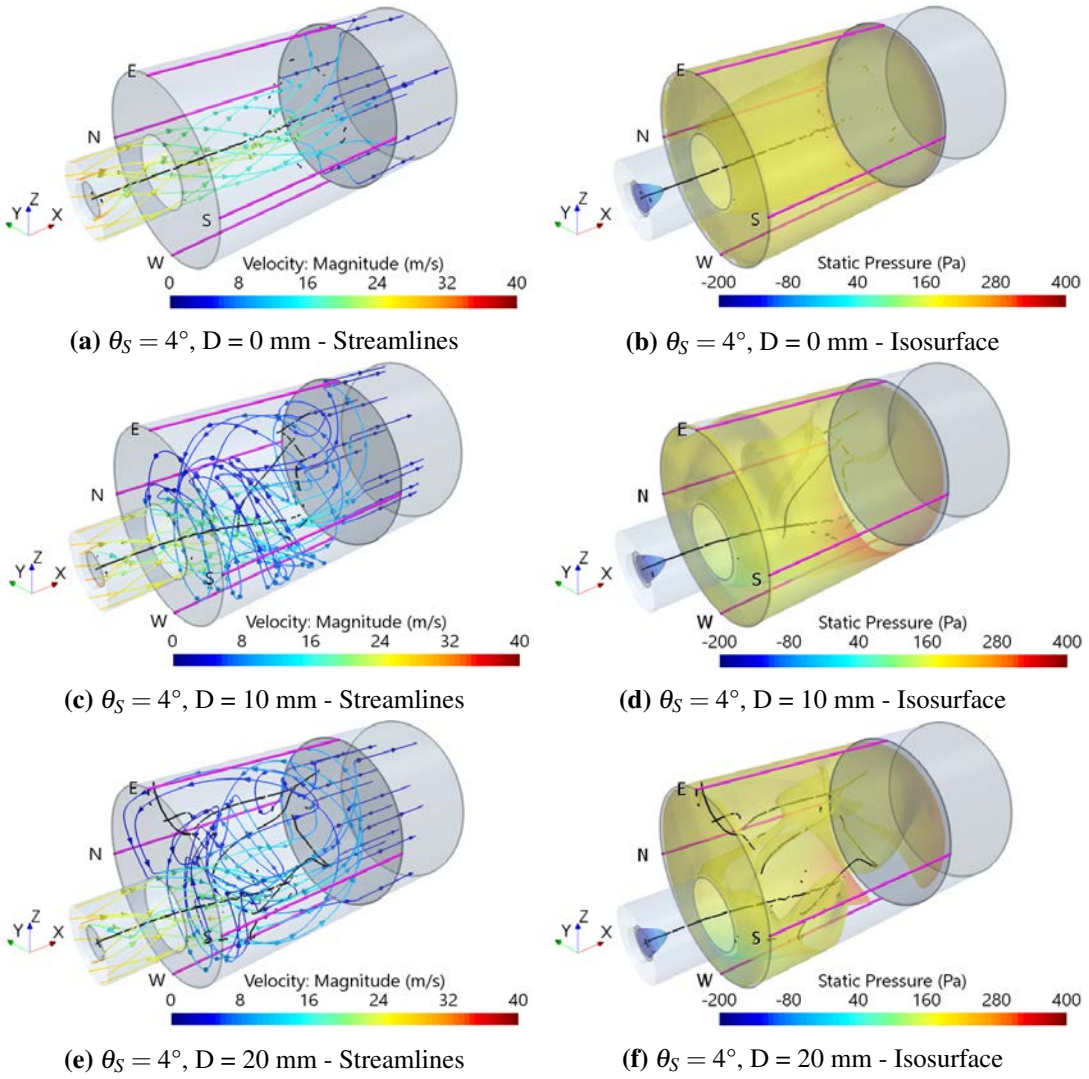

(a) $\theta_S = 4°$, D = 0 mm - Streamlines

(b) $\theta_S = 4°$, D = 0 mm - Isosurface

(c) $\theta_S = 4°$, D = 10 mm - Streamlines

(d) $\theta_S = 4°$, D = 10 mm - Isosurface

(e) $\theta_S = 4°$, D = 20 mm - Streamlines

(f) $\theta_S = 4°$, D = 20 mm - Isosurface

Figure 6.17 3D visualisation of the flow inside the sudden expansion. Streamlines on the left column, isosurface of axial velocity U = 0 m/s and vortex line (black). Effects of displacement: D = 0 mm (a-b), D = 10 mm (c-d), D = 20 mm (e-f). Inlet swirl generator angle: $\theta_S = 4°$.

The introduction of the asymmetry causes a more complex flow redistribution compared to the axial inflow condition. The secondary cross-flow patterns observed with the highest asymmetry for the axial inflow case (Figure 6.17 (e)) are clearly visible with the lower displacement of 10 mm (Figure 6.17 (c)) and become more pronounced with the highest displacement of 20 mm.

The vortex core of the main jet is diverted towards the West line. A secondary rotating structure can be seen for the displacement of 10 mm in towards the North-East region of the sudden expansion (Figure 6.17c and d). The cross-flow is more intense for the 20 mm case with more "tilting" of the streamlines compared to the axial inflow condition (Figure 6.17e). As a consequence, the iso-surface in the South-West region (Figure 6.17f) can not reach the monolith surface, as can be seen in Figure 6.12b and d.

With further increasing swirl, the central recirculation bubble is formed around the vortex core of the jet. The recirculation zone towards the wall is present only close to the sudden expansion section, with the flow re-attaching at around half size of the diffuser (Figure 6.18).

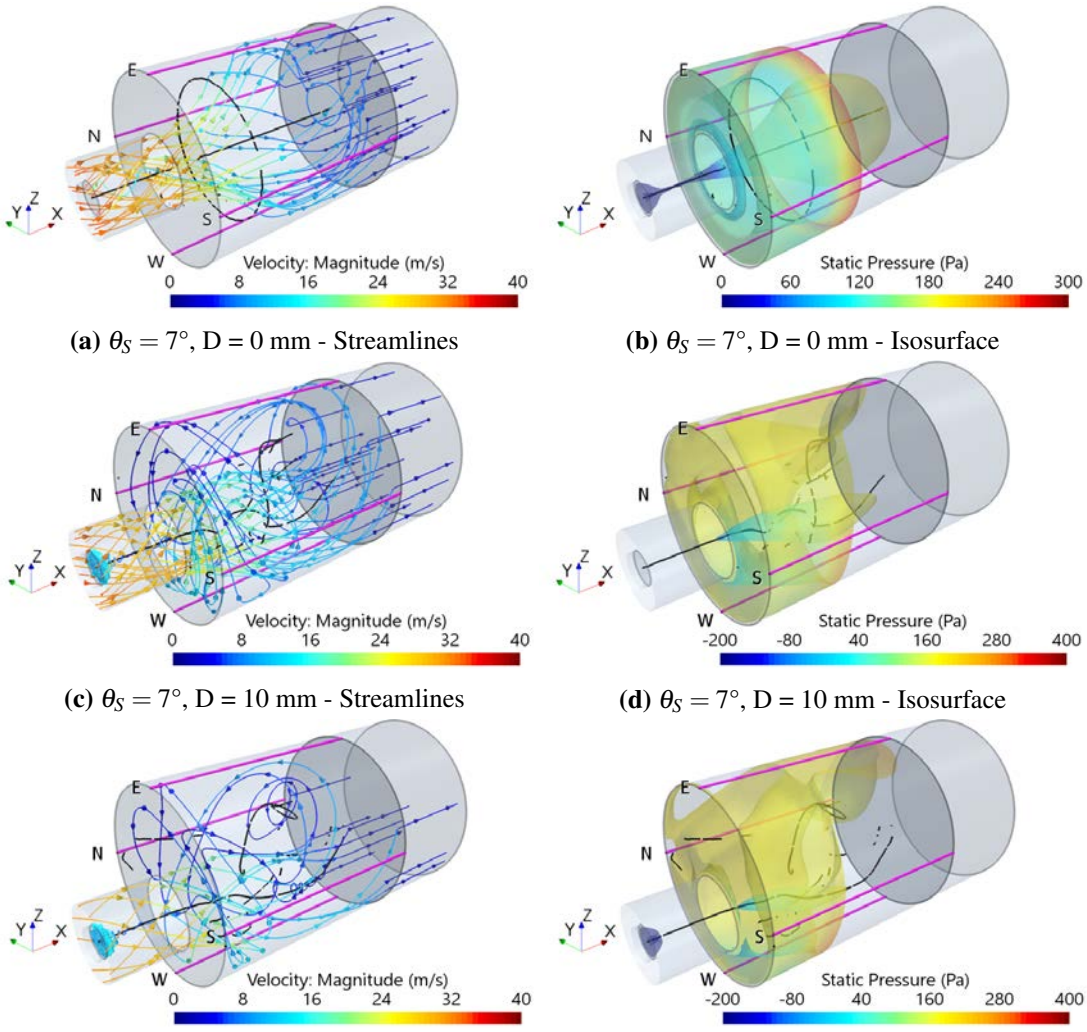

(a) $\theta_S = 7°$, D = 0 mm - Streamlines

(b) $\theta_S = 7°$, D = 0 mm - Isosurface

(c) $\theta_S = 7°$, D = 10 mm - Streamlines

(d) $\theta_S = 7°$, D = 10 mm - Isosurface

(e) $\theta_S = 7°$, D = 20 mm - Streamlines

(f) $\theta_S = 7°$, D = 20 mm - Isosurface

Figure 6.18 3D visualisation of the flow inside the sudden expansion. Streamlines on the left column, isosurface of axial velocity U = 0 m/s and vortex line (black). Effects of displacement: D = 0 mm (a-b), D = 10 mm (c-d), D = 20 mm (e-f). Inlet swirl generator angle: $\theta_S = 7°$.

The presence of asymmetry causes the vortex core line to divert initially towards the closer wall (West) and then deflect towards the centreline, towards the sudden expansion axis (Figure 6.18c to f). The central recirculation bubble is consequently formed around the main vortex axis, shrinking with increasing asymmetry in all the three directions (Figure 6.18d and f). The recirculation zone towards the walls appears extended towards the North-East region, in the positive Z direction.

The secondary cross flow observed for the lower swirl case is visible for this case too (Figure 6.18c and e). The secondary flow streamlines follow the displacement, as a consequence of the modified shape of the recirculation zone towards the wall in the North-East region. The effect of swirl is more pronounced, so that the two flow patterns interweave in the sudden expansion. This phenomenon is clearly visible in the downstream flow distribution presented in the following section.

A similar behaviour has been observed for the two higher swirl levels of $\theta_S = 10°$ and $\theta_S = 18°$.

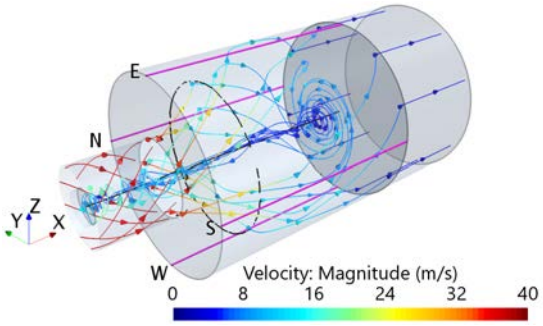

(a) $\theta_S = 10°$, D = 0 mm - Streamlines

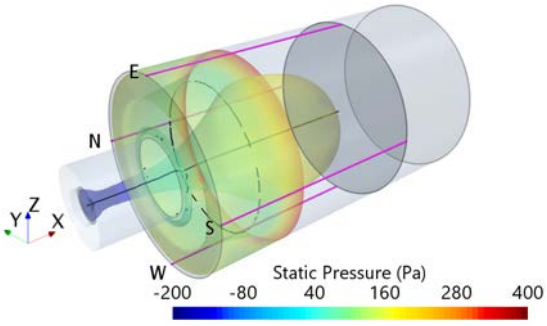

(b) $\theta_S = 10°$, D = 0 mm - Isosurface

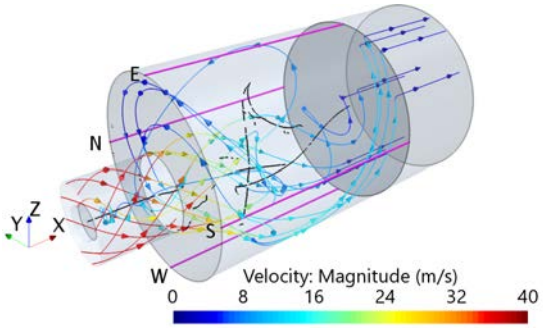

(c) $\theta_S = 10°$, D = 10 mm - Streamlines

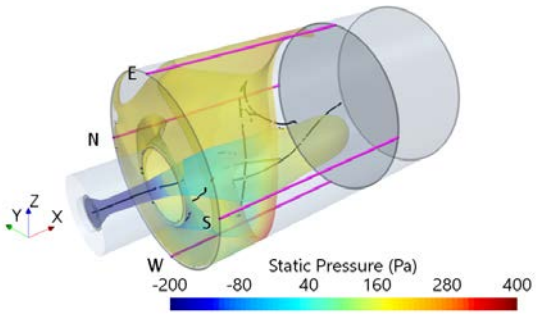

(d) $\theta_S = 10°$, D = 10 mm - Isosurface

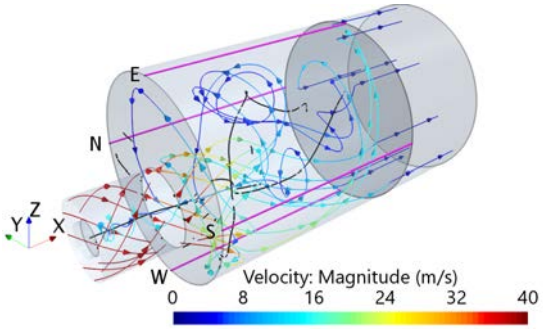

(e) $\theta_S = 10°$, D = 20 mm - Streamlines

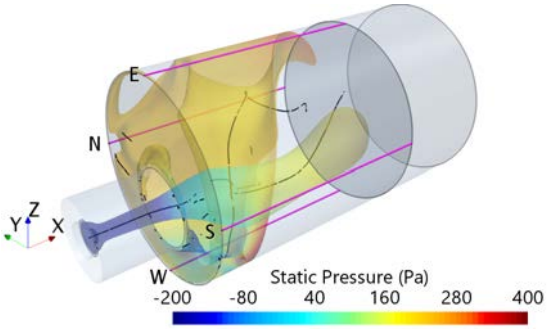

(f) $\theta_S = 10°$, D = 20 mm - Isosurface

Figure 6.19 3D visualisation of the flow inside the sudden expansion. Streamlines on the left column, isosurface of axial velocity U = 0 m/s and vortex line (black). Effects of displacement: D = 0 mm (a-b), D = 10 mm (c-d), D = 20 mm (e-f). Inlet swirl generator angle: $\theta_S = 10°$.

For $\theta_S = 10°$, the presence of swirl forces the wall recirculation zone to shrink, with the reattachment line moving upstream towards the inlet of the diffuser at the West wall

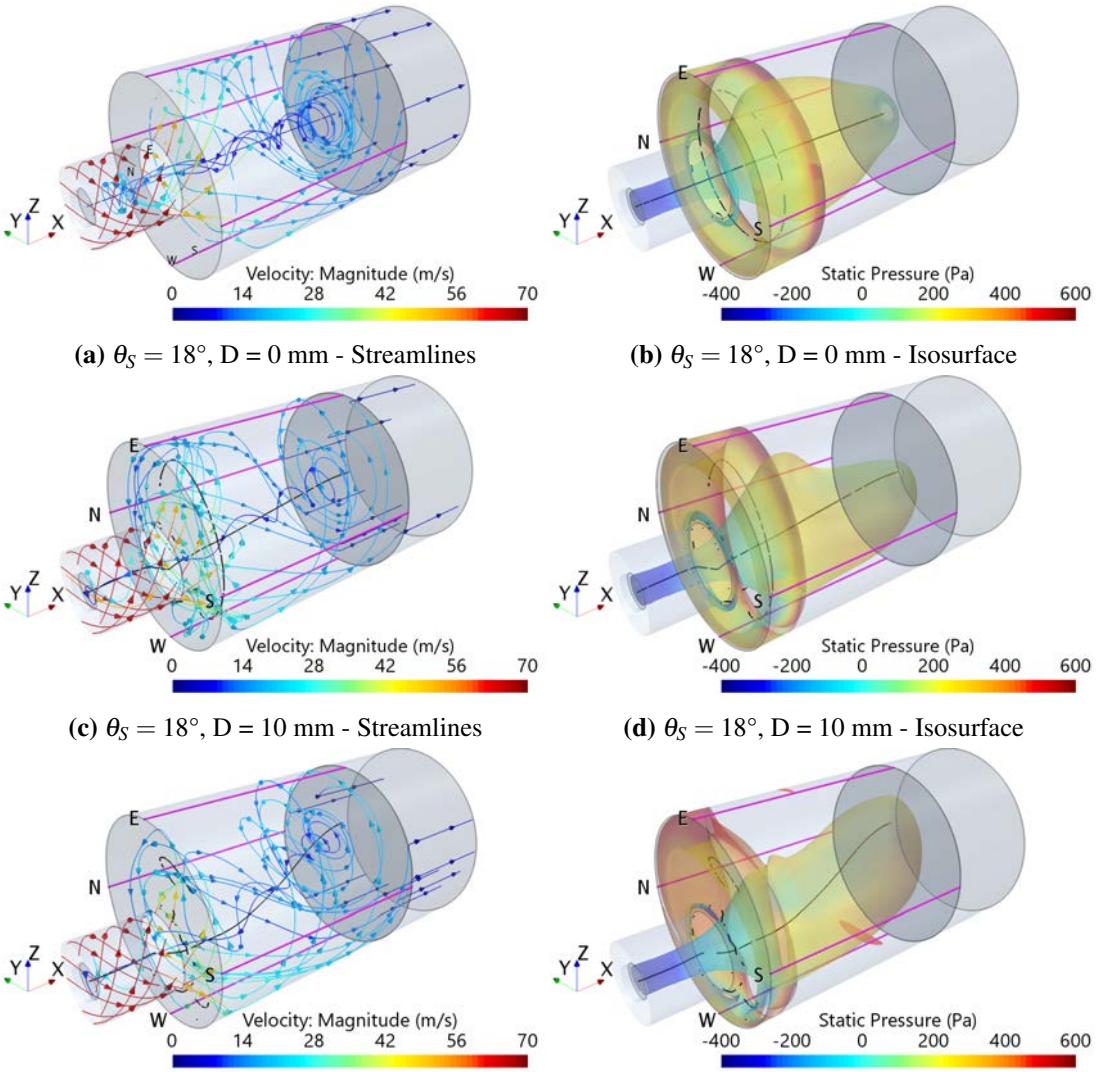

(a) $\theta_S = 18°$, D = 0 mm - Streamlines

(b) $\theta_S = 18°$, D = 0 mm - Isosurface

(c) $\theta_S = 18°$, D = 10 mm - Streamlines

(d) $\theta_S = 18°$, D = 10 mm - Isosurface

(e) $\theta_S = 18°$, D = 20 mm - Streamlines

(f) $\theta_S = 18°$, D = 20 mm - Isosurface

Figure 6.20 3D visualisation of the flow inside the sudden expansion. Streamlines on the left column, isosurface of axial velocity U = 0 m/s and vortex line (black). Effects of displacement: D = 0 mm (a-b), D = 10 mm (c-d), D = 20 mm (e-f). Inlet swirl generator angle: $\theta_S = 18°$.

(Figure 6.19). At the East wall, however, the separation zone does not shrink as much in the axial direction and actually slightly expands towards the monolith. Therefore, the separation zone "doughnut" becomes tilted, with its part at the East wall moving closer to the diffuser.

For $\theta_S = 18°$, the rapidly expanding annular jet causes the separation zone to shrink considerably (Figure 6.20). This overcomes the "tilting" effect of asymmetry, and overall the separation resembles the axisymmetric case, but the reattachment position moves upstream with the increasing displacement.

The size and shape of the central recirculation zone are also affected significantly by the asymmetry, as already described from the PIV data in subsection 6.2.2. The

central recirculation zone is initially diverted towards the nearest West-South wall and then move towards the opposite side (North-East). As a result, the central recirculation bubble with $\theta_S = 10°$ features an axis (vortex core line in Figure 6.19) that starts at the inlet displacement (Z = 0 mm) and ends almost at the centre of the monolith front face for both displacements (Z $\approx$ 10 mm and 20 mm respectively). For the highest swirl number $\theta_S = 18°$ the effect is more pronounced, with the swirl forcing its principal rotation axis towards the North-East portion of the domain (Figure 6.20).

As observed from the PIV data, the shape of the central recirculation bubble is not "regular", in particular for the highest swirl case. The combined effect of asymmetry and swirl causes not only a diversion of the rotation axis of the flow, but highly alters the shape of the central recirculation bubble. The restriction of the size of the central recirculation zone towards the centre of the sudden expansion (X $\approx$ 80 mm) observed from the PIV data is captured by the CFD model (bearing in mind the limitations described in the previous section). This effect can be visualised from the iso-surfaces in Figure 6.19 and in Figure 6.20.

The rotation and associated radial spread of the jet prevails in the initial portion of the expansion, until the jet impinges on the closest (West) wall and the effect of the asymmetry becomes significant (X $\approx$ 50 mm, about one third of the expansion). The flow deviates towards the expansion axis because of the acceleration caused by the asymmetry near the closer (West) wall. The combined effect of the swirl and the acceleration caused by wall proximity tends to "tilt" the jet towards the opposite direction causing the stretch of the central recirculation bubble. The cross-section of the central recirculation bubble is consequently reduced, with the flow expanding towards the far wall. In the remaining portion of the domain, the flow impinges on the monolith, which breaks the equilibrium of forces around the jet. A further radial redistribution occurs, spreading the recirculation zone core on the monolith face. The negative flow re-entering the monolith opposes the swirling flow and causes a strong recirculation area (due to shear) that merges with the central recirculation bubble, with a consequent increased size of the cross-section.

6.3.4 Vorticity distribution

The vorticity component perpendicular to the XZ section (ζ_Y) has been calculated. Although in this configuration the swirling flow features high vorticity in the X-direction, the vorticity in the azimuthal direction is important for identification of the 3-dimensional flow structures and recirculation bubbles in the XZ cross-section. A comparison between the PIV and CFD data is presented here for the axisymmetric case and the asymmetric case with displacement of 20 mm.

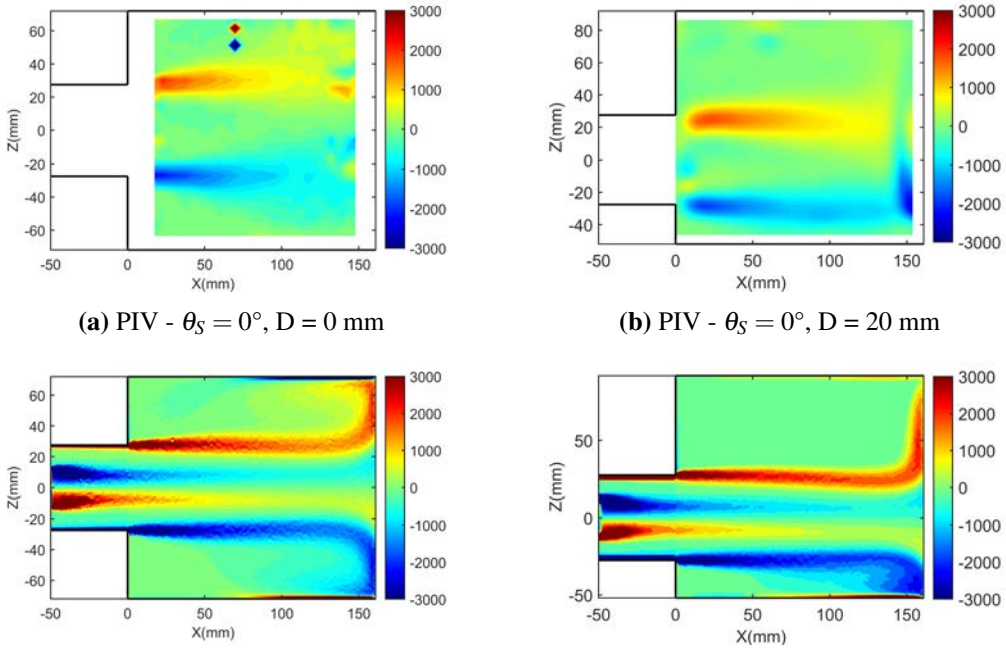

(a) PIV - $\theta_S = 0°$, D = 0 mm

(b) PIV - $\theta_S = 0°$, D = 20 mm

(c) CFD - $\theta_S = 0°$, D = 0 mm

(d) CFD - $\theta_S = 0°$, D = 20 mm

Figure 6.21 Vorticity component ζ_Y. Case: $\theta_S = 0°$, axisymmetric case on the left (a-c) and asymmetric case with displacement of 20 mm on the right (b-d). Comparison between PIV (a-b) and CFD (c-d).

The comparison between the CFD simulations and the PIV results is good for both the axisymmetric and the asymmetric case for all the cases, with the exception of the highest swirl case (Figure 6.21 to Figure 6.25). Generally, the high vorticity is present in the shear layers at the outside and the inside boundaries of the swirling jet, which helps to visualise the flow.

The main effect of the asymmetry on the vorticity in the initial portion of the sudden expansion is a shift towards the closest wall (negative Z) for all the cases, compared to the respective axisymmetric ones (Figure 6.21 to Figure 6.25).

For the axial case (Figure 6.21) two main regions can be identified, spanning the entire length of the expansion up to the monolith region. The origin of the vorticity in those areas can be mainly attributed to shear, since it is at the borders of the core jet. The under-prediction of the shear in the CFD model is clearly shown in the vorticity plots. The CFD results exhibit two secondary areas in the central core (between the two main ones), barely visible in the PIV data.

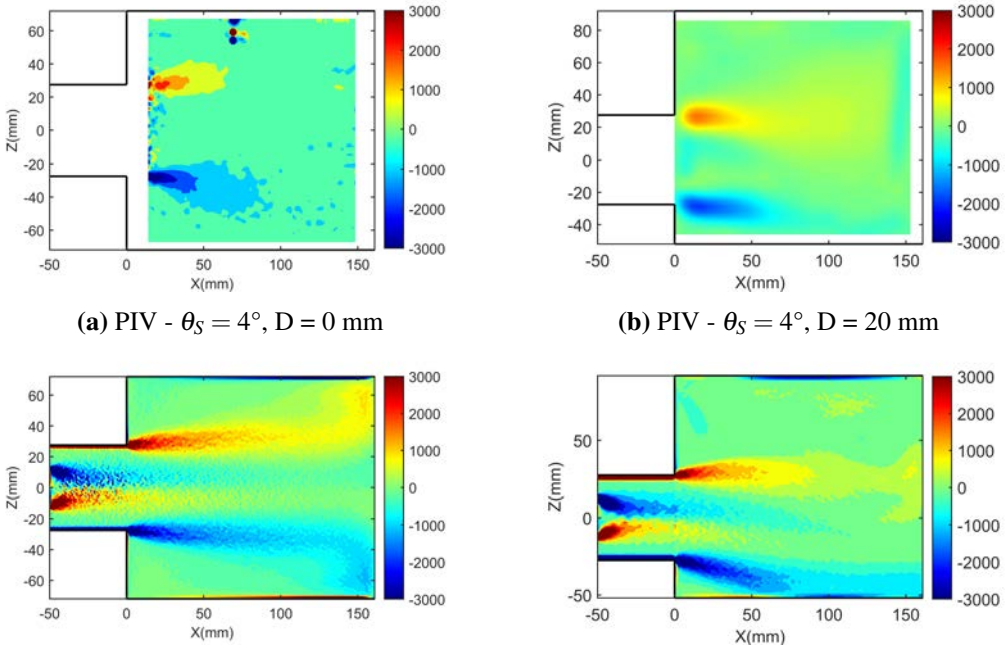

(a) PIV - $\theta_S = 4°$, D = 0 mm

(b) PIV - $\theta_S = 4°$, D = 20 mm

(c) CFD - $\theta_S = 4°$, D = 0 mm

(d) CFD - $\theta_S = 4°$, D = 20 mm

Figure 6.22 Vorticity component ζ_Y. Case: $\theta_S = 4°$, axisymmetric case on the left (a-c) and asymmetric case with displacement of 20 mm on the right (b-d). Comparison between PIV (a-b) and CFD (c-d).

Similarly to the axial case ($\theta_S = 0°$), the low swirl case exhibit a shift of the main structures identified by the vorticity, in both PIV and CFD data (Figure 6.22). The redistribution of the flow towards the walls due to the presence of swirl is captured well by the CFD model, in particular for the asymmetric case. The vorticity loses its strength around half of the domain, due to the radial redistribution caused by the swirl. As discussed before, the CFD simulations under-predict the radial spread of the jet and axial velocity flattening, therefore strong shear layers are still present in the CFD results for $\theta_s = 4°$.

With further increasing swirl (Figure 6.23 and Figure 6.24) the vorticity is initially radially diverted towards the walls. A more pronounced radial redistribution can be seen from the PIV data compared to the CFD model, in particular for the axisymmetric case. This is a further confirmation of the RANS model limitations in the prediction of the radial components of the swirling flows.

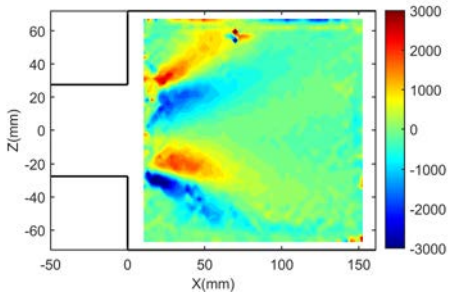

(a) PIV - $\theta_S = 7°$, D = 0 mm

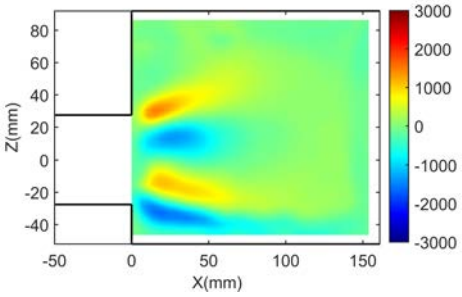

(b) PIV - $\theta_S = 7°$, D = 20 mm

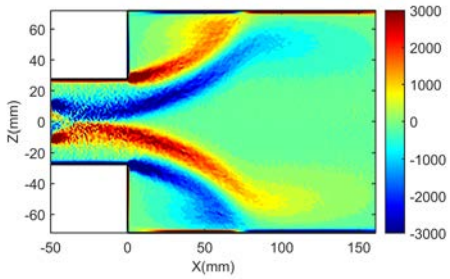

(c) CFD - $\theta_S = 7°$, D = 0 mm

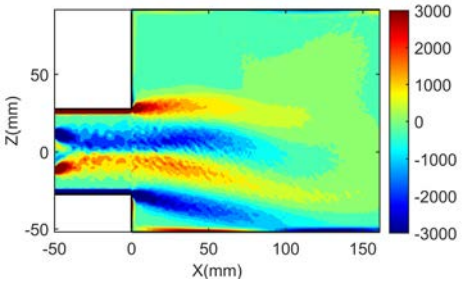

(d) CFD - $\theta_S = 7°$, D = 20 mm

Figure 6.23 Vorticity component ζ_Y. Case: $\theta_S = 7°$, axisymmetric case on the left (a-c) and asymmetric case with displacement of 20 mm on the right (b-d). Comparison between PIV (a-b) and CFD (c-d).

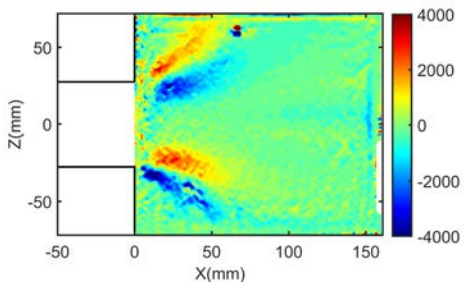

(a) PIV - $\theta_S = 10°$, D = 0 mm

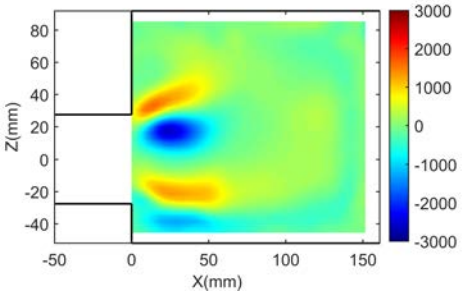

(b) PIV - $\theta_S = 10°$, D = 20 mm

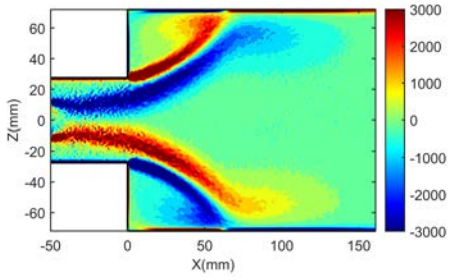

(c) CFD - $\theta_S = 10°$, D = 0 mm

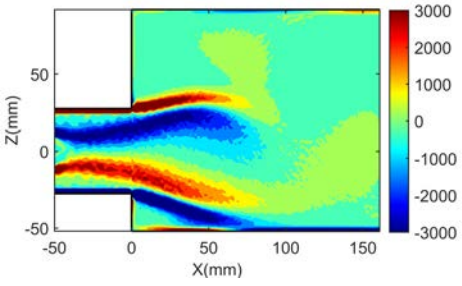

(d) CFD - $\theta_S = 10°$, D = 20 mm

Figure 6.24 Vorticity component ζ_Y. Case: $\theta_S = 10°$, axisymmetric case on the left (a-c) and asymmetric case with displacement of 20 mm on the right (b-d). Comparison between PIV (a-b) and CFD (c-d).

For the maximum swirl level (Figure 6.25), the presence of the asymmetry forces the flow to divert in the positive Z direction, as discussed earlier. As a consequence the vortex is clearly visible in the upper part of the domain for the non symmetric case, while for the axisymmetric case it spans the entire region. No evidence can be found on the CFD data, confirming that the effect of the negative flow re-entering the monolith is too weak to alter the vorticity in the model, resulting in the over-prediction of the vorticity towards the inlet.

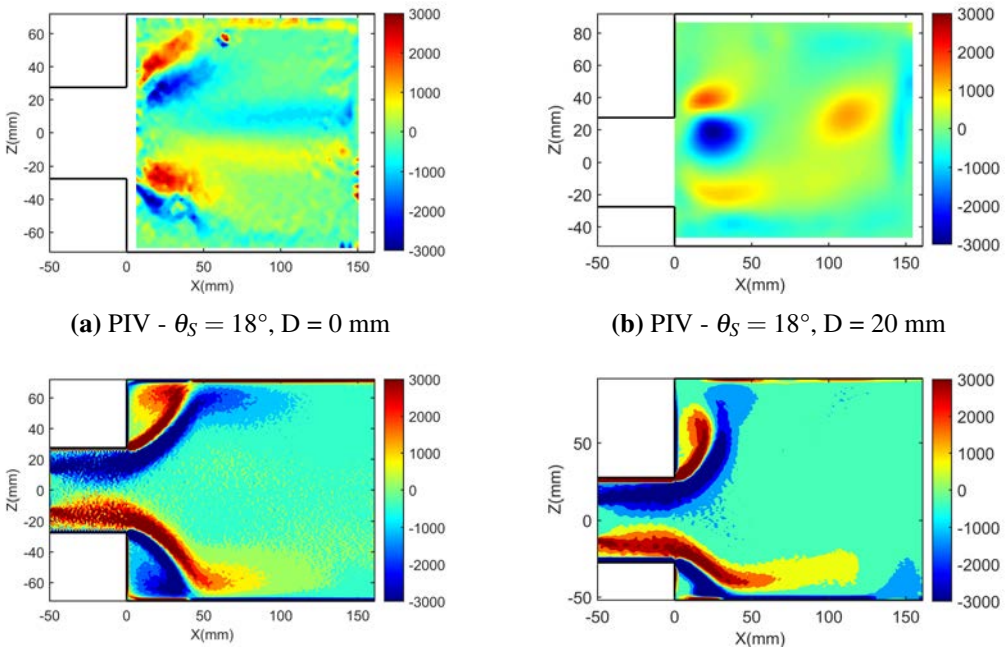

(a) PIV - $\theta_S = 18°$, D = 0 mm

(b) PIV - $\theta_S = 18°$, D = 20 mm

(c) CFD - $\theta_S = 18°$, D = 0 mm

(d) CFD - $\theta_S = 18°$, D = 20 mm

Figure 6.25 Vorticity component ζ_Y. Case: $\theta_S = 18°$, axisymmetric case on the left (a-c) and asymmetric case with displacement of 20 mm on the right (b-d). Comparison between PIV (a-b) and CFD (c-d).

6.3.5 Pressure distribution

The pressure field inside the domain gives further insight into the changes to the flow distribution caused by the asymmetry.

The pressure distribution for the non swirl case ($\theta_S = 0°$) confirms that the primary effect of the asymmetry is a shift of the jet core, for both displacements considered (Figure 6.26 i-j).

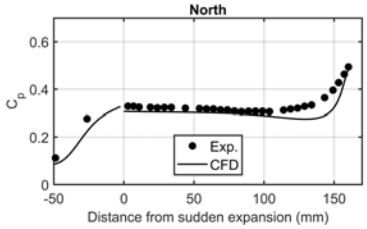

(a) $\theta_S = 0°$, D = 10 mm

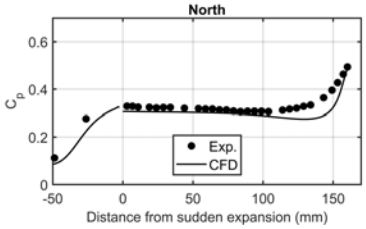

(b) $\theta_S = 0°$, D = 20 mm

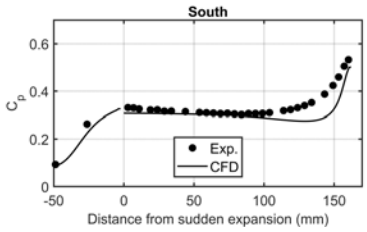

(c) $\theta_S = 0°$, D = 10 mm

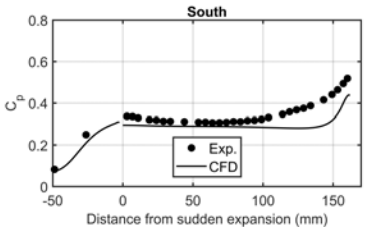

(d) $\theta_S = 0°$, D = 20 mm

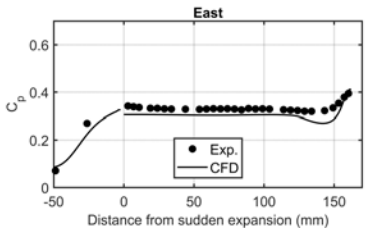

(e) $\theta_S = 0°$, D = 10 mm

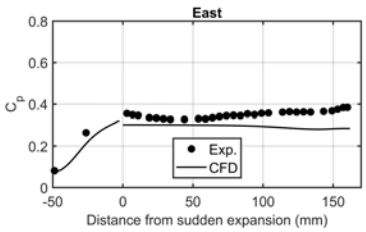

(f) $\theta_S = 0°$, D = 20 mm

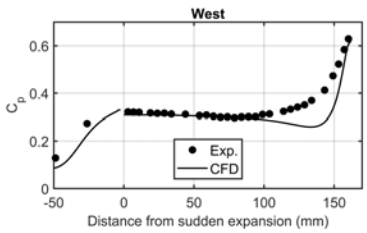

(g) $\theta_S = 0°$, D = 10 mm

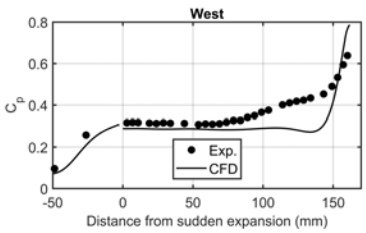

(h) $\theta_S = 0°$, D = 20 mm

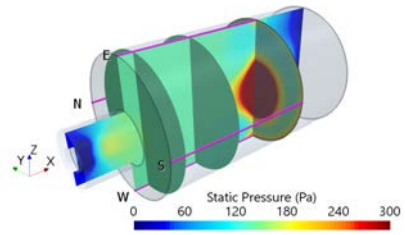

(i) $\theta_S = 0°$, D = 10 mm - Planes

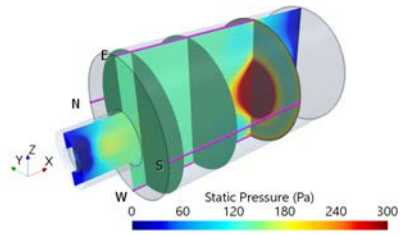

(j) $\theta_S = 0°$, D = 20 mm - Planes

Figure 6.26 Asymmetric sudden expansion - $\theta_S = 0°$, D = 10 mm. Static pressure distribution. Comparison between experimental data (dots) and CFD (line) at the sudden expansion wall: *North* line (a), *East* line (b), *South* line (c) and *West* line (d). CFD contours at XZ section and cross-sections at 15mm, 75 mm and 162 mm (monolith front face) after the sudden expansion. Magenta lines represent the static pressure measurements locations.

The pressure at the inlet appears symmetrical for both displacements considered, as can be seen from the CFD pressure contours. Further confirmation of this point is given

by the static pressure at the walls in the inlet pipe (X < 0), which is symmetrical for both experiments and CFD model (Figure 6.26 a to h).

The flow redistribution in the diffuser due to asymmetry highlighted in the previous sections can be identified from the static pressure plots at the wall. After the expansion point (X > 0) the pressure distribution is similar in the North and South lines (Figure 6.26 a to d) in both model and experiments, confirming the observations made for the velocity (Figure 6.11). The symmetry is not preserved in the XZ cross-section along the West and East lines. A rapid increase of pressure can be seen towards the monolith for the West line (Figure 6.26 g-h), which is closest to the wall (negative Z), confirming the radial spread. At the opposite wall (East line), the pressure rise at the monolith face is not as pronounced. With the D = 20 mm displacement the profile at the East wall is almost flat in both experiments and CFD model (Figure 6.26 f), which indicates that the separation zone spans the whole length of the diffuser at the wall.

The overall agreement with the experimental data is good, with the most appreciable differences just upstream the monolith front face. The pressure build up from X $\approx$ 160 mm is more pronounced in the CFD results, compared to the experiments. This aspect is the result of a combination of factors already discussed for the axisymmetric case (Chapter 5). The RANS model adopted under-predicts jet spread in the radial direction as it traverses the diffuser (Figure 6.5), resulting in a more dramatic flow deceleration just upstream of the monolith face.

The trend already seen for the low swirl case ($\theta_S = 4°$) in the axisymmetric configuration is confirmed for both non symmetric cases (Figure 6.27). The presence of swirl causes the increase in the radial pressure gradient, and thus a general increase of the pressure towards the diffuser wall, which is correctly captured by the CFD model (Figure 6.27).

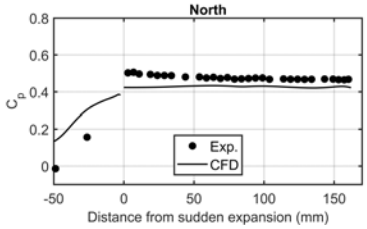

(a) $\theta_S = 4°$, D = 10 mm

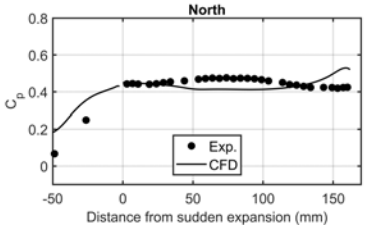

(b) $\theta_S = 4°$, D = 20 mm

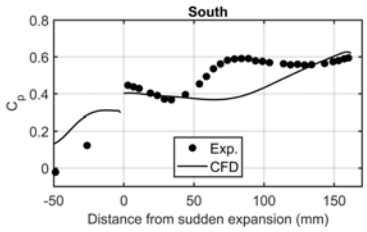

(c) $\theta_S = 4°$, D = 10 mm

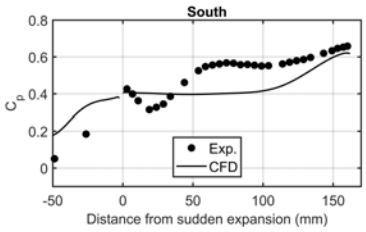

(d) $\theta_S = 4°$, D = 20 mm

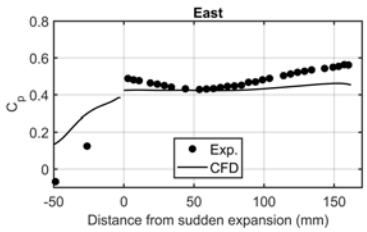

(e) $\theta_S = 4°$, D = 10 mm

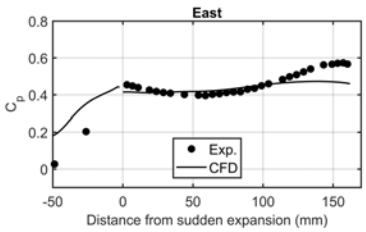

(f) $\theta_S = 4°$, D = 20 mm

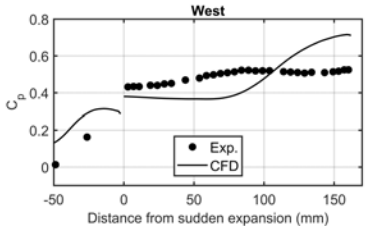

(g) $\theta_S = 4°$, D = 10 mm

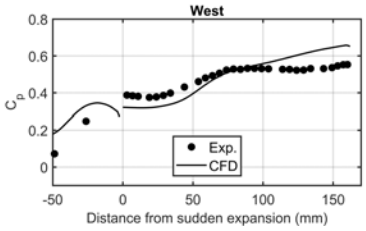

(h) $\theta_S = 4°$, D = 20 mm

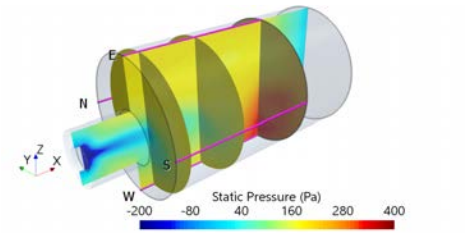

(i) $\theta_S = 4°$, D = 10 mm - Planes

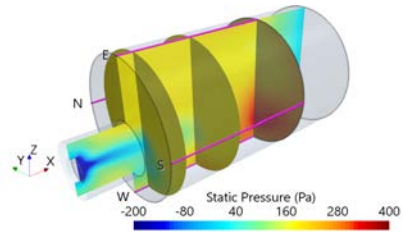

(j) $\theta_S = 4°$, D = 20 mm - Planes

Figure 6.27 Asymmetric sudden expansion - $\theta_S = 4°$, D = 10 mm. Static pressure distribution. Comparison between experimental data (dots) and CFD (line) at the sudden expansion wall: *North* line (a), *East* line (b), *South* line (c) and *West* line (d). CFD contours at XZ section and cross-sections at 15mm, 75 mm and 162 mm (monolith front face) after the sudden expansion. Magenta lines represent the static pressure measurements locations.

The pressure contours in the inlet pipe confirm that the flow is almost symmetrical for both cases in the CFD model (Figure 6.27 i-j), with small effects of the asymmetry just upstream the sudden expansion section. These changes can be identified in the static

pressure distribution at the inlet wall between X $\approx$ -30 mm and X = 0 mm (Figure 6.27 a-h). Unfortunately, no data are available from the experiments in that area to confirm this effect.

The pressure distribution in the sudden expansion exhibits a similar trend for both displacements. Differences with the experimental data can be seen in the prediction of the pressure distribution at the walls, confirming that the CFD model tends to under-predict the radial distribution of the flow, as already discussed for the same swirl level in Chapter 5. While the wall pressure distribution at the North and East lines is predicted reasonably well by the CFD (Figure 6.27 a,b,e,f), the predictions for the South and West lines differ significantly. The experimental data feature a clear pressure peak at the West wall, where the swirling jet impinges on the wall, indicating that the effect of swirl caused the wall separation zone to shrink. The simulations, however, still show the wall pressure profile indicating the separation zone spanning the whole length of the diffuser. This confirms the earlier conclusions that the flow in the simulations for the low swirl case still behaves very similarly to the no swirl case, while in the experiments the effect of swirl on flow redistribution is already very pronounced.

The pressure distribution for the high swirl cases of $\theta_S = 7°$ and $\theta_S = 10°$ and the very high swirl case of $\theta_S = 18°$ reflect the complexity of the flow (Figure 6.28 to Figure 6.30).

The negative pressure area clearly visible at the inlet in Figure 6.28i,j and Figure 6.29i,j (downstream the annular pipe insert, where a small wake is present) expands up to the sudden expansion section, confirming the presence of the adverse axial pressure gradient typical of high swirl cases already observed in Chapter 5. The formation of the central recirculation bubble is a consequence of this adverse pressure gradient (higher pressure at the wall, lower pressure towards the axis), which extends further downstream inside the sudden expansion, more obvious for the $\theta_S = 10°$ case. The effect of the asymmetry is clearly visible, with the area of low pressure indicating the centre of the recirculation zone being diverted towards the closer wall (South - West area) and then shifted towards the opposite side (North - East area).

This is reflected in the plots of the static pressure at the wall (Figure 6.28 a to h and Figure 6.29 a to h), with high pressure gradient clearly visible at the South and West lines, confirming that the flow is initially driven towards the closer wall (West), impinges on it (X $\approx$ 50 mm, where the maximum is observed) and it is then diverted towards the South wall, for which a smoother pressure raise can be seen towards the monolith front face.

The overall agreement between experiments and CFD is good, with the CFD predicting the peak pressure slightly downstream for both swirl levels, confirming the trend observed in the previous section.

Similar changes in the pressure distribution can be seen for the high swirl level $\theta_S = 18°$ considered, for both displacements. A more pronounced adverse pressure gradient towards the expansion axis can be seen for both displacements (Figure 6.30 i-j). The lower pressure area follows the displacement of the central recirculation bubble observed in the previous sections and reaches the monolith front face.

Similar to the lower swirl cases ($\theta_S = 7°$ and $\theta_S = 10°$), high pressure impingement points are clearly visible in the measurements at the West line and South line, followed by a slight increase at the East line.

The under-prediction of the swirl level at the inlet (subsection 6.3.1) is reflected by the under-prediction of static pressure at the inlet (Figure 6.30). However, the CFD over-predicts the pressure at the impingement points inside the sudden expansion, confirming the tendency of the RANS model to under-estimate the radial redistribution of the flow.

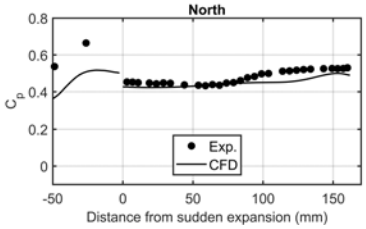

(a) $\theta_S = 7°$, D = 10 mm

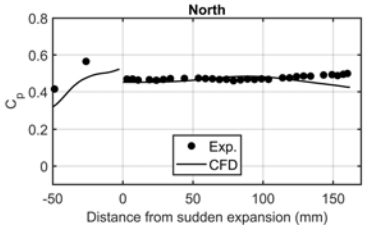

(b) $\theta_S = 7°$, D = 20 mm

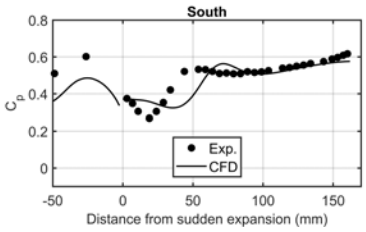

(c) $\theta_S = 7°$, D = 10 mm

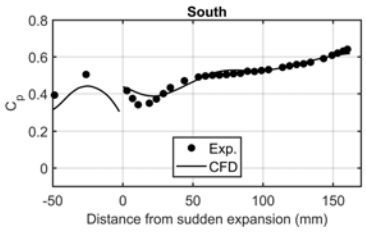

(d) $\theta_S = 7°$, D = 20 mm

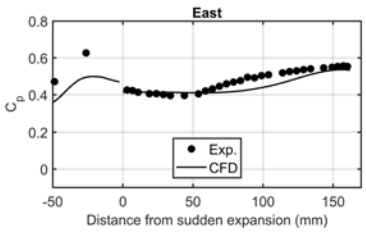

(e) $\theta_S = 7°$, D = 10 mm

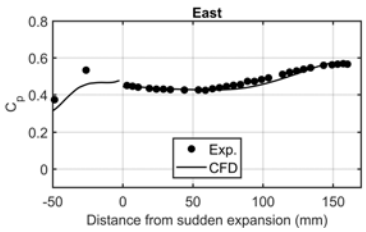

(f) $\theta_S = 7°$, D = 20 mm

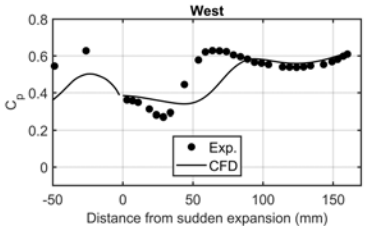

(g) $\theta_S = 7°$, D = 10 mm

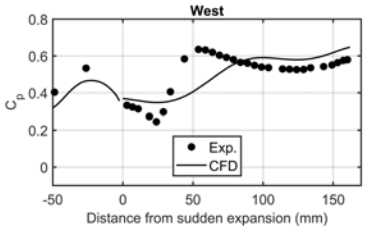

(h) $\theta_S = 7°$, D = 20 mm

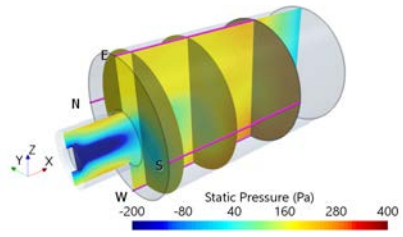

(i) $\theta_S = 7°$, D = 10 mm - Planes

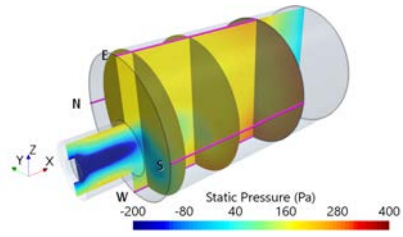

(j) $\theta_S = 7°$, D = 20 mm - Planes

Figure 6.28 Asymmetric sudden expansion - $\theta_S = 7°$, D = 10 mm. Static pressure distribution. Comparison between experimental data (dots) and CFD (line) at the sudden expansion wall: *North* line (a), *East* line (b), *South* line (c) and *West* line (d). CFD contours at XZ section and cross-sections at 15mm, 75 mm and 162 mm (monolith front face) after the sudden expansion. Magenta lines represent the static pressure measurements locations.

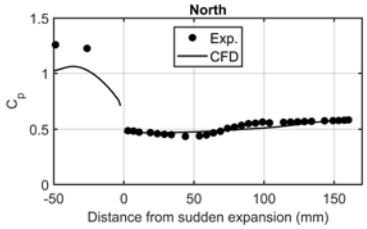

(a) $\theta_S = 10°$, D = 10 mm

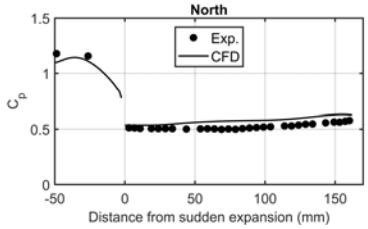

(b) $\theta_S = 10°$, D = 20 mm

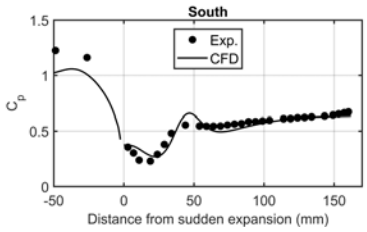

(c) $\theta_S = 10°$, D = 10 mm

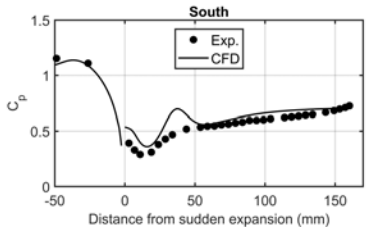

(d) $\theta_S = 10°$, D = 20 mm

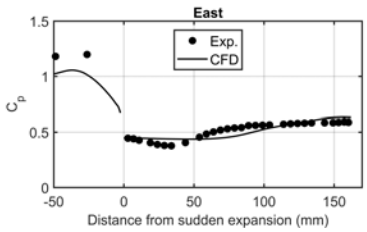

(e) $\theta_S = 10°$, D = 10 mm

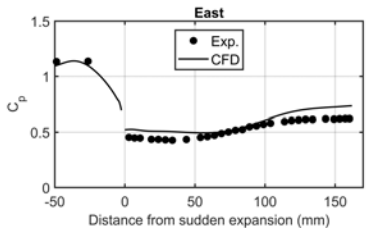

(f) $\theta_S = 10°$, D = 20 mm

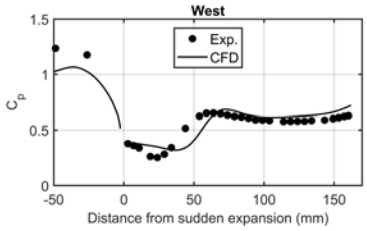

(g) $\theta_S = 10°$, D = 10 mm

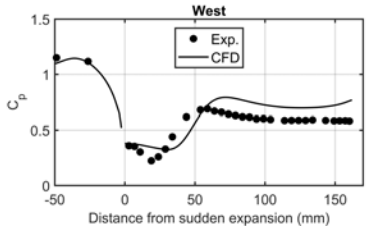

(h) $\theta_S = 10°$, D = 20 mm

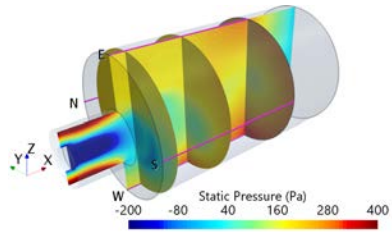

(i) $\theta_S = 10°$, D = 10 mm - Planes

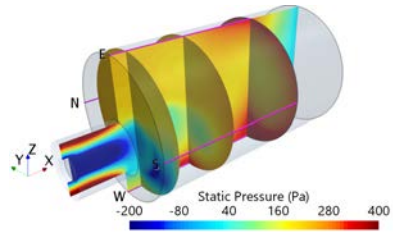

(j) $\theta_S = 10°$, D = 20 mm - Planes

Figure 6.29 Asymmetric sudden expansion - $\theta_S = 10°$, D = 10 mm. Static pressure distribution. Comparison between experimental data (dots) and CFD (line) at the sudden expansion wall: *North* line (a), *East* line (b), *South* line (c) and *West* line (d). CFD contours at XZ section and cross-sections at 15mm, 75 mm and 162 mm (monolith front face) after the sudden expansion. Magenta lines represent the static pressure measurements locations.

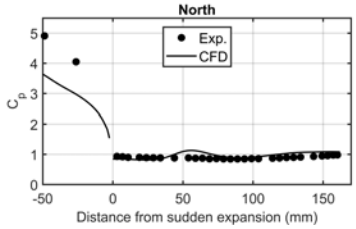

(a) $\theta_S = 18°$, D = 10 mm

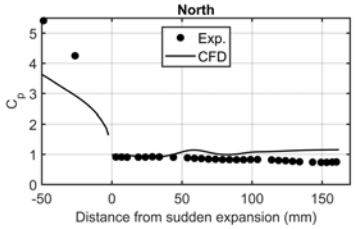

(b) $\theta_S = 18°$, D = 20 mm

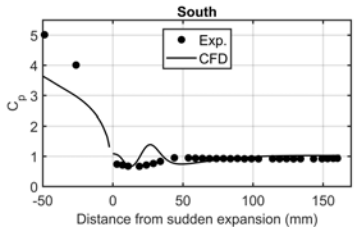

(c) $\theta_S = 18°$, D = 10 mm

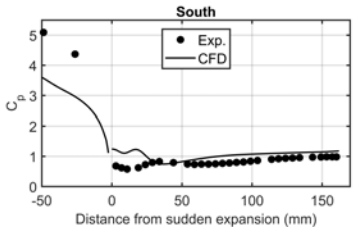

(d) $\theta_S = 18°$, D = 20 mm

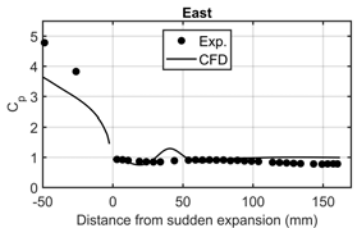

(e) $\theta_S = 18°$, D = 10 mm

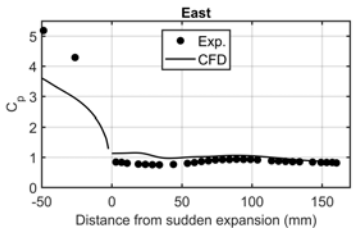

(f) $\theta_S = 18°$, D = 20 mm

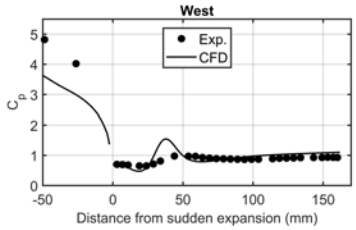

(g) $\theta_S = 18°$, D = 10 mm

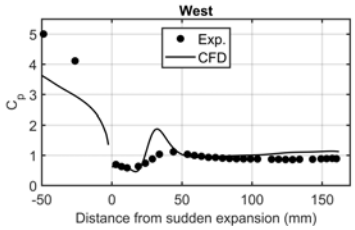

(h) $\theta_S = 18°$, D = 20 mm

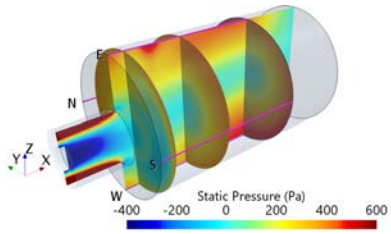

(i) $\theta_S = 18°$, D = 10 mm - Planes

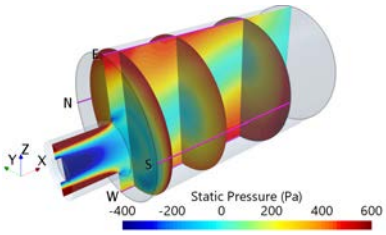

(j) $\theta_S = 18°$, D = 20 mm - Planes

Figure 6.30 Asymmetric sudden expansion - $\theta_S = 18°$, D = 20 mm. Static pressure distribution. Comparison between experimental data (dots) and CFD (line) at the sudden expansion wall: *North* line (a), *East* line (b), *South* line (c) and *West* line (d). CFD contours at XZ section and cross-sections at 15mm, 75 mm and 162 mm (monolith front face) after the sudden expansion. Magenta lines represent the static pressure measurements locations.

6.3.6 Flow downstream the diffuser

The velocity contours downstream of the monolith provide further evidence that the sudden expansion displacement does not result in a simple shift of the jet.

The shape of the jet core for the non swirl case ($\theta_S = 0°$) is modified by the presence of the asymmetry, causing a change from a circular pattern (Figure 5.22 a and b) to a oval pattern elongated in the direction of the asymmetry (Z) for both displacements considered (10 mm in Figure 6.31a and b and 20 mm in Figure 6.32 a and b). This effect is well captured by the CFD model, as shown by the good agreement with the HWA data. The presence of the secondary flow pattern discussed in subsection 6.3.2, where purely axial flow was observed in the XZ plane for Z > 0, causes an extra axial velocity peak observed in the positive Y direction (towards the East line), in both CFD and HWA results (10 mm in Figure 6.31a and b and 20 mm in Figure 6.32 a and b).

With introduction of swirl, the measurements show flow redistribution towards the walls (10 mm in Figure 6.31 c to j and 20 mm in Figure 6.32 c and j)), as expected from the axisymmetric case, given the transition to wall jet (Figure 5.23).

The position of the low velocity region in the middle, however, does not correspond to the position of the inlet pipe upstream. This is consistent with the distortion of the central recirculation zone and the swirling jet position in the diffuser observed from the PIV data and correctly predicted by the CFD (subsection 6.2.2).

The shift of the low velocity area is consistent with the observations made in the previous sections. The combined effect of swirl and asymmetry causes a distortion of the vortex core line. The change of the rotation axis of the flow, that no longer corresponds to the sudden expansion axis, is consistent for all the cases. The initial diversion towards the closer wall is caused by the presence of the asymmetry. The change in the direction of the rotation axis (towards the positive Z direction) is caused by the swirl, with more pronounced shift with increasing swirl level. This change is reflected in the downstream low velocity areas (blue).

The complex structure of the central recirculation zone, which features two counter-rotating parts inside the sudden expansion from the CFD model (Figure 6.17 to Figure 6.20) are confirmed by the presence of the high velocity areas downstream the monolith, with the two zones "enclosing each other". This effect is clearly visible for the cases from $\theta_S = 4°$, $\theta_S = 7°$ and $\theta_S = 10°$ (10 mm in Figure 6.31 c to h and 20 mm in Figure 6.32 c and h). It is less pronounced in the experimental results, however still visible in many cases, e.g. Figure 6.31g.

The overall agreement with the HWA data is good, with the CFD model capturing the general trend of transition to the "wall flow" jet. A reasonable agreement is reached between the experiments and the simulations in terms of velocity magnitudes and

general flow structure, with the CFD model under-predicting the minimum velocities, towards the centre of the sudden expansion section. This is related to the absence of negative flow in the CFD model at that section, which can be inferred from the experimental data. This needs further confirmation, since the experimental technique adopted could not determine the flow direction, as already discussed in subsection 5.1.2. In addition, the over-sampling towards the axis of the section (Figure 5.5 b) captures a smoother velocity profile compared to the other areas due to the local averaging adopted for the experimental data, as already discussed in subsection 5.1.2 and subsection 5.3.4.

The CFD model, as discussed in subsection 6.2.2 can correctly capture the diversion of the central recirculation bubble towards the positive Z direction observed from PIV. In addition, the similarity with the other data analysed suggests that the same trend should be observed for all the cases also downstream the monolith. The under-prediction of the jet axis rotation from CFD (Figure 6.31 i and j) can not explain the sudden shift observed for the $\theta_S = 18°$ with 20 mm, so the differences observed between the HWA data and the CFD model in Figure 6.32 i and j can be attributed to experimental error.

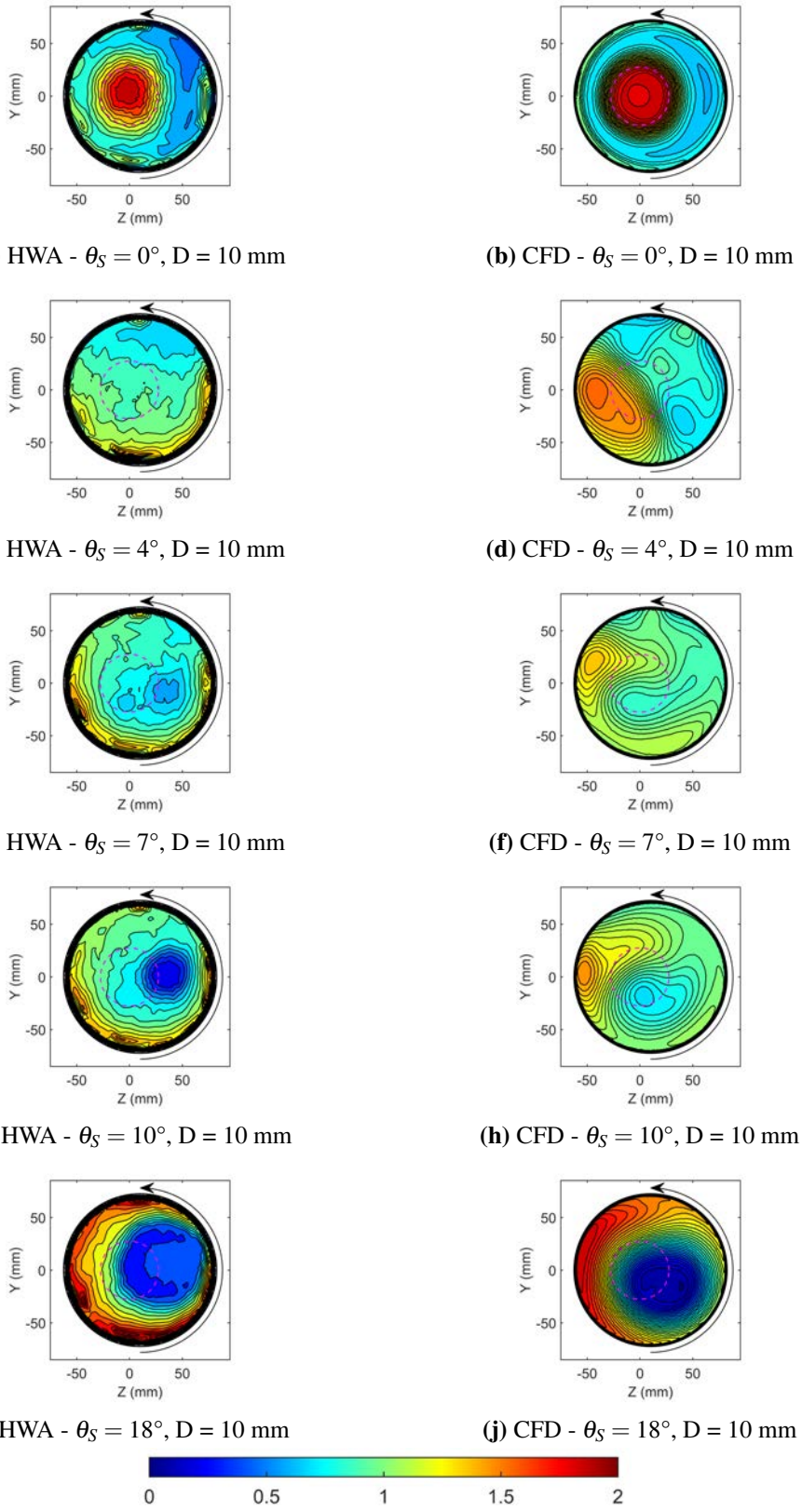

(a) HWA - $\theta_S = 0°$, D = 10 mm

(b) CFD - $\theta_S = 0°$, D = 10 mm

(c) HWA - $\theta_S = 4°$, D = 10 mm

(d) CFD - $\theta_S = 4°$, D = 10 mm

(e) HWA - $\theta_S = 7°$, D = 10 mm

(f) CFD - $\theta_S = 7°$, D = 10 mm

(g) HWA - $\theta_S = 10°$, D = 10 mm

(h) CFD - $\theta_S = 10°$, D = 10 mm

(i) HWA - $\theta_S = 18°$, D = 10 mm

(j) CFD - $\theta_S = 18°$, D = 10 mm

Figure 6.31 HWA (left) and CFD (right) velocity data comparison 30 mm downstream the monolith section. Velocity has been non-dimensionalised with the average value at the section ($\bar{U} = 3.22$, more details in subsection 5.1.4.) Displacement of 10 mm, increasing swirl levels from top to bottom. Velocity in m/s.

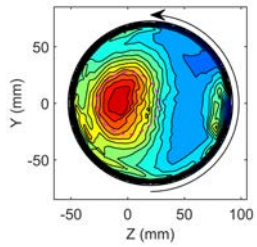

(a) HWA - $\theta_S = 0°$, D = 20 mm

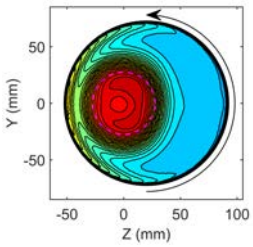

(b) CFD - $\theta_S = 0°$, D = 20 mm

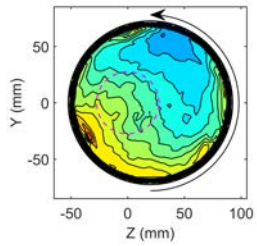

(c) HWA - $\theta_S = 4°$, D = 20 mm

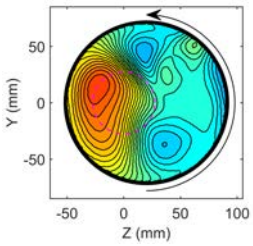

(d) CFD - $\theta_S = 4°$, D = 20 mm

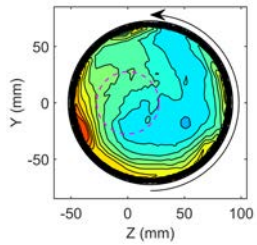

(e) HWA - $\theta_S = 7°$, D = 20 mm

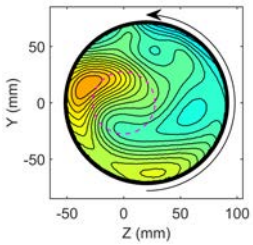

(f) CFD - $\theta_S = 7°$, D = 20 mm

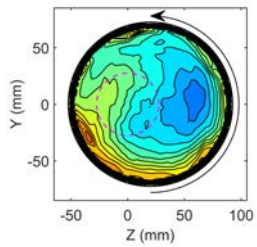

(g) HWA - $\theta_S = 10°$, D = 20 mm

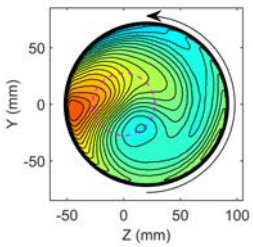

(h) CFD - $\theta_S = 10°$, D = 20 mm

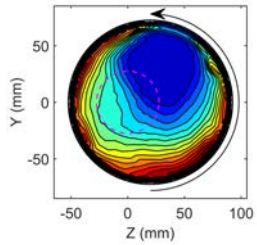

(i) HWA - $\theta_S = 18°$, D = 20 mm

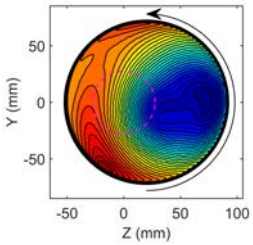

(j) CFD - $\theta_S = 18°$, D = 20 mm

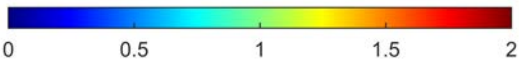

Figure 6.32 HWA (left) and CFD (right) velocity data comparison 30 mm downstream the monolith section. Velocity has been non-dimensionalised with the average value at the section ($\bar{U} = 3.22$, more details in subsection 5.1.4.) Displacement of 20 mm, increasing swirl levels from top to bottom. Velocity in m/s.

6.4 Global flow parameters

Pressure drop

The pressure drop through the entire domain and through the monolith region is an important global characteristic for practical applications, and thus has been estimated from the CFD simulations, similarly with the axisymmetric case (section 5.3.3).

The general trend for the asymmetric case (Figure 6.33) is similar to that observed for the axisymmetric case (Figure 5.21).

The increase of the pressure drop with the increasing swirl level is seen for both displacements, confirming that the main contribution to the energy loss is due to the formation of the swirl trough the swirl generator. The effects of the asymmetry are not appreciable.

The pressure drop through the monolith confirms that it is almost independent from the asymmetry, with slight differences between the two displacements considered for all the cases.

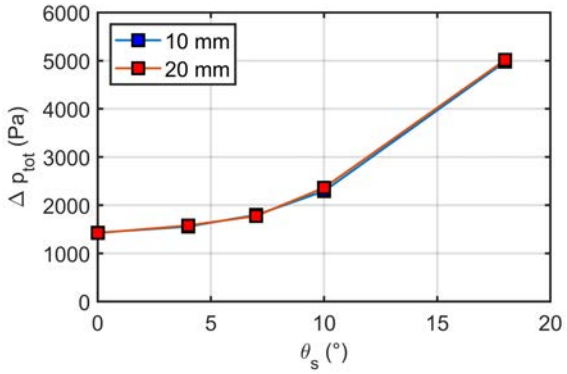

(a) Δp - Inlet/Outlet

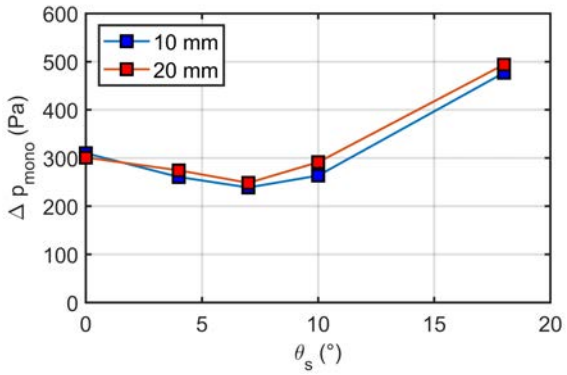

(b) Δp - Monolith

Figure 6.33 Asymmetric diffuser: total pressure drop through the entire domain, inlet section - outlet section (a), through the monolith region (b). Displacement of 10 mm (blue squares), displacement of 20 mm (red squares).

The Δp through the monolith (Figure 6.33b) exhibits the same trend observed for the axisymmetric case, suggesting the presence of an optimal swirl level at which the swirl is beneficial to minimise the pressure losses. A reduction of the pressure drop through the monolith can be observed for the swirl levels of $\theta_S = 4°$ and $\theta_S = 7°$, compared to the non swirl case.

This trend confirms a reduction of pressure losses with low swirl between S = 0.26 and S = 0.50, as for the axisymmetric case. It is possible to conclude that the presence of swirl is still beneficial in terms of pressure losses, even in presence of asymmetry.

Uniformity index

Another parameter important in practical applications is the flow uniformity index inside the device (catalyst monolith in this case). The uniformity index has been calculated downstream the monolith section for all the cases presented, using the definition presented in subsection 3.3.2.

As already discussed in subsection 5.3.4 and subsection 6.3.6 with the sampling technique used by Rusli (2019) (presented in subsection 5.1.2) it is not possible to establish the flow direction and determine the presence of negative flow. The results presented in Table 6.3 include the results of the UI index from the HWA data, however the data corresponding to $\theta_S = 10°$ and $\theta_S = 18°$ are affected by this error.

The most uniform flow distribution for the axisymmetric configuration corresponds to $\theta_s = 4°$ in the experiments and $\theta_s = 7°$ in the CFD model. In presence of asymmetry, similar values can be seen for the $\theta_s = 4°$ and $\theta_s = 7°$ cases from HWA, while the CFD model predicts a better uniformity index for the $\theta_s = 7°$ case. This suggests that the effect of the asymmetry might be beneficial for better flow mixing for low swirl levels. The overall trend suggests that the flow uniformity is driven by the changes in the swirl level, rather then by changes due to the asymmetry. This is reassuring for the engineering applications, where the configuration is rarely symmetric. The benefit in terms of flow uniformity is linked to the benefit in pressure drop through the monolith (section 6.4), confirming that an optimal swirl level exists (between S $\approx$ 0.29 and S $\approx$ 0.50), at which the presence of swirl is beneficial for flow uniformity and pressure drop.

Table 6.3 Asymmetric diffuser: uniformity index (UI). Comparison between the value calculated from HWA data and CFD for each swirl generator angle considered (θ_s) and for the three inlet pipe displacements.

θ_s	D (mm)	HWA data [a]	CFD model
0°	0	0.79	0.83
	10	0.80	0.83
	20	0.80	0.83
4°	0	0.91	0.88
	10	0.88	0.87
	20	0.87	0.87
7°	0	0.88	0.93
	10	0.88	0.94
	20	0.88	0.93
10°	0	0.84 [b]	0.90
	10	0.62 [b]	0.93
	20	0.69 [b]	0.91
18°	0	0.71 [b]	0.78
	10	0.58 [b]	0.77
	20	0.63 [b]	0.75

[a] From (Rusli, 2019)

[b] Possible negative flow

6.5 Chapter summary

The analysis of the effects of asymmetry in turbulent flows, for a wide range of swirl levels, represent a novel aspect of this thesis. A review of the effects of small disturbances introduced in swirling flows has been presented in section 2.4, mostly for laminar flow and theoretical considerations. As already mentioned, not many studies have been found in literature on the characterisation of turbulent non-axisymmetric swirling flows.

The combined effect of asymmetry and swirling flows in a sudden expansion with downstream resistance has been studied using PIV and a numerical model for the first time. The experimental study carried out using the PIV technique has been presented for the first time and represent a database that can be used for model validation.

The numerical study has focused on several important questions, aiming to identify potential and limitations of the CFD model, understand the complex flow physics governed by the combined effect of asymmetry and swirl, and provide useful guidelines for engineering applications. An assessment of the RANS turbulence model capabilities in such flows has been performed, starting with the comparison between PIV and using an additional dataset for pressure and velocity measurements available. It has been shown that the model is able to predict most of the flow features for most of the cases analysed. Further analysis on the intrinsically 3D flow features has been made using the CFD model, which represents an advantage of the numerical model over the limited access of the experimental data. The use of CFD visualization techniques inside the diffuser has allowed a better understanding of the changes due to the asymmetry.

The strong dependence between the inflow swirl level and the downstream flow properties has been demonstrated, in particular for the lowest swirl level considered (S $\approx$ 0.26) and the highest swirl level considered (S $\approx$ 1.70). Since the inlet conditions were not imposed at the start of the test section, but full swirl geometry of the swirl generator was replicated upstream, this resulted in noticeable under-prediction of the swirl level at the inlet. This suggests that the model damps the tangential components of the swirling flow.

For intermediate swirl levels the comparison with the experimental data is generally better. The flow structures obtained numerically can be clearly identified and show a good agreement with the PIV data, both qualitatively and quantitatively.

The complex change in the flow structure for the axial inlet flow suggests a strong coupling in all 3 directions, which has not been observed before in similar configurations that where focused on planar studies. The combination of asymmetry and swirl has been shown to have a much more complex three-dimensional effect on the flow features inside the diffuser when compared to an axial, axisymmetric turbulent flow.

Without swirl, inlet pipe displacement causes the jet to accelerate towards the nearest diffuser wall. Adding swirl results in this effect spreading azimuthally in the swirl direction. High swirl levels (S above 0.50) also cause appearance of the central recirculation zone. At high swirl levels, the introduced asymmetry results in the central recirculation zone twisting around the diffuser axis.

The shape and size of the wall separation zone caused by the flow path expansion are also affected by the asymmetry (which causes the zone to incline away from the expansion point at the wall opposite to the displacement direction) and swirl (which is known to result in the separation zone size reduction in the axial direction).

The downstream velocity predictions depend on the accuracy of the combination of the RANS model and the porous medium model. The positions of local minima

and maxima in the velocity are predicted reasonably well in most cases. The differences between CFD and experiments can be attributed to the turbulence kinetic energy suppression and the over-prediction of the pressure drop in the monolith caused by the porous medium model. Thus, the RANS model used here captures the main flow features and can be used to understand the mechanisms governing the flow.

The global effect of the asymmetry on the flow is manifested in changes in flow uniformity and total pressure drop. The results indicate that introducing asymmetry does not have a considerable detrimental effect on either characteristics and may even be beneficial for flow uniformity and/or pressure loss, although more experimental data would be needed to confirm these results definitively. The effect on the pressure losses is important in aftertreatment systems, since it affects engine efficiency and space constraint often result in exhaust system asymmetry.

It is necessary to observe that the flow uniformity index is a global quantity, averaged over the area, so the changes in the flow structures cannot be evident when using only that parameter. This aspect is relevant for aftertreatment systems and more generally for the engineering applications where flow uniformity is linked to the species conversion efficiency, heat transfer and device durability.

In conclusion, this study provides, for the first time, an insight into the mechanisms of the complex interaction of swirl and asymmetry on flows in sudden expansions and assesses performance of RANS modelling in capturing such flows.

Chapter 7

A new porous medium approach for modelling high resistance devices

The advantages and disadvantages of the porous medium modelling approach presented in subsection 3.2.5 have been discussed in the previous chapters (Chapter 5 and Chapter 6). The model, referred as *classic* model in the following sections, offers a great advantage in terms of computational efficiency. The flow losses predicted by the model are in good agreement with the experimental data on a system level, as shown by the results presented for the diffuser with a sudden expansion. However, such modelling approach can not provide details about the flow structures downstream the device.

This aspect is relevant for a wide range of applications, e.g. automotive catalysts and heat exchangers, and more in general when a device with high resistance presents multiple flow passages. The formation of the single jets exiting the device influence the turbulent structures, which are directly linked to the mass and heat transfer, but it is not practical to include the single channels in the full scale model, since the computational requirement would be too high.

A new formulation for the porous medium modelling approach is proposed and analysed in the current chapter. This formulation mostly keeps the computational efficiency of the classic porous medium approach, but allows to retain the information about the flow path through the device, thus ensuring better accuracy of flow predictions downstream. It also allows great flexibility in the device geometry set up, which can be useful in optimisation studies.

To demonstrate the new approach, the porous medium model has been applied to the planar diffuser test section (section 3.1.1). The validation of the approach has been made by comparing the experimental data and the the full scale model of the channels presented in the study of Porter (2016).

The flexibility of the proposed formulation has been tested by defining an optimisation algorithm to reduce the pressure drop through the monolith, based on the redefinition of the channel's dimensions.

A selection of the results presented in the current chapter has been published in Padula et al. (2019).

7.1 Model definition and implementation to catalysts

The method has been developed to implement a customised resistance function able to describe the flow passages through the resistance device. The method has been developed for a catalyst monolith, but it can be ideally extended to device with any flow passage pattern.

7.1.1 Model formulation

The resistance device (monolith) considered here can be modelled using three different strategies:

1. full scale domain (all the single channels Figure 7.1a) ;
2. porous medium region (Figure 7.1b);
3. condensed porous medium region (Figure 7.1c).

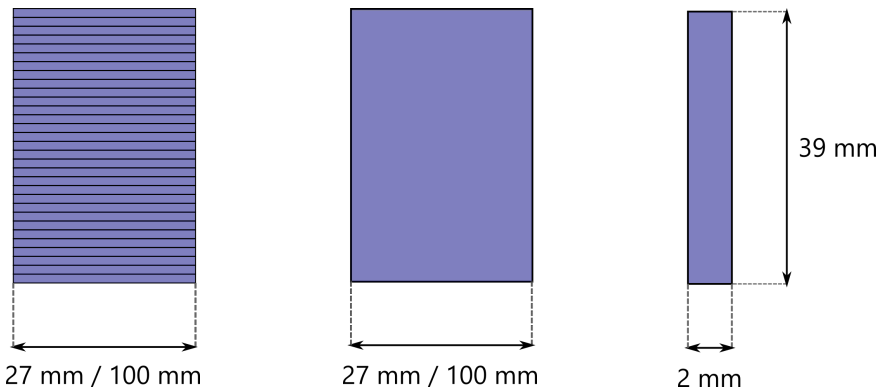

(a) Channels **(b)** Porous medium region **(c)** Condensed monolith

Figure 7.1 Modelling strategies for a catalyst/monolith: full scale, which includes each channel (a), porous medium approach applied to the entire region (b), condensed monolith approach (c).

The first approach means including all the single channels (more in general the device geometry) in the computational domain (Figure 7.1a). This approach is not practical for 3D configurations, since it requires more computational resources, as already discussed in subsection 2.3.2.

The porous medium model allows a consistent simplification of the domain geometry, thus resulting in a reduction of the computational effort. The porous medium model can give a good representation of the pressure drop and of the velocity change downstream the device. With a *classic* porous medium approach it is also possible to force the flow in a preferred direction, by appropriately defining the resistance coefficients, as proven for the other test sections shown in Chapter 5 and Chapter 6.

A further reduction of the computational effort can be achieved using a *condensed* modelling approach, e.g. Figure 7.1c, which consists in a reduced size of the porous region in the domain. The use of a condensed monolith approach has been proven to be effective in the work of Porter (2016). The idea is to prescribe the same resistance coefficients as for the full region model, but scaled with the length of the monolith. This aspect confirms the findings presented in the preliminary analysis of the diffuser with sudden expansion (subsection 5.2.1): the change in the flow structure is driven by the solution calculated at the entrance of the porous medium region. The use of a shorter region for the modelling allows further reduction of the number of cells used for the discretisation. Another advantage of the condensed model approach is that the change in monolith type can be simply accounted by scaling the resistance coefficients, without the need to change the entire region in the computational domain. This represent a great advantage for the design optimisation, since the changes in device resistance can be rapidly accounted for in the model, without the need to re-mesh the domain. For the above reasons, the condensed monolith approach has been preferred in the current chapter.

The formulation proposed here aims to not only force the flow in one preferred direction (e.g. the axial direction for a monolith), but to reproduce the flow passages with more fidelity, defining a variable resistance in the cross section. Thus, the complex flow passage through the device can be modelled by defining the resistance function through the porous region, rather than by including the entire geometry into the computational domain. The new formulation will be referred in the following sections as *modified* approach, to distinguish from the *classic* porous medium approach used in the previous chapters.

7.1.2 Application to catalyst

The *classic* approach formulation of the porous medium has been presented in subsection 3.2.5. In the current chapter, the same formulation has been adopted, with the exception of the correction used for the entrance effects (Equation 3.21), which has not been included in the current analysis. The pressure drop through the section (Equation 3.21) is modified for the condensed monolith approach as

$$\Delta p = \alpha \cdot \frac{L_{exp}}{L_{sim}} \cdot u_s + \beta \cdot \frac{L_{exp}}{L_{sim}} \cdot u_s |u_s| \tag{7.1}$$

in which L_{exp} is the monolith length used in the experiments, L_{sim} is the length of the porous region in the computational domain, u_s is the superficial velocity and α and β are the viscous and inertial coefficients through the region, respectively. From Equation 7.1 it can be seen that if $L_{sim} = L_{exp}$, the formulation is equal to Equation 3.21.

In presence of a device with a preferred direction, such as the monoliths considered throughout the current study, the resistance coefficients in the other two directions are imposed much higher than α and β, forcing the flow inside the porous region to be axial, as explained in subsection 3.2.5.

The main drawback of this formulation is that the complex flow passage of the device is not accounted for in the computational domain, since the change in the monolith type is only accounted through the change in the overall pressure drop. In other words, if the downstream monolith has a different characteristics, e.g. cells density or channels shape, which result in a change of the channels dimensions, the *classic* porous medium model can not account for this changes, but only for the global effect on the pressure drop, included by redefining the porous region coefficients.

The *modified* approach proposed here is based on variable resistance coefficients across the section. The resistance across the section varies according to the geometry, defining the resistance in a different way for channels and walls, as shown in Figure 7.2b. The resistance through the channels is determined from experiments or semi-empirical correlations and correspond to the axial resistance through the region imposed in the classic formulation. The walls are treated as very high resistance areas, imposing a high viscous resistance, compared to the channels, e.g. $10^6\ kg/m^3 s$. This is achieved by scaling the resistance coefficients using a user-defined function, referred as *shape function* (SF)

$$SF(x,y,z) = \begin{cases} 1, & \text{if (x,y,z) at the walls} \\ 0, & \text{otherwise (open to the flow)} \end{cases}$$

As a consequence, the resistance coefficients are not constant, but become a function of the position, defined by the shape function. For example, the viscous coefficient α is rewritten as α_{mod}

$$\alpha_{mod} = \alpha \cdot OFA \cdot \frac{L_{exp}}{L_{sim}} + SF \cdot C_{hr} \tag{7.2}$$

in which OFA is the Open Frontal Area ratio (defined as the ratio between the cross-sectional area open to the flow and the total cross-section area), the fraction $\frac{L_{exp}}{L_{sim}}$ accounts for the condensed monolith approach and the shape function (SF) accounts for the high resistance at the walls, and C_{hr} is the high resistance coefficient (set to 10^6 in the current study). The scaling factor OFA (Open Frontal Area) accounts for the change in the formulation, which does not use the superficial velocity from Equation 3.21 or Equation 7.1, but actual mean velocity in the channel. The OFA calculated for the current study is OFA = 0.8819.

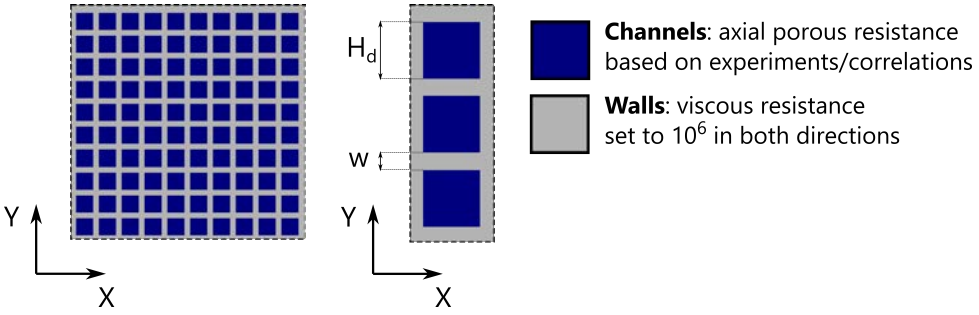

(a) Monolith surface **(b)** Channel resistance

Figure 7.2 Schematic view of a monolith surface (a). Channels area in blue, walls in grey. Detail of a row of three channels with description of the prescribed resistance coefficients (b).

The simple definition of the shape function represents a main advantage of the proposed formulation. The geometry of the device is accounted for in the model through the use of a simple function, which can be expanded and modified to be applied to a wide range of geometries.

7.1.3 Catalyst resistance coefficients

The resistance coefficients in the areas open to the flow can be calculated from experimental data or from semi-empirical correlations. In the configuration used here, the experimental pressure drop has been measured using uniform flow upstream the monolith, obtaining a correlation between the pressure drop measured and the mean velocity at the monolith entrance. The advantage of this approach is, obviously, the increased accuracy of the model, since the coefficients are determined for the specific

monolith. The resistance coefficients determined from the experiments are summarised in Table 7.1.

Table 7.1 Resistance coefficients calculated from experiments for the planar diffuser model.

Monolith length (mm)	Viscous resistance coefficient (α) (kg/m^3s)	Inertial resistance coefficient (β) (kg/m^4)
27	734.38	14.053
100	259.5	19.806

However, such definition presents a drawback during the design phase, when the characteristics of the monolith are yet to be defined. An alternative approach is using empirical correlations available for flow losses in straight channels.

The semi-empirical correlation used here has been proposed in the study of Shah (1978) and it is commonly used in the automotive industry, e.g. (Abu-Khiran et al., 2003), to describe the pressure losses in a channel with developing laminar flow. The non-dimensional pressure drop through the channel, in Shah's formulation, is calculated as

$$\Delta p = \frac{\Delta p}{\rho u^2/2} = (f_{app} Re_x)(4x^+) \tag{7.3}$$

in which f_{app} is the apparent Fanning friction factor, Re_x is the Reynolds number calculated using the hydraulic diameter of the channel H_d and the mean axial velocity in the channel and x^+ is the non-dimensional axial coordinate. The non-dimensional axial coordinate in Equation 7.3 is defined using the hydraulic diameter as reference length

$$x^+ = \frac{x}{H_d \cdot Re_x} \tag{7.4}$$

The apparent Fanning friction factor is calculated using the semi-empirical equation proposed by Shah (1978)

$$f_{app} Re_x = \frac{3.44}{\sqrt{x^+}} + \frac{(k \cdot Re_x) + \frac{K(\infty)}{4x^+} - \frac{3.44}{\sqrt{x^+}}}{1 + C(x^+)^{-2}} \tag{7.5}$$

The constants proposed by Shah (1978) for a square channel have been used for the current study, substituting in Equation 7.5 the following values: the Fanning friction factor $fRe = 14.227$, the incremental pressure drop number $K(\infty) = 1.43$ and the constant $C = 0.00029$.

In order to demonstrate that experimental data and empirical correlations can be used to reasonably approximate flow losses in catalyst channels, the losses in the channels

of the monolith considered in Porter et al. (2014) are compared here for a range of mass flow rates. The velocity entering the channels has been varied from 0 m/s to 30 m/s, obtaining a local Reynolds number (Re_x) range from 0 to 2000. The pressure drop calculated from the experimental data (Equation 7.1) is compared with the pressure drop calculated from Shah (Equation 7.3) in Figure 7.3 for two monolith lengths of 27 mm and 100 mm, respectively Figure 7.3a and Figure 7.3b. The blue line represents the experimental pressure drop, while the black line shows the pressure drop calculated from Shah. The difference between experimental pressure loss and the one calculated from Equation 7.3 has been calculated for all the cases (green dots, reference axis on the right). Only two inlet Re numbers of 22000 and 60000 are used here, with the mean velocities in the monolith equal to 2.75 m/s and 7.50 m/s respectively. This value has been used to estimate the local Re_x and to mark the corresponding value in the plots in Figure 7.3. The resistance calculated using the formulation Figure 7.3 can over-predict the resistance for the two inflow conditions considered here, up to a maximum of 60%. Further analysis of this result is presented in the next sections.

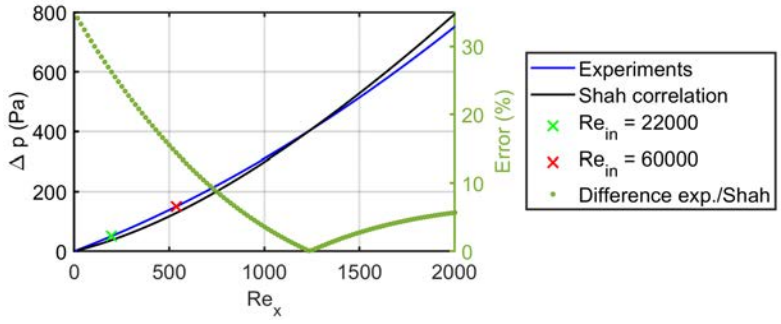

(a) L_1 = 27 mm

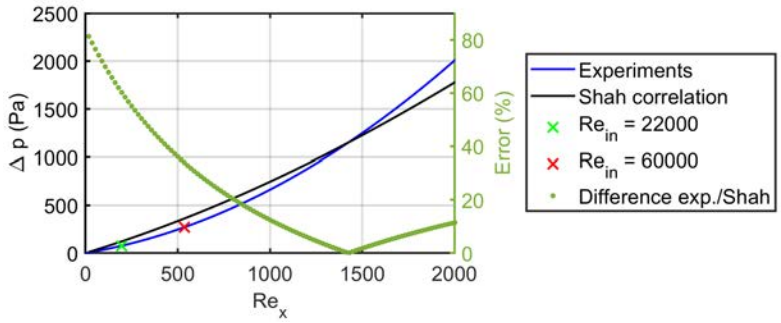

(b) L_2 = 100 mm

Figure 7.3 Pressure drop predicted using Shah's correlation (black line) compared with the experimental data (blue line), imposing uniform flow at the monolith entrance. Green cross corresponds to the mean velocity obtained for Re = 22000, red cross for the Re = 60000. Monolith length of 27 mm (a) and monolith length of 100 mm (b).

7.2 Case study: Planar diffuser with a catalyst monolith

In order to demonstrate the implementation and assess the perfomance of the modified porous medium approach, CFD simulations replicating the configuration considered by Porter (2016) have been performed in StarCCM+. The domain is a reproduction of the experimental test section presented in section 3.1.1. The 2D numerical model has been implemented in StarCCM+, following the methodology presented in section 3.2. Air has been used as working fluid and the flow has been assumed to be steady and incompressible. The flow properties are the same used for the other test sections, reported in Table 3.4.

The experimental study of the *planar* diffuser has been carried out by Porter (2016). The experimental test section has been shown in Figure 3.9a, together with the schematic representation of the computational domain adopted for the current study. The configuration has been tested in the study of Porter (2016) for a range of Reynolds numbers at the inlet and different monolith lengths downstream. The plenum nozzle upstream (Figure 3.9a) has been used to obtain a uniform flow distribution inside the test section. It has been shown by the experimental data, for a range of inlet Re, that the the velocity distribution far from the walls was nearly Z-independent. Therefore modelling only the XY plane is a suitable approximation for the configuration.

The monoliths used downstream the diffuser had a cell density of 62 cells/cm^2, with square channels with hydraulic diameter (H_d) of 1.12 mm. Two monolith lengths have been used corresponding to $L_1 = 27$ mm and $L_2 = 100$ mm. The global pressure loss through the monolith has been measured with uniform axial flow prescribed at the inlet. Those measurements have been used to calculate the resistance coefficients for the porous medium model, using the same approach described in subsection 3.2.5 for the diffuser with sudden expansion. As already mentioned for the experimental studies carried out for the diffuser with sudden expansion, the flow downstream the monolith is expected to be mainly axial. The velocity downstream the monolith has been consequently sampled using a single hot-wire probe normal to the section.

7.2.1 Computational domain

The inflow conditions for both Reynolds numbers considered (22000 and 60000), indicate that the flow is expected to be turbulent, since the minimum Reynolds number at the inlet is 22000. Consequently, the $\bar{v}^2 - f$ turbulence model has been used for the implementation in StarCCM+, based on the considerations presented in the previous

chapters. The boundary conditions have been implemented using the methodology described in section 3.2.3. A constant velocity has been imposed at the inlet section, using the values shown in Table 3.6. A pressure outlet condition has been imposed at the diffuser outlet, while a wall boundary condition has been used at the planar diffuser walls and a symmetry boundary condition has been imposed on the planar diffuser axis. The convergence for all the cases has been monitored using the residuals and it has been satisfactory when a value of at least 10^{-5} has been achieved for the equations.

7.2.2 Mesh independence study

Since the flow has been shown to be nearly two dimensional, a 2D domain is used. Hexahedral cells have been used for the entire domain, with 8 prism layers near the wall, aiming for a structured mesh throughout the entire domain.

The use of the shape function requires that the values are interpolated on a fine mesh distribution, to account for the small geometry of each channel and the even smaller thickness of the walls. A section of the mesh inside the porous region is shown in Figure 7.4. A small size of the cells inside the porous region has been chosen, in order to guarantee to capture the wall thickness of the monolith with at least one cell. This approach, inevitably increases the number of cells used to discretize the domain. However, the number of cells required for this case is still lower then the number of cells used for the full scale model of the channels. In the case of the monolith length of 27 mm, about 200000 cells have been used by Porter (2016) to model the channels region, while only 48850 cells have been used here. In addition, this approach still retains the main advantage of the porous medium formulation, which requires less computational resources then the flow simulation in each channel.

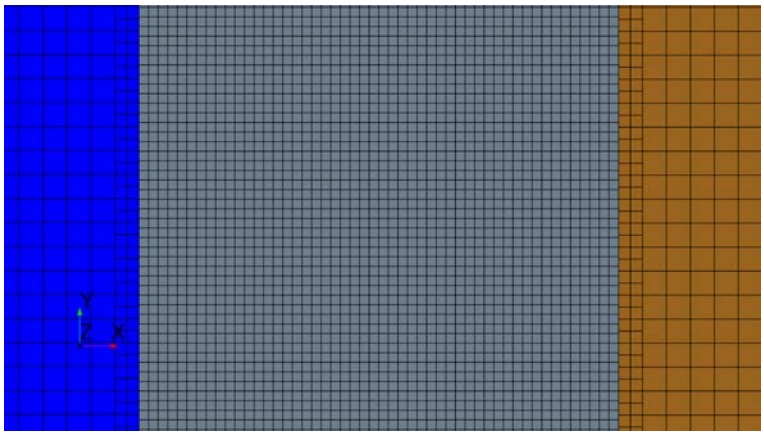

Figure 7.4 Detail of the mesh chosen for the planar diffuser case (mesh corresponding to Case #2 of Table 7.2). Diffuser region (blue), porous region (grey) and outlet sleeve (brown).

The mesh independence of the results has been assessed on the reference case of Reynolds 60000, since it is the case for which higher changes in the flow field are expected for this configuration. The monolith resistance was based on the experimental results for the monolith length of 27 mm. A selection of the results is presented here by comparing the results obtained with 3 different meshes, identified from now on as *coarse* mesh (Mesh #1), *reference* mesh (Mesh #2) and *fine* mesh (Mesh #3). The methodology used to assess the independence of the results from the mesh is similar to the one used for the test sections presented in the previous chapters. The independence has been assessed by comparing the effects of the solution on some parameters of interest.

The velocity at the outlet boundary has been compared for the three cases. It can be seen from Figure 7.5 that the difference between the reference mesh (Mesh #2) and the finer mesh (Mesh #3) is lower then 1% (blue and green lines are barely distinguishable) and that for the coarser mesh (Mesh #1) is about 2% lower near the axis (0 mm).

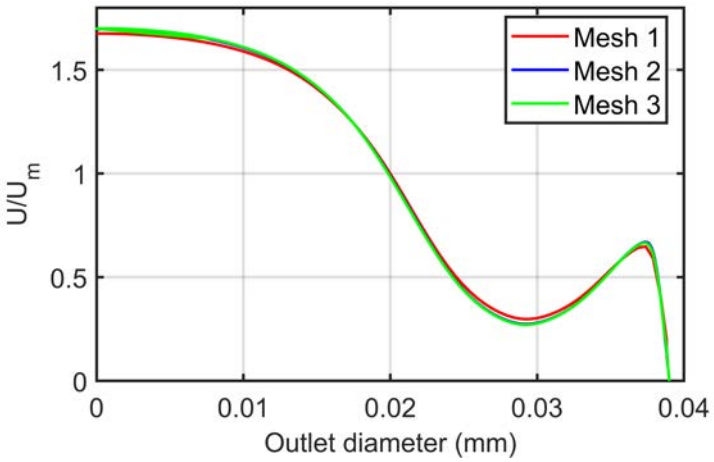

Figure 7.5 Planar diffuser, case: $Re_{in} = 60000$, monolith length $L_2 = 27mm$. Outlet velocity profile for the *coarse* mesh (Mesh #1), *reference* mesh (Mesh #2) and *fine* mesh (Mesh #3).

The effect of the mesh on some global parameters is reported in Table 7.2. The pressure drop through the domain has been calculated for all the meshes, together with the pressure drop through the monolith section, using the methodology presented in subsection 3.3.3. It can be seen that the difference between the reference mesh and the finer mesh is lower then 1% for both values considered, while the number of cells used for Mesh #3 considerably higher, resulting in a computational time of about 30% higher.

The uniformity index of the flow downstream the monolith section has been calculated using the methodology described in section 3.3. It can be seen from Table 7.2 that there is no variation between the reference mesh and the finer mesh.

Table 7.2 Planar diffuser. Summary of the mesh independence study: comparison between some global flow parameters for the *coarse* mesh (Mesh #1), *reference* mesh (Mesh #2) and *fine* mesh (Mesh #3), obtained using the *classic* porous medium model.

	Mesh #1	**Mesh** #2	**Mesh** #3
Number of cells	108554	145890	266253
Uniformity index	0.75	0.74	0.74
Total pressure drop (Pa)	339.58	344.87	345.89
Monolith pressure drop (Pa)	265.13	268.13	269.44

In conclusion, the mesh independence of the solution has been confirmed, since the results have not shown appreciable variation between $Mesh$#2 and $Mesh$#3.

7.2.3 Optimisation algorithm

The approach proposed for the porous medium modelling offers great flexibility in terms of the geometry modelling through the use of the *shape function*. This advantage has been demonstrated in the current study exploring a possible strategy to *optimise* the monolith channels size, aiming to improve the uniformity of the flow distribution downstream the device.

The problem of the flow maldistribution is common to a wide range of applications, e.g. for automotive aftertreatment systems and heat exchangers, as described in section 2.3. However, the method can be used to optimise other device performance parameters such as pressure drop or heat transfer characteristics. In most of the catalyst monoliths currently produced, all flow channels have identical size. This is mostly the result of the manufacturing process, as the catalyst honeycomb is produced by extrusion. However, it is well known that because of the expansion upstream of the catalyst the flow is highly non-uniform with a peak in the middle (e.g. Benjamin et al. (2003)). It is natural to assume that reshaping the monolith so that the flow in the middle encounters higher resistance would result in more uniform flow across the catalyst cross-section. This can be achieved using different approaches, such as adjusting channel length (Benjamin et al., 2004) or channel diameter. With the advances in 3D printing technologies, uneven channel diameter distribution may become possible. Therefore, the optimisation procedure presented here aims to adjust the channel diameters across the monolith to obtain more uniform flow between the channels.

Although the approach used here is only one of the possible strategies that can be used to optimise such devices, it allows to test the flexibility of the function proposed, using the CFD model as a design optimisation tool.

The optimisation procedure has been implemented using a Java macro to allow the integration in StarCCM+, but such methodology can be easily adapted to different CFD packages. The strategy adopted for the optimisation is based on the velocity calculated inside each channel. An iterative algorithm has been used to obtain the new channel distribution, more details can be found in section D.2.

The initial solution for the entire domain is obtained using a uniform size distribution of the channels for which the hydraulic diameter (H_d) of each channel is kept constant.

The mean velocity downstream is calculated and used for comparison in each channel. When the velocity inside the channel is higher then the mean, the size of the channel is reduced. This will increase the resistance of the channel, so that the flow is diverted towards other, bigger channels with lower overall resistance to the flow. The maximum change in the hydraulic diameter at each step of the optimisation is limited to $\pm 10\%$. The new size of the channels is used for the new step, in which the solution is recalculated for a fixed number of iterations (2000), to achieve convergence of the CFD solution. The process is repeated up to 60 steps, sufficient to obtain a stable solution.

7.3 Results and analysis

The main focus of the current study is the flow distribution downstream the monolith section. Consequently, the model validation and the comparison between the different cases is made mainly in that portion of the domain.

The velocity downstream the monolith has been normalised with the mean velocity at the outlet section, respectively 2.70 m/s for Re = 22000 and 7.40 m/s for Re = 60000.

7.3.1 Model validation

The proposed approach has been initially compared with the *classic* approach, the experimental data from the HWA and the full channels model from Porter (2016).

The non dimensional velocity downstream the monolith is shown in Figure 7.6 for the case with inlet Re = 60000 and monolith length of 27 mm.

The prediction of the downstream flow with with the current model is in good quantitative agreement with the prediction of the full scale model (Porter, 2016), for both the *classic* and *modified* porous medium approaches considered here. The flow distribution is in good qualitative agreement with the experimental results. The underestimation of the flow velocity has been attributed to three dimensional effects that are not accounted for using the planar model.

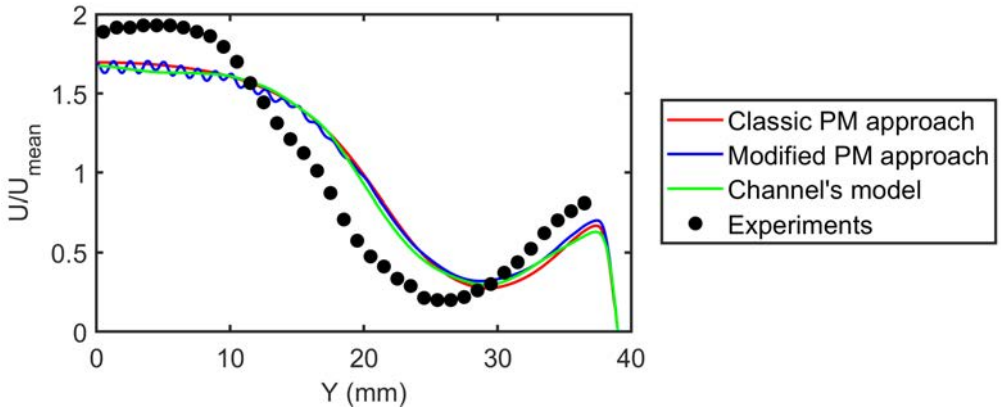

Figure 7.6 Planar diffuser. Case: inlet Re = 60000, monolith length L_1 = 27 mm. Non dimensional velocity downstream the monolith section. Comparison between: experimental data (dots), channels model (green), *classic* porous medium approach (red) and *modified* porous medium approach (blue).

The new model implemented exhibits local peaks in the velocity, due to the incomplete mixing of the jets downstream the porous region section, which are consistent with the results obtained with LES from Hettel et al. (2020).

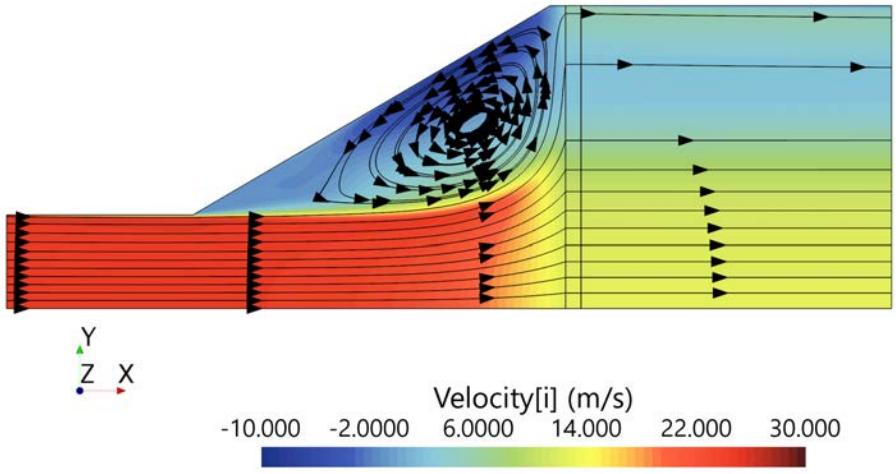

Figure 7.7 Planar diffuser. Case: inlet Re = 60000, monolith length L_1 = 27 mm. Axial velocity contour plots, with superimposed streamlines (black).

The outlet flow exhibits a maximum near the axis and a secondary peak near the wall (Figure 7.6). This feature is the result of the flow redistribution upstream the monolith, as could be seen from Figure 7.7. The mechanism is similar to the one observed for the axial flow case for the diffuser with the sudden expansion (subsection 5.3.4). The flow impinges on the monolith surface and redistributes radially (Y direction in Figure 7.7), with part of the diverted flow entering the monolith near the wall, causing the secondary peak.

7.3.2 Comparison of the catalyst models

As already shown for the case reported in Figure 7.6, the approach proposed in the current study is in good agreement with the *classic* porous medium modelling approach. This aspect has been further investigated by comparing the two modelling approaches for both inlet Re and both monolith lengths.

The velocity predicted downstream for the inlet Re = 22000 is shown in Figure 7.8 for both monolith lengths L_1 = 27 mm (a) and L_2 = 100 mm (b). A good agreement between the different modelling approaches is observed, both qualitatively and quantitatively.

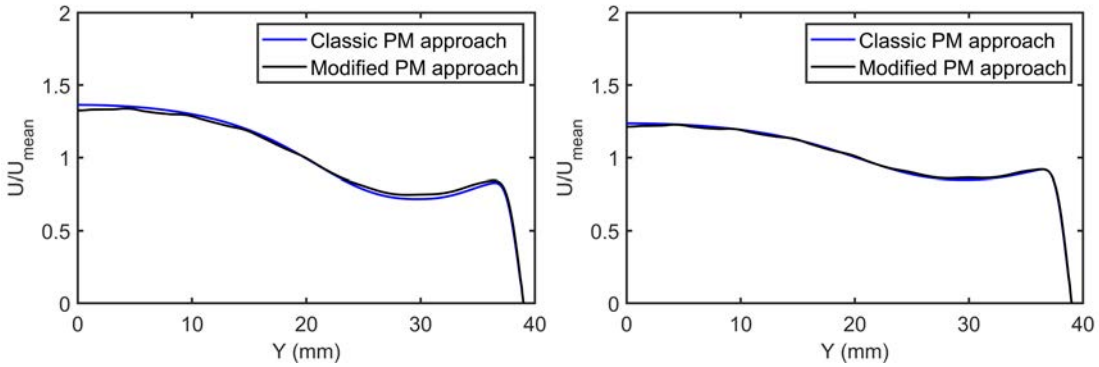

(a) L_1 = 27 mm, Re = 22000 **(b)** L_2 = 100 mm, Re = 22000

Figure 7.8 Planar diffuser. Non dimensional velocity downstream the monolith section. Comparison between the *classic* and *modified* approach for the porous medium modelling. Inlet Re = 22000, monolith length L_1 = 27 mm (a) and L_2 = 100 mm (b).

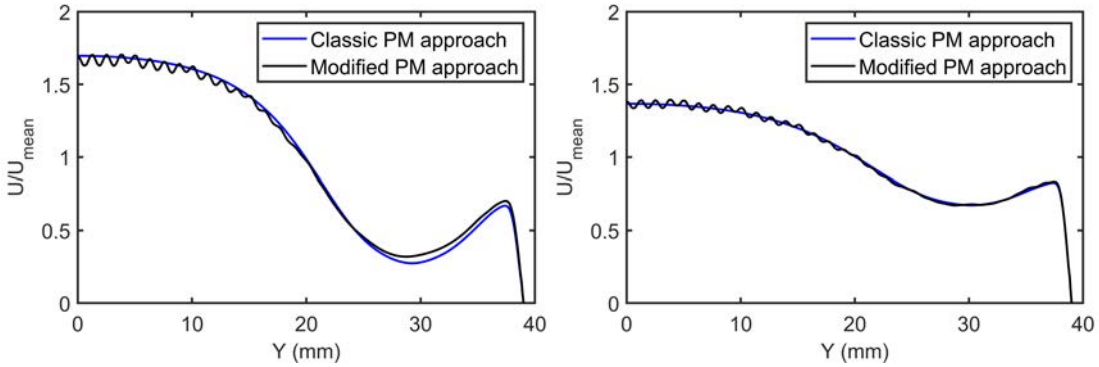

(a) L_1 = 27 mm, Re = 60000 **(b)** L_2 = 100 mm, Re = 60000

Figure 7.9 Planar diffuser. Non dimensional velocity downstream the monolith section. Comparison between the *classic* and *modified* approach for the porous medium modelling. Inlet Re = 60000, monolith length L_1 = 27 mm (a) and L_2 = 100 mm (b).

Similar results are observed for the highest Re = 60000 (Figure 7.9), confirming that the formulation proposed for the porous medium model retains the capability of the

porous medium formulation in the prediction of the flow velocity. Some differences can be observed near the axis, in which a *wavy* velocity profile can be observed for the *modified* approach, with the maximum variation around the mean value of about $\pm 4\%$, observed for the higher Re = 60000 with monolith length of 27 mm. This is the effect of the higher velocity of the jets exiting the monolith in that region, which have not sufficiently mixed downstream. This behaviour has been recently observed in the study by Hettel et al. (2020) with LES.

The presence of the single jets downstream is more clear from the velocity contour plots shown for all the cases in Figure 7.10 and Figure 7.11. On the left hand side, the results obtained with the *classic* porous medium approach are shown, on the right hand side the ones obtained with the *modified* approach proposed in the current thesis. The single jets exiting the monolith channels are clearly visible when the *modified* approach is used for both inlet Re = 22000 (Figure 7.10) and Re = 60000 (Figure 7.11). This is one of the main advantages of the current formulation and it is confirmed for both Re numbers at the inlet and for the different monolith lengths, so it is independent from the flow conditions upstream and from the overall resistance of the monolith.

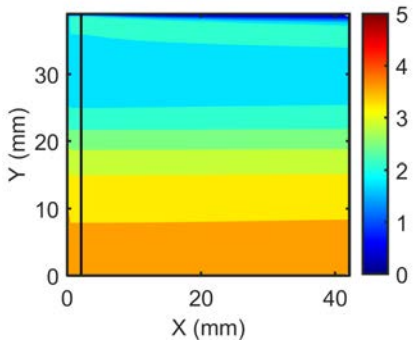

(a) *Classic* approach - L_1 = 27 mm

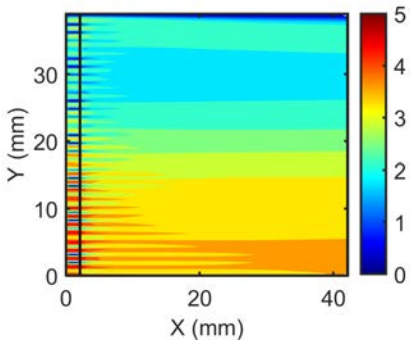

(b) *Modified* approach - L_1 = 27 mm

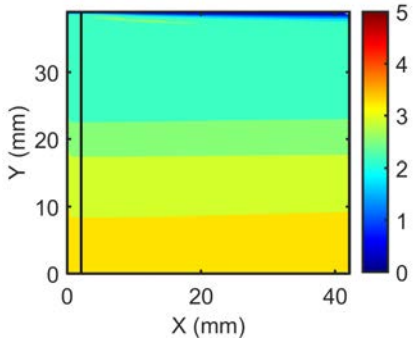

(c) *Classic* approach - L_2 = 100 mm

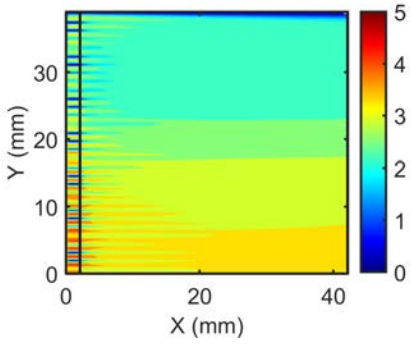

(d) *Modified* approach - L_2 = 100 mm

Figure 7.10 Planar diffuser. Contours of axial velocity downstream the monolith section. Comparison between the *classic* - left column, (a) and (c) - and *modified* - right column, (b) and (d) - approach for the porous medium modelling. Inlet Re = 22000, monolith length L_1 = 27 mm (a-b) and L_2 = 100 mm (c-d).

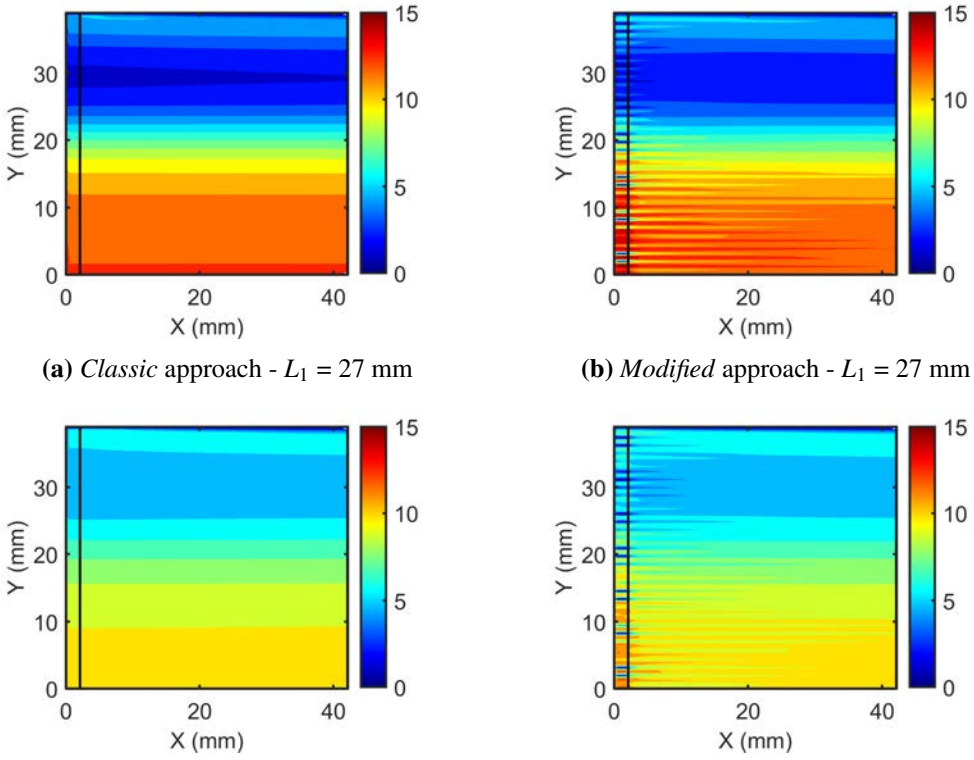

(a) *Classic* approach - L_1 = 27 mm

(b) *Modified* approach - L_1 = 27 mm

(c) *Classic* approach - L_2 = 100 mm

(d) *Modified* approach - L_2 = 100 mm

Figure 7.11 Planar diffuser. Contours of axial velocity downstream the monolith section. Comparison between the *classic* - left column, (a) and (c) - and *modified* - right column, (b) and (d) - approach for the porous medium modelling. Inlet Re = 60000, monolith length L_1 = 27 mm (a-b) and L_2 = 100 mm (c-d).

Differences between the models can be seen in the calculation of the pressure drop through the monolith, reported in Table 7.3. Unfortunately, no experimental data are available to assess which model is performing better, so no further analysis has been made.

Table 7.3 Planar diffuser. Pressure drop comparison between the *classic* model approach and the *modified* model approach.

	Re = 22000		**Re = 60000**	
Monolith length (mm)	27	100	27	100
Monolith region Δp (Pa)				
Classic approach	67	95	268	398
Modified approach	78	109	286	431
Difference	+ 14 %	+ 12 %	+ 6 %	+ 7 %
Uniformity index				
Classic approach	0.88	0.92	0.74	0.87
Modified approach	0.89	0.92	0.75	0.87
Difference	+ 1 %	0 %	+ 1 %	0 %

7.3.3 Downstream turbulence predictions

The poor prediction of the downstream turbulence is one of the drawbacks of the classic porous medium formulation. The $\bar{v}^2 - f$ turbulence model used for the study, as already remarked in the previous chapters and emphasised in the section 2.2.2, has a limited capability in terms of turbulence prediction. The model is inherently limited by the eddy viscosity formulation of the RANS family and by the forced isotropic assumption of the 2 equations models derived from the $k - \varepsilon$.

In order to assess capabilities of the new formulation proposed in the current thesis a comparison between the predicted turbulence downstream the monolith section with the different modelling approaches has been made. The case analysed is the one with inlet Re = 60000 and monolith length of 27 mm, already used for the assessment of the velocity distribution (Figure 7.6).

The turbulence intensity has been calculated from the numerical model as

$$T_i = \frac{u'}{\bar{U}} \tag{7.6}$$

where u' is the velocity fluctuation and $\bar{U}$ is the mean velocity at the section. The velocity fluctuation is not directly computed by the model, but can be extracted from the turbulent kinetic energy (k), under the assumption of isotropic turbulence

$$u' = \sqrt{\frac{2}{3}k} \tag{7.7}$$

The turbulence intensity calculated from the numerical model for both porous medium modelling approaches has been compared, as for the velocity in Figure 7.6, with the experimental data and with the channels model from Porter (2016) and it is shown in Figure 7.12.

The trend observed with the proposed approach (blue line) is similar to the one observed with the channels model from Porter (2016) (green line). However, overall turbulence intensity is lower. On the other hand, a better agreement of the turbulence intensity with the experiments is observed for the *modified* approach close to the axis, while the full channel model over-predicts the turbulence intensity considerably.

The *classic* approach under-predicts the turbulence intensity near the wall, but seems to better predict the redistribution that occurs near the wall, following a the trend obtained from the experimental data. Therefore, none of the three approaches discussed here provide a good agreement with experiments in all three different areas of the flow, namely: near wall region, the large shear layer between the central higher velocity area and lower velocity area caused by the upstream expansion, and the central high velocity region near Y = 0. This difference between the modelling approaches is attributed to the different length scales involved in the evolution of the flow structures caused by the different origins of the turbulence in these areas. The increased shear stress in the boundary layer is causing the increase in turbulence intensity near the wall, while the smaller scales due to the small jets formation are predominant near the axis Y = 0.

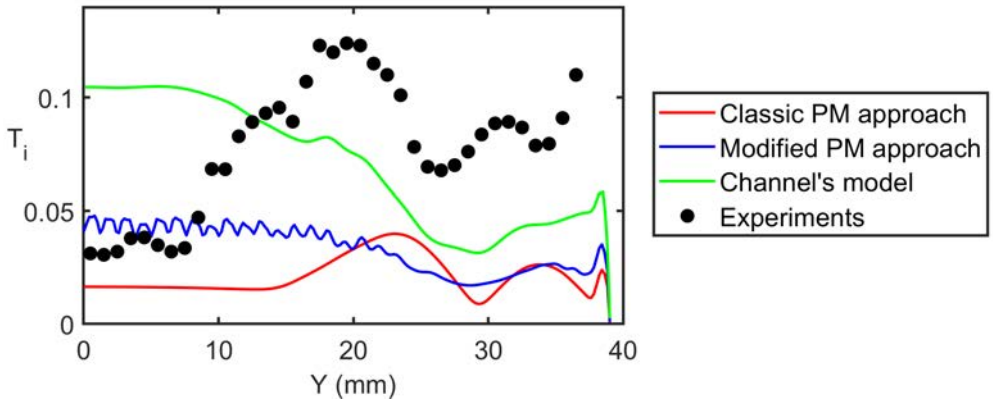

Figure 7.12 Planar diffuser. Case: inlet Re = 60000, monolith length L_1 = 27 mm. Turbulence intensity (T_i) downstream the monolith section. Comparison between: experimental data (dots), channels model (green), *classic* porous medium approach (red) and *modified* porous medium approach (blue).

In order to get a better insight into the turbulence properties, the turbulence length scale (l_t) has been calculated from the modelling results as

$$l_t = C_\mu \frac{k^{\frac{2}{3}}}{\varepsilon} \tag{7.8}$$

where $C_\mu = 0.09$ is a constant from the model, k is the turbulent kinetic energy and ε is the turbulent dissipation. The length scale calculated for both porous medium approaches and from the channels model is shown in Figure 7.13. Please note that the scales used in the plot are different: the axis used for the *classic* approach (red line) is the one on the left side of the plot, while the axis used for the other two cases is on the right side of the plot (blue axis).

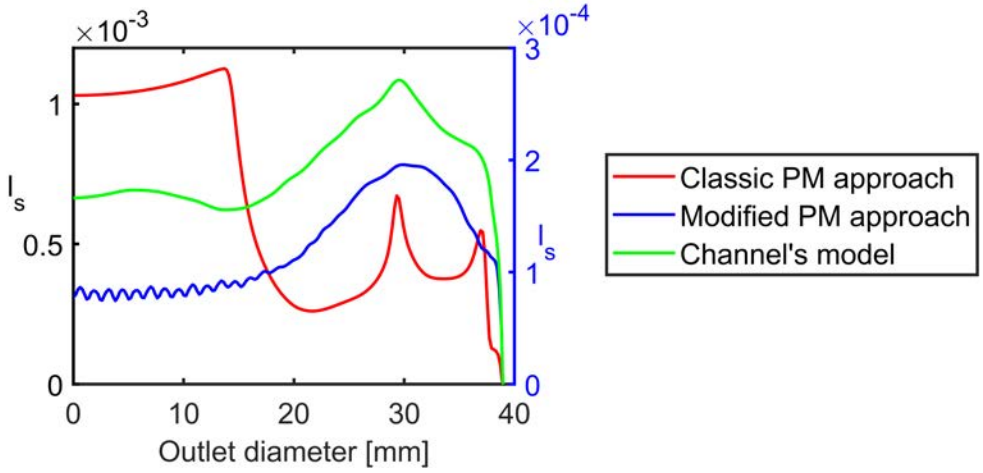

Figure 7.13 Planar diffuser. Case: inlet Re = 60000, monolith length L_1 = 27 mm. Turbulence length scale (l_T) downstream the monolith section. Comparison between: channels model (green), *classic* porous medium approach (red) and *modified* porous medium approach (blue).

The most evident result is that order of magnitude of the length scale captured with the *classic* approach is higher then the length scale calculated with the *modified* approach and with the channels model.

From this analysis it can be suggested that the macroscopic changes in the flow properties, often referred as first order properties such as velocity and pressure, can be correctly estimated using a *classic* porous medium approach. The formulation proposed in the current study retains that property, but can model also the smaller scales, leading to a prediction of the turbulent properties similar to the one obtained with a full scale model of the channels.

It is expected that by using more complex formulations of the turbulence model, the prediction can be further improved and be closer to the experimental data also in the near wall region. However, this goes beyond the objectives of this thesis and it is left to future studies. While turbulence level prediction by the current model is still not very accurate, it captures the turbulence length scales better. Combined with the better

mean velocity distribution (capturing the jets exiting the monolith) this provides a better overall prediction of the flow downstream of the monolith.

7.3.4 Catalyst resistance coefficients assessment

The effects of the resistance coefficient formulation have been compared for all the configurations analysed in the previous section. The comparison aims only to assess the differences between the coefficients calculated from Shah's correlation and the experimental ones. Therefore, the comparison is limited to the downstream velocity and to the pressure drop.

The differences between the two formulations under the hypothesis of uniform flow upstream have been shown in subsection 7.1.3. Under the assumption of uniform flow, the difference between the pressure drop calculated from the experimental curve and Shah's correlation is shown in Table 7.4, under the column "Uniform flow" difference (corresponding to green and red crosses in Figure 7.3).

It can be seen that the numerical model predicts lower pressure drop then the one calculated under the hypothesis of uniform flow for all the cases. This is not surprisingly, since the pressure drop calculated with the numerical model depends on the local flow distribution. In addition, the same trend in the difference between the experimental resistance and Shah's pressure drop can be seen.

Table 7.4 Planar diffuser. Pressure drop variation between the resistance coefficients from the experiments and the resistance coefficients from Shah's correlation. *Theoretical* refers to the difference estimated under the hypothesis of uniform flow (Figure 7.3). *Numerical model* is the difference between the pressure drop extracted from the CFD using the resistance coefficients from the respective formulation.

Inlet Mean velocity	**Re = 22000** **2.75 m/s**		**Re = 60000** **7.50 m/s**	
Monolith length (mm)	27	100	27	100
Uniform flow (%)	-26.23	+60.23	-14.42	+ 33.91
Numerical model (CFD) (%)	-17.65	+ 48.52	-2.27	+ 22.44

Despite the differences observed in the total pressure drop, a good agreement between the two methods can be seen for the velocity downstream the monolith in Figure 7.14 and Figure 7.15.

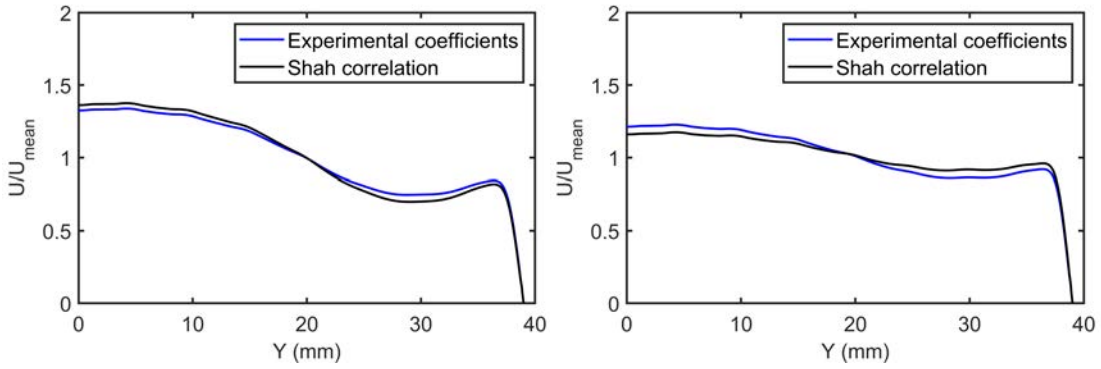

(a) L_1 = 27 mm, Re = 22000 **(b)** L_2 = 100 mm, Re = 22000

Figure 7.14 Planar diffuser. Non dimensional velocity downstream the monolith section. Comparison between the experimental coefficients and Shah's correlation using the *modified* approach for the porous medium modelling. Inlet Re = 22000, monolith length L_1 = 27 mm (a) and L_2 = 100 mm (b).

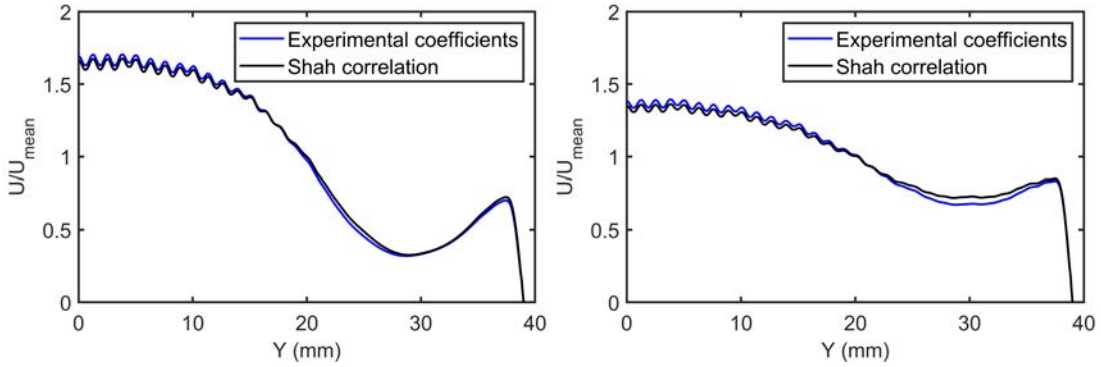

(a) L_1 = 27 mm, Re = 22000 **(b)** L_2 = 100 mm, Re = 22000

Figure 7.15 Planar diffuser. Non dimensional velocity downstream the monolith section. Comparison between the experimental coefficients and Shah's correlation using the *modified* approach for the porous medium modelling. Inlet Re = 60000, monolith length L_1 = 27 mm (a) and L_2 = 100 mm (b).

7.3.5 Channel optimisation

Now that it has been established that the modified porous medium approach performs generally better than the classic approach, and nearly as good as the full channel model, it is shown how the flexibility of its formulation can be used for improving design of catalysts and similar devices. The algorithm described in subsection 7.2.3 has been applied for two inlet conditions (Re = 22000 and Re = 60000), using a monolith length of 27 mm. The optimised distribution obtained with the low Re = 22000 is referred in the following text as *Opti* #1, while the channels distribution obtained using the high Re = 60000 is referred as *Opti* #2.

The effects on the channels size redistribution and the change in the resistance across the region are shown in Figure 7.16. The hydraulic diameter obtained with the first optimization has been identified as H_{d1}, while the second one with H_{d2}. It can be seen in Figure 7.16a that the size of the channels H_{d1}/H_d is reduced near the axis and increased near the wall. The opposite trend can be observed for the resistance $\Delta po1/\Delta pu1$ (Figure 7.16b), which is higher near the axis and lower near the wall. Similar considerations can be made for the higher Re of 60000. The change in the resistance $\Delta po2/\Delta pu2$ Figure 7.16d is opposite to the change in the channels size H_{d2}/H_d. This confirms that, in order to achieve a more uniform flow distribution downstream the monolith, the resistance through the region should not be uniform.

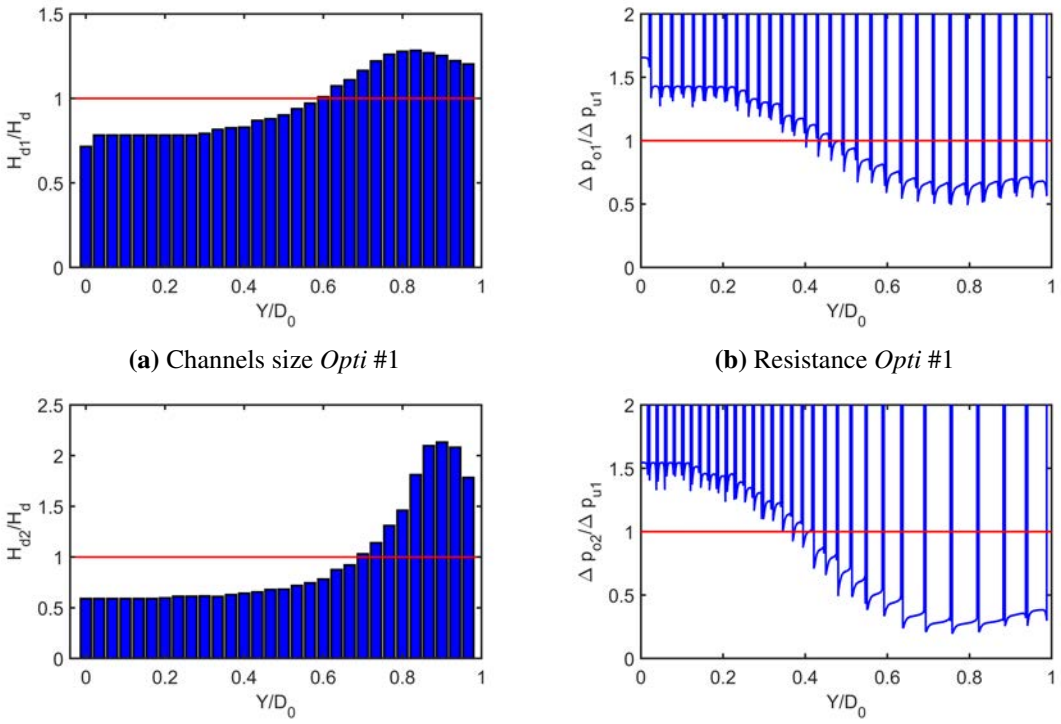

(a) Channels size *Opti* #1

(b) Resistance *Opti* #1

(c) Channels size *Opti* #2

(d) Resistance *Opti* #2

Figure 7.16 Planar diffuser. Channels size normalised with the initial H_d. Red line indicates the size of the initial H_d, blue bars indicate the size of the optimised channels. Distribution obtained with Re = 22000 - H_{d1} (a), distribution obtained with Re = 60000 - H_{d2} (c). Right side: local pressure drop trough the monolith. Distribution obtained with Re = 22000 - $\Delta po1/\Delta pu1$ (b), distribution obtained with Re = 60000 - $\Delta po2/\Delta pu2$ (d).

As could be seen for both cases, the channels hydraulic diameter is increased towards the wall and decreased towards the axis. As explained in subsection 7.3.1, the flow impinging on the monolith surface is forced to move in the radial direction, causing a redistribution of the flow towards the wall, resulting in the secondary peak of the velocity observed in that region. In order to achieve a uniform flow distribution

the diameter of the channels toward the centreline has been reduced, causing higher resistance in that area. Consequently, more flow has been diverted towards the wall, resulting the velocity flattening downstream.

The results of the optimisation on the flow velocity are shown in Figure 7.17 and Figure 7.18 respectively. For clarity, only the monolith section and the outlet sleeve are shown for the 4 cases.

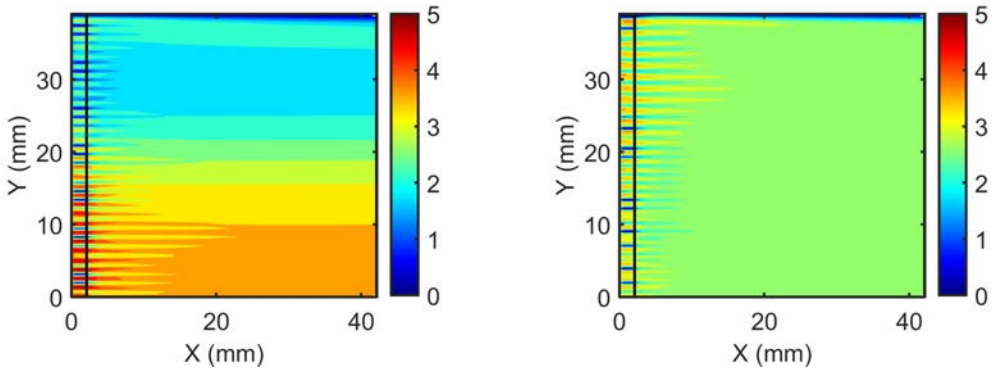

(a) Uniform channels distribution **(b)** *Opti* #1 channels distribution

Figure 7.17 Planar diffuser. Axial velocity contours at the monolith section and at the outlet sleeve. Inlet Re = 22000, monolith length L_1 = 27 mm. Initial solution on the left (a), optimised distribution *Opti* #1 on the right (b).

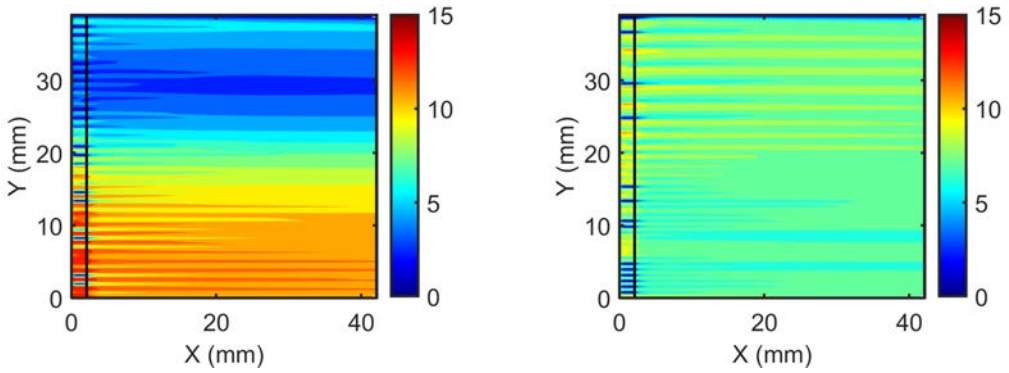

(a) Initial solution **(b)** Optimised solution

Figure 7.18 Planar diffuser. Axial velocity contours at the monolith section and at the outlet sleeve. Inlet Re = 60000, monolith length L_1 = 27 mm. Initial solution on the left (a), optimised distribution *Opti* #2 on the right (b).

The effect of the optimised distribution catalyst geometry on the flow upstream the monolith section (inside the diffuser) has been evaluated by comparing the axial velocity profiles at 5 different sections. The velocity sampled at 20 mm, 15 mm, 10 mm, 5 mm and 1 mm upstream the monolith section is shown in Figure 7.19.

The comparison between the velocity profile obtained using a uniform size of the channels (blue continuous line) and the one obtained with the optimised distribution (dotted blue line) shows that for both cases, the velocity profile immediately upstream the monolith is modified considerably as a consequence of the change in the resistance through the region, with the effect almost disappearing at the section of 20 mm upstream the monolith.

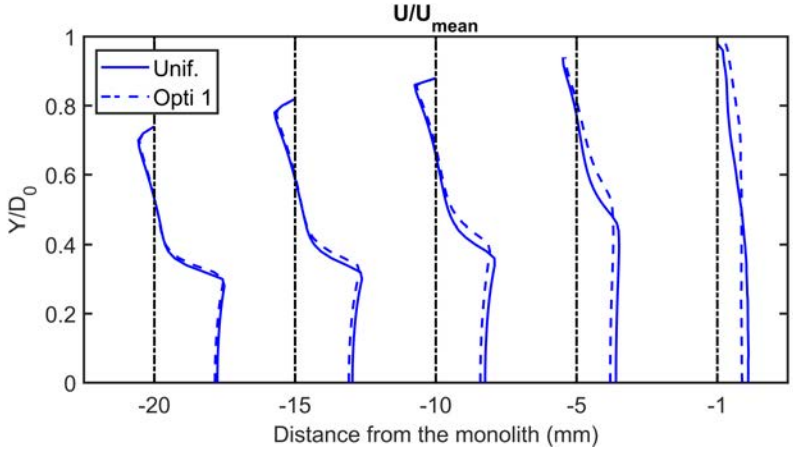

(a) Diffuser velocity *Opti* #1

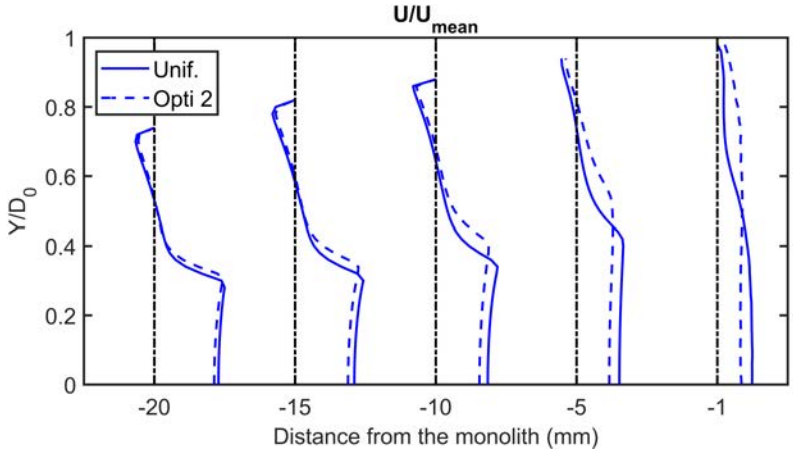

(b) Diffuser velocity *Opti* #2

Figure 7.19 Planar diffuser. Axial velocity profiles upstream the monolith (sections at 20 mm, 15 mm, 10 mm, 5 mm and 1 mm upstream). Blue lines represent the solution obtained with constant channels size, blue dotted line represent the solution obtained with the optimised distribution. Re = 22000 (a), Re = 60000 (b).

Since the mass flow in the catalyst or any other device will change with time and operating regime, it is obviously not possible to create different channel size distribution for every possible inlet mass flow. To ensure good performance for a range of mass flow rates, a multi-dimensional optimisation can be performed, optimising channel size distribution for a range of mass flow rates. A simpler alternative solution is a

compromise, where two limiting mass flow rates are considered, and the best channel distribution is chosen.

Two more scenarios have been analysed, aiming to evaluate the impact of the optimised distribution with a different inlet condition. In this case, the two inlet conditions have been "swapped": the distribution *Opti* #2 has been used with the lower inlet Re = 22000, while the distribution *Opti* #1 has been used with the higher inlet Re = 60000. The results are referred to as *Opti* #3 and *Opti* #4 respectively.

The effects on pressure drop through the monolith and uniformity index at the outlet are summarised in Table 7.5 for all the cases.

The UI obtained for the initial channel's distribution (constant H_d) has been calculated as 0.87 for Re = 22000 and 0.76 for Re = 60000 and it is used for comparison with the other cases. With the optimised distributions Opti #1 and Opti #2 a high uniformity index has been obtained for both Re. In addition, a reduction of the pressure drop through the monolith has been observed.

Interesting effects have been observed for the other two scenarios considered here. The pressure drop is smaller in the case Opti #3, with a minimal reduction of the UI. This means that using the optimised distribution of the channels obtained with the Re = 60000 is beneficial in terms of pressure loss also for a lower Re at the inlet.

On the other hand, an opposite behaviour can be seen for the case Opti #4, for which the inlet Re = 60000 has been used with the optimised distribution obtained for the lower Re = 22000 (Opti #1). A slight increase in the pressure drop is observed, while an improvement in the UI is observed.

This result suggests that if the channel's diameter is optimised for a certain mass flow rate at the inlet, a benefit for lower and higher mass flow rates can be obtained, either in terms of pressure drop reduction, either in terms of increased flow uniformity. This aspect should be further analysed in future studies, since it was not the main objective of the current thesis.

Table 7.5 Planar diffuser. Uniformity index for the optimised distribution.

	Re = 22000			**Re = 60000**		
Case	Unif.	Opti #1	Opti #2	Unif.	Opti #3	Opti #4
Δp var.	-	-1.6%	-16%	-	-4.3%	$+3\%$
UI	0.87	0.98	0.82	0.76	0.97	0.87

7.4 Chapter summary

A new approach for modelling multi-channel devices based on the porous medium approach has been proposed. The main advantages of the classic approach, such as good prediction of the downstream velocity and low computational expenses, are kept with the proposed modification. The approach has been used for modelling two-dimensional flow in a diffuser with an automotive catalyst. An improvement in the prediction of the downstream turbulence properties has been shown with the proposed modification, with respect to the classic porous medium approach. In particular, the single jets exiting the channels of the monolith can be captured by the proposed model, as well as turbulence generation associated with jet mixing, with a reasonable agreement with 2D models that include the channels' geometry, published in literature.

The main limitations of the accuracy of the results with the experimental data have been assessed. The use of a RANS turbulence model based on the eddy viscosity hypothesis limits the prediction of the multiple turbulent length scales involved - in particular, the smaller scales associated with individual jet mixing downstream of the monolith, and larger scales associated with the global shear layer formed when the flow enters the expansion from the smaller inlet pipe.

The model should therefore be tested with more complex turbulence models, such as Reynolds Stress Models and Large Eddy Simulation. The proposed approach can also be further improved by prescribing variable resistance coefficients inside the monolith channels, based on quadratic, cubic or high-order laws.

Flexibility of the proposed model in the device geometry description has been demonstrated by implementing a channel size optimisation algorithm in order to improve flow uniformity. The results of the optimisation study have shown a considerable improvement of the flow uniformity index downstream the monolith and the total pressure loss across the monolith. This formulation can be easily extended to a three-dimensional case, to improve the optimization procedure and to better validate the model against experimental data.

Chapter 8

Conclusions

An experimental and numerical investigation of swirling flows relevant to applications such as aftertreatment devices has been carried out in this study. The aim of the project was to improve our understanding of the fundamental properties of swirling flows in general, the physics behind the complex flow structure in configurations relevant to aftertreatment devices, to refine the experimental and modelling techniques used for studying such flows, and to provide some practical guidance for the applications.

In order to achieve this aim, several swirling flow configurations of increasing complexity were considered, including an annular pipe, a symmetric expansion with a downstream resistance and an asymmetric expansion with a downstream resistance (automotive catalyst in both cases). These studies involved design and construction of experimental rigs, flow and pressure measurements and CFD simulations, and allowed to get an insight into the flow physics and establish advantages and limitations of different measurement and modelling techniques. In particular, a comprehensive study of the effect of pressure tapping geometry and spacing on measurement accuracy has been carried out, suitability of using single wire HWA measurements has been assessed, and performance of different RANS models in modelling swirling flows has been assessed. An experimental database has been collected and used for model validation.

While swirling flow studies focused on the flow properties in the diffuser, a different challenge was addressed in the last chapter. A known limitation of the porous medium approach is its inability to preserve detailed flow information in multi-channel geometries, which leads to inaccurate flow representation downstream of the catalyst (or heat exchanger or similar device), and large errors in prediction of turbulence levels. To tackle this problem, an improved novel formulation of the porous medium model used for the numerical model of high resistance devices has been developed and its capabilities demonstrated on a 2-dimensional flow example. The new modelling approach features the high flexibility of the formulation and improves the prediction of the flow

downstream the device, compared to a standard approach. The simplicity of describing any channel geometry (regular or irregular) is also a powerful tool that can be used for new device design and optimisation. This has been demonstrated on a case study where flow uniformity through a catalyst was considerably improved using the new modelling framework.

8.1 Experimental studies

The methodology used to experimentally investigate confined swirling flows has been analysed in detail, providing some practical guidelines for the application of standard fluid dynamics techniques to the study of confined flows.

Hot-Wire Anemometry measurements The limitations of the use of single wire HWA probes to study flows with unknown direction have been highlighted and demonstrated, providing a critical assessment of such velocity measurements when applied to high swirling flows. Despite the low accuracy (compared with, for example, cross-wire probe measurements), the technique can be used to gather general information about the flow and get a qualitative evaluation of the flow structures.

An investigation of the effects of the sampling frequency on the velocity measurements has been presented. It has been demonstrated that the sampling frequency has a negligible impact on the mean velocity measurements, but presents a strong impact on the measurement of the instantaneous fluctuations for the category of flows analysed. It was demonstrated that sampling frequency of 200 Hz was insufficient to resolve the dominant frequency of the flow, and higher sampling rate (600 Hz) was required to ensure this was captured.

Wall pressure measurements and pressure tappings geometry No previous studies exist on the effect of pressure tapping geometry and spacing in complex flows featuring high coupling between velocity component and pressure gradients normal to the wall. Therefore, a comprehensive study has been carried out in order to establish practical guidelines on pressure tapping configuration optimal for highly swirling flows.

The study of the pressure tappings geometry has shown that a hole depth to diameter ratio of 6 is beneficial for the reduction of the experimental error associated with wall pressure measurements of confined swirling flows, in accordance with studies found in literature for pure axial flows. The effects of the distance between the pressure tappings demonstrated that for distances up to 20 hole diameters the accuracy of the pressure measurements is not considerably affected, but with smaller distances, 10 and

5 diameters, a significant effect is shown. From the data analysis it can be inferred that with the smaller distances, the wall pressure measured at one location features a periodic fluctuation due to the upstream neighbours, suggesting that disturbances in the boundary layer affect the pressure distribution downstream.

PIV measurements For the study of the flow structures inside a sudden expansion presented for axisymmetric and asymmetric configurations a non-intrusive laser measurement technique (PIV) was used. The use of a glycerine-water solution for the seeding has been explored for such application, identifying some advantages of the solution over other materials commonly used for seeding. The use of a glycerine-water solution has been proven to be effective for PIV studies, based on theoretical considerations. From the practical point of view, the main advantage of this material is represented by the reduced residual dirt observed in the test sections, which in other cases has been found to be detrimental in presence of swirl (e.g. olive oil).

A wealth of experimental data has been collected for the three considered flow configurations (annular pipe, symmetric sudden expansion and asymmetric sudden expansion), which provided several important contributions.

Effect of Reynolds number and swirl number on the flow structure The results for the annular pipe demonstrated that the swirl number is the key parameter controlling the flow structure, and the results showed almost no dependence on the Reynolds number. This allowed to limit the consequent studies in sudden expansions to one mass flow rate.

Turbulence properties When performed with sufficient time resolution as discussed above, hot wire measurements can provide invaluable flow statistics such as turbulent fluctuations, turbulent intensity and the dominant frequency of the flow. It has been shown that in an annular pipe the fluctuations have the same frequency regardless of the radial position.

8.2 Effect of asymmetry on swirling flows

As mentioned above, effect of asymmetry on confined swirling flows has not been studied in detail before in 3-dimensional configurations. In this project, a combination of experiments and modelling has been used to improve our understanding of the complex flow structures of confined swirling flows entering a sudden expansion with downstream resistance in presence of offset between the inlet pipe and the sudden expansion.

Model assessment A study of the performance of different RANS models in an annular pipe confirmed that $\bar{v}^2 - f$ model is a reasonable choice of turbulence models for swirling flows. This model has revealed a reasonable capability of predicting the qualitative trend of the flow inside the axisymmetric expansion, being able to capture the most important features of the swirling flow undergoing the asymmetric expansion. As expected, the model has shown limitations in the prediction of the radial pressure and velocity redistribution in such complex environment. Nonetheless, it has been possible to use the CFD simulations to get more insight into the evolution of the complex 3D structures encountered in the application. It has been demonstrated that the asymmetry induces a twisted vortex line in the swirling flow. Thus, for increasing swirl levels, a significant change in the shape and size of the central recirculation zone has been observed with increasing asymmetry. The swirling flow entering the sudden expansion initially diverts towards the closest wall, following the geometrical path of the asymmetry. The effect of swirl then prevails, overcoming the distortion induced by the asymmetry, causing a twisted profile of the vortex core line towards the opposite wall. This is an interesting behaviour of the swirling jet not observed before. Although very complex flows are observed in flows featuring precessing vortex core, such a complex behaviour in a steady flow is novel. This twisting of the swirling jet core is linked to a significant "tilting" and "twisting" of the wall separation and central recirculation zones, affecting flow distribution inside the catalyst, which has implications for practical applications.

Practical results for engineering applications From a practical point of view, focusing on the application of such case to an automotive monolith, it has been found that the optimal range of swirl levels identified in the axisymmetric case still exists in presence of asymmetry. A reduction of the pressure losses through the monolith and an improved flow uniformity has been confirmed for $0.25 \leq S \leq 0.50$, thus suggesting that for practical applications the presence of asymmetry does not alter considerably the global flow parameters. However, changes in the flow distribution entering the monolith have been observed, with considerable shifts of local flow minima and maxima that might be detrimental for the monolith durability and might impact its conversion efficiency.

8.3 High resistance devices modelling

Modelling high resistance devices represents a challenge which does not depend on the CFD model considered. The use of a porous medium model has been proven to be

effective for several engineering applications and represents an invaluable tool for the prediction of the high level distribution of first order properties such as velocity and pressure with reasonable accuracy. However, the standard porous medium model lacks in providing detailed information about the local features of the flow exiting the device, e.g. can not provide information about the single jets exiting the automotive monolith. The influence of the local structures on the flow turbulence and related properties (such as heat and mass transfer) requires a detailed understanding.

A novel formulation of the porous medium model, thus retaining its low computational requirements and its capabilities of predicting the high level properties, has been presented in this project. The new model uses a resistance function to represent flow passages inside the monolith (or any other device), so that it does not require complex CAD geometry for individual flow passages (channels), the boundary layers do not need to be resolved (as boundary layer development losses are included in the resistance formulation) and the geometry can be changed easily, allowing a great flexibility in describing and modifying the flow passage/channel geometry.

The model has been applied to a 2 dimensional case study with monolith catalyst, validating the results with experimental and other numerical data. It has been shown to offer a significant improvement in the prediction of the local flow structures compared to a standard approach. The single jets exiting the channels are clearly visible in the downstream flow, improving the prediction of the downstream turbulence.

Another important advantage of the proposed formulation (simple definition of the geometry of the flow passage, which can be easily extended to more complex shapes and applications) has been demonstrated by carrying out an optimisation study of the monolith, aiming to identify an optimal distribution of the channels to improve the flow uniformity. The model represents a promising technique for the improvement and design of high resistance devices.

8.4 Original contributions

The contributions to knowledge resulting from the current study are:

- Evaluation of the various flow measurements techniques of confined swirling flows, providing a better insight of the flow and a comprehensive database of experimental data for CFD model validation. In particular, the effect of pressure tapping geometry and spacing on the accuracy of the pressure measurements in highly swirling flows has been investigated for the first time.

- Critique assessment of RANS-based models for the prediction of confined swirling flows.
- Assessment of the impact of swirling flows undergoing a sudden expansion with downstream resistance, providing practical guidelines for the identification of the optimal swirl level corresponding to lower pressure losses and higher flow uniformity with and without asymmetry.
- Identification of the changes in the flow structures in presence of asymmetry, swirl and downstream resistance, providing a better insight into the flow physics.
- Formulation, development, implementation and validation of a new formulation for the modelling of high resistance devices, able to capture the flow passages of the device and to improve the prediction of the flow details downstream a high resistance device.

8.5 Recommendations for future work

Although considerable advances have been made in our understanding of complex swirling flows relevant to automotive aftertreatment and other applications, several important questions still remain that were outside the scope of this thesis. Some recommendations for further research, based on the findings of the study presented in the current thesis are:

- Assessment of the capabilities of URANS, LES and DES models for the prediction of swirling flows inside asymmetric sudden expansions.
- Extension of the frequency analysis study to more complex geometries (i.e. the sudden expansion), for the development of inflow and outflow boundary conditions for complex modelling approaches.
- High-fidelity modelling of the flow at the low swirl numbers ($S \approx 0.25$) for which RANS models failed to predict the flow structure well. This may offer an insight into the complex interaction between different forces acting on the fluid that results in the "transition" from the central "free jet" configuration to a swirling "wall jet" observed at high swirl numbers.
- Extension of the work presented to other swirl levels and other types of asymmetry to study the topology of the flow structures in asymmetric configuration in more detail.

References

Abu-Khiran, E., Douglas, R. and Mccullough, G., 2003. Pressure Loss Characteristics in Catalytic Converters [Online]. *Small engine technology conference & exposition*. 724. Available from: https://doi.org/10.4271/2003-32-0061.

Adrian, R.J., 1991. Particle-Imaging Techniques for Experimental Fluid Mechanics. *Annual review of fluid mechanics* [Online], 23(1), pp.261–304. Available from: https://doi.org/10.1146/annurev.fl.23.010191.001401.

Adrian, R.J., Johnson, R.E., Jones, B.G., Merati, P. and Tung, A.T., 1984. Aerodynamic disturbances of hot-wire probes and directional sensitivity. *Journal of physics e: Scientific instruments* [Online], 17(1), pp.62–71. Available from: https://doi.org/10.1088/0022-3735/17/1/012.

Alahmadi, Y.H. and Nowakowski, A.F., 2016. Modified shear stress transport model with curvature correction for the prediction of swirling flow in a cyclone separator. *Chemical engineering science* [Online], 147, pp.150–165. Available from: https://doi.org/10.1016/j.ces.2016.03.023.

Alekseenko, S.V., Kuibin, P.A. and Okulov, V.L., 2007. *Theory of concentrated vortices: An introduction* [Online]. Springer Berlin Heidelberg. Available from: https://doi.org/10.1007/978-3-540-73376-8.

Anantharamu, S. and Mahesh, K., 2020. Analysis of wall-pressure fluctuation sources from direct numerical simulation of turbulent channel flow. *Journal of fluid mechanics* [Online], 898. Available from: https://doi.org/10.1017/jfm.2020.412.

Andersson, R. and Andersson, B., 2006. On the breakup of fluid particles in turbulent flows. *Aiche journal* [Online], 52(6), pp.2020–2030. Available from: https://doi.org/10.1002/aic.10831.

Arter, A. and Meier, U., 1990. *Hydraulics Engineering Manual* [Online]. SKAT. Available from: https://skat.ch/wp-content/uploads/2017/03/02-Hydraulics-Engineering-Manual.pdf.

Ashgriz, N., ed., 2011. *Handbook of Atomization and Sprays* [Online], vol. 1. Toronto Ontario Canada: Springer US. Available from: https://doi.org/10.1007/978-1-4419-7264-4.

Bailly, C. and Comte-Bellot, G., 2015. *Turbulence* [Online], Experimental Fluid Mechanics 1. Cham: Springer International Publishing. Available from: https://doi.org/10.1007/978-3-319-16160-0.

Baker, R.C., 2016. *Flow Measurement Handbook* [Online]. Cambridge University Press. Available from: https://doi.org/10.1017/cbo9781107054141.

Baldwin, B. and Lomax, H., 1978. Thin-layer approximation and algebraic model for separated turbulentflows [Online]. *16th aerospace sciences meeting*. Reston, Virigina: American Institute of Aeronautics and Astronautics. Available from: https://doi.org/10.2514/6.1978-257.

Beall, D.M. and Cutler, W.A., 2020. Smog begone! How development of ceramic automotive catalytic substrates and filters helped to reduce air pollution. *American ceramic society bulletin* [Online], pp.24–31. Available from: https://ceramics.org/wp-content/uploads/2020/03/April-2020{_}Feature.pdf.

Bella, G., Rocco, V. and Maggiore, M., 1991. A study of inlet flow distortion effects on automotive catalytic converters. *Journal of engineering for gas turbines and power* [Online], 113(3), pp.419–426. Available from: https://doi.org/10.1115/1.2906247.

Benjamin, S.F., Haimad, N., Roberts, C.A. and Wollin, J., 2001. Modelling the flow distribution through automotive catalytic converters. *Proceedings of the institution of mechanical engineers, part c: Journal of mechanical engineering science* [Online], 215(4), pp.379–383. Available from: https://doi.org/10.1243/0954406011520779.

Benjamin, S.F., Liu, Z. and Roberts, C.A., 2004. Automotive catalyst design for uniform conversion efficiency. *Applied mathematical modelling* [Online], 28, pp.559–572. Available from: https://doi.org/10.1016/j.apm.2003.10.008.

Benjamin, S.F., Zhao, H. and Arias-Garcia, A., 2003. Predicting the flow field inside a close-coupled catalyst - The effect of entrance losses. *Proceedings of the institution of mechanical engineers part c-journal of mechanical engineering science* [Online], 217(3), pp.283–288. Available from: https://doi.org/10.1243/095440603762870036.

Benjamin, T.B., 1962. Theory of the vortex breakdown phenomenon. *Journal of fluid mechanics* [Online], 14(04), p.593. Available from: https://doi.org/10.1017/S0022112062001482.

Bergqvist, S., 2014. *Prediction of Turbo Compressor Maps using CFD*.

Bertrand, F., Devals, C., Vidal, D., Préval, C.S.D. and Hayes, R.E., 2012. Towards the simulation of the catalytic monolith converter using discrete channel-scale models. *Catalysis today* [Online], 188(1), pp.80–86. Available from: https://doi.org/10.1016/j.cattod.2011.12.011.

Biau, D.J., 2011. In brief: Standard deviation and standard error. *Clinical orthopaedics and related research* [Online], 469(9), pp.2661–2664. Available from: https://doi.org/10.1007/s11999-011-1908-9.

Brezzi, F., Lipnikov, K., Shashkov, M. and Simoncini, V., 2007. A new discretization methodology for diffusion problems on generalized polyhedral meshes. *Computer methods in applied mechanics and engineering* [Online], 196(37-40 SPEC. ISS.), pp.3682–3692. Available from: https://doi.org/10.1016/j.cma.2006.10.028.

Bruun, H.H., 1996. Hot-Wire Anemometry: Principles and Signal Analysis. *Measurement science and technology* [Online]. Available from: https://doi.org/10.1088/0957-0233/7/10/024.

Buice, C.U. and Eaton, J.K., 2000. Experimental Investigation of Flow Through an Asymmetric Plane Diffuser. *Journal of fluids engineering* [Online], 122(2), pp.433–435. Available from: https://doi.org/10.1115/1.483278.

Cavazzini, G., Dazin, A., Pavesi, G., Dupont, P. and Bois, G., 2013. Post-Processing Methods of PIV Instantaneous Flow Fields for Unsteady Flows in Turbomachines. *The particle image velocimetry - characteristics, limits and possible applications* [Online]. Available from: https://doi.org/10.5772/37273.

CD-Adapco, 2018. Star CCM+.

Ceglia, G., Discetti, S., Ianiro, A., Michaelis, D., Astarita, T. and Cardone, G., 2014. Three-dimensional organization of the flow structure in a non-reactive model aero engine lean burn injection system. *Experimental thermal and fluid science* [Online], 52, pp.164–173. Available from: https://doi.org/10.1016/j.expthermflusci.2013.09.007.

Chanaud, R.C., 1965. Observations of oscillatory motion in certain swirling flows. *Journal of fluid mechanics* [Online], 21(1), pp.111–127. Available from: https://doi.org/10.1017/S0022112065000083.

Chang, F. and Dhir, V.K., 1995. Mechanisms of heat transfer enhancement and slow decay of swirl in tubes using tangential injection. *International journal of heat and fluid flow* [Online], 16(2), pp.78–87. Available from: https://doi.org/10.1016/0142-727X(94)00016-6.

Chorin, A.J., 1968. Numerical solution of the Navier-Stokes equations. *Mathematics of computation* [Online], 22(104), pp.745–745. Available from: https://doi.org/10.1090/s0025-5718-1968-0242392-2.

Chue, S.H., 1975. Pressure probes for fluid measurement. *Progress in aerospace sciences* [Online], 16(2), pp.147–223. Available from: https://doi.org/10.1016/0376-0421(75)90014-7.

Clarkson, R.J., 1995. *A theoretical and experimental study of automotive catalytic converters*. Phd thesis. Coventry University.

Clayton, B.R. and Morsi, Y.S., 1985. Determination of principal characteristics of turbulent swirling flow along annuli. Part 2: Measurement of turbulence components. *International journal of heat and fluid flow* [Online], 6(1), pp.31–41. Available from: https://doi.org/10.1016/0142-727X(85)90029-3.

Coleman, H.W. and Steele, W.G., 2009. *Experimentation, validation, and uncertainty analysis for engineers* [Online]. Third edit ed. John Wiley & Sons, Ltd. Available from: https://doi.org/10.1002/9780470485682.

Colvile, R.N., Hutchinson, E.J., Mindell, J.S. and Warren, R.F., 2001. The transport sector as a source of air pollution. *Atmospheric environment* [Online], 35(9), pp.1537–1565. Available from: https://doi.org/10.1016/S1352-2310(00)00551-3.

Cornejo, I., Nikrityuk, P. and Hayes, R.E., 2018a. Multiscale RANS-based modeling of the turbulence decay inside of an automotive catalytic converter. *Chemical engineering science* [Online], 175, pp.377–386. Available from: https://doi.org/10.1016/j.ces.2017.10.004.

Cornejo, I., Nikrityuk, P. and Hayes, R.E., 2018b. Turbulence generation after a monolith in automotive catalytic converters. *Chemical engineering science* [Online], 187, pp.107–116. Available from: https://doi.org/10.1016/j.ces.2018.04.041.

Das, P. and Horton, R., 2018. Pollution, health, and the planet: time for decisive action. *The lancet* [Online], 391(10119), pp.407–408. Available from: https://doi.org/10.1016/S0140-6736(17)32588-6.

De Langhe, C., Merci, B. and Dick, E., 2006. Application of a RG hybrid RANS/LES model to swirling confined turbulent jets. *Journal of turbulence* [Online], 7(January), pp.1–19. Available from: https://doi.org/10.1080/14685240600873710.

Dellenback, P.A., Metzger, D.E. and Neitzel, G.P., 1988. Measurements in turbulent swirling flow through an abrupt axisymmetric expansion. *Aiaa journal* [Online], 26(6), pp.669–681. Available from: https://doi.org/10.2514/3.9952.

Denton, J.D., 1963. *Turbulent flow in concentric and eccentric annuli*. Msc. British Columbia.

Dhakal, T.P., Walters, D.K. and Strasser, W., 2014. Numerical study of gas-cyclone airflow: An investigation of turbulence modelling approaches. *International journal of computational fluid dynamics* [Online], 28(1-2), pp.1–15. Available from: https://doi.org/10.1080/10618562.2013.878800.

Di Mare, L., Jelly, T.O., Day, I.J., Mare, L., Jelly, T.O. and Day, I.J., 2017. Angular response of hot wire probes. *Measurement science and technology* [Online], 28(3). Available from: https://doi.org/10.1088/1361-6501/aa5014.

Ducruet, C. and Dyment, A., 1984. The pressure-hole problem. *Journal of fluid mechanics* [Online], 142, pp.251–267. Available from: https://doi.org/10.1017/S0022112084001099.

Durbin, P.A., 1995. Separated flow computations with the k-ε-v2 model. *Aiaa journal* [Online], 33(4), pp.659–664. Available from: https://doi.org/10.2514/3.12628.

Durst, F., Pereira, J.C.F. and Tropea, C., 1993. The plane Symmetric sudden-expansion flow at low Reynolds numbers. *Journal of fluid mechanics* [Online], 248, pp.567–581. Available from: https://doi.org/10.1017/S0022112093000916.

Dwyer, 2009. *Series OP Orifice Plate Flow Meter - Specifications, Installation and Operating Instructions*.

Edwards, M.R., Klemun, M.M., Kim, H.C., Wallington, T.J., Winkler, S.L., Tamor, M.A. and Trancik, J.E., 2017. Vehicle emissions of short-lived and long-lived climate forcers: Trends and tradeoffs. *Faraday discussions* [Online], 200(0), pp.453–474. Available from: https://doi.org/10.1039/c7fd00063d.

EEA, 2020. *Air quality in Europe — 2020 report — European Environment Agency* [Online]. (5). European Environment Agency. Available from: https://www.eea.europa.eu//publications/air-quality-in-europe-2020-reporthttp://www.eea.europa.eu/publications/air-quality-in-europe-2015{#}tab-data-references.

El-Gabry, L., Thurman, D. and Poinsatte, P., 2014. *Procedure for Determining Turbulence Length Scales Using Hotwire Anemometry* [Online]. Available from: https://ntrs.nasa.gov/citations/20150000733.

Escudier, M.P., Bornstein, J. and Zehnder, N., 1980. Observations and LDA measurements of confined turbulent vortex flow. *Journal of fluid mechanics* [Online], 98(1), pp.49–63. Available from: https://doi.org/10.1017/S0022112080000031.

Escudier, M.P. and Keller, J.J., 1985. Recirculation in swirling flow: A manifestation of vortex breakdown. *Aiaa journal* [Online], 23(1), pp.111–116. Available from: https://doi.org/10.2514/3.8878.

Escudier, M.P., Nickson, A.K. and Poole, R.J., 2006. Influence of outlet geometry on strongly swirling turbulent flow through a circular tube. *Physics of fluids* [Online], 18(12), pp.1–18. Available from: https://doi.org/10.1063/1.2400075.

European Commission, 2013. *The clean air package: Improving Europe's air quality* [Online]. Available from: https://www.consilium.europa.eu/en/policies/clean-air/{#}http://ec.europa.eu/governance/impact/ia{_}carried{_}out/docs/ia{_}2013/swd{_}2013{_}0531{_}{%}0Aen.pdf.

Fadhila, H., Medina, H., Aleksandrova, S. and Benjamin, S., 2020. A new non-linear RANS model with enhanced near-wall treatment of turbulence anisotropy. *Applied mathematical modelling* [Online], 82, pp.293–313. Available from: https://doi.org/10.1016/j.apm.2020.01.056.

Farokhi, S., Taghavi, R. and Rice, D.J., 1988. Effect of initial tangential velocity distribution on the mean evolution of a swirling turbulent free jet. *1st national fluid dynamics conference, 1988* [Online]. Available from: https://doi.org/10.2514/6.1988-3592.

Fattorini, D. and Regoli, F., 2020. Role of the chronic air pollution levels in the Covid-19 outbreak risk in Italy [Online]. Available from: https://doi.org/10.1016/j.envpol.2020.114732.

FCO, 2013. Model 318 Panel Mounted Pressure Transmitter - User Guide [Online]. Available from: http://www.furness-controls.com.

Fefferman, C.L., 2000. Existence and smoothness of the Navier-Stokes equation. *The millennium prize problems* [Online], pp.1–5. Available from: https://claymath.org/sites/default/files/navierstokes.pdf.

Ferziger, J.H. and Perić, M., 2002. *Computational Methods for Fluid Dynamics* [Online]. Springer Berlin Heidelberg. Available from: https://doi.org/10.1007/978-3-642-56026-2.

Figliola, R.S. and Beasley, D.E., 2011. *Theory and Design for Mechanical Measurements, Fifth Edition* [Online]. 5th ed. John Wiley & Sons, Inc. Available from: https://www.wiley.com/en-gb/Theory+and+Design+for+Mechanical+Measurements,+5th+Edition+International+Student+Version-p-9781118506530.

Fowler, D., Brimblecombe, P., Burrows, J., Heal, M.R., Grennfelt, P., Stevenson, D.S., Jowett, A., Nemitz, E., Coyle, M., Lui, X., Chang, Y., Fuller, G.W., Sutton, M.A., Klimont, Z., Unsworth, M.H. and Vieno, M., 2020. A chronology of global air quality: The development of global air pollution [Online]. Available from: https://doi.org/10.1098/rsta.2019.0314.

Franklin, R.E. and Wallace, J.M., 1970. Absolute measurements of static-hole error using flush transducers. *Journal of fluid mechanics* [Online], 42(1), pp.33–48. Available from: https://doi.org/10.1017/S0022112070001052.

Fraser, N., Blaxill, H., Lumsden, G. and Bassett, M., 2009. Challenges for increased efficiency through gasoline engine downsizing. *Sae technical papers* [Online], 2(1), pp.991–1008. Available from: https://doi.org/10.4271/2009-01-1053.

Furuichi, N. and Terao, Y., 2015. Static pressure measurement error at a wall tap of a flow nozzle for a wide range of Reynolds number. *Flow measurement and instrumentation* [Online], 46, pp.103–111. Available from: https://doi.org/10.1016/j.flowmeasinst.2015.10.007.

Gao, X., Zhu, Y.P. and Luo, Z.h., 2011. CFD modeling of gas flow in porous medium and catalytic coupling reaction from carbon monoxide to diethyl oxalate in fixed-bed reactors. *Chemical engineering science* [Online], 66(23), pp.6028–6038. Available from: https://doi.org/10.1016/j.ces.2011.08.031.

Garcia, D., 2011. A fast all-in-one method for automated post-processing of PIV data. *Experiments in fluids* [Online], 50(5), pp.1247–1259. Available from: https://doi.org/10.1007/s00348-010-0985-y.

García-Villalba, M., Fröhlich, J. and Rodi, W., 2006. Identification and analysis of coherent structures in the near field of a turbulent unconfined annular swirling jet using large eddy simulation. *Physics of fluids* [Online], 18(5), pp.1–18. Available from: https://doi.org/10.1063/1.2202648.

Gatski, T.B., 2004. Constitutive equations for turbulent flows. *Theoretical and computational fluid dynamics* [Online], 18(5), pp.345–369. Available from: https://doi.org/10.1007/s00162-004-0119-3.

Gatski, T.B. and Speziale, C.G., 1993. On Explicit Algebraic Stress Models for Complex Turbulent Flows. *Journal of fluid mechanics* [Online], 254, pp.59–78. Available from: https://doi.org/10.1017/S0022112093002034.

Giannadakis, A., Perrakis, K. and Panidis, T., 2008. A swirling jet under the influence of a coaxial flow. *Experimental thermal and fluid science* [Online], 32(8), pp.1548–1563. Available from: https://doi.org/10.1016/j.expthermflusci.2008.04.010.

Girimaji, S., Haase, W., Peng, S.H. and Schwamborn, D., eds, 2012. *Progress in Hybrid RANS-LES Modelling* [Online], *Notes on Numerical Fluid Mechanics and Multidisciplinary Design*, vol. 117. Cham: Springer International Publishing. Available from: https://doi.org/10.1007/978-3-642-31818-4.

Gonzalez, W. and Woods, R.E., 2004. *Digital Image Processing Using MATLAB* [Online]. 4th ed. Pearson. Available from: https://www.pearson.com/store/p/digital-image-processing-global-edition/P100000998582/9781292223049.

Govender, S. and Friedrich, H., 2017. Monoliths: A Review of the Basics, Preparation Methods and Their Relevance to Oxidation. *Catalysts* [Online], 7(2), p.62. Available from: https://doi.org/10.3390/catal7020062.

Graftieaux, L., Michard, M. and Grosjean, N., 2001. Combining PIV, POD and vortex identification algorithms for the study of unsteady turbulent swirling flows. *Measurement science and technology* [Online], 12(9), pp.1422–1429. Available from: https://doi.org/10.1088/0957-0233/12/9/307.

Gullman-Strand, J., Törnblom, O., Lindgren, B., Amberg, G. and Johansson, A.V., 2004. Numerical and experimental study of separated flow in a plane asymmetric diffuser. *International journal of heat and fluid flow* [Online], 25(3), pp.451–460. Available from: https://doi.org/10.1016/j.ijheatfluidflow.2004.02.012.

Guo, B., Langrish, T.A.G. and Fletcher, D.F., 2002. CFD simulation of precession in sudden pipe expansion flows with low inlet swirl. *Applied mathematical modelling* [Online], 26(1), pp.1–15. Available from: https://doi.org/10.1016/S0307-904X(01)00041-5.

Gupta, A.K., Lilley, D.G. and Syred, N., 1984. *Swirl flows* [Online]. 1st ed. Abacus Press. Available from: https://ui.adsabs.harvard.edu/abs/1984tw...book.....G/abstract.

Gursul, I., 1994. Unsteady flow phenomena over delta wings at high angle of attack. *Aiaa journal* [Online], 32(2), pp.225–231. Available from: https://doi.org/10.2514/3.11976.

Haimad, N., 1997. *A theoretical and experimental investigation of the flow performance of automotive catalytic converters* [Online]. Phd thesis. Coventry University. Available from: http://curve.coventry.ac.uk/open/items/3f51aa95-571c-73d5-bee3-4b523cab0a1c/1/.

Haller, G., 2005. An objective definition of a vortex. *Journal of fluid mechanics* [Online], 525, pp.1–26. Available from: https://doi.org/10.1017/S0022112004002526.

Hanjalić, K. and Launder, B., 2009. *Modelling turbulence in engineering and the environment: Second-moment routes to closure* [Online]. Cambridge ;;New York: Cambridge University Press. Available from: https://doi.org/10.1017/CBO9781139013314.

Harvey, J.K., 1962. Some observations of the vortex breakdown phenomenon. *Journal of fluid mechanics* [Online], 14(4), pp.585–592. Available from: https://doi.org/10.1017/S0022112062001470.

Hayes, R.E., Fadic, A., Mmbaga, J. and Najafi, A., 2012. CFD modelling of the automotive catalytic converter. *Catalysis today* [Online], 188(1), pp.94–105. Available from: https://doi.org/10.1016/j.cattod.2012.03.015.

Hettel, M., Daymo, E., Schmidt, T. and Deutschmann, O., 2020. CFD-Modeling of fluid domains with embedded monoliths with emphasis on automotive converters. *Chemical engineering and processing - process intensification* [Online], 147, p.107728. Available from: https://doi.org/10.1016/j.cep.2019.107728.

Heywood, J.B., 2018. *Internal combustion engine fundamentals* [Online]. 2nd ed. McGraw-Hill Education. Available from: https://www.accessengineeringlibrary.com/content/book/9781260116106.

Hiereth, H. and Prenninger, P., 2007. *Charging the Internal Combustion Engine* [Online]. Springer Vienna. Available from: https://doi.org/10.1007/978-3-211-47113-5.

Hinze, J.O., 1955. Fundamentals of the hydrodynamic mechanism of splitting in dispersion processes. *Aiche journal* [Online], 1(3), pp.289–295. Available from: https://doi.org/10.1002/aic.690010303.

Hoekstra, A.J., Derksen, J.J. and Van Den Akker, H.E., 1999. An experimental and numerical study of turbulent swirling flow in gas cyclones. *Chemical engineering science* [Online], 54(13-14), pp.2055–2065. Available from: https://doi.org/10.1016/S0009-2509(98)00373-X.

Hogg, S. and Leschziner, M.A., 1989. Computation of highly swirling confined flow with a reynolds stress turbulence model. *Aiaa journal* [Online], 27(1), pp.57–63. Available from: https://doi.org/10.2514/3.10094.

Hooftman, N., Messagie, M., Van Mierlo, J. and Coosemans, T., 2018. A review of the European passenger car regulations – Real driving emissions vs local air quality. *Renewable and sustainable energy reviews* [Online], 86, pp.1–21. Available from: https://doi.org/10.1016/j.rser.2018.01.012.

Hreiz, R., Gentric, C. and Midoux, N., 2011. Numerical investigation of swirling flow in cylindrical cyclones. *Chemical engineering research and design* [Online], 89(12), pp.2521–2539. Available from: https://doi.org/10.1016/j.cherd.2011.05.001.

Iaccarino, G., Ooi, A., Durbin, P.A. and Behnia, M., 2003. Reynolds averaged simulation of unsteady separated flow. *International journal of heat and fluid flow* [Online], 24(2), pp.147–156. Available from: https://doi.org/10.1016/S0142-727X(02)00210-2.

ISO, 2003a. *5167 -1 Measurement of fluid flow by means of pressure differential devices inserted in circular cross-section conduits running full —Part 1: General principles and requirements*. (5167-1). International Standard Organisation, ISO.

ISO, 2003b. *5167 -2 Measurement of fluid flow by means of pressure differential devices inserted in circular cross-section conduits running full —Part 2: Orifice plates*. International Standard Organisation.

ISO, 2009. *Uncertainty of measurement — Part 1 : Introduction to the expression of uncertainty in measurement*. ISO.

Jakirlić, S., Hanjalić, K. and Tropea, C., 2002. Modeling rotating and swirling turbulent flows: A perpetual challenge. *Aiaa journal* [Online], 40(10), pp.1984–1996. Available from: https://doi.org/10.2514/2.1560.

Javadi, A. and Nilsson, H., 2015. LES and DES of strongly swirling turbulent flow through a suddenly expanding circular pipe. *Computers and fluids* [Online], 107, pp.301–313. Available from: https://doi.org/10.1016/j.compfluid.2014.11.014.

JCGM, 2008. *Evaluation of measurement data-Guide to the expression of uncertainty in measurement Évaluation des données de mesure-Guide pour l'expression de l'incertitude de mesure* [Online]. Available from: www.bipm.org.

Jørgensen, F.E., 2002. *How to measure turbulence with hot-wire anemometers - a practical guide* [Online]. Dantec Dynamics. Available from: https://www.dantecdynamics.com/wp-content/uploads/2020/08/pratical-guide-how-to-measure-turbulence.pdf.

Joshi, A., 2020. Review of Vehicle Engine Efficiency and Emissions [Online]. *Sae technical papers*. SAE International, April. Available from: https://doi.org/10.4271/2020-01-0352.

Karniadakis, G.E., 2002. Quantifying Uncertainty in CFD. *Journal of fluids engineering* [Online], 124(1), p.2. Available from: https://doi.org/10.1115/1.1447925.

Kašpar, J., Fornasiero, P. and Hickey, N., 2003. Automotive catalytic converters: current status and some perspectives. *Catalysis today* [Online], 77(4), pp.419–449. Available from: https://doi.org/10.1016/S0920-5861(02)00384-X.

Kolář, V., 2007. Vortex identification: New requirements and limitations. *International journal of heat and fluid flow* [Online], 28(4), pp.638–652. Available from: https://doi.org/10.1016/j.ijheatfluidflow.2007.03.004.

Kolmogorov, A.N., 1941. The local structure of turbulence in incompressible viscous fluid for very large Reynolds numbers. *C. r. acad. sci. urss* [Online], 30, pp.301–305. Available from: https://ci.nii.ac.jp/naid/20000584634.

Kolmogorov, A.N., 1962. A refinement of previous hypotheses concerning the local structure of turbulence in a viscous incompressible fluid at high Reynolds number. *Journal of fluid mechanics* [Online], 13(1), pp.82–85. Available from: https://doi.org/10.1017/S0022112062000518.

Koltsakis, G.C., Konstantinidis, P.A. and Stamatelos, A.M., 1997. Development and application range of mathematical models for 3-way catalytic converters. *Applied catalysis b: Environmental* [Online], 12(2-3), pp.161–191. Available from: https://doi.org/10.1016/S0926-3373(96)00073-2.

Koltsakis, G.C. and Stamatelos, A.M., 1997. Catalytic automotive exhaust aftertreatment. *Progress in energy and combustion science* [Online], 23(1), pp.1–39. Available from: https://doi.org/10.1016/S0360-1285(97)00003-8.

Kuwata, Y., Suga, K. and Sakurai, Y., 2014. Development and application of a multi-scale k- \epsilon model for turbulent porous medium flows. *International journal of heat and fluid flow* [Online], 49(C), pp.135–150. Available from: https://doi.org/10.1016/j.ijheatfluidflow.2014.02.007.

Landrigan, P.J., Fuller, R. and Acosta, N.J., 2018. The Lancet Commission on pollution and health. *The lancet* [Online], 391(10119), pp.462–512. Available from: https://doi.org/10.1016/S0140-6736(17)32345-0.

Launder, B. and Spalding, D., 1974. The numerical computation of turbulent flows. *Computer methods in applied mechanics and engineering* [Online], 3(2), pp.269–289. Available from: https://doi.org/10.1016/0045-7825(74)90029-2.

Le, H., Moin, P. and Kim, J., 1997. Direct numerical simulation of turbulent flow over a backward-facing step. *Journal of fluid mechanics* [Online], 330, pp.349–374. Available from: https://doi.org/10.1017/S0022112096003941.

Lecointe, B. and Monnier, G., 2003. Downsizing a gasoline engine using turbocharging with direct injection. *Sae technical papers* [Online], 2003(724). Available from: https://doi.org/10.4271/2003-01-0542.

Lee, M. and Moser, R.D., 2015. Direct numerical simulation of turbulent channel flow up to Reτ = 5200. *Journal of fluid mechanics* [Online], 774, pp.395–415. Available from: https://doi.org/10.1017/jfm.2015.268.

Lefebvre, A.H. and McDonell, V.G., 2017. *Atomization and Sprays* [Online]. Second edition. | Boca Raton : Taylor & Francis, CRC Press, 2017.: CRC Press. Available from: https://doi.org/10.1201/9781315120911.

Legrand, M., Nogueira, J., Rodriguez, P.A., Lecuona, A. and Jimenez, R., 2017. Generation and droplet size distribution of tracer particles for PIV measurements in air, using propylene glycol/water solution. *Experimental thermal and fluid science* [Online], 81, pp.1–8. Available from: https://doi.org/10.1016/j.expthermflusci.2016.09.015.

Leuckel, W., 1973. Swirl intensities, swirl types and energy losses of different swirl generating devices. *International flame research foundation*.

Lewellen, W.S., 1971. A review of condined vortex flows. *Security*.

Li, Z., Wu, Y., Yang, H., Cai, C., Zhang, H., Hashiguchi, K., Takeno, K. and Lu, J., 2013. Effect of liquid viscosity on atomization in an internal-mixing twin-fluid atomizer [Online]. *Fuel*. Elsevier, vol. 103, pp.486–494. Available from: https://doi.org/10.1016/j.fuel.2012.06.097.

Lilley, D.G., 1977. Swirl Flows in Combustion: A Review. *Aiaa journal* [Online], 15(8), pp.1063–1078. Available from: https://doi.org/10.2514/3.60756.

Livesey, J., Jackson, J. and Southern, C., 1962. The Static Hole Error Problem. *Aircraft engineering and aerospace technology* [Online], 34(2), pp.43–47. Available from: https://doi.org/10.1108/eb033517.

Lucca-Negro, O. and O'Doherty, T., 2001. Vortex breakdown: A review. *Progress in energy and combustion science* [Online], 27(4), pp.431–481. arXiv:1011.1669v3, Available from: https://doi.org/10.1016/S0360-1285(00)00022-8.

Luginsland, T. and Kleiser, L., 2015. Effects of boundary conditions on vortex breakdown in compressible swirling jet flow simulations. *Computers and fluids* [Online], 109, pp.72–84. Available from: https://doi.org/10.1016/j.compfluid.2014.12.012.

Magazzino, C., Mele, M. and Schneider, N., 2020. The relationship between air pollution and COVID-19-related deaths: An application to three French cities. *Applied energy* [Online], 279, p.115835. Available from: https://doi.org/10.1016/j.apenergy.2020.115835.

Majewski, W.A., 2000. Emission Control Catalysts [Online]. Available from: https://dieselnet.com/tech/catalysts.php [Accessed 2021-01-08].

Mak, H. and Balabani, S., 2007. Near field characteristics of swirling flow past a sudden expansion. *Chemical engineering science* [Online], 62(23), pp.6726–6746. Available from: https://doi.org/10.1016/j.ces.2007.07.009.

Marquès, M., Rovira, J., Nadal, M. and Domingo, J.L., 2021. Effects of air pollution on the potential transmission and mortality of COVID-19: A preliminary case-study in Tarragona Province (Catalonia, Spain). *Environmental research* [Online], 192, p.110315. Available from: https://doi.org/10.1016/j.envres.2020.110315.

Martemianov, S. and Okulov, V.L., 2004. On heat transfer enhancement in swirl pipe flows. *International journal of heat and mass transfer* [Online], 47(10-11), pp.2379–2393. Available from: https://doi.org/10.1016/j.ijheatmasstransfer.2003.11.005.

MATLAB, 2019. version 9.7 (R2019b).

Matsumoto, M., 1999. VORTEX SHEDDING OF BLUFF BODIES: A REVIEW. *Journal of fluids and structures* [Online], 13(7-8), pp.791–811. Available from: https://doi.org/10.1006/jfls.1999.0249.

McDonald, A.T., Fox, R.W. and Van Dewoestine, R.V., 1971. Effects of swirling inlet flow on pressure recovery in conical diffusers. *9th aerospace sciences meeting* [Online], 9(10), pp.2014–2018. Available from: https://doi.org/10.2514/6.1971-84.

McKeon, B.J. and Smits, A.J., 2002. Static pressure correction in high Reynolds number fully developed turbulent pipe flow. *Measurement science and technology* [Online], 13(10), pp.1608–1614. Available from: https://doi.org/10.1088/0957-0233/13/10/314.

MECA, 2009. *Aftermarket Converter Technology for Gasoline Light-Duty Vehicles* [Online]. (December). Manufacturers of Emission Controls Association. Available from: www.meca.org.

Mechel, F.P., ed., 2008. *Formulas of Acoustics* [Online]. Berlin, Heidelberg: Springer Berlin Heidelberg. Available from: https://doi.org/10.1007/978-3-540-76833-3.

Menter, F.R., 1994. Two-equation eddy-viscosity turbulence models for engineering applications. *Aiaa journal* [Online], 32(8), pp.1598–1605. Available from: https://doi.org/10.2514/3.12149.

Mera, Z., Fonseca, N., López, J.M. and Casanova, J., 2019. Analysis of the high instantaneous NOx emissions from Euro 6 diesel passenger cars under real driving conditions. *Applied energy* [Online], 242, pp.1074–1089. Available from: https://doi.org/10.1016/j.apenergy.2019.03.120.

Miller, R.W., 1996. *Flow measurement engineering handbook* [Online]. 3rd ed. New York ; London: McGraw-Hill. Available from: https://doi.org/10.1016/0142-727x(83)90065-6.

Mishriky, F. and Walsh, P., 2017. Towards understanding the influence of gradient reconstruction methods on unstructured flow simulations. *Transactions of the canadian society for mechanical engineering* [Online], 41(2), pp.169–179. Available from: https://doi.org/10.1139/tcsme-2017-0012.

Moffat, R.J., 1988. Describing the uncertainties in experimental results. *Experimental thermal and fluid science* [Online], 1(1), pp.3–17. Available from: https://doi.org/10.1016/0894-1777(88)90043-X.

Moin, P. and Mahesh, K., 1998. Direct numerical simulation: A Tool in Turbulence Research. *Annual review of fluid mechanics* [Online], 30(1), pp.539–578. Available from: https://doi.org/10.1146/annurev.fluid.30.1.539.

Moon, S., Abo-Serie, E. and Bae, C., 2008. The spray characteristics of a pressure-swirl injector with various exit plane tilts. *International journal of multiphase flow* [Online], 34(7), pp.615–627. Available from: https://doi.org/10.1016/j.ijmultiphaseflow.2008.01.003.

Moulden, T.H., Wu, J.M., Collins, F.G., Ramm, H.J., Kuwand, H., Wu, C.I. and Ray, R., 1974. *Experimental study of static pressure orifice interference* [Online]. University of Tennessee Space Institute. Available from: https://apps.dtic.mil/dtic/tr/fulltext/u2/a046403.pdf.

NEL, 2010. *Good Practice Guide Flow Measurement Uncertainty and Data Reconciliation*. National Measurement System.

Nikolaos D. Katopodes, 2019. *Free-Surface Flow* [Online]. Elsevier. Available from: https://doi.org/10.1016/C2016-0-04780-0.

Obi, S., Aoki, K. and Masuda, S., 1993. Experimental and computational study of turbulent separating flow in an asymmetric plane diffuser. *Ninth symposium on turbulent shear flows*. January 1993.

Okhio, C.B., Horton, H.P. and Langer, G., 1983. Effects of swirl on flow separation and performance of wide angle diffusers. *International journal of heat and fluid flow* [Online], 4(4), p.199. Available from: https://doi.org/10.1016/0142-727X(83)90039-5.

Padula, G., Saul, J., Aleksandrova, S., Medina, H. and Benjamin, S., 2019. A New Take on Porous Medium Approach for Modelling Monoliths and Other Multiple Channel Devices. *Sae technical papers* [Online]. Available from: https://doi.org/10.4271/2019-24-0049.

Palm, R., Grundmann, S., Weismüller, M., Šarić, S., Jakirlić, S. and Tropea, C., 2006. Experimental characterization and modelling of inflow conditions for a gas turbine swirl combustor. *International journal of heat and fluid flow* [Online], 27(5), pp.924–936. Available from: https://doi.org/10.1016/j.ijheatfluidflow.2006.03.016.

Parchen, R.R., 1993. *Decay of swirl in turbulent pipe flows* [Online]. Phd. Technische Universiteit Eindhoven. Available from: https://doi.org/https://doi.org/10.6100/IR389647.

Parra-Cabrera, C., Achille, C., Kuhn, S. and Ameloot, R., 2018. 3D printing in chemical engineering and catalytic technology: Structured catalysts, mixers and reactors. *Chemical society reviews* [Online], 47(1), pp.209–230. Available from: https://doi.org/10.1039/c7cs00631d.

Patankar, S., 1980. Numerical Heat Transfer and Fluid Flow.

Peckham, D.H. and Atkinson, S.A., 1957. Preliminary Results of Low Speed Wind Tunnel Tests on a Gothic Wing of Aspect Ratio 1.0. *A. r. c. technical report*, p.38.

Pemberton, R., 2010. *an Overview of Dynamic Pressure Measurement Considerations*. Scanivalve.

Perić, M., 2004. Flow Simulation using Control Volumes of Arbitrary Polyhedral Shape. *Ercoftac bulletin*, 62, pp.25–29.

Peric, M. and Ferguson, S., 2005. The advantage of polyhedral meshes. *Star-ccm+ guide* [Online], p.2. Available from: https://www.semanticscholar.org / paper / The-advantage-of-polyhedral-meshes-Peri{ć}-Ferguson / 51ae90047ab44f53849196878bfec4232b291d1c.

Persoons, T., 2006. *Experimental flow dynamics in automotive exhaust systems with close-coupled catalyst*. Phd. KATHOLIEKE UNIVERSITEIT LEUVEN.

Persoons, T., Vanierschot, M. and Van den Bulck, E., 2008. Oblique inlet pressure loss for swirling flow entering a catalyst substrate. *Experimental thermal and fluid science* [Online], 32(6), pp.1222–1231. Available from: https://doi.org/10.1016/j.expthermflusci.2008.04.011.

Pierce, C.D. and Moin, P., 1998. Method for generating equilibrium swirling inflow conditions. *Aiaa journal* [Online], 36(7), pp.1325–1327. Available from: https://doi.org/10.2514/2.518.

Piumetti, M., Bensaid, S., Fino, D. and Russo, N., 2015. Catalysis in Diesel engine NOx aftertreatment: a review [Online]. Available from: https://doi.org/10.1080/2055074X.2015.1105615.

Pizer, S.M., Amburn, E.P., Austin, J.D., Cromartie, R., Geselowitz, A., Greer, T., ter Haar Romeny, B., Zimmerman, J.B. and Zuiderveld, K., 1987. Adaptive histogram equalization and its variations. *Computer vision, graphics, and image processing* [Online], 39(3), pp.355–368. Available from: https://doi.org/10.1016/S0734-189X(87)80186-X.

Pope, S.B., 1975. A more general effective-viscosity hypothesis. *Journal of fluid mechanics* [Online], 72(2), pp.331–340. Available from: https://doi.org/10.1017/S0022112075003382.

Pope, S.B., 1999. A Perspective on Turbulence Modeling [Online]. *Modeling complex turbulent flows*. Springer International Publishing, pp.53–67. Available from: https://doi.org/978-94-010-5986-2.

Pope, S.B., 2000. *Turbulent Flows* [Online], vol. 1. Cambridge University Press. Available from: https://www.cambridge.org/gb/academic/subjects/physics/nonlinear-science-and-fluid-dynamics/turbulent-flows?format=PB{#}bookPeople.

Pope, S.B., 2004. Ten questions concerning the large-eddy simulation of turbulent flows. *New journal of physics* [Online], 6. Available from: https://doi.org/10.1088/1367-2630/6/1/035.

Porter, S., Mat Yamin, A.K., Aleksandrova, S., Benjamin, S., Roberts, C.A. and Saul, J., 2014. An Assessment of CFD Applied to Steady Flow in a Planar Diffuser Upstream of an Automotive Catalyst Monolith. *Sae international journal of engines* [Online], 7(4), pp.1697–1704. Available from: https://doi.org/10.4271/2014-01-2588.

Porter, S., Saul, J., Yamin, A.K.M., Aleksandrova, S., Benjamin, S.F. and Medina, H.J., 2015. Pulsating flow in a planar diffuser upstream of automotive catalyst monoliths [Online]. *10th pacific symposium on flow visualization and image processing*. Naples, vol. 40, pp.43–53. Available from: https://www.psfvip10.unina.it/Ebook/web/papers/028{_}PSFVIP10.pdf.

Porter, S.J., 2016. *An Assessment Of CFD Applied To A Catalytic Converter System With Planar Diffuser* [Online]. Phd thesis. Coventry University. Available from: https://curve.coventry.ac.uk/open/items/84bb21f6-7856-44a8-923e-acb5337f6a3c/1/.

Prithiviraj, M. and Andrews, M.J., 1998. Three dimensional numerical simulation of shell-and-tube heat exchangers. PART I: Foundation and fluid mechanics. *Numerical heat transfer; part a: Applications* [Online], 33(8), pp.799–816. Available from: https://doi.org/10.1080/10407789808913967.

Promvonge, P., Pethkool, S., Pimsarn, M. and Thianpong, C., 2012. Heat transfer augmentation in a helical-ribbed tube with double twisted tape inserts. *International communications in heat and mass transfer* [Online], 39(7), pp.953–959. Available from: https://doi.org/10.1016/j.icheatmasstransfer.2012.05.015.

Raffel, M., Willert, C.E., Wereley, S.T. and Kompenhans, J., 2007. *Particle Image Velocimetry* [Online]. Berlin, Heidelberg: Springer Berlin Heidelberg. Available from: https://doi.org/10.1007/978-3-540-72308-0.

Rayle, R.E., 1949. *An investigation of the influence of orifice geometry on static pressure measurements*. Ph.D. thesis. Massachusetts Institute of Technology.

Roach, P.E. and Turner, J.T., 1988. Premature boundary layer transition caused by surface static pressure tappings. *The aeronautical journal* [Online], 92(912), pp.63–68. Available from: https://doi.org/10.1017/S0001924000021898.

Roache, P.J., 1997. Quantification of uncertainty in computational fluid dynamics. *Annual review of fluid mechanics* [Online], 29, pp.123–160. Available from: https://doi.org/10.1146/annurev.fluid.29.1.123.

Roback, R. and Johnson, B.V., 1983. *Mass and momentum turbulent transport experiments with confined swirling coaxial jets*. NASA.

Rosenberg, B.J., Hultmark, M., Vallikivi, M., Bailey, S.C. and Smits, A.J., 2013. Turbulence spectra in smooth- and rough-wall pipe flow at extreme Reynolds numbers. *Journal of fluid mechanics* [Online], 731, pp.46–63. Available from: https://doi.org/10.1017/jfm.2013.359.

Roth, M., 2000. *Automatic Extraction of Vortex Core Lines and Other Line-Type Features for Scientific Visualization* [Online]. Phd thesis. Swiss Federal Institute of Technology Zurich. Available from: https://doi.org/https://doi.org/10.3929/ethz-a-004016407.

Roux, S., Lartigue, G., Poinsot, T., Meier, U. and Bérat, C., 2005. Studies of mean and unsteady flow in a swirled combustor using experiments, acoustic analysis, and large eddy simulations. *Combustion and flame* [Online], 141(1-2), pp.40–54. Available from: https://doi.org/10.1016/j.combustflame.2004.12.007.

Ruiz-Morales, J.C., Tarancón, A., Canales-Vázquez, J., Méndez-Ramos, J., Hernández-Afonso, L., Acosta-Mora, P., Marín Rueda, J.R. and Fernández-González, R., 2017. Three dimensional printing of components and functional devices for energy and environmental applications. *Energy and environmental science* [Online], 10(4), pp.846–859. Available from: https://doi.org/10.1039/c6ee03526d.

Rusli, I.H., 2019. *Experimental study of swirling flows in symmetric and asymmetric sudden expansions with downstream resistance* [Online]. Phd thesis. Coventry University. Available from: https://pureportal.coventry.ac.uk/en/studentTheses/experimental-study-of-swirling-flows-in-symmetric-and-asymmetric-.

Rusli, I.H., Aleksandrova, S., Medina, H. and Benjamin, S.F., 2017. The Effect of Swirl on the Flow Uniformity in Automotive Exhaust Catalysts. *Sae technical papers* [Online]. Available from: https://doi.org/10.4271/2017-01-2384.

Sahasrabudhe, S.N., Rodriguez-Martinez, V., O'Meara, M. and Farkas, B.E., 2017. Density, viscosity, and surface tension of five vegetable oils at elevated temperatures: Measurement and modeling. *International journal of food properties* [Online], 20, pp.1965–1981. Available from: https://doi.org/10.1080/10942912.2017.1360905.

Salehi, S., Raisee, M. and Cervantes, M.J., 2017. Computation of developing turbulent flow through a straight asymmetric diffuser with moderate adverse pressure gradient. *Journal of applied fluid mechanics* [Online], 10(4), pp.1029–1043. Available from: https://doi.org/10.18869/acadpub.jafm.73.241.26311.

Saul, J.M., Porter, S.J., Mat Yamin, A.K., Medina, H.J., Aleksandrova, S. and Benjamin, S.F., 2015. Influence of cycle variance on the performance of URANS for pulsating flow upstream of an automotive catalyst monolith [Online]. *Internal combustion engines*. London. Available from: https://pureportal.coventry.ac.uk/en/publications/influence-of-cyclic-variance-on-the-performance-of-urans-for-puls-2.

Scanivalve, 2016. *Electronic Pressure Scanning Module Instruction and Service Manual*.

Scheffel, J., 2001. *On Analytical Solution of the Navier-Stokes Equations On Analytical Solution of the* [Online]. The Alfvén Laboratory Division of Fusion Plasma Physics Royal Institute of Technology. Available from: http://www.fusion.kth.se.

Schetz, J.A., Fuhs, A.E. and Telionis, D.P., 1996. Handbook of Fluid Dynamics and Fluid Machinery. *Journal of fluids engineering* [Online], 118(2), pp.218–218. Available from: https://doi.org/10.1115/1.2817366.

Schluter, J.U. and Pitsch, H., 2001. Consistent boundary conditions for integrated LES / RANS simulations: LES outflow conditions. *Center for turbulence research annual research briefs*, pp.19–30.

Schmitt, F.G., 2007. About Boussinesq's turbulent viscosity hypothesis: historical remarks and a direct evaluation of its validity [Online]. Available from: https://doi.org/10.1016/j.crme.2007.08.004.

Shah, R.K., 1978. A Correlation for Laminar Hydrodynamic Entry Length Solutions for Circular and Noncircular Ducts. *Journal of fluids engineering* [Online], 100(2), pp.177–179. Available from: https://doi.org/10.1115/1.3448626.

Sharif, M.A. and Wong, Y.K., 1995. Evaluation of the performance of three turbulence closure models in the prediction of confined swirling flows. *Computers and fluids* [Online], 24(1), pp.81–100. Available from: https://doi.org/10.1016/0045-7930(94)E0004-H.

Shaw, R., 1960. The influence of hole dimensions on static pressure measurements. *Journal of fluid mechanics* [Online], 7(4), pp.550–564. Available from: https://doi.org/10.1017/S0022112060000281.

Shih, T.H. and Lumley, J.L., 1993. Remarks on turbulent constitutive relations. *Mathematical and computer modelling* [Online], 18(2), pp.9–16. Available from: https://doi.org/10.1016/0895-7177(93)90002-G.

Shih, T.H., Zhu, J., Liou, W.W., Chen, K.H., Liu, N.S. and Lumley, J.L., 1997. *Modeling of Turbulent Swirling Flows*. NASA.

Shiri, A., George, W.K. and Naughton, J.W., 2008. Experimental Study of the Far Field of Incompressible Swirling Jets. *Aiaa journal* [Online], 46(8), pp.2002–2009. Available from: https://doi.org/10.2514/1.32954.

Shur, M., Strelets, M., Travin, A. and Spalart, P.R., 1998. Turbulence modeling in rotating and curved channels: Assessment of the spalart-shur correction term [Online]. *36th aiaa aerospace sciences meeting and exhibit*. Available from: https://doi.org/10.2514/6.1998-325.

Skusiewicz, P., 2012. *Effect of swirl on the flow distribution across automotive emissions after-treatment*. M res. Coventry University.

Sloan, D.G., Smoot, L.D., Smith, P.J. and Smoot, L.D., 1986. Modeling of swirl in turbulent flow systems. *Progress in energy and combustion science* [Online], 12, pp.163–250. Available from: https://doi.org/10.1016/0360-1285(86)90016-X.

Smagorinsky, J., 1963. General circulation experiments with the primitive equations. *Monthly weather review* [Online], 91(3), pp.99–164. Available from: https://doi.org/10.1175/1520-0493(1963)091<0099:gcewtp>2.3.co;2.

Smirnov, P.E. and Menter, F.R., 2009. Sensitization of the SST turbulence model to rotation and curvature by applying the Spalart-Shur correction term. *Journal of turbomachinery* [Online], 131(4), pp.1–8. Available from: https://doi.org/10.1115/1.3070573.

Smith, A.M., Cebeci, T. and Smith, A.M. and Cebeci, T., 1967. Numerical solution of the turbulent boundary layer equations [Online]. Available from: https://apps.dtic.mil/sti/citations/AD0656430.

So, K.L., 1967. Vortex phenomena in a conical diffuser. *Aiaa journal* [Online], 5(6), pp.1072–1078. Available from: https://doi.org/10.2514/3.4139.

So, R.M., Ahmed, S.A. and Mongia, H.C., 1984. *An Experimental Investigation of Gas Jets in Confined Swirling Air Flow*. (June). NASA.

Sobey, I.J., 1982. Oscillatory flows at intermediate Strouhal number in asymmetric channels. *Journal of fluid mechanics* [Online], 125, pp.359–373. Available from: https://doi.org/10.1017/S0022112082003371.

Somers, D.M., Stack, J.P. and Harvey, W.D., 1982. *Influence of Surface Static-Pressure Orifices on Boundary-Layer Transition*. Langley Research Center, Hampton, Virginia: NASA.

Sosnowski, M., Krzywanski, J. and Gnatowska, R., 2017. Polyhedral meshing as an innovative approach to computational domain discretization of a cyclone in a fluidized bed CLC unit. *E3s web of conferences* [Online], 14. Available from: https://doi.org/10.1051/e3sconf/20171401027.

Sozer, E., Brehm, C. and Kiris, C.C., 2014. Gradient calculation methods on arbitrary polyhedral unstructured meshes for cell-centered CFD solvers. *52nd aiaa aerospace sciences meeting - aiaa science and technology forum and exposition, scitech 2014* [Online], pp.1–24. Available from: https://doi.org/10.2514/6.2014-1440.

Spalart, P.R., Jou, W.H., Strelets, M. and Allmaras, S.R., 1997. Comments on the feasibility of LES for wings, and on a hybrid RANS/LES approach. In: G.P. Columbus, ed. *Afors international conference on dns/les*. Ruston, Louisiana, pp.137–147.

Spalart, P.R. and Shur, M., 1997. On the Sensitization of Turbulence Models to Rotation and Curvature. *Aerospace science and technology* [Online], 1(5), pp.297–302. Available from: https://doi.org/10.1016/S1270-9638(97)90051-1.

Spiegel, M., Redel, T., Zhang, Y.J., Struffert, T., Hornegger, J., Grossman, R.G., Doerfler, A. and Karmonik, C., 2009. Tetrahedral and polyhedral mesh evaluation for cerebral hemodynamic simulation - A comparison. *Proceedings of the 31st annual international conference of the ieee engineering in medicine and biology society: Engineering the future of biomedicine, embc 2009* [Online], pp.2787–2790. Available from: https://doi.org/10.1109/IEMBS.2009.5333829.

Steenbergen, W., 1995. *Turbulent Pipe Flow with Swirl* [Online]. Phd. Technische Universiteit Eindhoven. Available from: https://doi.org/https://doi.org/10.6100/IR430720.

Stern, F., Wilson, R. and Shao, J., 2006. Quantitative V&V of CFD simulations and certification of CFD codes. *International journal for numerical methods in fluids* [Online], 50(11), pp.1335–1355. Available from: https://doi.org/10.1002/fld.1090.

Su, C., Brault, J., Munnannur, A., Gerald Liu, Z., Milloy, S., Harinath, A., Dunnuck, D. and Federle, K., 2019. Model-Based Approaches in Developing an Advanced Aftertreatment System: An Overview. *Sae technical papers* [Online], 2019-Janua(January), pp.1–14. Available from: https://doi.org/10.4271/2019-01-0026.

Syrakos, A., Varchanis, S., Dimakopoulos, Y., Goulas, A. and Tsamopoulos, J., 2017. A critical analysis of some popular methods for the discretisation of the gradient operator in finite volume methods. *Physics of fluids* [Online], 29(12), pp.1–40. 1606.05556, Available from: https://doi.org/10.1063/1.4997682.

Syred, N., 2006. A review of oscillation mechanisms and the role of the precessing vortex core (PVC) in swirl combustion systems. *Progress in energy and combustion science* [Online], 32(2), pp.93–161. Available from: https://doi.org/10.1016/j.pecs.2005.10.002.

Syred, N., 2011. 40 years with Swirl, Vortex, Cyclonic Flows, and Combustion [Online]. *49th aiaa aerospace sciences meeting*. Available from: https://doi.org/doi:10.2514/6.2011-10510.2514/6.2011-105.

Taulbee, D.B., 1992. An improved algebraic Reynolds stress model and corresponding nonlinear stress model. *Physics of fluids a* [Online], 4(11), pp.2555–2561. Available from: https://doi.org/10.1063/1.858442.

Teitelbaum, J., Zatorre, J., Carpenter, S., DANIEL, G., EVANS, A., GJEDDE, A. and CASHMAN, N., 1993. An association between air pollution and mortality in six U.S. cities. *Neurologic sequelae of domoic acid intoxication due to the ingestion of contaminated mussels*, 322, p.2012.

Thakkar, H., Eastman, S., Al-Naddaf, Q., Rownaghi, A.A. and Rezaei, F., 2017. 3D-Printed Metal-Organic Framework Monoliths for Gas Adsorption Processes. *Acs applied materials and interfaces* [Online], 9(41), pp.35908–35916. Available from: https://doi.org/10.1021/acsami.7b11626.

Thakkar, H., Eastman, S., Hajari, A., Rownaghi, A.A., Knox, J.C. and Rezaei, F., 2016. 3D-Printed Zeolite Monoliths for CO2 Removal from Enclosed Environments. *Acs applied materials and interfaces* [Online], 8(41), pp.27753–27761. Available from: https://doi.org/10.1021/acsami.6b09647.

Thakrar, S.K., Balasubramanian, S., Adams, P.J., Azevedo, I.M., Muller, N.Z., Pandis, S.N., Polasky, S., Pope, C.A., Robinson, A.L., Apte, J.S., Tessum, C.W., Marshall, J.D. and Hill, J.D., 2020. Reducing Mortality from Air Pollution in the United States by Targeting Specific Emission Sources. *Environmental science and technology letters* [Online], 7(9), pp.639–645. Available from: https://doi.org/10.1021/acs.estlett.0c00424.

Thielicke, W. and Stamhuis, E.J., 2014. PIVlab – Towards User-friendly, Affordable and Accurate Digital Particle Image Velocimetry in MATLAB. *Journal of open research software* [Online], 2. Available from: https://doi.org/10.5334/jors.bl.

Thulukkanam, K., 2013. *Heat Exchanger Design Handbook* [Online]. CRC Press. Available from: https://doi.org/10.1201/b14877.

Tropea, C., Yarin, A.L. and Foss, J.F., 2007. *Handbook of Experimental Fluid Mechanics* [Online]. Springer Berlin Heidelberg. Available from: https://doi.org/10.1007/978-3-540-30299-5.

TSI, 2010. Ifa 300 Constant Temperature Anemometer System - Operation Manual.

TSI, 2015. *Seed Particle Generation from model 9306 Six-Jet atomizer* [Online]. Available from: https://www.tsi.com/getmedia/0c2909e2-ad70-4b9b-8878-9ef8d8da7017/9306-001{_}Seed{_}Particle{_}Generation{_}Model{_}9306{_}A4-web(1){_}1.

TSI, 2017. Insight 4G Global Image, Acquisition, Analysis, & Display Software.

USEPA Office of Air and Radiation, 2010. *The Benefits and Costs of the Clean Air Act: 1990 to 2020*. (April).

Vedantam, S. and Joshi, J.B., 2006. Annular centrifugal contactors - A review. *Chemical engineering research and design* [Online], 84(7 A), pp.522–542. Available from: https://doi.org/10.1205/cherd.05219.

Venkatakrishnan, V., 1993. On the accuracy of limiters and convergence to steady state solutions. *31st aerospace sciences meeting & exhibit*. pp.1–11.

Vercauteren, J., Bosschaerts, W., Baelmans, M. and Persoons, T., 2010. Numerical investigation on the measurement error of static pressure taps in small scale channels [Online]. *Proceedings power mems, proceedings of the 10th international workshop on micro and nanotechnology for power generation and energy conversion applications (powermems)*. pp.295–298. Available from: http://cap.ee.ic.ac.uk/{~}pdm97/powermems/2010/poster-pdfs/295{_}Vercauteren{_}69.pdf.

Volk, A. and Kähler, C.J., 2018. Density model for aqueous glycerol solutions [Online]. Available from: https://doi.org/10.1007/s00348-018-2527-y.

Vondál, J. and Hájek, J., 2011. Prediction of flow through swirl generator and validation by measured data. *Journal of physics: Conference series* [Online], 318. Available from: https://doi.org/10.1088/1742-6596/318/2/022026.

Vu, B.T., Gouldin, F.C., T. Vu, B., Gouldin, F.C., Vu, B.T. and Gouldin, F.C., 1982. Flow Measurements in a Model Swirl Combustor. *Aiaa journal* [Online], 20(5), pp.642–651. Available from: https://doi.org/10.2514/3.51122.

Wagner, T.C. and Kent, J.C., 1988. On the directional sensitivity of hot-wires: a new look at an old phenomenon. *Experiments in fluids* [Online], 6(8), pp.553–560. Available from: https://doi.org/10.1007/BF00196602.

Wallington, T.J., Anderson, J.E., He, X., Ruona, W.C., Shen, W., Vogt, R. and Winkler, S.L., 2020. *Light-Duty Vehicle Emissions: An Automotive Perspective*. Ford Motor Company.

Wang, S., Ren, C., Gui, N., Sun, Y., Tu, J., Yang, X. and Jiang, S., 2017. Experimental and numerical study on the circumferential pressure distribution on the wall of a 90° elbow pipe with circular section. *Annals of nuclear energy* [Online], 109, pp.419–430. Available from: https://doi.org/10.1016/j.anucene.2017.05.047.

Wang, W., Guo, J., Zhang, S., Yang, J., Ding, X. and Zhan, X., 2014. Numerical study on hydrodynamic characteristics of plate-fin heat exchanger using porous media approach. *Computers and chemical engineering* [Online], 61, pp.30–37. Available from: https://doi.org/10.1016/j.compchemeng.2013.10.010.

Wegner, B., Maltsev, A., Schneider, C. and Sadiki, A., 2003. Evaluation of U-Rans performance in predicting an unconfined swirling flow with precessing vortex core based on LES and experiments. *Proceedings of turbulence and shear flow phenomena* [Online], 3, pp.51–56. Available from: http://scholar.google.com/scholar?hl=en{&}btnG=Search{&}q=intitle:Evaluation+of+U-RANS+performance+in+predicting+an+unconfined+swirling+flow+with+precessing+vortex+core+based+on+LES+and+experiments{#}0.

Wegner, B., Maltsev, A., Schneider, C., Sadiki, A., Dreizler, A. and Janicka, J., 2004. Assessment of unsteady RANS in predicting swirl flow instability based on LES and experiments. *International journal of heat and fluid flow* [Online], 25(3), pp.528–536. Available from: https://doi.org/10.1016/j.ijheatfluidflow.2004.02.019.

Wernert, P. and Favier, D., 1999. Considerations about the phase averaging method with application to ELDV and PIV measurements over pitching airfoils. *Experiments in fluids* [Online], 27(6), pp.473–483. Available from: https://doi.org/10.1007/s003480050372.

Westerweel, J. and Scarano, F., 2005. Universal outlier detection for PIV data. *Experiments in fluids* [Online], 39(6), pp.1096–1100. Available from: https://doi.org/10.1007/s00348-005-0016-6.

Wilcox, D.C., 2008. Formulation of the k-w Turbulence Model Revisited. *Aiaa journal* [Online], 46, pp.2823–2838. Available from: https://doi.org/10.2514/1.36541.

Win Naung, S., Rahmati, M. and Farokhi, H., 2020. Direct Numerical Simulation of Interaction between Transient Flow and Blade Structure in a Modern Low-Pressure Turbine. *International journal of mechanical sciences* [Online], 192, p.106104. Available from: https://doi.org/10.1016/j.ijmecsci.2020.106104.

Winkler, S.L., Anderson, J.E., Garza, L., Ruona, W.C., Vogt, R. and Wallington, T.J., 2018. Vehicle criteria pollutant (PM, NOx, CO, HCs) emissions: how low should

we go? *npj climate and atmospheric science* [Online], 1(1), p.26. Available from: https://doi.org/10.1038/s41612-018-0037-5.

Xia, J.L., Smith, B.L., Benim, A.C., Schmidli, J. and Yadigaroglu, G., 1997. Effect of inlet and outlet boundary conditions on swirling flows. *Computers and fluids* [Online], 26(8), pp.811–823. Available from: https://doi.org/10.1016/S0045-7930(97)00026-1.

Yowakim, F.M. and Kind, R.J., 1988. Mean flow and turbulence measurements of annular swirling flows. *Journal of fluids engineering, transactions of the asme* [Online], 110(3), pp.257–263. Available from: https://doi.org/10.1115/1.3243542.

Zhang, X. and Romzek, M., 2008. Computational fluid dynamics (CFD) applications in vehicle exhaust system. *Sae technical papers* [Online], 2008(724), pp.776–790. Available from: https://doi.org/10.4271/2008-01-0612.

Zhang, Y. and Vanierschot, M., 2021. Modeling capabilities of unsteady RANS for the simulation of turbulent swirling flow in an annular bluff-body combustor geometry. *Applied mathematical modelling* [Online], 89, pp.1140–1154. Available from: https://doi.org/10.1016/j.apm.2020.07.037.

Zhou, L., 2017. Two-fluid turbulence modeling of swirling gas-particle flows — A review. *Powder technology* [Online], 314, pp.253–263. Available from: https://doi.org/10.1016/j.powtec.2016.07.021.

Zingg, D.W. and Godin, P., 2009. A perspective on turbulence models for aerodynamic flows. *International journal of computational fluid dynamics* [Online], 23(4), pp.327–335. Available from: https://doi.org/10.1080/10618560902776802.

Zuiderveld, K., 1994. Contrast Limited Adaptive Histogram Equalization [Online]. *Graphics gems*. Academic Press, pp.474–485. Available from: https://doi.org/10.1016/b978-0-12-336156-1.50061-6.

Appendix A

Experimental apparatus geometry

The CAD drawings used for the manufacturing of the test sections used in the current study are included here. The drawings are reproduced in scale from the CAD software used.

AutoCAD 2017 has been used for the design of the pipe with annular cross section and CATIA v5 for all the other drawings. Please note that to respect the scale specified under each drawing it is necessary to print the figure enclosed in the rectangular box on the specified paper size.

A.1 Convergent nozzle

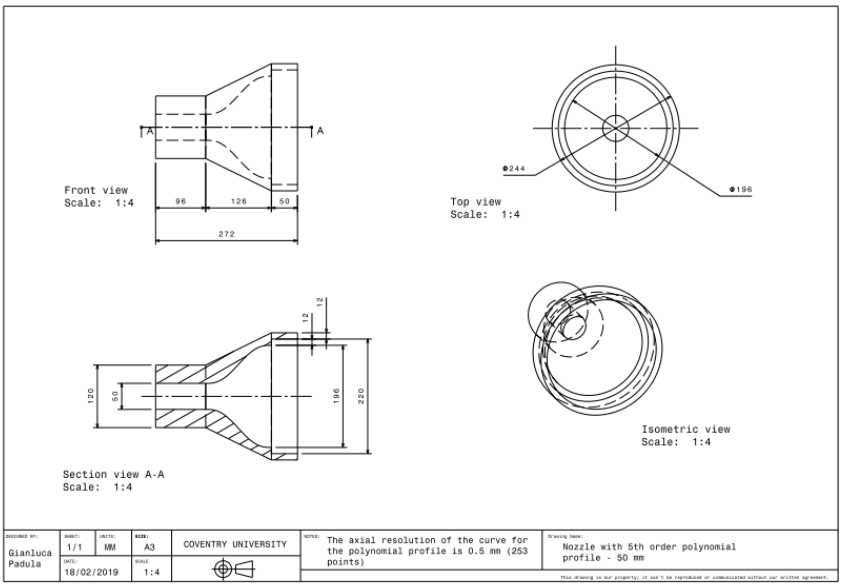

Figure A.1 Convergent nozzle used to prescribe uniform flow for the orifice plate measurements.

A.2 Pipe with annular cross section

A.2.1 Test section

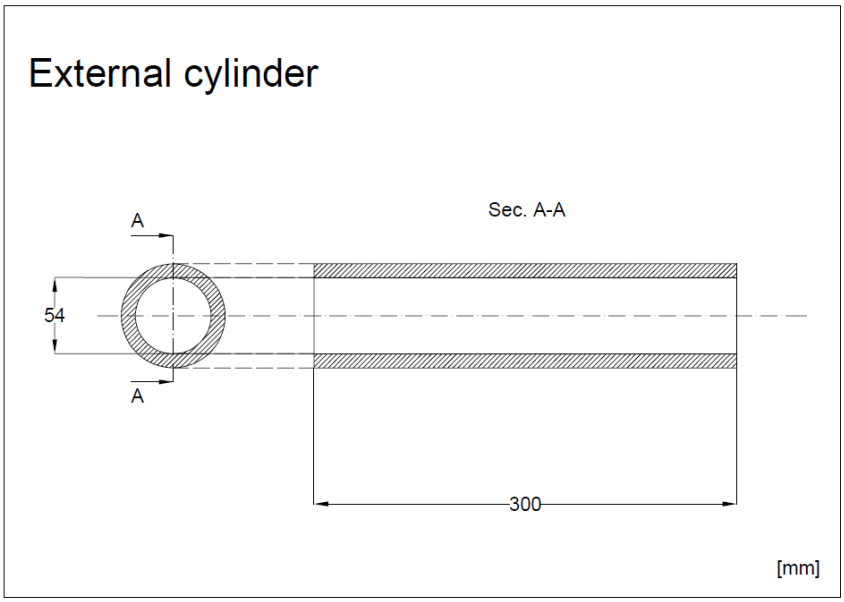

(a) External pipe

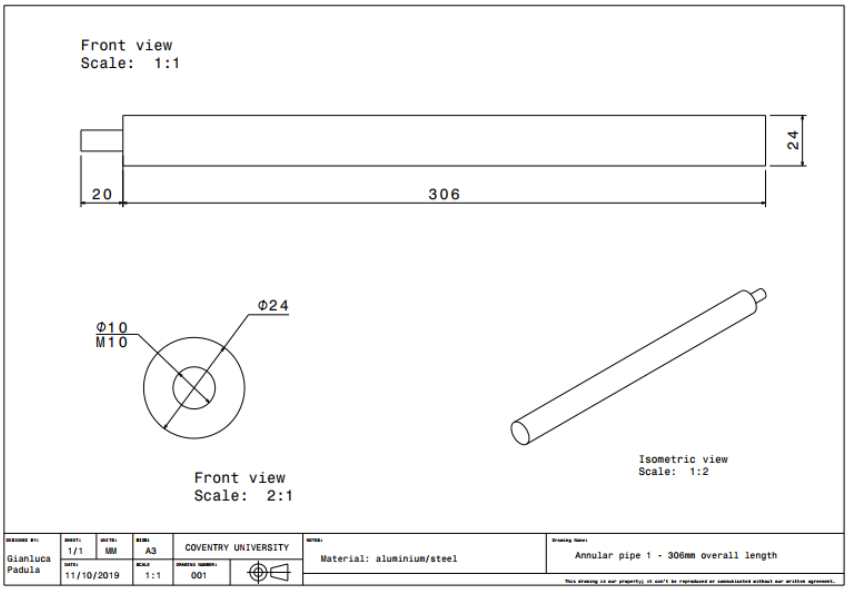

(b) Inner pipe

Figure A.2 Pipe with annular cross section drawings. External pipe dimensions (a), inner pipe dimensions (b).

A.2.2 Pressure tapping spacing

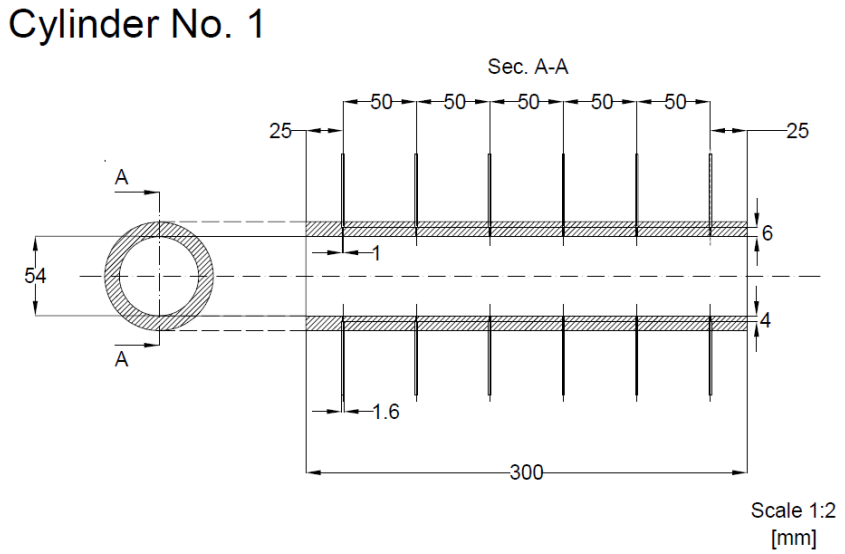

(a) Section AA

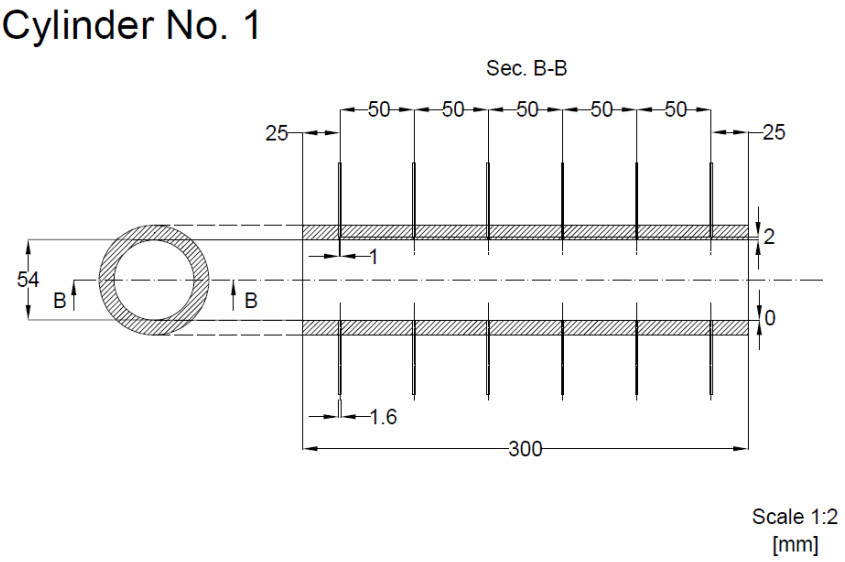

(b) Section BB

Figure A.3 Pipe with annular cross section drawings. Pressure holes distribution on *Cylinder 1*, section AA (a) and section BB (b).

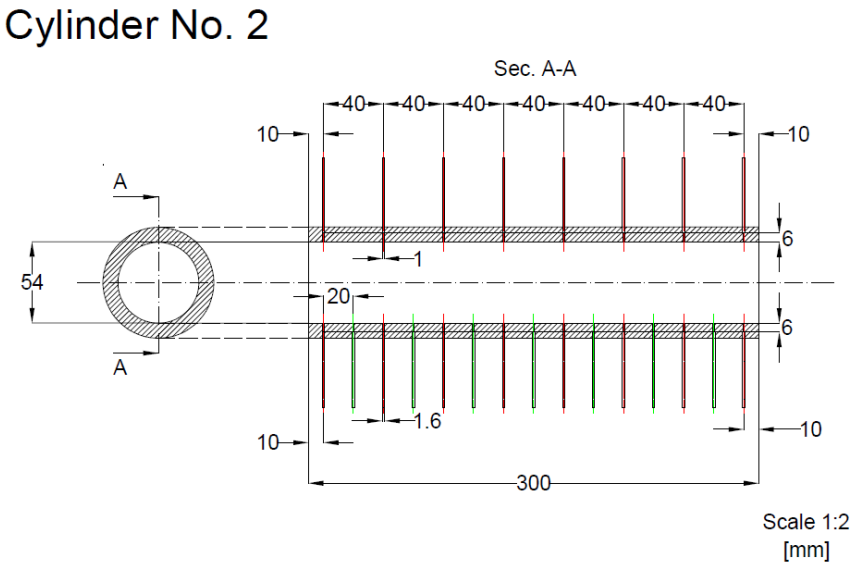

(a) Section AA

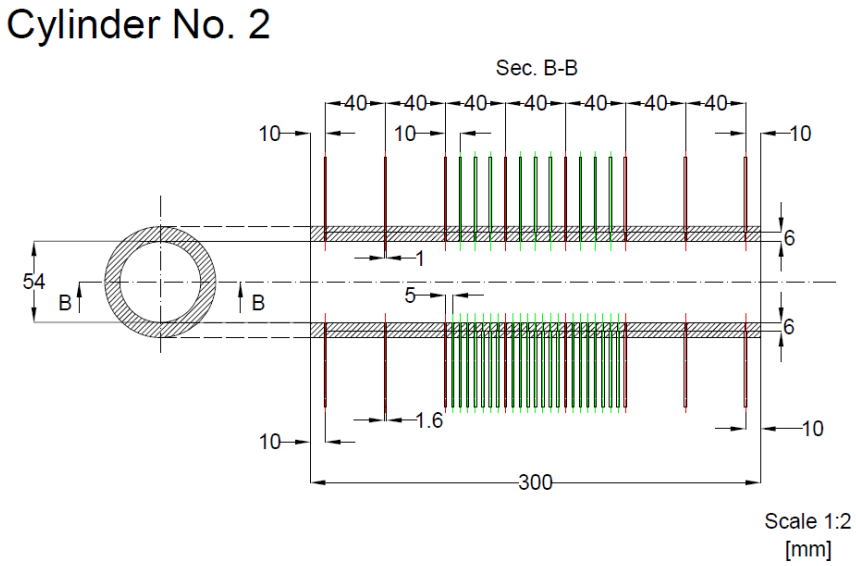

(b) Section BB

Figure A.4 Pipe with annular cross section drawings. Pressure holes distribution on *Cylinder 2*, section AA (a) and section BB (b).

A.3 Diffuser with sudden expansion

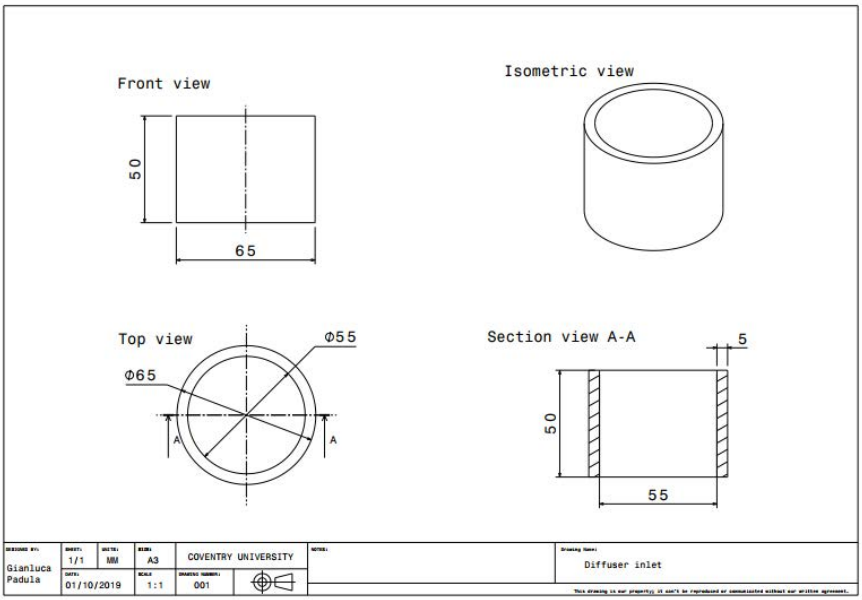

(a) Inlet pipe

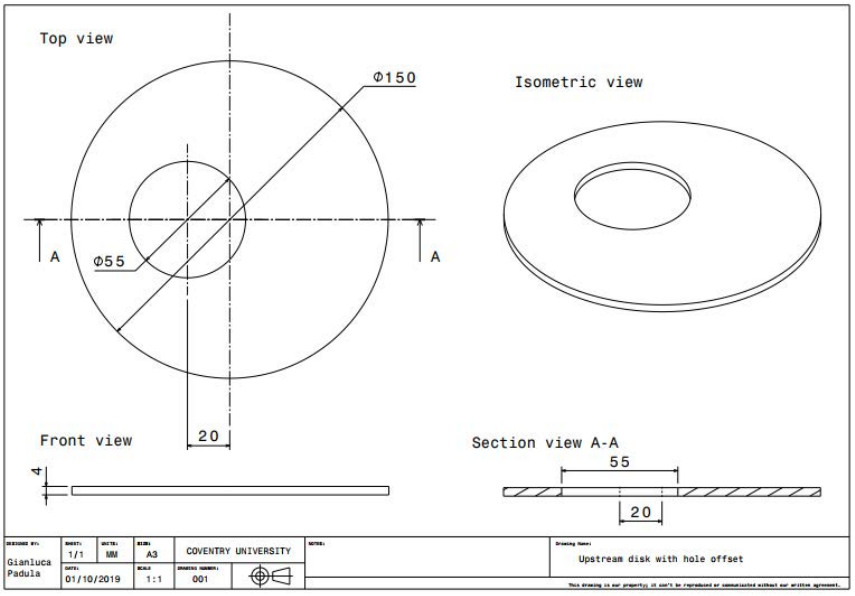

(b) Sudden expansion top

Figure A.5 Asymmetric glass diffuser with sudden expansion drawings. Diffuser inlet pipe (a) and asymmetric sudden expansion glass disk (b).

Appendix B

Viscous flow meter calibration

This appendix provides a review of the experimental process and of the numerical algorithm used to calculate the calibration curve for the mass flow rate trough the VFM. The experimental set-up and the numerical analysis of the results have been made following the standard ISO 5167-1:2003.

Differential pressure devices, such as orifice plates and Venturi flow meters, are commonly used to estimate the mass flow rate in both laminar and turbulent regimes. The mass flow rate calibration curve used for the current study (Figure 3.2) has been obtained using an orifice plate device, which presents several advantages over other methods, as discussed in (Miller, 1996).

The instrumentation used for the measurements trough the orifice plate is summarised in Table B.1. The uncertainty associated with the experiment is discussed in section 3.4.

Table B.1 Variables recorded for the VFM calibration, with the instrumentation used.

Measured quantity	**Instrumentation**
Orifice plate pressure	Furness Controls - Model 318
VFM pressure	Furness Controls - Model 318
VFM back-pressure	Furness Controls - Model 318
Ambient pressure	GE PACE 1000
VFM Temperature	Tenmars TM-747DU (K-type TC)
Ambient Temperature	Tenmars TM-747DU (K-type TC)

B.1 Experimental methodology

The experimental apparatus used for the mass flow rate estimation is shown in Figure B.1 and consists of a plenum device (1), a convergent nozzle (2), an upstream pipe (3), the orifice plate (4) and a downstream pipe. The plenum device has been connected to the VFM by using a reinforce plastic hose. The plenum houses a flow straightener and holds in place the convergent nozzle, aiming to obtain a uniform flow profile upstream the pipe.

The upstream and downstream pipes have been manufactured to hold the orifice plate and fulfil the requirements prescribed by the ISO, which prescribes that recommended pipe lengths are $10D_{op}$ and $5D_{op}$ respectively.

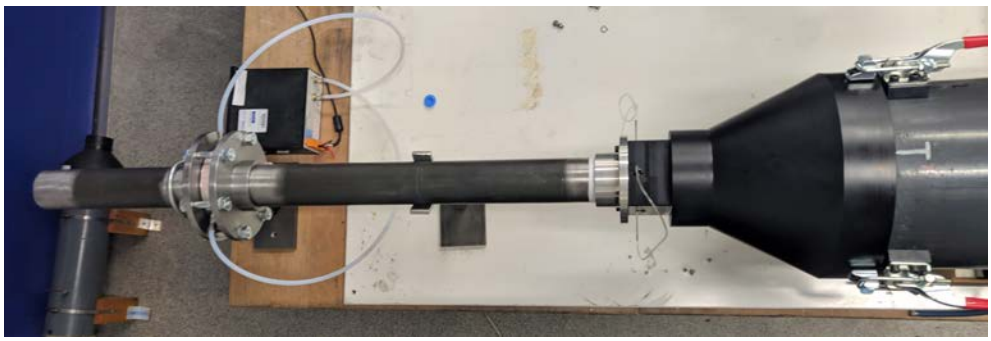

Figure B.1 Orifice plate device

B.1.1 Convergent nozzle design

The design of the convergent nozzle is based on the study by Bell 1988. The shape of the internal profile has been made using a 5^{th} order polynomial curve (shown in Figure B.2 a). A 3D CAD model has been prepared in CATIA v5 by revolving the profile around its axis (Figure B.2 b). The CAD drawing and the dimensions can be found in section A.1. The nozzle has been manufactured in Nylon by the Coventry University Technical Department using an Haas VF-3 machine, obtaining a uniform and smooth inner surface.

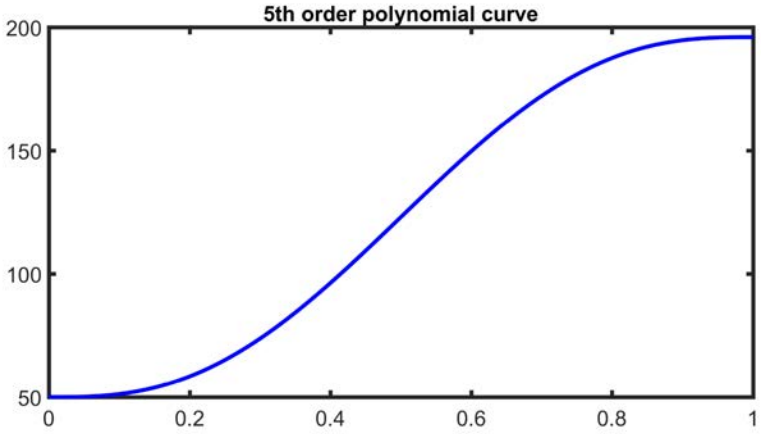

(a) Inner profile

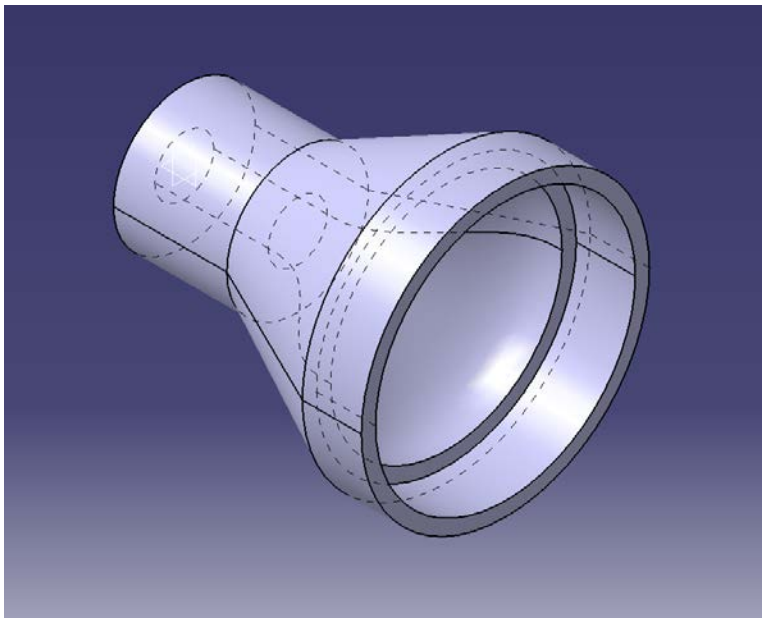

(b) 3D CAD

Figure B.2 Convergent nozzle design. Inner surface profile (a) and CAD model 3D view (b).

B.1.2 Orifice plate

The orifice plate device is a **Flowmeter OP-F-3** manufactured by Dwyer (2009) (schematic shown in Figure B.3).

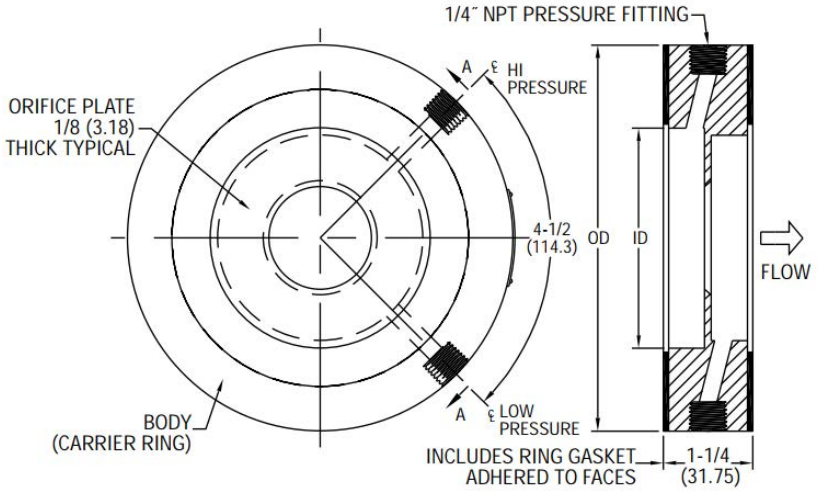

Figure B.3 Schematic of the orifice plate from the manufacturer manual (Dwyer, 2009)

The orifice plate design is based on the ISO 5167 (ISO, 2003b), respecting the proportions for the corner taps. The mounting and installation have been made fulfilling the guidelines reported in the manufacturer datasheet. The model used for the current analysis is the **OP-F-3**, with an internal diameter of 50 mm and a diameter ratio $\beta = 0.70 \pm 0.7\%$ (Dwyer, 2009).

B.1.3 Experimental procedure

The mass flow rate through the VFM can be controlled through the two valves upstream (Figure 3.1). The independent variable in the experiment has been assumed to be the differential pressure through the VFM, measured with the digital pressure transmitter Model 318 - Furness Controls (as described in section 3.1.1). Pressure has been varied between 0 Pa and 1500 Pa, with a step of 50 Pa up to 1000 Pa and a step of 100 Pa for the remaining values.

For each VFM pressure value, the stability of the VFM has been verified, waiting for a settled value on the digital transmitter. A maximum oscillation around the mean value imposed has been calculated to be 0.6 %. The corresponding differential pressure value measured at the orifice plate has been recorded, exhibiting an oscillation around the mean value within 1 %.

B.1.4 Measurements sets

The first set of experiments has been made without any downstream resistance device, keeping the experimental configuration represented in Figure B.1. Two other experimental sets have been carried out using two filters (shown in Figure B.4) to increase the downstream resistance.

A filter holder has been fitted downstream the convergent nozzle to house two different core filters, with consequent different resistance. The experimental rig has been modified as shown in Figure B.4a. Both filters are 300/8 Cpsi uncoated filters, with nominal length of 150 mm and diameter of 58 mm. The cross section of the two filters used is shown in Figure B.4b and Figure B.4c respectively for the plugged filter sample 568 and the unplugged filter sample 574.

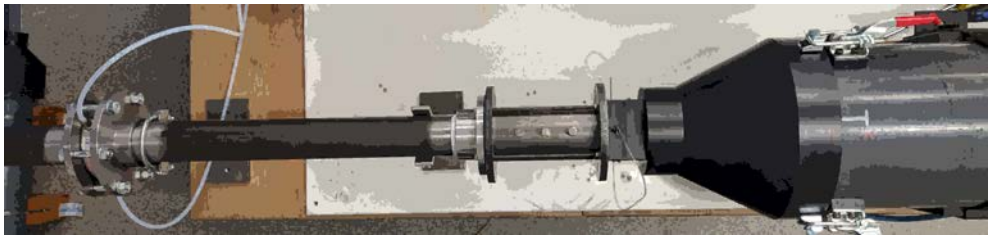

(a) Modified RIG with filter holder

(b) Filter 568

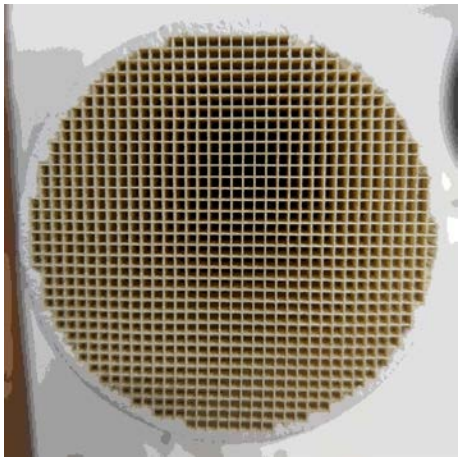

(c) Filter 574

Figure B.4 Modified test rig for the orifice plate measurements with high downstream resistance (a). Filter 568 section (b) and Filter 574 section (c).

B.2 Mass flow rate calculation

The calculation of the mass flow rate from the differential pressure measured at the orifice plate is based on the standard ISO (2003b). The mass flow rate equation can be

derived combining the continuity equation with Bernoulli equation. The final equation obtained rearranging the terms for the orifice plate (ISO, 2003b) is

$$q_m = \frac{C}{\sqrt{1-\beta^4}}\varepsilon\frac{\pi}{4}d^2\sqrt{2\Delta p\rho_1} \tag{B.1}$$

in which C is the discharge coefficient, β the diameter ratio of the orifice plate, ε is the expansibility factor, d is the throat diameter of the orifice plate, Δp is the differential pressure though the device and ρ_1 is the fluid density.

B.2.1 Gas coefficients estimation

The two coefficients C and ε approximate the real gas behaviour. The estimation of both coefficients is presented in the following paragraphs.

Discharge coefficient

The discharge coefficient is used to account for the differences between the mass flow rate calculated in ideal conditions and the real mass flow rate. It is defined as the ratio between the experimental mass flow rate and the ideal mass flow rate (Miller, 1996). The discharge coefficient is a function of the geometry of the orifice plate and of the flow entering the device. The semi-empirical correlation (ISO, 2003b) to calculate the discharge coefficient is

$$\begin{aligned} C = 0.5961 + 0.0261\beta^2 - 0.216\beta^8 + 0.000521\left(\frac{10^6\beta}{Re_D}\right)^{0.7} + \\ +(0.0188+0.0063A)\beta^{3.5}\left(\frac{10^6}{Re_D}\right)^{0.3} + \\ +(0.043+0.080e^{-10L_1}-0.123e^{-7L_1})(1-0.11A)\frac{\beta^4}{1-\beta^4}+ \\ -0.031(M'_2-0.8{M'_2}^{1.1})\beta^{1.3} \end{aligned} \tag{B.2}$$

where β is the diameter ratio of the orifice plate, Re_D is the Reynolds number of the flow entering the device based on the pipe diameter (D), while the other terms are explained as follows.

The term A is calculated from

$$A = \left(\frac{19000\beta}{Re_D}\right)^{0.8} \tag{B.3}$$

while M'_2 accounts for the correction due to the distance of the downstream pressure tapping

$$M'_2 = \frac{2L'_2}{1-\beta} \tag{B.4}$$

The terms L_1 and L'_2 account for the pressure tappings positioning, more details are given in ISO (2003b). For corner tappings, like the ones used in the orifice plate here (Figure B.3), the standard prescribes that $L_1 = L'_2 = 0$, with a consequent simplification of Equation B.2.

Since C depends on Re_D (Equation B.2), which means that it depends on the upstream flow. An iterative procedure is therefore needed for the calculation of the discharge coefficient. A MATLAB function has been created for this purpose (`dischargecoefficient`) and integrated in the final script used to calculate the mass flow rate.

An example of the results obtained for the discharge coefficient without downstream resistance is shown in Figure B.5. The coefficient is converging (top plot) with an absolute tolerance below the threshold of 10^{-11} (middle plot), within a limited number of iterations (bottom plot).

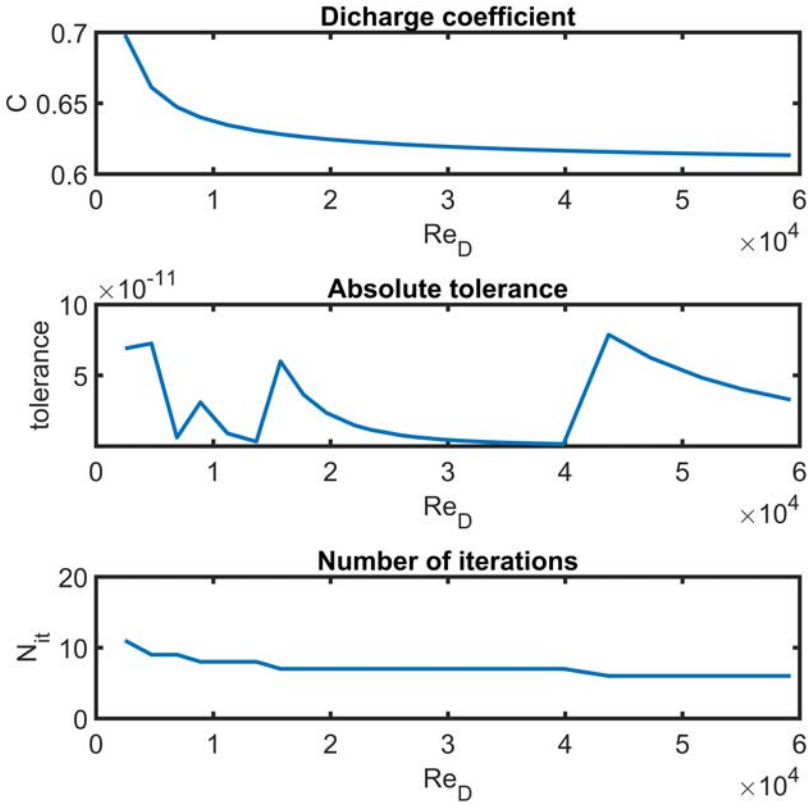

Figure B.5 Discharge coefficient (Set 1, no additional resistance). From top to bottom: discharge coefficient C, relative tolerance imposed between iterations and number of iterations N_{it}.

Expansibility factor coefficient

The expansibility factor ε accounts for the fluid compressibility in Equation B.1. A correlation exist to calculate the expansibility factor (ISO, 2003b) based on experimental observations

$$\varepsilon = 1 - (0.351 + 0.256\beta^4 + 0.93\beta^8)\left[1 - \left(\frac{p_2}{p_1}\right)\right]^{1/k} \tag{B.5}$$

in which β is the orifice plate diameter ratio, k is the isentropic coefficient, p_1 is the pressure measured at the upstream pressure tapping, while p_2 is the pressure measured at the downstream pressure tapping.

The measurements made for the current thesis have been made under the hypothesis of incompressible flow, which means that $\varepsilon = 1$. The assumption leads to an over-estimation of the mass flow rate for the cases in which compressibility should be

accounted for. More details will be given in the next sections with the analysis of the results.

B.2.2 Back-pressure correction

The back-pressure (p_{back}) introduced in section 3.1.1 accounts for the changes from the ideal conditions at which the calibration has been made.

The approach used in a previous calibration was based on the following correction

$$\Delta P_{cal} = \Delta P_{exp} \left(\frac{P_{exp}}{P_{cal}} \frac{T_{cal}}{T_{exp}} \right) \tag{B.6}$$

in which ΔP_{cal} is the differential pressure to apply at the VFM based on the ideal calibration curve, ΔP_{exp} is the corrected differential pressure to apply in the experiment, P_{cal} and T_{cal} respectively the pressure and temperature measured at the VFM during the calibration, while P_{exp} and T_{exp} represent the pressure and temperature measured at the VFM during the experiment.

The correction from Equation B.6 can be justified for an ideal gas, for which Boyle's law and Charle's law are verified.

From Boyle's law, if the temperature is kept constant, the increased back-pressure leads to a volume (Vol) change of the flow passing through the VFM, since it states that

$$p \cdot Vol = cost \tag{B.7}$$

From Equation B.7 if the back-pressure increases (so the pressure in the line upstream the VFM P_{exp}) the differential pressure though the VFM should be lower then the calibration one to target a certain mass flow rate.

The changes in temperature should be treated in the opposite way. From Charle's law, if the pressure is kept constant, the change in temperature leads to a volume (Vol) change of the flow passing through the VFM

$$\frac{T}{Vol} = cost \tag{B.8}$$

Consequently, if the temperature in the experiments (T_{exp}) is higher then the calibration temperature (T_{cal}) it is necessary to increase the VFM differential pressure to target the specific mass flow rate.

The above considerations do not account for compressibility effects, when the back-pressure exceeds $\approx$ 10 kPa ($\approx$ 0.1 % of the ambient pressure). This can happen in several experimental situations, e.g. when the mass flow rate is above $\approx$ 70 g/s and

becomes more significant when high resistance devices (catalysts or filters are used downstream).

It is therefore necessary to introduce corrections based on the real gas behaviour, which can be derived from theoretical considerations or from semi-empirical approaches.

Here, the correction from Equation B.6 has been compared with a new correction based on the mass flow rate equation.

The flow rate equations derived for differential devices are derived from theoretical assumptions and corrected using coefficients based on empirical evidence, with further re-arrangements and/or simplifications based on the device geometry (Miller, 1996). From Equation B.1 it can be seen that

$$q_m \propto \sqrt{\rho} \tag{B.9}$$

The ideal gas law

$$p \cdot Vol = \gamma RT \tag{B.10}$$

can be rewritten introducing the molar mass of the fluid (M) as

$$p \cdot M = \rho RT \tag{B.11}$$

from which it is possible to derive that

$$\rho \propto \frac{p}{T} \tag{B.12}$$

By substituting Equation B.12 in Equation B.9, it is possible to get

$$q_m \propto \sqrt{\frac{p}{T}} \tag{B.13}$$

The use of the *square root* approach (Equation B.13) mitigates the over-correction for the back-pressure that comes from the use of Equation B.6 when correcting the experimental values for the compressibility effects. This aspect will be clarified and demonstrated in the results section.

B.3 Results and discussion

B.3.1 Comparison between different calibration methods

The calculation of the mass flow rate Equation B.1 trough the orifice plate has been made using an iterative algorithm, as suggested by the guidelines in ISO (2003b).

The correlation between the mass flow rate and the VFM pressure (referred as *VFM calibration curve* has been made interpolating the available data with a 3^{rd} order polynomial equation

$$\dot{m}_{emp} = C_1 {p_{VFM}}^4 + C_2 {p_{VFM}}^3 + C_3 {p_{VFM}}^2 + C_4 p_{VFM} + C_5 \tag{B.14}$$

The 4 coefficient in Equation B.14 have been calculated using the MATLAB built-in function `polyfit` and are reported in Table B.2.

Table B.2 Interpolation coefficients for the $\dot{m}_{emp}$ (Equation B.14)

C_1	$-2.05 \cdot 10^{-12}$
C_2	$1.65 \cdot 10^{-8}$
C_3	$-3.84 \cdot 10^{-5}$
C_4	0.10
C_5	0.01

The calibration curve obtained from the orifice plate measurements without downstream resistance is shown in Figure B.6.

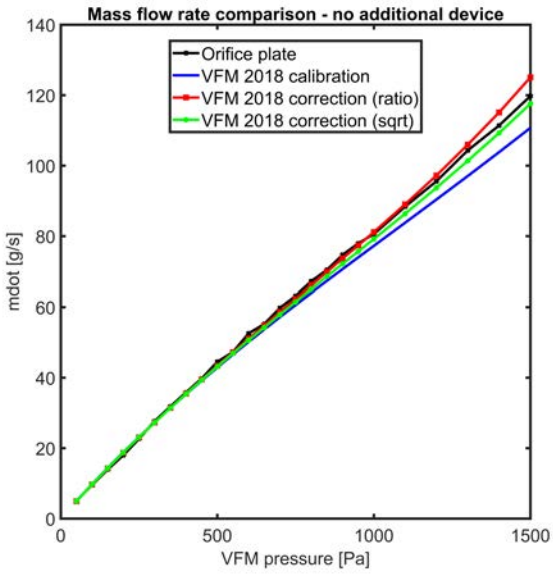

Figure B.6 Mass flow rate calibration curve

The baseline calibration from previous experiments is shown in blue, while the two curves obtained with the *ratio* and *square root* are shown in red and green respectively. By comparing the results obtained with the orifice plate (black line) it can be seen that

the effects of compressibility become relevant from ≈ 70 g/s, when the two corrected curve start to diverge from the orifice plate one. As mentioned in the previous section, it is expected that the orifice plate calculations over-predict the real mass flow rate, since the expansibility factor has been kept equal to 1.

The observation of the curves suggest that the *ratio* correction should be mitigated, since the flow rate is even more over-predicted then the orifice plate measurements (red line compared with black line). The use of the *square root* correction mitigates this effect and appears to be more in agreement with the theoretical expectations. However, more data are needed to validate this approach.

For the experiments carried out in the current thesis, the difference between the two corrections is small, therefore the effect has been neglected and the *ratio* correction has been used.

B.3.2 Effect of high back-pressure

The presence of the high resistance devices has been used to further evaluate the effects of the increased back-pressure. A comparison between the back-pressure obtained for the 3 measurement sets presented in the previous paragraph is shown in Figure B.7.

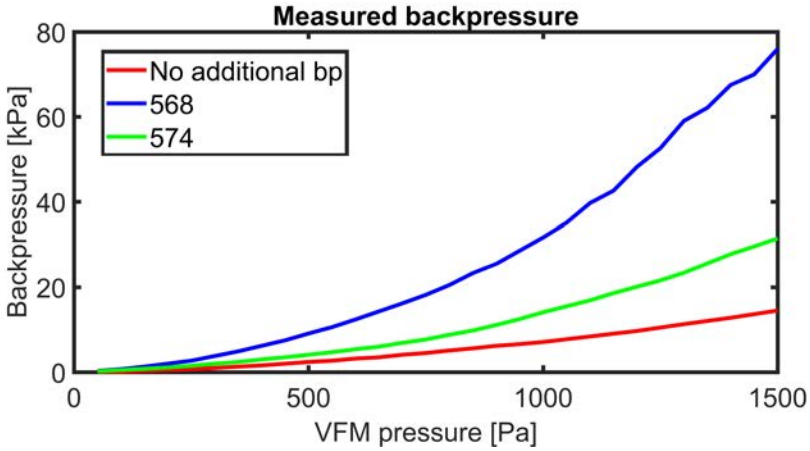

Figure B.7 Back-pressure curve

As a consequence of the increased back-pressure, the mass flow rate measured with filter 568 is shown in Figure B.8, while the one measured with 574 is shown in Figure B.9. It can be seen from both cases that the considerations made on the back-pressure correction are still valid. The over-prediction in the mass flow rate calculation obtained with the *ratio* correction, when compared to the orifice plate measurements, can be mitigated by the use of the *square root* correction.

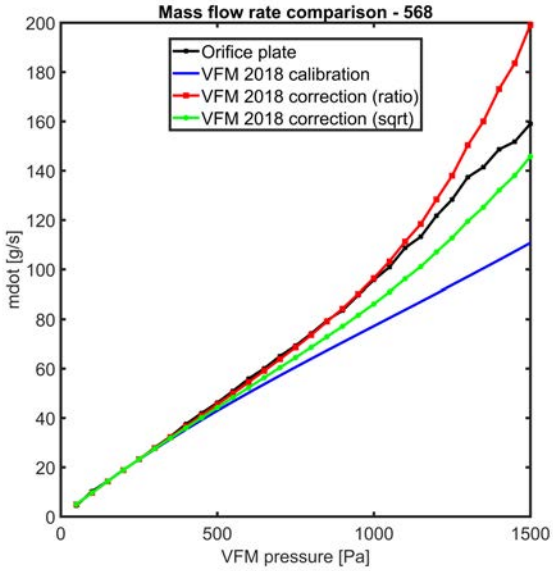

Figure B.8 Mass flow rate calculated with the high back pressure caused by Filter 568.

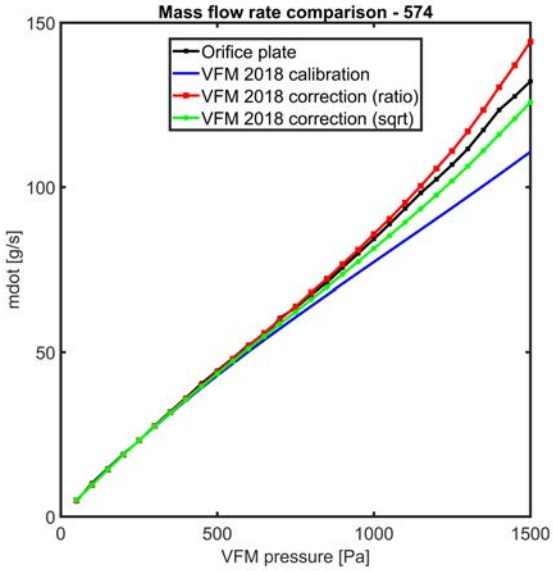

Figure B.9 Mass flow rate calculated with the high back pressure caused by Filter 574.

B.4 Use of the calibration curve

The use of the VFM calibration curve to determine the mass flow rate is summarised here. The procedure requires an iterative approach to minimise the error.

1. Calculate the VFM pressure to impose with the desired mass flow rate from the calibration curve.
2. Regulate the VFM valves to apply the VFM pressure using the estimated initial value from point 1.
3. Measure the VFM back-pressure and the VFM temperature.
4. Calculate the mass flow rate correction with the values from point 3 and estimate the new value for the VFM pressure.
5. Re-apply the VFM pressure based on the new corrected value.
6. Repeat steps 3,4 and 5 until a stable value is reached for VFM back-pressure and temperature.

Appendix C

Lab view interface

The VFM pressure and back pressure (section 3.1.1) have been monitored and recorded by using a LabView interface. Both differential pressures have been measured using a Furness Control Pressure Transmitter - Model 318 (FCO, 2013).

The pressure transmitters have been connected to a LabJack U6 Pro, which is a USB Data Acquisition (DAQ) used to acquire the signal and send it to a Workstation. A graphic user interface (GUI) in LabView has been made to monitor and log the pressure values.

The GUI welcome interface is shown in Figure C.1. The user can select two options:

1. manometer calibration
2. measurement mode

The first option allows to define the manometer calibration values used to convert the signal from voltage to pressure, as explained in section C.1. The second option enters in the measurement mode directly (section C.2), skipping the calibration.

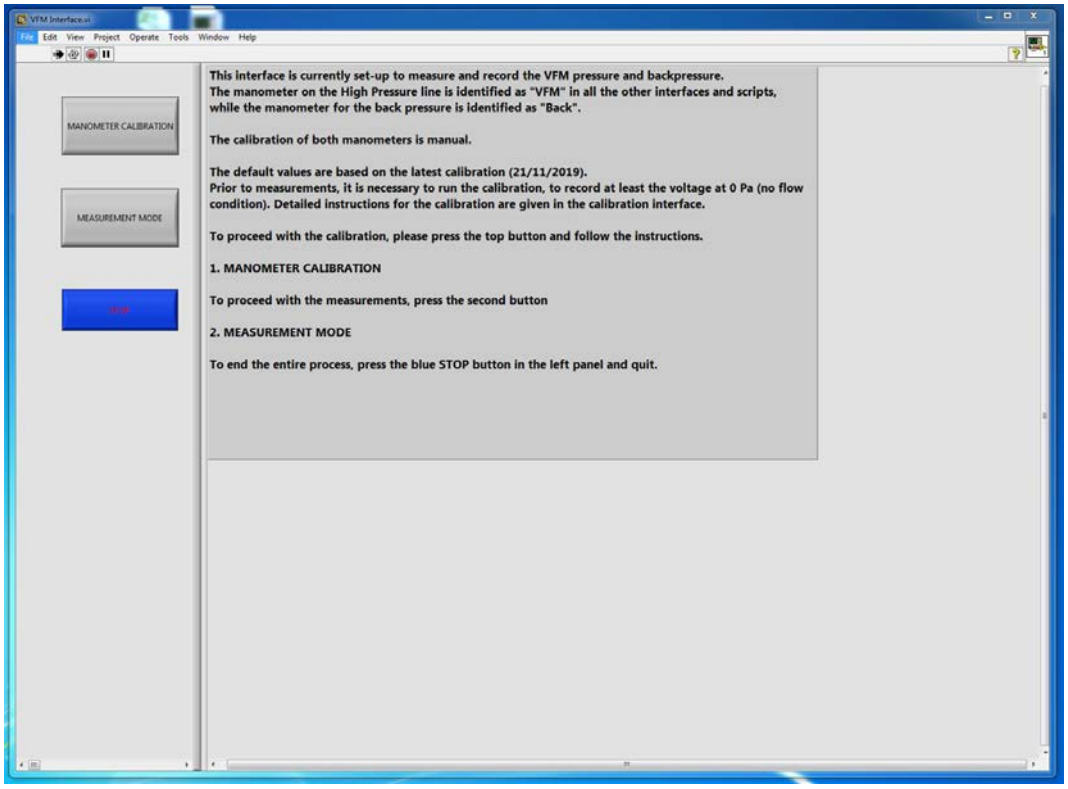

Figure C.1 LabView interface for VFM pressure logs.

C.1 Calibration mode

The *manometer calibration* allows the acquisition of the voltages corresponding to the minimum pressure and maximum pressure values for the transmitter. The pressure range on the FCO 318 transmitter can be manually set within the instrumentation range, by setting the minimum and maximum differential pressure (FCO, 2013).

The pressure/voltage conversion is linear, so a linear function is created using the input voltages in the calibration phase and used to calculate the slope of the curve.

The user should set the manometer in *TEST* mode (FCO, 2013) and acquire the low (DP MIN on FCO 318) and high voltage (DP MAX on FCO 318). The acquisition in the GUI is made by pressing the red button relative to the manometer, respectively the VFM differential pressure on top (Figure C.2) or the back-pressure button on the bottom (Figure C.2).

Detailed instructions are given in the interface, to guide the user through the different steps. More details about the FCO 318 settings and functions can be found in the manufacturer manual (FCO, 2013).

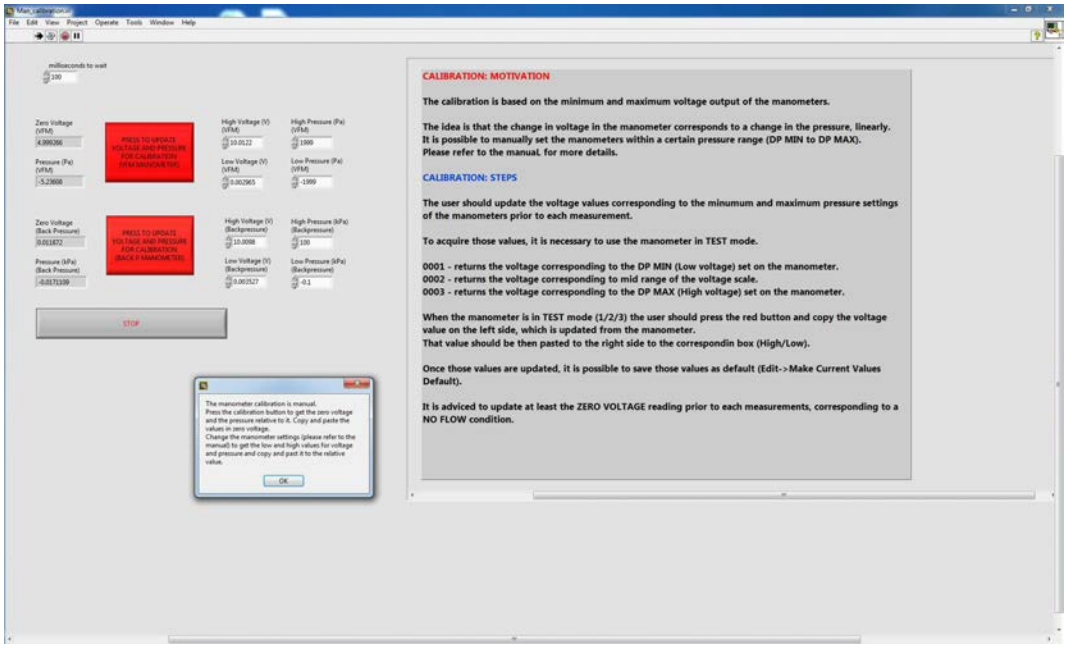

Figure C.2 VFM log GUI: calibration mode interface

C.2 Measurement mode

The measurement mode section allows to decide the time step used for the data acquisition, visualise the data in real time and store the data in a log file.

The user is prompted at the start of the interface with a separate window (Figure C.3a) which allows to define the number of samples (N_{log}) used to average the pressure value. The data acquired from the DAQ will be averaged every N_{log} before displaying and storing. The default option for both transmitters is to show the *real time* data ($N_{log} = 0$), which corresponds to the transmitter output update frequency of 50 ms.

A second window (Figure C.3b) prompts after the averaging choice setting, which allows to specify a file name and select the path to store the log file. The file is created as a standard Microsoft Excel file (.xlsx) and consists of 4 columns: acquisition time (1) and pressure for the VFM (2), acquisition time (3) and pressure for the VFM backpressure (4).

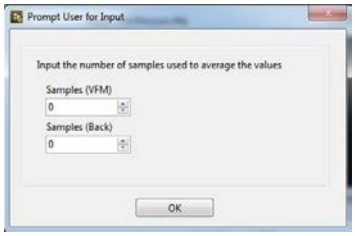

(a) Number of samples

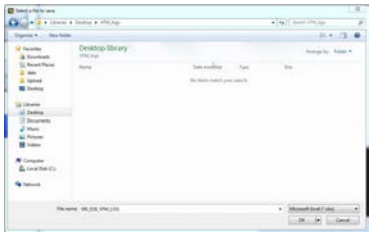

(b) Save window

Figure C.3 VFM log GUI: acquisition interface. Number of samples window (a), File save window (b).

The measurement GUI window is shown in Figure C.4. The plot on the right shows the VFM pressure, while the plot on the right shows the VFM backpressure. The current value is shown in the display at the bottom of both plots. The acquisition ends when the *STOP* button is clicked and the log file is saved.

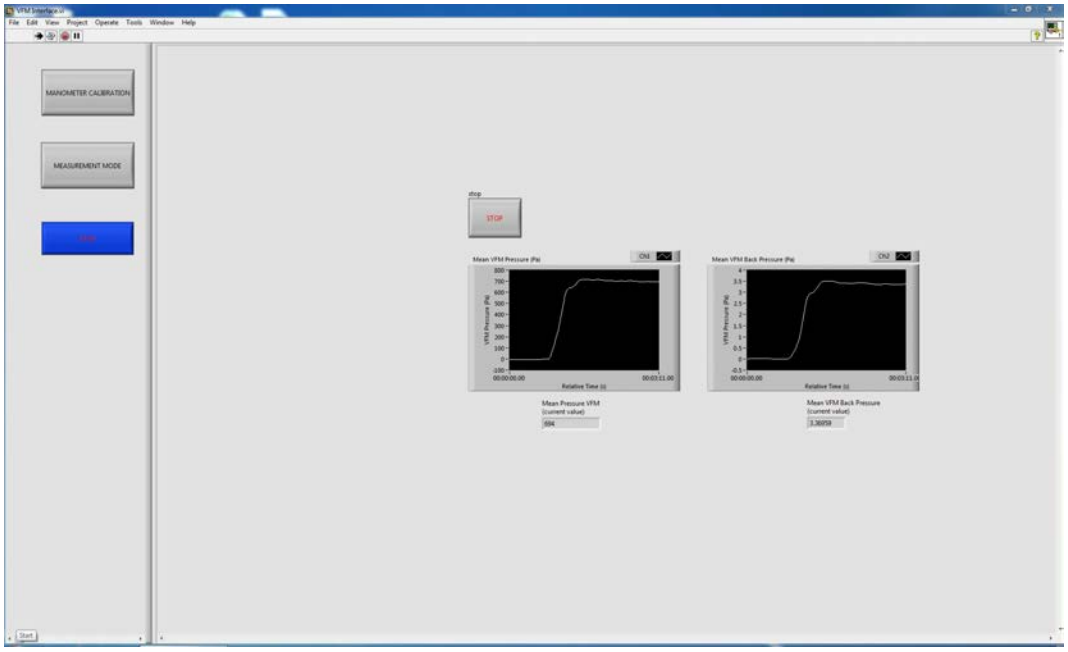

Figure C.4 VFM log GUI: acquisition interface

Appendix D

Porous medium implementation

The porous medium model has been defined in subsection 3.2.5. The implementation in StarCCM+ is described here.

D.1 Porous region modelling

The monolith region is defined as a porous region, which means that a porous source term (f_p) is included to the momentum equations

$$f_p = -P \cdot \underline{u} \tag{D.1}$$

The porous resistance tensor P is defined as

$$P = P_i|u| + P_u \tag{D.2}$$

in which P_i is the inertial resistance tensor and P_u is the viscous resistance tensor (CD-Adapco, 2018).

D.1.1 Porous resistance

The resistance trough the region should be imposed in terms of the tensor components. For the cases analysed in the current thesis, the inertial and resistance coefficients defined in subsection 3.2.5 are included in the respective resistance tensors as axial components, obtaining that $P_{ix} = \beta$ and $P_{ux} = \alpha$, while for the other two directions a high resistance equal to 10^6 is imposed, to account for the axial uni-directionality of the flow.

D.1.2 Entrance effect

The entrance effects (described in subsection 3.2.5) are specified in the porous medium model as an additional momentum source term, which is implemented in vectorial form $[0,0,-p_l](N/m^3)$.

The resulting scalar value p_l is calculated as a function of the flow velocity using the user-defined field function `PsourceScalar`, which is defined as

```
(abs(\$PLoss) > 0.1 ) ? \$PLoss : -\$PLossNeg
```

The two scalars used in the above formulation (`PLoss` and `PLossNeg`) are used to calculate the pressure loss due to the flow entering the monolith and the pressure loss due to negative flow re-entering it downstream respectively.

The upstream velocity is sampled at the `Pre-Cat` plane, while the downstream velocity is sampled at the `Post-Cat` plane. The pressure losses are updated at every iteration extracting the velocity at the two sampling planes defined above.

`PLoss` is calculated from

```
-interpolatePositionTable( @Table ( "PLossPlane" ) ,
 "PLossFormula")
```

`PLossNeg` is calculated from

```
-interpolatePositionTable( @Table ( "PLossPlaneNeg" ) ,
"PLossFormulaNeg")
```

The two field functions `PLossFormula` and `PLossFormulaNeg` are calculated at the `Pre-Cat` and `Post-Cat` planes respectively. This has been implemented extracting the two internal tables `PLossPlane` and `PLossPlaneNeg`.

The additional pressure loss due to the flow entering the monolith at a certain angle (defined in Equation 3.22) has been implemented in StarCCM+ using two separate user-defined functions, to distinguish between positive and negative sign of the equation. The loss at the entrance is calculated using the function `PLossFormula`, defined as

```
(\$\$Velocity[0] > 0.0001) ?
(0.5 * \$Density*(pow(\$\$Velocity[1],2)
+ pow( \$\$Velocity[2],2) )/ \$L ) : 0
```

In case of negative flow re-entering the monolith, the function is implemented in a similar way in `PLossFormulaNeg`

```
(\$\$Velocity[0] < 0) ?
(0.5 * \$Density*(pow(\$\$Velocity[1],2)
+ pow( \$\$Velocity[2],2) )/ \$L ) : 0
```

In both the above formulations, L is the monolith length, which is defined in a separate user-function.

D.2 Optimisation function

The optimisation algorithm has been implemented using a Java macro, to integrate with StarCCM+. The macro needs to be saved in the same folder of the simulation and can be run on a High Parallel Computing (HPC) cluster to speed up the simulation.

D.2.1 Simulation preparation

The porous medium region and the functions required for its implementation should be implemented as described in the previous sections.

The simulation should be created following the procedure described in section 3.2. The mesh should be prepared using the methodology presented in subsection 7.2.2. After the extraction of the 2D mesh, it is not necessary to initialise the solution.

D.2.2 Shape function implementation

A fundamental step during the preparation of the simulation for the optimisation is the definition of the shape function and of the global parameters used to define the geometry.

The channel diameter `Hd` and the `CellPitch` have been defined as global parameters. For the catalyst used in the current thesis, the shape function has been defined as

```
(mod(($${Position}[1]-${Hd}/2+${CellPitch}),
${CellPitch}) <=${w}) ? 1:0
```

D.2.3 Optimisation algorithm

The algorithm is presented for the catalyst model adopted in the current thesis. Modifications are required if other geometries are considered.

1. Define the number of optimisation cycles (N_{opti}).
2. Define the number of iterations of the simulation for each optimisation cycle (N_{sim}).
3. Define the initial distribution of the channels from the parameters defined in the simulation.
4. Allocate the variables for the shape function.
5. Calculate the solution with the initial distribution of the channels for N_{sim} iterations.
6. Calculate the average velocity downstream the porous medium section ($\bar{U}_{out}$).
7. Calculate the average velocity in each channel ($\bar{U}_{ch}$).
8. If $\bar{U}_{ch} > \bar{U}_{out}$, reduce the size of the channel for the next iteration (maximum change allowed set to 10%).
9. Calculate the solution with the new geometry for N_{sim} iterations.
10. Repeat the process from step 6 until the maximum number of cycles (N_{opti}) is reached.

Appendix E

HWA: additional data sets

E.1 Flow angle

The flow angle estimated using Equation 3.5 is shown in for all the cases. The same trend observed for the swirl level can be seen for all the cases, with a more dramatic decrease of the angle between Section 1 and Section 2 with the increasing swirl. The trend is independent from the Reynolds number.

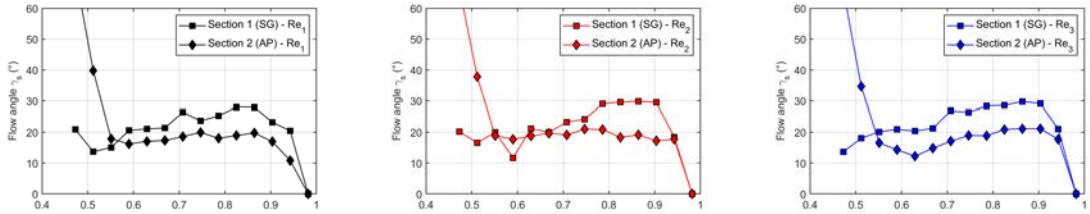

(a) $\theta_s = 4°$ - $Re_{noz_1} = 21720$ **(b)** $\theta_s = 4°$ - $Re_{noz_2} = 54374$ **(c)** $\theta_s = 4°$ - $Re_{noz_3} = 86880$

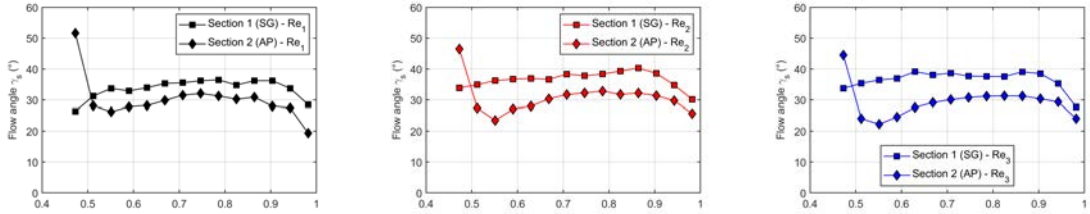

(d) $\theta_s = 7°$ - $Re_{noz_1} = 21720$ **(e)** $\theta_s = 7°$ - $Re_{noz_2} = 54374$ **(f)** $\theta_s = 7°$ - $Re_{noz_3} = 86880$

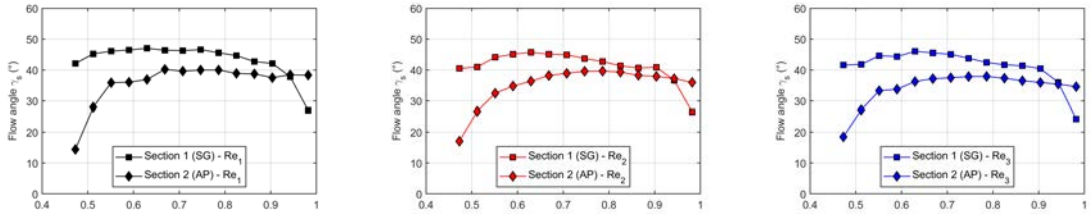

(g) $\theta_s = 10°$ - $Re_{noz_1} = 21720$ **(h)** $\theta_s = 10°$ - $Re_{noz_2} = 54374$ **(i)** $\theta_s = 10°$ - $Re_{noz_3} = 86880$

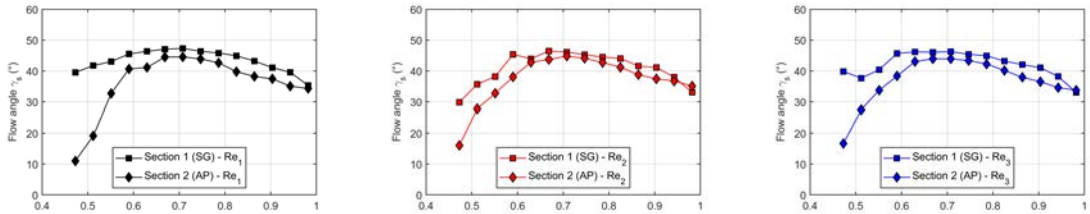

(j) $\theta_s = 14°$ - $Re_{noz_1} = 21720$ **(k)** $\theta_s = 14°$ - $Re_{noz_2} = 54374$ **(l)** $\theta_s = 14°$ - $Re_{noz_3} = 86880$

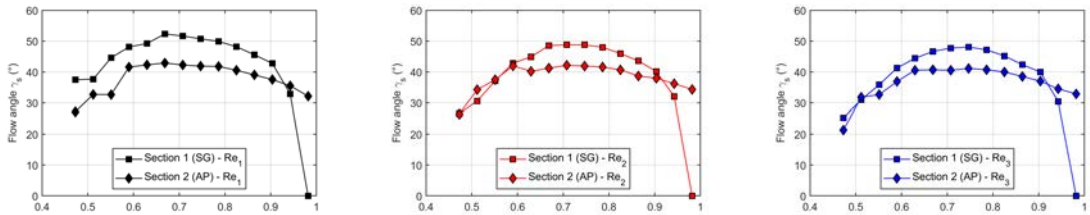

(m) $\theta_s = 18°$ - $Re_{noz_1} = 21720$ **(n)** $\theta_s = 18°$ - $Re_{noz_2} = 54374$ **(o)** $\theta_s = 18°$ - $Re_{noz_3} = 86880$

Figure E.1 Flow angle comparison between swirl generator section (Section 1, Figure 3.10, squares) and pipe outlet section (Section 2, Figure 3.10, diamonds). Reynolds number increasing from left to right: $Re_{noz_1} = 21720$ in black, $Re_{noz_2} = 54374$ in red, $Re_{noz_3} = 86880$ in blue. Swirl generator angle increasing from top to bottom.

E.2 Energy spectra

The analysis of the energy spectra is not within the objectives of the current study, so only the general trend is discussed here. The results can be used as reference at both boundaries for the development of boundary conditions and for validation of more complex modelling approaches, such as LES and DES.

The energy spectra have been extracted at $r/r_o = 0.73$ mm in the upper quadrant (positive Y in Figure 3.12b) for all the inflow conditions analysed (Table 3.3). The energy spectra are presented in Figure E.2 for Section 1 (pipe inlet), and in Figure E.3 for Section 2 (pipe outlet).

The energy increases with the Reynolds number (Rosenberg et al., 2013) for all the swirl levels, in both sections. An interesting effect on the energy cascade at frequencies higher then 100 Hz is observed for increasing swirl levels. By comparing the decay between low swirl (Figure E.2a, b) and the high swirl (Figure E.2c to f), it can be seen that the decay becomes less pronounced with increasing swirl. This trend is confirmed downstream the pipe (Figure E.2), suggesting that the energy cascade for increasing swirl behaves differently then the pipe flow. Further studies are needed to confirm this trend.

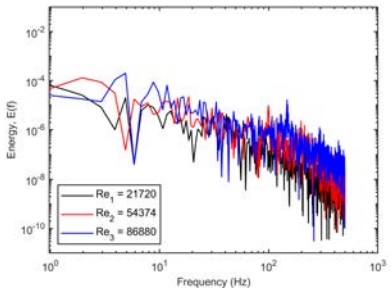

(a) $\theta_s = 0°$ (IN)

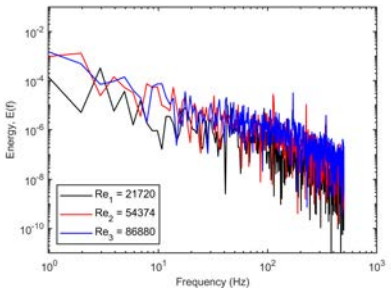

(b) $\theta_s = 4°$ (IN)

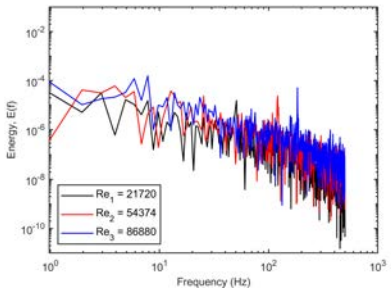

(c) $\theta_s = 7°$ (IN)

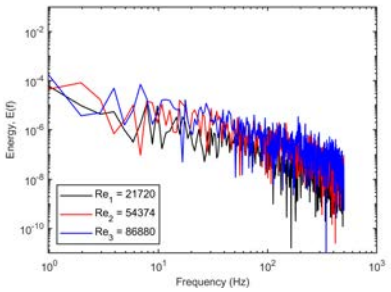

(d) $\theta_s = 10°$ (IN)

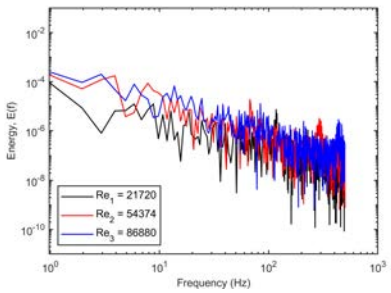

(e) $\theta_s = 14°$ (IN)

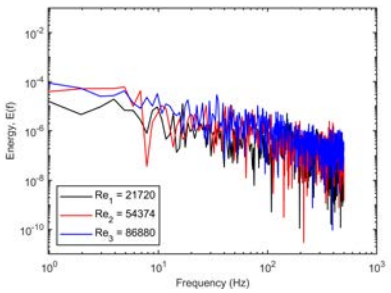

(f) $\theta_s = 18°$ (IN)

Figure E.2 Energy spectra at $r/r_o = 0.73$. Swirl level increasing from a to f. $Re_1 = 21720$ in black ($\bar{U} = 10.98$ m/s), $Re_2 = 54374$ in red ($\bar{U} = 27.66$ m/s), $Re_3 = 86880$ in blue ($\bar{U} = 43.91$ m/s). Section 1: pipe inlet.

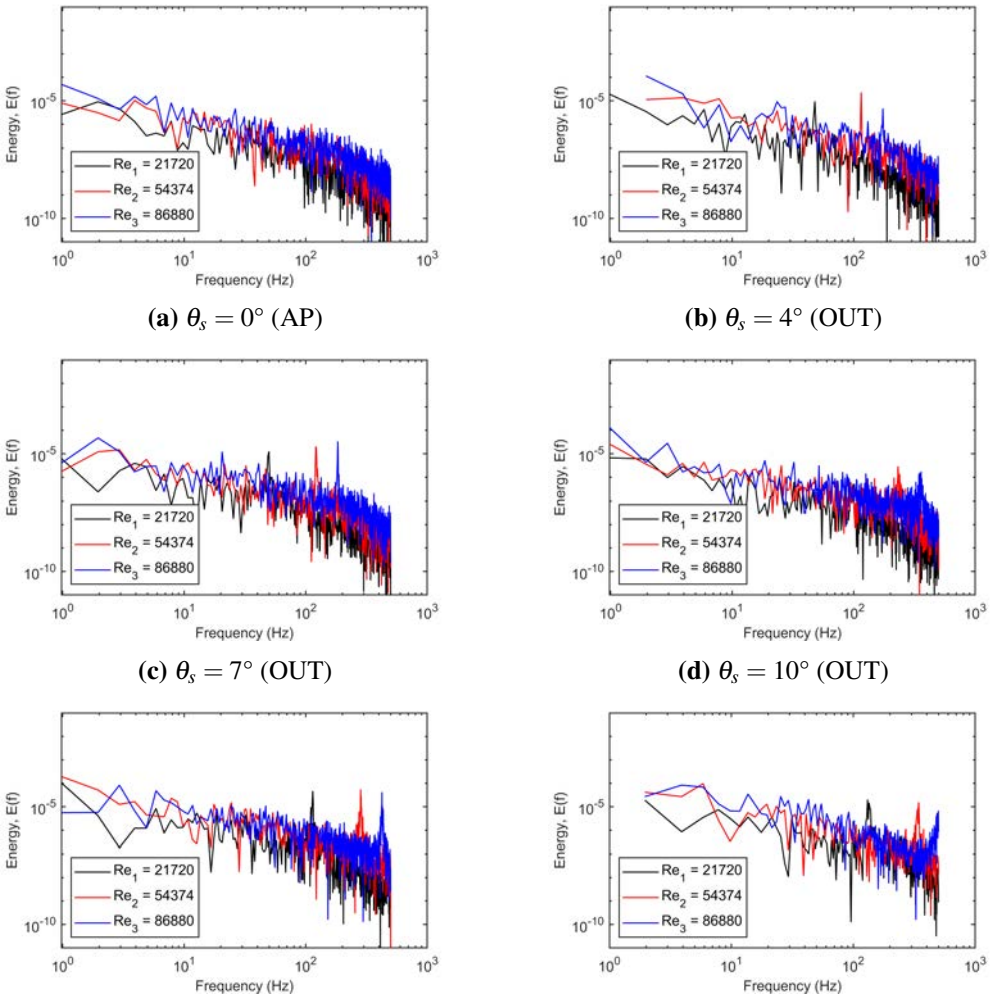

(a) $\theta_s = 0°$ (AP)

(b) $\theta_s = 4°$ (OUT)

(c) $\theta_s = 7°$ (OUT)

(d) $\theta_s = 10°$ (OUT)

(e) $\theta_s = 14°$ (OUT)

(f) $\theta_s = 18°$ (OUT)

Figure E.3 Energy spectra at $r/r_o = 0.73$. Swirl level increasing from a to f. $Re_1 = 21720$ in black ($\bar{U} = 10.98$ m/s), $Re_2 = 54374$ in red ($\bar{U} = 27.66$ m/s), $Re_3 = 86880$ in blue ($\bar{U} = 43.91$ m/s). Section 2: pipe outlet.

Appendix F

Certificates of Ethical Approval

Certificate of Ethical Approval

Applicant:

Gianluca Padula

Project Title:

CFD modeling of swirling flows in automotive aftertreatment systems.

This is to certify that the above named applicant has completed the Coventry University Ethical Approval process and their project has been confirmed and approved as Low Risk

Date of approval:

29 June 2017

Project Reference Number:

P51556

Certificate of Ethical Approval

Applicant:

Gianluca Padula

Project Title:

CFD modeling of swirling flows in automotive aftertreatment systems

This is to certify that the above named applicant has completed the Coventry University Ethical Approval process and their project has been confirmed and approved as Low Risk

Date of approval:

26 September 2018

Project Reference Number:

P71012